10pt

Optical Sub-Pixel Matching and Active Tectonics

Ivana Barišin

Thesis submitted to the University of Oxford

for the degree of Doctor of Philosophy

in

Earth Sciences

Department of Earth Sciences

and St.Cross College

University of Oxford

Trinity Term, 2015

Supervised by Prof. B. Parsons and Prof. I. Dowman

"To find yourself, think for yourself"

Socrates

Declaration

The contents of this thesis are all my own work, except where otherwise stated. The views and opinions expressed herein are mine and not necessarily those of any other person or body unless so attributed.

Citation: Barisin, I. (2011), D.Phil. thesis, University of Oxford, Department of Earth Sciences, Oxford, UK.
Keywords: Sub-pixel optical matching, InSAR, Afar, Dabbahu, Mexico, El Mayor-Cucapah, Iran, Zirkuh

This thesis has been typeset using LaTeX 2$_\varepsilon$, released under the LaTeX Project Public License (LPPL), and references were compiled using BibTeX. Most of the figures were produced using the open source Generic Mapping Tools (GMT) software, released under the GNU General Public License. All of the sub-pixel satellite optical matching results were obtained using COSI-Corr software , copyright 2004 Tectonics Observatory/CALTECH. Interferometric SAR processing was performed using ROI_PAC, released through Open Channel Foundation, copyright 2002–2008 Caltech/Jet Propulsion Laboratory.

Thank you Pete, Ed, Helen, Marcus, Victoria, Richard, Rich, Laura, Suzi, Mike, John, Tim, Yu, Sam, Al, Isabell. It has been a real privilage to get to know so many wonderfull people. Thank you to my parents. And the biggest thank you goes to Rob. I dedicate this thesis to my precious daughter Helena and my loving husband Rob.

Abstract

Investigating continental deformation using sub-pixel satellite optical matching

Ivana Barišin
St. Cross, Oxford
Doctor of Philosophy in Earth Sciences

Trinity Term, 2015

In this thesis I use sub-pixel optical matching, Interferometric Synthetic Aperture Radar (InSAR), and Light Detection and Ranging (lidar) spatial geodetic observations to produce reliable 3D displacement fields caused by co-seismic events and reliable earthquake source models with slip distribution on fault planes.

I produce horizontal displacement maps for the 2005 Dabbahu segment, Afar using SPOT4 satellite images. By combining InSAR descending data and range offsets with optical sub-pixel I produced a vertical displacement map of the event. I attempted to perform the inversion of the dataset obtained by sub-pixel matching but I found that datasets are not well suited for the typical numerical inversion, and I fit data with direct dislocation modelling instead.

I identify biases and errors that arise from optical sub-pixel matching of satellite images using many horizontal datasets constructed using SPOT5 images for the El Mayor-Cucapah earthquake. I develop algorithms for removal of some of these biases from horizontal displacement maps. Using sub-pixel matching I asses the quality of several DEMs available to me for study of the El Mayor-Cucapah earthquake.

I developed a novel technique for producing vertical displacement maps caused by an earthquake by combining archived pre-event satellite images with post-event acquired lidar. I use this technique to produce a vertical displacement map of the El Mayor-Cucapah earthquake.

I produce a source model of the El Mayor-Cucapah earthquake by inverting InSAR datasets using the method. After attempts to do joint inversion of InSAR and optical sub-pixel matching I developed the code to use Bayesian inversion instead, because its advantages when it comes to joint modelling of datasets. I sucessfully invert four InSAR datasets on seven fault planes using the Bayesian approach. I found that the results of the Bayesian inversion are very similar to the results of the optimization inversion.

Extended Abstract

Investigating continental deformation using sub-pixel satellite optical matching

Ivana Barišin
St. Cross, Oxford
Doctor of Philosophy in Earth Sciences

Trinity Term, 2015

Sub-pixel satellite optical matching is a theme common to all chapters in this thesis. Optical matching with sub-pixel resolution is a powerful tool for measuring crustal deformation, in particular deformation that goes right up to the earthquake making it possible to study features of the deformation in fine detail and to measure the displacements on the fault remotely. The basic idea of the technique is to match the image before with the image after the event to obtain the displacements caused by an earthquake or any tectonics or geomorphological phenomena.

Pre- and post-event images are acquired continuously by mid-range spatial resolution sensors (2.5-30 m) with SPOT(1, 2, 4, 5), Landsat(6, 7) and Aster satellite families. The images have been obtained over last 30 years, and have built a large global archive of satellite optical images. Large earthquakes will have several meters of displacements but the rupture may not be visible by directly comparing the image before and the image after. Sub-pixel matching technique can make measurements of the surface displacements that are smaller than the nominal spatial resolution used for matching. An ideal tool for investigating co-seismic event. A new generation of sub-meter spatial resolution cameras on satellites such as for example GeoEye, Worldview, Pleiades, KOMPSAT, Quickbird acquire images that in the future can be used for measuring post-seismic motion.

There are a number of theories, algorithms and methods that are compiled in order to make sub-pixel image matching possible. They include two families of techniques: photogrammetric and signal processing. Photogrammetric methods correctly place the

acquired image from the satellite into a ground coordinate system and correct any topographic distortions resulting from non-ideal position of the satellite during the acquisition. Sub-pixel matching used in this thesis is based on the Fourier analysis and signal-processing techniques are vital for correct noise removal in the frequency domain and for determining the sub-pixel part of the displacement.

I create horizontal offsets using sub-pixel optical matching for therifting episode of Dabbahu Magmatic Segment in Afar to reveal a detailed picture of the surface deformation not only in the far field of the rifting event but also a very detailed deformation above the rift itself. Next, I derive the vertical offsets by combining the InSAR and its range offsets with horizontal displacements obtained by sub-pixel matching of the images. Using the horizontal displacements, I fit a dislocation model of the event with complex geometry of interplay between a dyke and normal faulting. Overlain horizontal and vertical displacements over topography reveal that the Dabbahu segment occurred away from the existing geomorphic axis. Even though the SPOT4 images I used were collected in ideal arid conditions without vegetation and in a relatively flat terrain, making the quality of correlation exceptional, I struggled to do the inversion to find the earthquake source model. I resorted to direct modelling only, and to fitting the data by trial and error. I found that exceptional conditions of the satellite images for sub-pixel matching are very rare and on the whole there are many limitations to optical sub-pixel matching, and inversions of such datasets are very limited.

My second case study: the 2010 El Mayor-Cucapah earthquake is used in three different ways to investigate the El Mayor-Cucapa earthquake. The first investigates various sources that cause bias signals in horizontal displacement maps derived by sub-pixel image matching. The second proposes a new way of directly deriving vertical displacements using Lidar measurements. Third study runs the inversion of observation of crustal defomrations to obtain an earthquake source model.

The optical sub-pixel matching technique is widely used in co-seismic earthquake studies to measure horizontal displacements on the faults directly. However, these studies are largely constrained to reading the offsets on the fault, but little progress has been made in the inversions of sub-pixel matching datasets for generation of the earthquake source models of the earthquakes. This has proven to be a difficult task because the matching measures displacements caused by the earthquakes, but also many other effects and biases, which then become part of the displacements maps. Although, the matching results do not suffer from the atmosperic errors the way InSAR does.

During the inversions the biases are mistaken for tectonic signals that can skew the result of inversion. I investigate these biases and errors in detail and find they can be separated in two groups: long and short wavelengths. I find that the long wavelength biases are caused by a step in the orthorectification stage of processing of post-event image. In order to achieve accurate orthorectification of the post-event image in respect to the pre-event image, the ground control points (also called tie-points in this case) must be selected from already orthrorectified pre-event images. However, by doing so, some tie points will be placed in the areas of deformation and will create a bias in determining the parameters used for post-event image correlation. I investigate the ways this can be mitigated and improved during the processing. I find several sources that are causing short wavelength error; vegetation and shadows, topography, and very dark or very bright areas on the images. I show that given the right sun position, vegetation, and general shadows can create a bias signal that can interfere with tectonic signal. I write two short algorithms: one for the removal of the signal created by the shadows caused by vegetation and the second for the removal of the signal caused by shadowing mountains. Topography used for orthorectification of the images can be a source of several types of biases, depending on the available topographic resolution, topographic accuracy and weather the topography is aligned with the images correctly or not. However, I show that the topographic misalignment may not always be a caveat.

Directly measuring vertical offsets directly using the satellite geodetic techniques was not possible until recently: InSAR observed the measurement in lin-of-sight, sub-pixel matching is only horizontal; GPS is too scarcely distributed and cannot capture accurate and detailed distributions of the vertical offsets. Lidar, which has emerged as a technology that can measure the topography with high accuracy, can be used to directly derive the vertical displacement map by differencing lidar topography collected before and after an earthquake. However, lidar coverage before the earthquake is very limited (only two cases so far), and more importantly, I show that simple differencing does not take into account the fact that earthquake displacements are three dimensional and that the horizontal displacement will have an impact on the vertical displacements. I outline a method by means of which it is possible to estimate high-resolution vertical displacements caused by an earthquake even when high-resolution dems are lacking before an event. I combine a highly accurate, post-event digital elevation model, (e.g. lidar), with archived satellite imagery. The resulting vertical dispalacement map traces the vertical offsets caused by the El Mayor-Cucapah earthquake that propagate through the high relief of the Sierra Cucapah mountain range. I compare the results of the vertical displacement with the vertical displacement obtained by differencing and they show a good agreement.

I produce the El Mayor-Cucapah sorce model in two ways: in the traditional well-conditioned optimised inversion that produces a single source model, and Bayesian sampling which returns a collection of solutions. To be ablt to run the inversions using Bayesian approach I have developed the code that can run joint inversions using data obtained by sub-pixel matching and InSAR. I run inversion with two asending and two descending InSAR datasets. Both inversion techniques produce very similar outcome.

Contents

List of Figures

List of Tables

Chapter 1

Introduction

Earth Sciences aims to understand the dynamic processes controlling the Earth's evolution. One branch of Earth Sciences focuses on tectonics, as continents drift across the globe colliding with each other or breaking apart, but constantly changing and deforming the Earth's surface. As a consequence of this drifting, colliding, and general movement of plates, some parts of the globe are exposed to earthquakes and volcanoes, which pose hazards to the people who live there. Earthquakes and volcanoes occur in response to physical forces acting on structures beneath the surface of the Earth. At present, deformation observations at depth are limited to seismic studies, but because they are equally sensitive to temperature and composition, descriptions of Earth structures at depth are ambiguous. There are a number of techniques that attempt to infer information about the Earth's interior from surface observations. My thesis uses space geodetic techniques to measure crustal movements at the surface, from which deformation sources at depth can be inferred. I briefly introduce four main space geodetic techniques: Global Positioning System (GPS), InSAR, optical subpixel matching, and lidar. I then look into ways that the observations from the space geodetic techniques are utilised to answer questions about the earthquake cycle.

1.1 Space geodetic measurements

Geodesy is the science of the shape, deformation, and gravity field of the Earth (Lambeck, 1988). Tectonic geodesy has been measuring crustal deformation caused by earthquakes

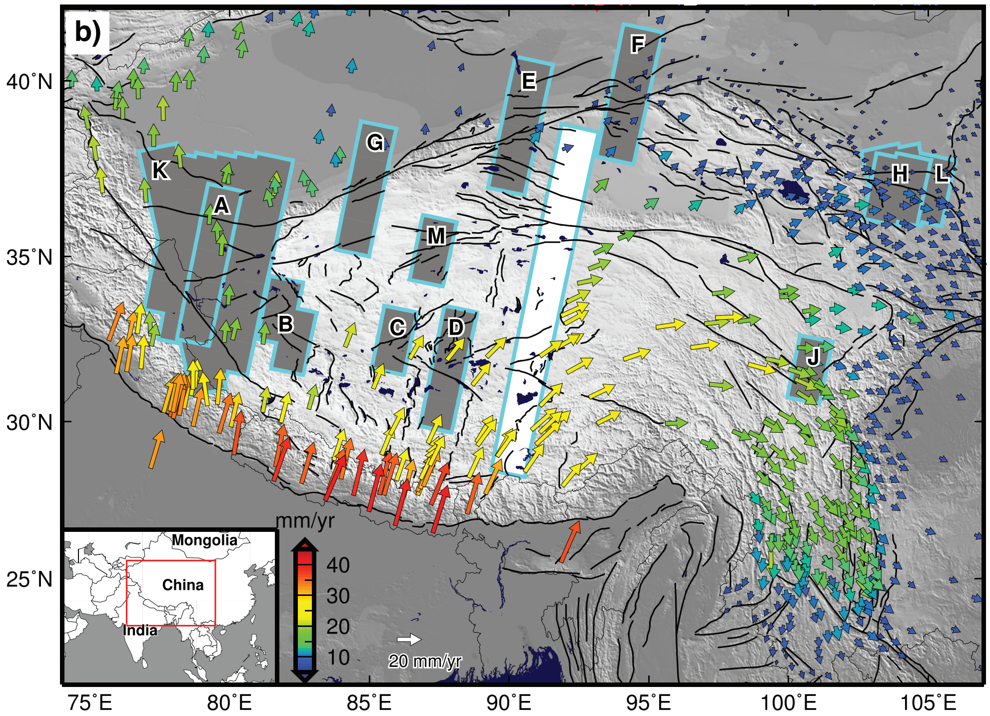

Figure 1.1: Arrows are horizontal-component GPS velocity vectors relative to stable Eurasia (Gan et al., 2007). The arrows are overlaid over the grey and white poligons outline spatial coverage of Synthetic Aperture Radar (SAR) data used in intersesmic studies up to the end of 2013. Adopted from Garthwaite et al. (2013)

and volcanoes for the last ≈ 100 years. In recent decades, with the launch of Earth-observation satellites such as Envisat, ERS, Sentinel, SPOT, Landsat, and 24 satellites that support the GPS network, space geodetic techniques have revolutionized the study of active tectonics, enabling measurements of crustal deformation on a global scale with high accuracy and precision.

1.1.1 GPS

Each GPS receiver is able to resolve 3D positioning within of a few millimetres, if it receives a signal from more than four satellites at the same time. Several sources of error such as ionospheric and tropospheric signal delays and multipath are mitigated by specially developed algorithms that include averaging. Crustal deformation due to coseismic, postseismic, or interseismic deformation (see Figure 1.4) can be observed with GPS. GPS was the first remote sensing technique to continuously monitor the complex nature of continental crustal deformation in the intraplate regions and at the plate boundaries (Figure 1.1).

1.1.2 InSAR

Differencing the phase between two satellite radar passes, known as interferometry, enables line-of-sight measurements of surface displacements with milimetric accuracy and high spatial resolution(from few meters), which can be used to identify the regions of high-strain. It has been widely used for coseismic studies (e.g. Wright et al., 2001; Simons et al., 2002), but due to the much smaller signal there have been fewer postseismic (e.g. Pollitz et al., 2000; Çakir et al., 2003; Ryder et al., 2007) and interseismic (e.g. Wright et al., 2001, 2004c; Wang et al., 2009; Peyret et al., 2011) studies. With the recent launch of Sentinel1A satellite and the anticipated launch of Sentinel1B due to take place in 2016, the frequency of satellite passes will be vastly improved resulting in higher spatial-temporal coverage leading to improved coherence, and better quality measurements. Garthwaite et al. (2013) showed that interseismic deformation can be mapped to asses seismic hazard and to identify previously unmapped faults for large areas covering 'hunderds' of kilometres (Figure 1.1). A number of authors, including Walters et al. (2011) and citetburgmann2006, showed that GPS and InSAR data can be combined to generate high resolution velocity maps with improved accuracy. (Figure 1.2). Although widely used, InSAR is still subject to various limitations: measurements are only in the satellites line-of-sight (LOS) (with reduced north-south sensitivity), temporal changes lead to reduced coherence of the displacement map, and it fails to observe deformation in the close vicinity of faults when the displacements are larger than half the width of the SAR wavelength (Massonnet et al., 1993; Massonnet & Feigl, 1998), and in the case of post-seismic and inter-seismic observations it is difficult to discriminate between the tectonic signal and atmospheric noise. Atmospheric artefacts can be mitigated by employing time series analysis over large sets of interferograms and using weather models (e.g. Li et al., 2005; Elliott et al., 2008; Jolivet et al., 2011)

1.1.3 Image matching with sub-pixel resolution

Optical geodetic technique measures horizontal crustal deformation by comparing pre-event and post-event images. By cross-correlating two images with sub-pixel resolution, surface displacements can be observed at higher resolution than the original images, which

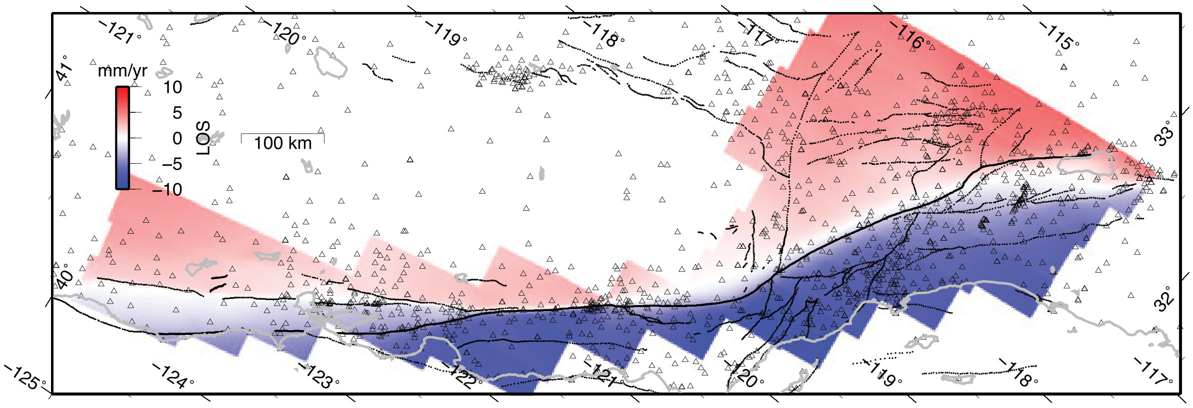

Figure 1.2: Crustal deformation across California shown as a map of relative range-change rates in the line-of-sight (LOS) for the period between June 2006 and 2010 obtained by ALOS satellites and constrained with GPS data for long-wavelength deformation. This is an example of integrations of GPS and InSAR measurements. Data from 18 tracks were also used in compiling this map. Positive velocities (reds) show the ground moving relatively away from the satellite. The small triangles mark the GPS stations used to constrain the velocity model. The black lines show the geological fault traces. Adapted from Tong et al. (2013).

makes this technique ideal for measuring coseismic events where the surface displacements vary significantly over short distances shown by van Puymbroeck et al. (2000) and Leprince et al. (2007), and in Chapter 2. Regions in close proximity to faults that are often decorrelated in InSAR, due to high velocity gradients, remain correlated in sub-pixel matching. Furthermore, regions that are decorrelated in optical images due to the cloud coverage are often correlated in InSAR. Consequently, the two techniques are complimentary and can be combined as shown in Chapter 5. Beside studying earthquakes, sub-pixel cross correlation of optical images has been used in a number of geomorphological studies such as examinations of variations in glacier velocities (Scherler et al., 2008, 2011; Herman et al., 2011), landslide movement (Suncar et al., 2013), and sand dune mitigation on the Earth (Scheidt & Lancaster, 2013) and Mars (Bridges et al., 2012).

1.1.4 LIDAR

Lidar is a remote sensing geodetic technique that measures surface topography, creating very accurate and detailed digital elevation models. The Lidar sensor emits pulses of light, which reflect off the ground and are received back at the lidar device. From the time interval between sending the pulse and receiving the return from the ground lidar generates high-resolution surface topographic maps. The location of the instrument is

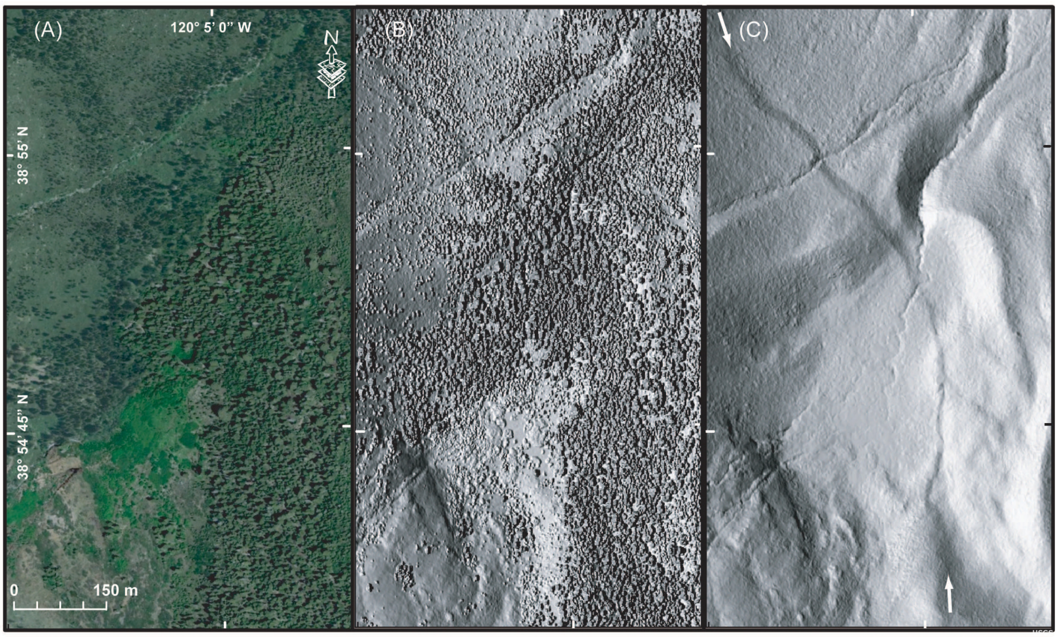

Figure 1.3: This is an example of aerial and lidar acquisition of the area near Lake Tahoe, California. (*a*) Image obtained by an aerial camera. (*b*) the same area surveyed with Lidar instrument. (*c*) after the vegetation is removed from (*b*) rupture scarp has become visible.

accurately determined by GPS and Inertial Measurement Units (IMU). Lidar yields high-resolution maps of topography, making it is possible to map faults and characterize their detailed surface expression without fieldwork. This is especially useful in areas of dense vegetation where removal of the early part of the return waveform (which is typically influenced by vegetation) allows the removal of vegetation cover, leaving a bare Earth's DEM. (Cunningham et al., 2006) and Figure 1.3. The detailed surface expressions of ruptures can reveal geomorphiv evidence for repeated past earthquakes (Zielke et al., 2010). Detailed maps of changes in surface topography before and after an earthquake can be used to estimate earthquake mechanisms and directly derive vertical displacements (Oskin et al., 2012; Nissen et al., 2012; Barišin et al., 2015).

1.2 Active tectonics questions geodetic space techniques can answer

The earthquake cycle was first identified in 1910 by Reid (1910) (Figure 1.4). It would be another 57 years before the theory of plate tectonics was introduced (McKenzie & Parker, 1967). Since then, there has been ongoing research into the origin of the forces

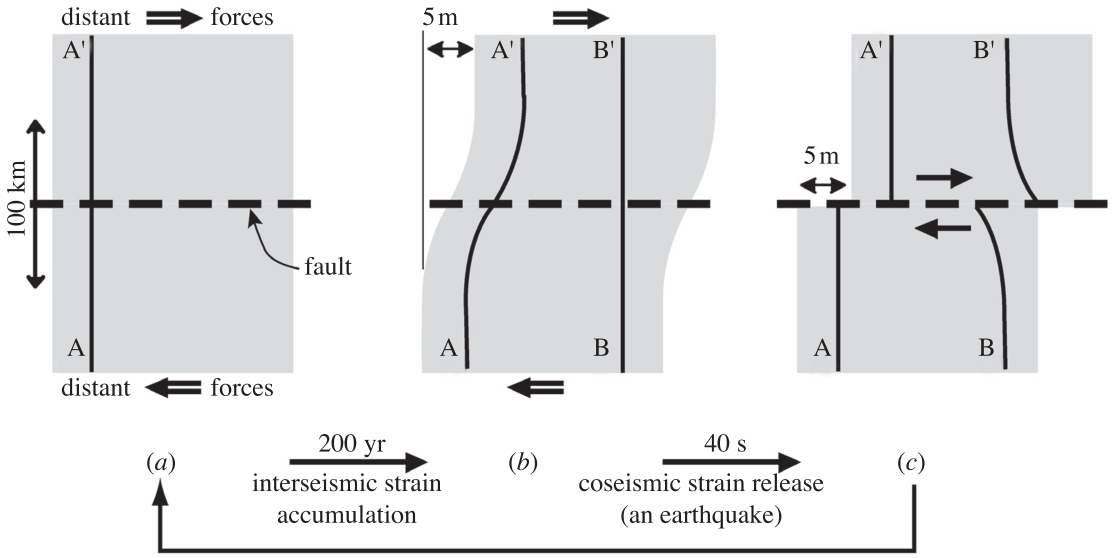

Figure 1.4: Reid's elastic rebound model of the earthquake cycle, reproduced from Wright (2002). (*a*) Map view of a region covering a hypothetical dextral strike-slip fault, just after the last earthquake. The profile A-A' is straight. (*b*) View of the same region after 200 years. The profile line A-A' has been wrapped across the locked fault by tectonic forces. This warping is known as interseismic strain accumulation. Note that the magnitude of the warping is exaggerated. (*c*) After an earthquake lasting 40s, all the strain accumulated in the past 200 years has been released leaving profile A-A' straight again, but with 5 m step in the fault. Profile B-B', straight immediately before the earthquake, is now warped to reflect the coseismic motion, with a 5 m step at the fault decaying with distance from the fault.

driving plate motion, and the properties of the interior structures that these forces act upon. The theory of plate tectonics is based on the assumption that the Earth's outer layer is broken into rigid plates that are in relative motion, with earthquakes occuring at plate boundaries where plates come into contact with each other. The abundance of crustal observations has enabled scientists to follow various lines of enquiry which can be examined in terms of continental scales and localised scales in the vicinity of earthquakes.

1.3 Lithospheric strength from interseismic observations

The theory of plate tectonics is based on the assumption that the Earth's outer layer is broken into rigid plates that are in relative motion to each other. These rigid plates are referred to as a lithosphere. The lithosphere comprises the Earth's upper crust, lower crust, and upper mantle, although it is unclear exactly where the lithosphere terminates.

The rheological and mechanical properties of the lithosphere hold the key to understanding tectonic deformations. The lithosphere responds in three ways to loading: brittle, elastic, and ductile. Quantifying these responses with rheological laws is one approach to investigating the strength of the continental lithosphere.

Lithospheric strength can be defined by the stress required to deform the lithosphere at varying rates of strain (England & Molnar, 2015). Elastic rebound theory is based on the principle that earthquake deformation is of the elastic-brittle type of deformation (Reid, 1910). When stress exceeds the rock strength or the friction on the fault, the upper part of the crust ruptures in the earthquake, resulting in the sudden release of strain. The material behaves according to Byerlee's law under low pressures and low temperatures in the Earth's crust (Byerlee, 1978). At depth, where temperatures and pressures are much higher, material under stress will deform in a ductile manner. Physical models, which attempt to simulate continental deformation, relate crustal strain rates with stresses present in the lithosphere with its rheological properties, such as viscosity.

1.3.1 Interseismic observations across broad regions

There are two key opposing models for continental deformation: the continuum model, and the block model. One way of inferring the rheology of the continental lithosphere is to model continental deformation on the assumption that the entire lithosphere is a single layer, which is approximated by viscous fluid that deforms by creeping according to the viscous flow law. The continuum approach is referred to as a the thin viscous sheet model (England & McKenzie, 1982). Strain rates on the surface are considered to be an expression of deformation within the lithosphere (e.g. Sonder & England, 1989), the result of body forces caused by variations in gravitational potential energy (Artyushkov, 1973), boundary forces (compressional and extensional), and shear forces at the base of the lithosphere (Bird & Piper, 1980; England & McKenzie, 1982; Molnar & Lyon-Caen, 1988). Stress balance equations relate gradients in deviatoric stresses to gradients in gravitational potential energy. The effective viscosity can be inferred using a power-law rheology which relates strain rates to deviatoric stress. This simplified approach makes several assumptions. The vertical strength of the layer is integrated strength across the lithospheric thickness, the horizontal velocities are constant throughout the sheet;

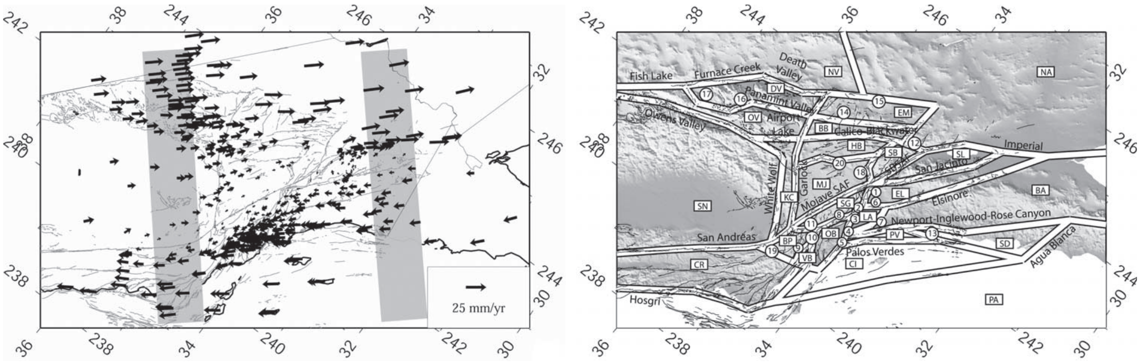

Figure 1.5: On the left is a map of Southern California with observed interseismic velocities from GPS measurements. On the right are shown the boundaries from the block model based on the known faults. Adapted from Meade & Hager (2005).

mantle traction forces at the base of the lithosphere are negligible; and the topography is locally isostatically compensated. Hearn et al. (2010) argue that different approaches to interpolations of the strain rate map will yield inconsistent results.

Rather than modelling continental deformation as a continuum, some studies have modelled continental deformation in forms of the relative motion of a number of blocks, where major active faults serve as boundaries to the blocks (e.g. McCaffrey, 2002; Meade & Hager, 2005; Peltzer & Tapponnier, 1988; Tapponnier et al., 1986) (Figure 1.5). It is assumed that deformation is a result of elastic strain accumulation on the locked faults, with the slip occurring below the locking depth and their expression is spread on the upper crust.

1.3.2 Interseismic observations in the vicinity of active faults

For large boundary strike-slip earthquakes continental interseismic deformation is greatest in the near vicinity of the fault (Figure 1.6).

During the interseismic period, the crustal part of the earthquake is locked and the ductile layer below the locked part moves aseismically. Deformation at the surface is typically modelled by an infinitely long fault that extends through the lithosphere, or as a distributed fault model with shear zone slip in a ductile layer beneath an elastic lid respectively (Molnar et al., 1999). The North Anatolian fault (Wright et al., 2001; Walters et al., 2011) and Alpine fault (Ellis et al., 2006; Wallace et al., 2007) are examples of faults where the deformation is localised on a deep fault plane, while the Marlborough

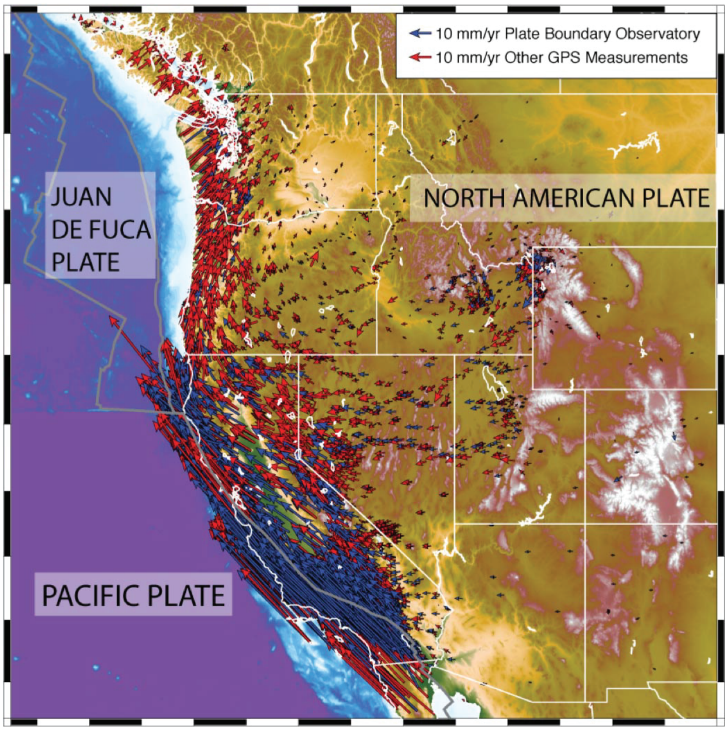

Figure 1.6: A map of North America with GPS velocities overlain on top of it. The velocities are much faster in the vicinity of the plate boundary than they are in the intraplate.

Fault Zone (Molnar et al., 1999), and San Andreas fault should be represented by the shear model as their crustal strain is distributed across several faults as shown Figure 1.2. Observed strain accumulation and locking depths derived from these models are indicators of earthquake hazards in region.

1.4 Lithospheric strength from postseismic observations

Ground motions immediately following an earthquake are observed to be greater than during the interseismic period. Stress changes caused by an earthquake in the upper crust act on the ductile material below, inducing flow in the ductile layer. Flow at depth creates a horizontal velocity field in the crust which can be observed using geodetic techniques,(GPS, InSAR, optical sub-pixel matching). Analysis of these transient displacements may shed some light on the rheology of the crust and mantle. Different authors have proposed that different mechanisms exists behind this phenomenon, including afterslip, viscoelastic relaxation and poroelastic rebound at the surface.

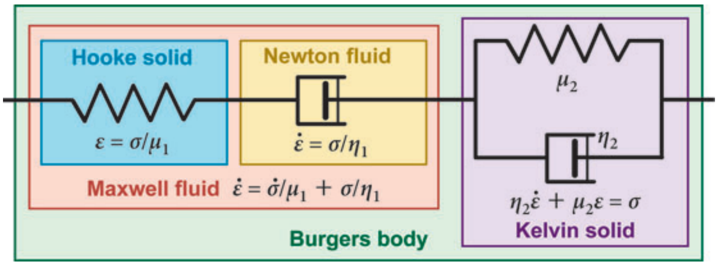

Figure 1.7: Viscoelastic rheologies can be graphically described by assemblies of springs and dashpots representing linear elastic (Hooke solid) and linear viscous (Newtonian fluid) elements. These elements and the equations they represent form idealized constitutive relationships that are the basis of most geodynamic, tectonic, and earthquake-cycle deformation models. Adapted from Bürgmann & Dresen (2008).

Viscoelastic relaxation

Materials in general will exhibit elastic and viscous properties in different environments, and it is assumed that materials of the lower crust and upper mantle will behave viscoelastically when under stress. The rheological properties of viscoelastic bodies can be described using a combination of elastic and viscous elements represented by springs and dashpots connected in series or parallel. The simplest of such analogies is the Maxwell solid which consists of an elastic and viscous element connected in series as shown in Figure 1.7 (Ryder et al., 2007). More complex analogies include the Kelvin solid which comprises elastic spring and viscous damper arranged in parallel. The lower crust and the upper mantle have been shown by a number of authors to behave with in a non-linear relationship between the stress and strain, referred to as power low creep. For simplicity, a linear relationship is more often used. Through viscoelastic relaxation modelling, many authors have tried to recover values of the viscosity of the lower crust and upper mantle (e.g. Pollitz et al., 2000; Hearn et al., 2002).

Afterslip

Afterslip is aseismic slip occuring on the fault plane itself or on its dominant extension following an earthquake (Bürgmann et al., 2002). It has been shown by a number of authors to yield good fits to measured data (e.g. Johnson et al., 2006; Chlieh et al., 2007). Afterslip studies can infer the frictional properties of the fault plane and improve our understanding of the change in frictional regime with increasing temperature at depth.

Distinguishing between afterslip and viscoelastic relaxation has proved to be difficult as they have been shown to be mathematically equivalent (i.e they produce similar surface signals) and there may be more than one type of deformation occurring simultanously (Ryder et al., 2007; Rollins et al., 2015). Some authors (Bürgmann et al., 2002; Hearn et al., 2002) suggest that afterslip can develop on the earthquake plane below where the actual earthquake occurred, although because the temperatures increase with depth, the frictional regime would be different.

Poroelastic rebound

Poroelastic rebound is a fluid related process in the upper crust, where, due to an earthquake, the fluid will migrate from high pressure areas to low pressure areas creating surface deformation (Jonsson et al., 2003; Peltzer & Tapponnier, 1988; Fialko, 2004). It will mainly create vertical deformation in the near field and the relaxation time is a relatively short period, usually months rather than years.

Summary

Thatcher & Pollitz (2008) compiled viscosity results of post-seimic relaxation studies for a large number of earthquakes in western North America and found that the lower crust is relatively strong, whilst the upper mantle is relatively weak (Figure 1.8(a)). Huang et al. (2014) compiled viscosity evaluations for the lower crust only, from postsesimic, interseismic, geodynamic (large areas), and lake rebound studies for Tibet. They found that low viscosity values for the lower crust are consistent (Figure 1.8(b)).

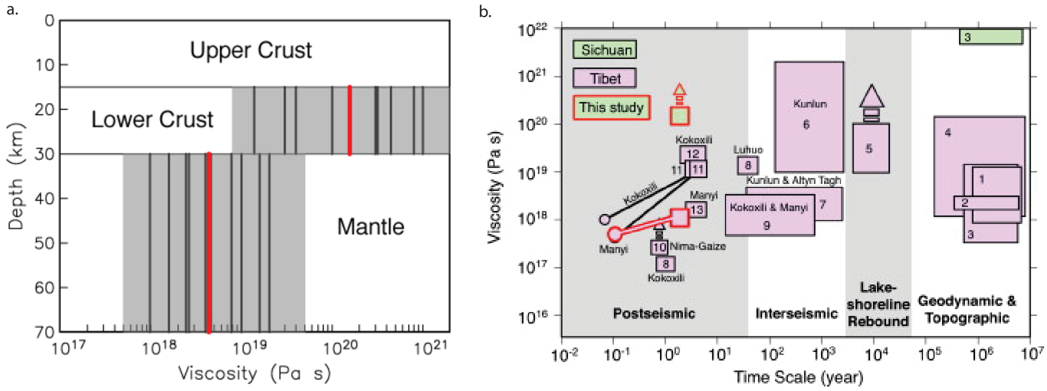

Figure 1.8: On the left is a compilation of the viscosity estimates for lower crust and upper mantle from numerouls postseismic studies that took place in western North America. Adopted from (Thatcher & Pollitz, 2008). On the right is a compilation of estimated viscosities for lower crust in Tibet derived from several different approaches. Adapted from Huang et al. (2014).

1.5 Elastic thickness as a measure of lithospheric strength

There have been attempts to define the properties of the lithosphere without geodetic space techniques but these are based mainly on seismic, thermal and gravity observations. The observations that Airy and Pratt's isostatic models were unable to describe behaviours over large regional scales, where plates act elastically and are able to support loading results, needing to define lithospheric elastic thickness on a regional scale. The lithosphere flexes in response to loading, for example from the deposition of sediments or the growth of a volcano, and bounces back when loads are removed, such as when ice sheets melt, or from erosion. Lithospheric strength can be defined by flexure rigidity, which is commonly expressed by the effective elastic thickness. Whilst plate tectonic theory provides a reasonable description of the behaviours of oceanic lithosphere, it became apparent that continental lithosphere could deform over large length scales on the order of hundreds of kilometres and that earthquakes occurr within plate interiors.

Oceanic lithosphere

There are many approaches to estimate the elastic thickness of the oceanic lithosphere, either by studying the flexural response of volcanic islands (e.g. Watts & Ten Brink, 1989), sediments (Watts et al., 1982), glacier retreat, or from deflection of the incoming oceanic plate at subduction zones, which is observed using bathymetric or gravity data (e.g. Levitt & Sandwell, 1995; Contreras-Reyes & Osses, 2010). Gravity anomalies can be used to infer

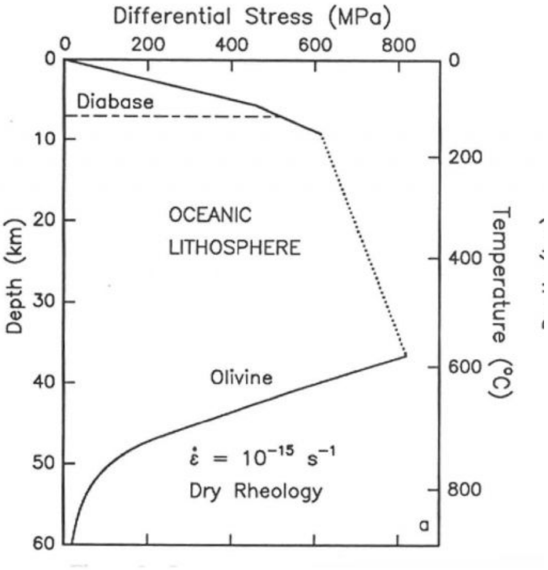

Figure 1.9: Oceanic lithosphere has a homogenous composition (olivine). Up to 30 km of depth the lithospheric strength increases, as the temperatures are low enough, after that the temperatures are so high that the power-law creep mechanism takes over as weakening mechanism.

the density of subsurface structures, and to access the degree of isostatic compensation of topography. Using free air gravity anomalies Watts et al. (1980) and Wessel (1992) found that the elastic thickness follows the depth of the 600 °C isotherm, which determines the depth to the base of the elastic plate thickness. The seismogenic thickness usually corresponds to elastic thickness in the case of oceanic lithosphere (Wiens & Stein, 1984). Oceanic plate thickness increases with distance from the oceanic ridges, and it is a function of age (Parsons & Sclater, 1977). The oceanic lithosphere has homogenous composition and it is believed to be composed of one single strong layer. The stress envelope of the oceanic lithosphere is based on Byerlee's law which relates the brittle part and the dry olivine flow law to the ductile part (Burov, 2011) (Figure 1.9).

Continental lithosphere

The determination of elastic thickness for continental lithosphere is more complex because it is stratified. It comprises upper crust, lower crust, and upper mantle, and the strength of each layer has different rheological and mechanical properties. Chen & Molnar (1983) inferred that the strength of the continental lithosphere lies in the upper (brittle) layer of the crust and in the upper mantle, whilst the lower crust is considered weak. This conclusion is supported by the fact that most earthquakes occur in the upper crust with few earthquakes occurring in the upper mantle. Similar behaviour can be simulated in laboratory experiments with rocks in an environment that simulates temperature gradients found at depth. Brace & Kohlstedt (1980) found that rock strength increases with depth, but it decreases according to ductile deformation laws (creep by power-law rheology). Although it could be argued that this experimental data are based on temperatures and pressures that are too low, strain rates that are too high, and time scales of an order of magnitude that are shorter than geological time scales (top part of Figure 1.10).

Jackson (2002) and Jackson et al. (2008) argue that the strength of the continental lithosphere lies in the Earth's crust whilst the lower crust and upper mantle are both weak. They argued that after more precise earthquake relocation no earthquakes were found in the mantle (Maggi et al., 2000). Using spectral methods based on the ratio between the free-air gravity anomalies and topography they also show an elastic thickness similar to continental seismogenic thickness, which is in the crust only. Furthermore, based on heat flow analysis McKenzie et al. (2005) show, based on heat flow analysis, that all earthquakes in the continental crust/mantle occur at temperatures of less than 600 °C.

Two approaches commonly used for calulating elastic thickness from gravity measurements are in use: (i) directly by calculating values of the elastic thickness and comparing them to measured gravity anomalies, and (2) indirectly using Fourier transform of the relationship between gravity anomalies and topography. These two methods should yield the same results, but it is found that they differ from continent to continent, which makes these methods ambiguous (Artemjev & Kaban, 1991; Crosby, 2007; Burov, 2011).

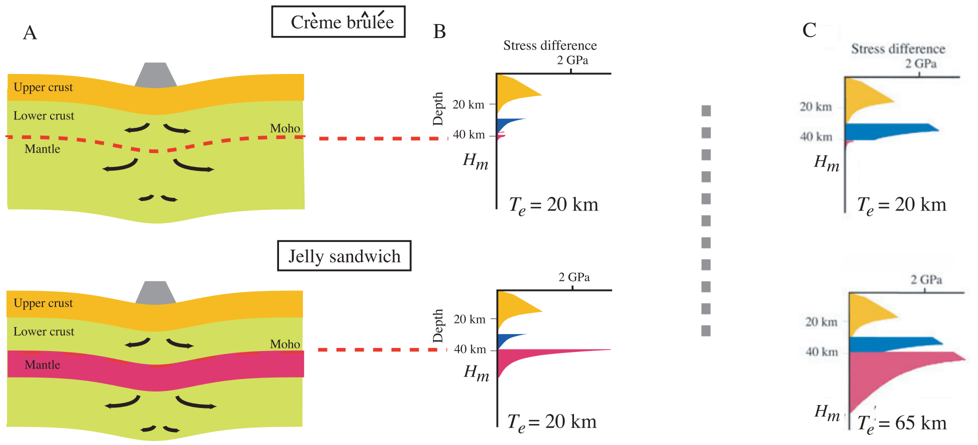

Figure 1.10: Schematic diagram illustrating contrastingly different models for the long-term strength of continental lithosphere. In the creme-brulee model, the strength is confined mainly to the uppermost brittle layer of the crust and compensation is achieved by flow in the weak upper mantle. In the jelly sandwich model, the mantle is strong and the compensation for surface loads occurs mainly in the underlying asthenosphere. Adapted from Burov (2011).

1.6 Tectonics for the two case studies in the thesis

This thesis focuses on tectonic events which occurred in extensional geological provinces: the rifting of the 2005 Dabbahu magmatic segment in Afar, and the primarily strike-slip $M_w 7.2$ 2010 Cucapah-El Mayor earthquake, in Baja, Mexico.

1.6.1 Dabbahu magmatic segment, Afar

The Afar region is part of the East African Rift System (EARS), which is a continental rifting zone in the final stages of continental breakup (e.g. Keir et al., 2009), Figure 1.13.

The mechanisms and forces that initially caused the break up of the lithosphere in the EARS continue to drive rifting and are poorly understood. White & McKenzie (1989) suggested that continental rifting in East Africa is driven by a hot plume below the region of South Africa and South Atlantic. Seismic tomography studies have identified the existence of an African superplume (e.g Hansen et al., 2012; Simmons et al., 2007, 2011; Bagley & Nyblade, 2013). Superplumes are large mantle upwellings that are convected to the Earth‘s surface, originating at the mantle-core boundary. However, a recent seismic tomographic study by Hammond et al. (2013) and a seismic anistropy study by Hammond et al. (2014) could not confirm the existence of a plume conduit under Afar able to drive present rifting or to cause the initiation of break-up of the lithosphere. Their findings

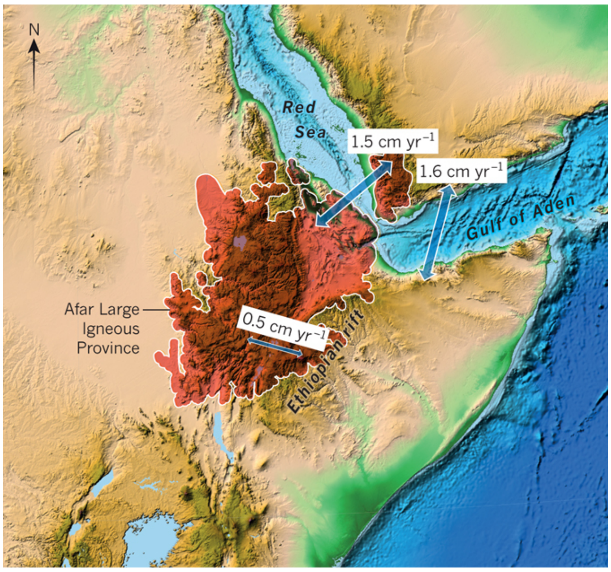

Figure 1.11: Illustration of the tectonic setting of the Afar

include evidence of the presence of melt, which could be an indication that the mantle currently behaves as a mid-ocean ridge. This would support evidence that there is an absence of continental lithosphere in the Afar area (Rychert et al., 2012).

Using the thin viscous sheet approximation, Stamps et al. (2014) and Buck (2006) concluded that the deviatoric stress in the African lithosphere mainly comes from horizontal gradients in Gravitational Potential Energy (GPE), but they also infer that the intrusion of magmatic dykes is required to break-up the lithosphere. Burov & Gerya (2014) have numerically modelled the interaction of mantle flow with a layered lithosphere in 3D in order to predict surface topography. Their model finds that the plume can help break-up an area that has been going through slow continental extension, but is unlikely to be the cause of break-up on its own (Figure 1.12).

Whatever the extensional forces in Afar, they allow the asthenosphere to passively upwell, which then feeds magmatic segments scattered across the Afar, of which Dabbahu is one. Dyke intrusion is marked by shallow, small magnitude and sometimes long-period earthquake swarms, with or without surface breaks and effusive volcanism. Because of these dyke intrusions, the crust tends to be thicker. Rheological properties of the crust and mantle can be determined for the Afar by studying the stress changes induced by rifting episodes. Extension rates after the intrusion of magma in the Dabbahu segment measured by GPS are much larger than pre-event extension rates associated with plate divergence rates. They can be modelled as visco-elastic deformation (Nooner et al., 2009).

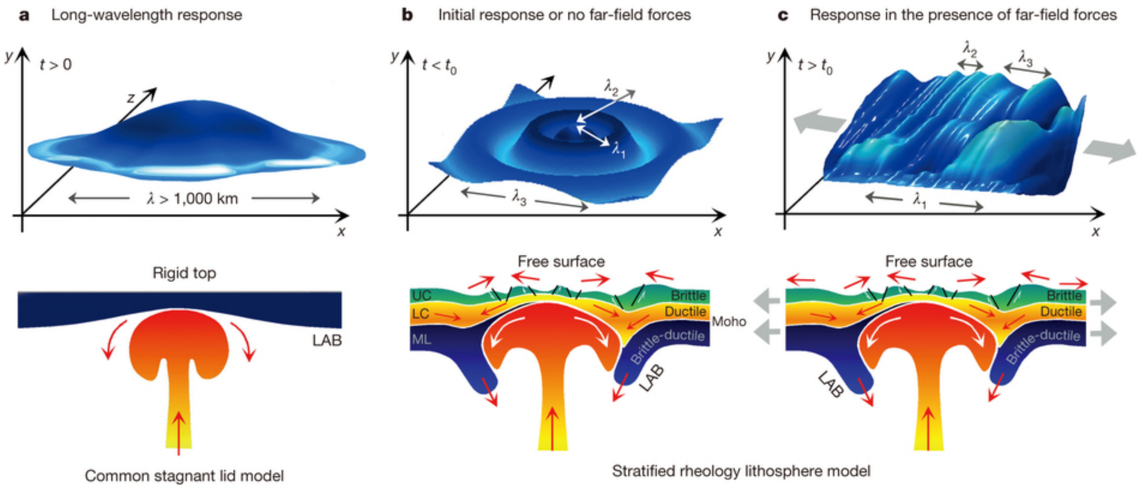

Figure 1.12: (*a*) Results of numerical analysis for evaluation of 3D deformation of the earth‘s surface caused by mantle flow acting on a single layer lithosphere estimates only long-wavelength topography. (*b*) Illustrated numerical results of the earth‘s 3D deformation, when mantle flow is acting on the stratified continental lithosphere. (*b*) Illustrated results of the earth‘s 3D deformation, when tectonic forces and forces from mantle flow act simultaneously on stratified continental lithosphere. In the bottom row, red and white arrows indicate the direction of surface and subsurface movements. Black lines indicate faults, and white half-arrows indicate the direction of movements on the fault interfaces. Adopted from (Burov & Gerya, 2014).

Grandin et al. (2010) and Hamling et al. (2014) used InSAR observations to observe the crust’s response to the post-event deformation/extension, and observe large vertical uplift and subsidence patterns. Grandin et al. (2010) suggest that this transient deformation is caused purely by the magma chamber continuously feeding the dykes. Hamling et al. (2014) conclude that viscoelastic relaxation of stress alone is not enough to explain the deformation and physical models should include magmatic sources. Studies by Nooner et al. (2009) and Hamling et al. (2014) both estimate the viscosity of the upper mantle to be relatively weak (10^{18-19} Pa s), suggestive of newly formed oceanic lithosphere. This is expected as the Afar area is characterised by high heat flow, widespread volcanism and shallow seismogenic thickness ($<$ 11 km). Similar studies for other magmatic segments yield very similar estimates for lithospheric strength (e.g. Árnadóttir et al., 2005; Cattin et al., 2005; Hofton & Foulger, 1996).

1.6.2 Baja, Mexico

The El Mayor-Cucapah earthquake occurred just south of the Salton Trough geological province in Baja, California, which is sandwiched between the complex plate boundary of the North American and Pacific plates. North of Baja, the deformation style is strike-

Figure 1.13: Map of North America that illustrates the transition in the style of plate boundary deformation between North American plate and Pacific plate

slip and the two plates slide past one another, whereas in the south the plates diverge, producing highly oblique oceanic floor spreading in the Gulf of California (Figure 1.13).

This region is also a zone of continental rifting, similar to the Afar. The area is characterized by high heat flow (Lachenbruch et al., 1985; Bonner et al., 2003), volcanism, thin crust (22 km) (Zhu & Kanamori, 2000; Yan & Clayton, 2007), and shallow seismic thickness (less than 11 km). High heat flow in the regions indicates that the strength of the lower crust is weak (Williams et al., 2012). This is indeed confirmed by seismic studies where the lithosphere-asthenosphere boundary is confined to depths of > 40 km (Lekić & Romanowicz, 2011). So far, there have been two GPS postseismic studies since the El Mayor-Cucapah earthquake; a viscoelastic study by Pollitz et al. (2012) confirms low viscosity in the lower crust. Rollins et al. (2015) find that a couple of models, both of which are a combination of viscoelastic relaxation and afterslip, give good fits to the data. They also find the strength of the upper crust to be weak, with a viscosity estimate of the order of 10^{18} Pa s.

1.7 The aims of this thesis

The main aim of this thesis is to use displacement maps generated using sub-pixel matching of optical images to study active tectonics and continental deformation. In addition to optical matching, I also use InSAR and Lidar measurements to provide complementary data. The main advantage of optical matching is the ability to measure continental deformation across an earthquake rupture with high spatial resolution, and good coherence. However, sub-pixel optical matching has its own sources of biases. As a part of this thesis, I investigate how inherent biases affect the displacements caused by active tectonics. I developed new techniques to mitigate some of the biases and systematically remove them from the datasets. In the process, I developed a new method to measure crustal vertical motion directly using space geodesy only. I invert surface displacements measured using sub-pixel matching to infer source mechanisms at depth. The integration of geodetic (and seismic) datasets for joint inversions remains to be further explored. I implement a Bayesian approach in an attempt to jointly invert InSAR and image matching datasets.

1.7.1 Layout of the thesis

Chapter 2 describes the theory of optical matching with sub-pixel resolution using a number of working examples.

Chapter 3 shows the results of displacements obtained by optical matching for the 2005 rifting Dabbahu segment in the Afar, with results of forward models of the deformation source at depth.

Chapter 4 explores sources of biases of the image matching technique and develops some algorithms for eliminating them.

Chapter 5 explains the methodology behind a novel technique for deriving vertical displacements occurring during an earthquake, and obtains a vertical deformation map for the El Mayor-Cucapah earthquake.

Chapter 6 describes a Bayesian approach to data inversion; combining this with the analytical/numerical solutions as well as Bayesian approach to constrain the mechanisms of the El Mayor-Cucapah earthquake.

Chapter 7 summarises the findings.

Chapter 2

Cross-correlation of images with sub-pixel resolution

In this chapter, I explain the theories, algorithms and methods used for measuring crustal displacements with aerial and satellite optical imagery. The focus of this chapter is on cross-correlating optical images with sub-pixel resolution. This enables the ground measurement of displacements smaller than the nominal spatial resolution of optical images in order to remotely map displacements across fault ruptures, which is of research interest in this thesis. For all the processing by sub-pixel matching in this thesis, I use the software package Co-registration of Optically Sensed Images and Correlation (COSI-Corr) (`www.tectonics.caltech.edu/slip_history/spot_coseis/download_software.html`), which uses a phase-correlation method. The satellite images throughout this thesis are taken from the SPOT (Satellite Pour l'Observation de la Terre) satellite.

The basic principle is that two raw images (either satellite or aerial) are collected before and after an event and converted into accurate image maps. The horizontal displacements are then inferred by matching the images from the two passes. The resulting horizontal displacements are decomposed into east-west and north-south components (Figure 2.1).

I divide this chapter into two main sections. The first section deals with the photogrammetric methods used for the transformation of raw satellite images into accurate image maps (orthoimages). I describe the sensor model, the acqusition technique, and the orthorectification process based on the SPOT satellite platform. The second section

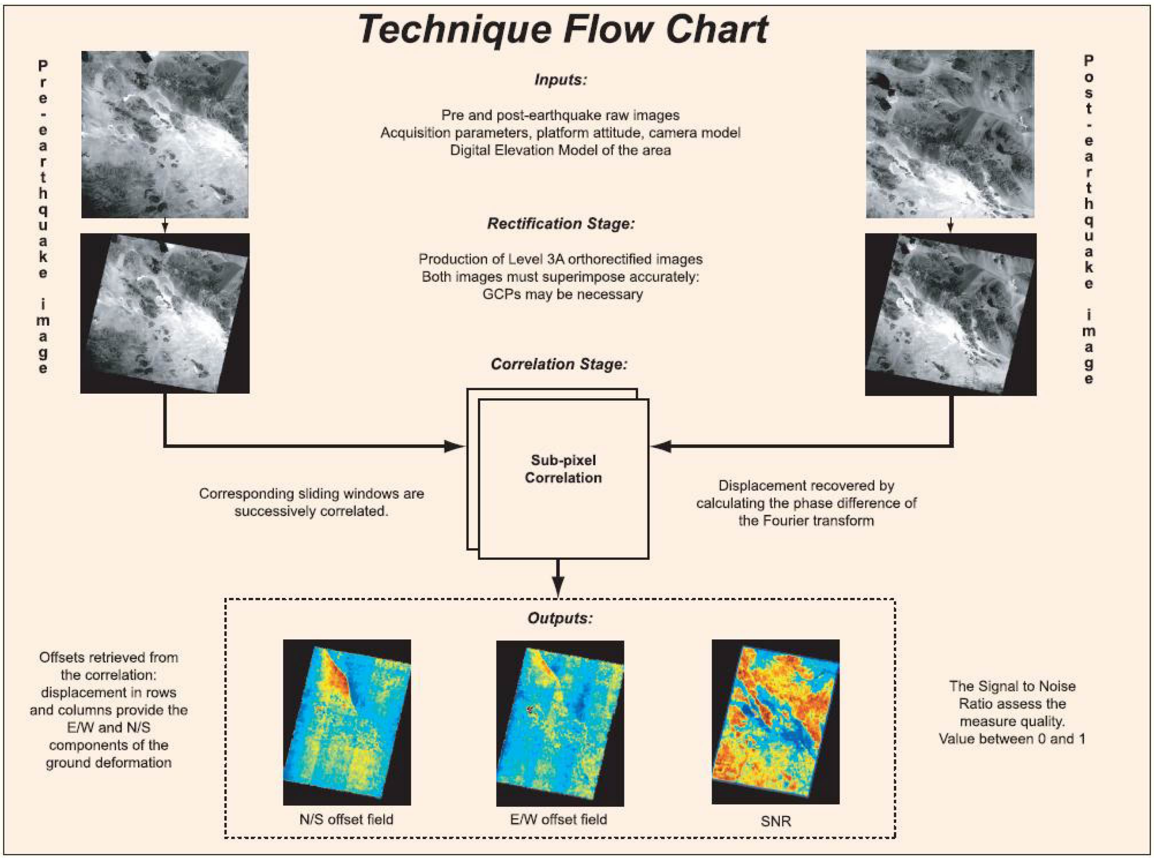

Figure 2.1: This is a basic flow-chart illustrating the processing practice of image matching. Pre- and post-earthquake images are rectified and sub-pixel correlation is then applied to retrieve the horizontal offsets, which are expressed in east-west and north-south diections. Adapted from `http://www.tectonics.caltech.edu/slip_history/spot_coseis`.

explains the signal processing techniques for the cross-correlation of the orthorectified image, with sub-pixel resolution. These techniques are then applied to some working samples.

2.1 How to make an orthophoto?

Photogrammetry is the science that recovers the exact positions of points on the Earth surface from photographs. Before a photograph taken from a plane or satellite can be used to accurately measure features on the ground we need to account for the effects of topographic relief, lens distortions, and camera tilt (which all affect the resulting image). The process correcting these effects is called orthorectification. An image that is geometrically corrected and has uniform scale is called an orthophoto and can be used for accurate measurements of true distances in the horizontal plane. Depending on the type of image acquisition and its metadata, different approaches and practices can be used to produce orthoimages. Below, I describe the practices used for orthorectifiying SPOT images based on the metadata provided from SPOT satellites. SPOT images come with look direction values for each charge coupled device (CCD) detector (Figure 2.2), geographic coordinates at the centre and at each of the four corners of the image, an incidence angle, and an image orientation angle. SPOT5 scenes have dimensions of 60 km by60 km, and the ground spatial resolution for the panchromatic band is ∼2.5 m. It has a high resolution stereoscopic (HRS) imaging instrument on board for instantaneous stereo-capability and the ground spatial resolution for these images is ∼10 m.

Digital satellite orthorectification can be regarded as a three-stage process. The first is to model the orbit and to find the satellite's orientation parameters, which is described in section 2.1.1; the second stage is to use these orbital parameters to generate a grid of known coordinates on the ground (section 2.1.2); the third is to resample the data (section 2.1.3).

2.1.1 SPOT's Sensor model

Accurate knowledge of the satellites' orbit is important for determining the positions of the satellite at the time of image acquistion. Satellite sensor models define the mathematical relationship between the image space (pixel coordinates) and the object space (ground coordinates). The rigorous sensor model (which is implemented in COSI-Corr) finds a direct geometrical link between the image space (2D image plane) and the object space (3D model of the Earth's surface) using the available physical properties of the SPOT satellite system. It uses attitude measurements, look direction vectors for each pixel, and ephemeredies information from the satellite.

However, all these measurements are referenced according to different reference systems and need to be brought into a common reference system. Satellite positions need to be constrained continuously as forces such as terrestrial gravity, solar radiation, and torques cause satellites to deviate from their theoretical trajectory. SPOT satellite orbits can be described as Keplerian, elliptic, sun-synchronous, and near-polar. SPOT5 provides eight to nine ephemerides per image, which are the satellite's orbital values of longitude, latitude and altitude at time intervals before, during and after the image acquisition.

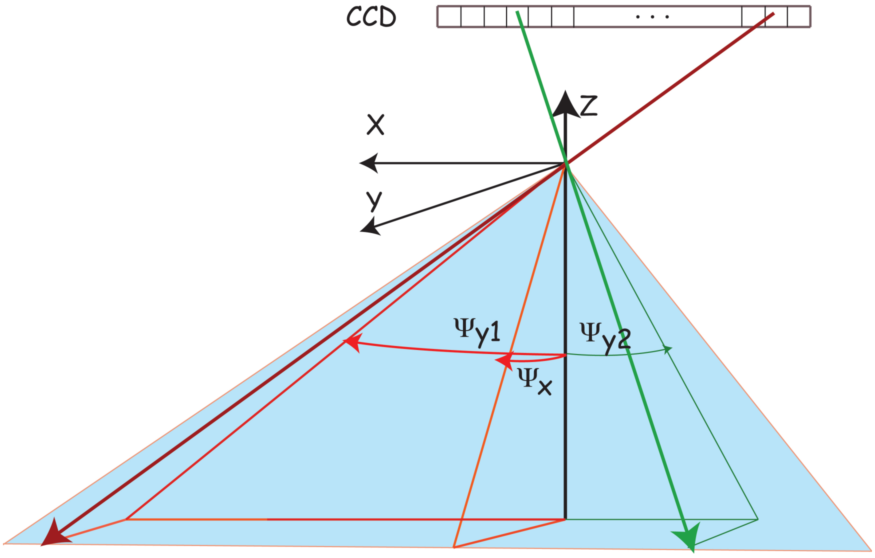

Figure 2.2: The look direction of each pixel in the CCD array is based on the two viewing angles Ψ_x and Ψ_y. Red and green lines illustrate two different pixels.

They are referenced according to the International Terrestrial Reference System (ITRF), which is a global, geocentric frame. The look direction vectors observed on the satellite are referenced according to the Navigation Reference Coordinate System (NRCS), which is a reference system fixed to the satellite body. Because of the satellite's drift, look direction vectors need to be adjusted to the idealised satellite trajectory, in the frame of the Local Orbital Coordinate System (LOCS). LOCS origin is not fixed and is shown in Figure 2.3 with red axes. The drift of the satellite is determined by attitude measurements (roll, pitch, and yaw) in the LOCS frame, whereby LOCS axes are specified for the case when roll, pitch, and yaw are zero. The attitude measurements are then used in the transformation of the look direction vectors from NRCS to LOCS, making the satellite point towards the ground. Look direction vectors are transformed from LOCS to ITRF (the ITRF origin is shown in Figure 2.3 with green axes) in order to match the frame in which the image ephemerides are defined. In total, three coordinate transformations are required to transform look direction vectors into the ITRF coordinate system (Riazanoff, 2004).

Look direction vectors determine a line that connects the optical centre of the sensor, the CCD detector, and a point on the ground (Figure 2.4). These form the basis for the collinearity equations which relate coordinates in the optical sensor plane to coordinates on the ground (or object coordinates). The intersection of the look direction vector with

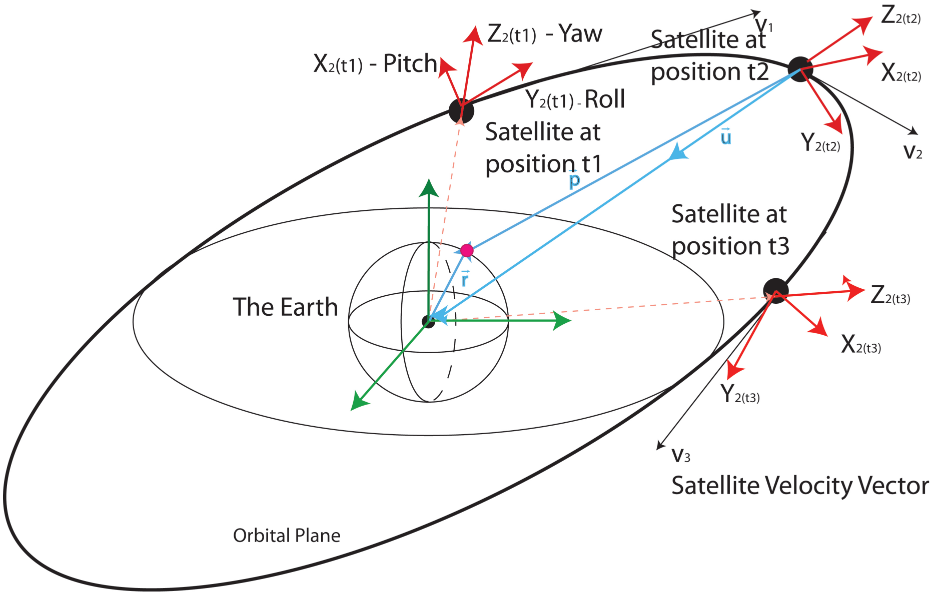

Figure 2.3: Green axes show the ITRF reference system. Red axes show NRCS and LOCS reference frames which when attitude values are zero are identical and fixed to the satellite's body. Blue vectors show the look direction vector $\vec{u}$, $\vec{r}$ from the centre of the Earth to a point on the ground, and $\vec{p}$ from the centre of the Earth to a point on the image. These are used to infer the image pixel coordinates.

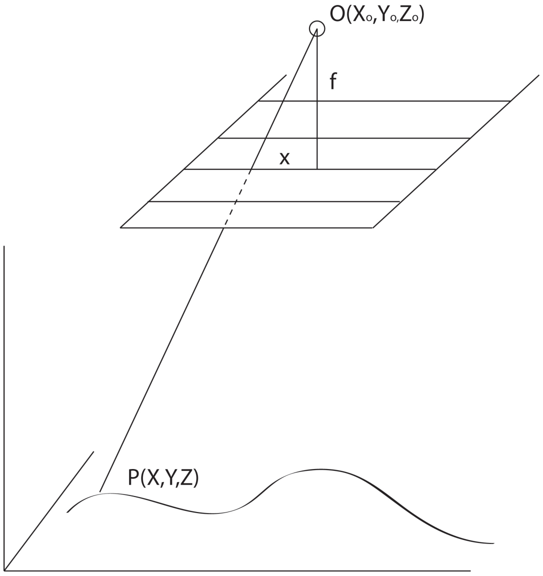

Figure 2.4: Linear collinearity condition. The optical projection centre (O), point in the image, and point on the ground (P) all lie on the same line.

the earth‘s surface will yield the coordinates for that pixel in the terrestrial coordinate system. Figure 2.3 shows the relation between the unit look direction vector $\vec{p}$, the vector from the centre of the Earth to the ground point $\vec{r}$, and the vector between the centres of the Earth and the centre of the satellite $\vec{u}$ (see Equation 2.1).

$$\vec{r} = \mu \vec{u}_3 + \vec{p} \tag{2.1}$$

where $\vec{u}_3$ is the unit vector of the look direction for the point on the ground, μ is the distance from the centre of the satellite to the ground, $\vec{r}$ is the vector from the centre of the Earth to a given point on the ground and $\vec{p}$ is the vector from the centre of the Earth to a given point on the image (Figure 2.3). A correction needs to be applied to the look direction due to uncertainty in the interpolation of ephemerides and attitude data, which means that the look direction vectors $\vec{u}$ will not always point to the correct point on the ground (Figure 2.5).

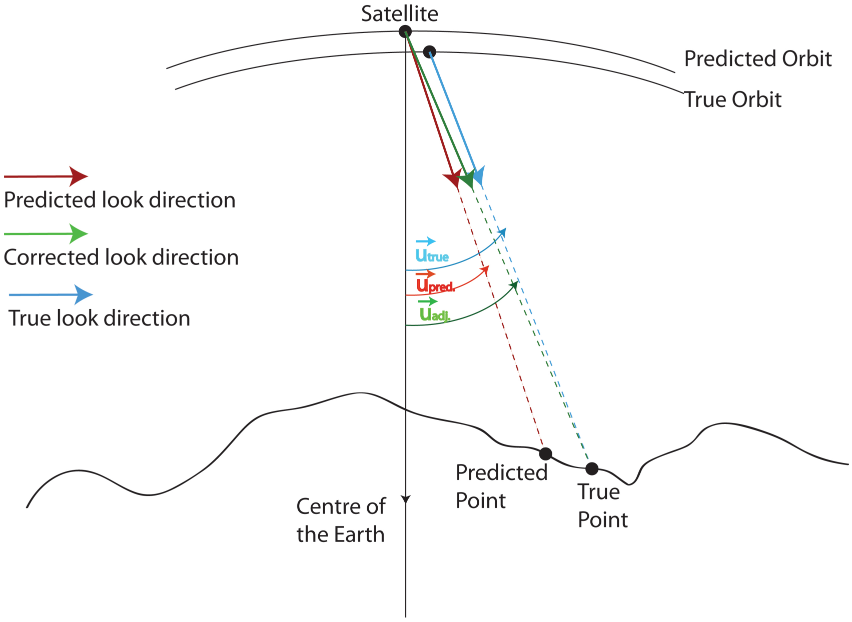

Figure 2.5: Look directions adjustments

$$\delta\vec{u} = \vec{u}_{\text{true ground position}} - \vec{u}_{\text{auxilary data}} \tag{2.2}$$

The look direction vectors are corrected by identifying a set of ground control points (GCPs), which are features that can be identified on both reference maps and in the raw images. The image point is allocated to the ground coordinates and the correct look direction for that point is thereby calculated. The difference between the calculated look direction from the GCPs and the look direction initially estimated gives the amount a given look direction needs to be adjusted for a particular point. A common correction for all look direction angles can then be obtained from a set (three or more) of GCPs. More details about the adjustment process of the look direction vectors are given in Leprince et al. (2007).

2.1.2 Removal of topographic distortion

Simple geo-referencing methods, often used as a first order approximation, do not address the topographic displacement error, which is present in the images (Mikhail et al., 2001). High terrain relief, buildings or any other tall objects in the images will have incorrect planimetric positions and will appear as if they are leaning if the look direction is not at nadir.

Pushbroom technique

Two points with the same planimetric position and different heights will, in central projection, project onto two points with different planimetric positions. The topographic displacement error in SPOT images is a result of the pushbroom scanning technique. This technique is employed by several other high spatial resolution satellites for image acquisition (e.g. IKONOS, QuickBird, Eros).

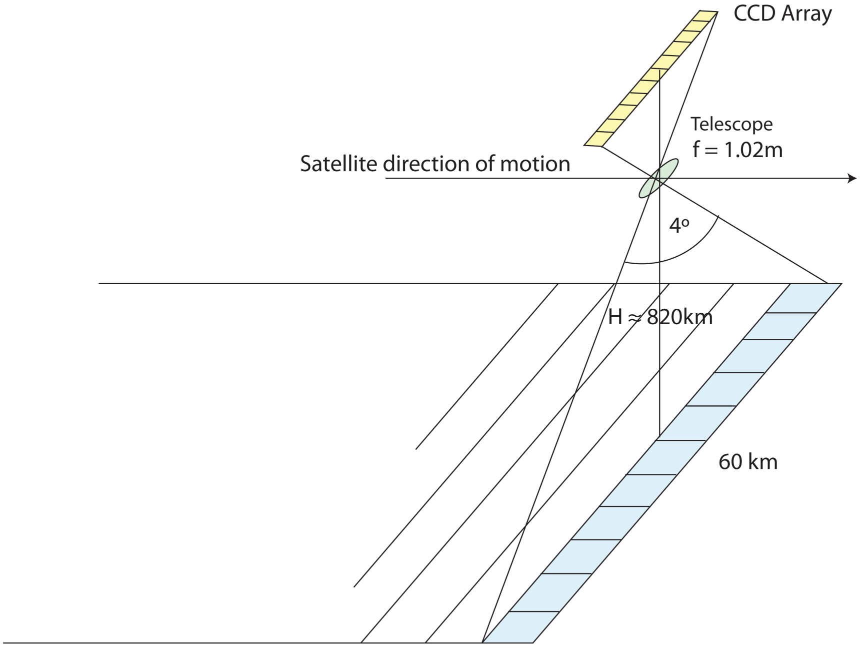

Figure 2.6: Pushbroom technique

The area on the ground is swept as the satellite moves along its orbit (Figure 2.6). The advantage of this technique is that the exposure time for the ground points is in line with the satellite location, and the projection forms a linear central projection across the track (Figure 2.7 (*right*)), instead of a typical aerial central projection (Chen & Lee,

1993) (Figure 2.7 (*middle*)). This means that the objects above ground (tall buildings, mountainous terrain) will be visible side on in the image, and the distances towards the edges of the image may be distorted. The image acquired by the pushbroom technique will have the same number of perspective centres, as there are lines in the image. Thus, this is considered to be a partial central projection, as it is only projected in the cross-flight direction (Figure 2.7), and the relief displacement is a result of SPOT's 'linear' central projection (Figure 2.7(*right*)). The pushbroom technique captures each line of the image with a linear array of CCDs mounted in the focal plane of the instrument. These 1D lines are then stitched together to create a 2D image.

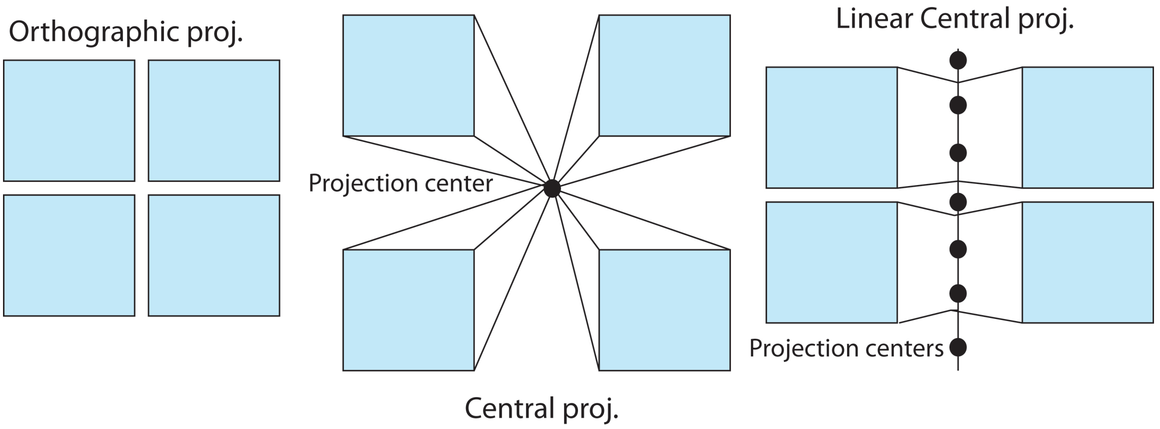

Figure 2.7: *left:* Corners of the four buildings in the orthographic projection. *middle:* The corners of the buildings in the central projection. *right:* The same corners of the four buildings in the linear central projection for pushbroom style acquisition. The buildings are leaning away from the center of the scene. The corner's planimetric position will change depending on the elevation of the buildings.

Direct and indirect determination of the ground coordinates

Direct orthorectification determines where the look direction corresponding to each pixel in the image intersects with a digital elevation model of the surface. Using this process, the correct geographic location of each pixel may be determined (Gugan & Dowman, 1988). The drawback of this method is that it results in an irregularly-spaced grid on the ground, the irregularities arising, for example, from topographic relief or variations in satellite attitude Figure 2.9.

Unlike direct orthorectification COSI-Corr employs an indirect orthorectification scheme, whereby a grid on the ground with regularly spaced horizontal coordinates is established,

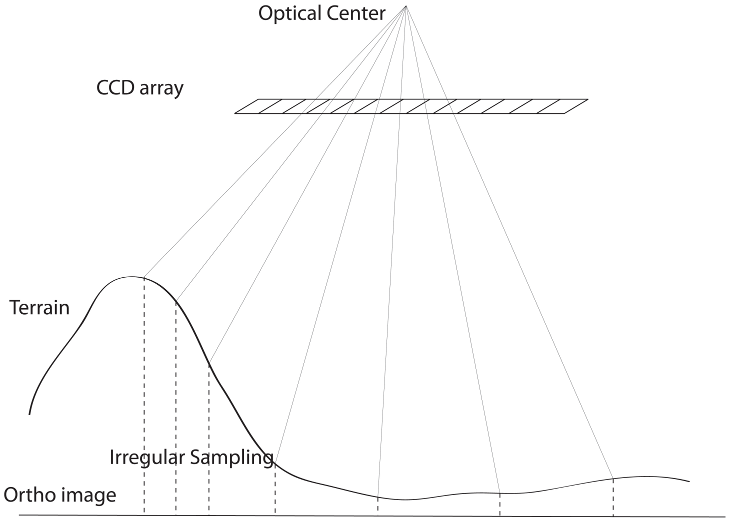

Figure 2.8: Irregular sampling

and the corresponding location on the image determined. The resulting digital ortho image gives an accurate planimetric representation on a map (Wolf & Dewitt, 2000).

Rigorous Indirect orthorectification

In order to avoid the gaps that the direct approach generates and irregular resampling, the indirect orthorectification approach starts with a regular grid on the ground where each point has horizontal terrestrial coordinates, and a geoid height (surface of equal gravitational potentional energy) from a DEM (Figure 2.10).

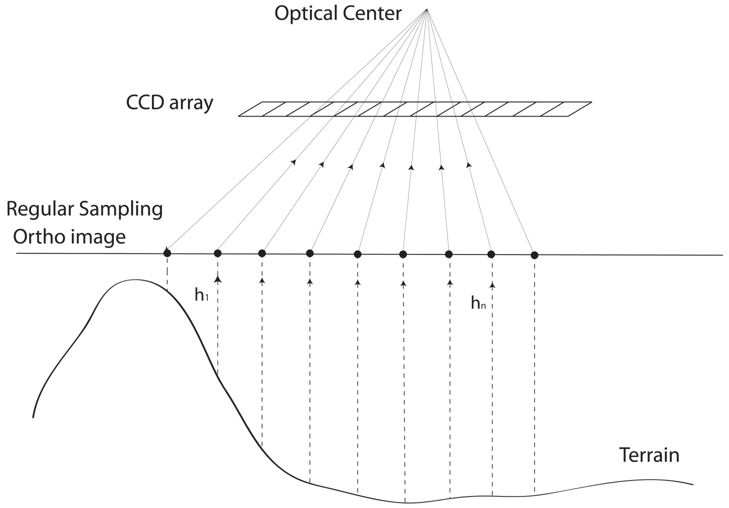

Figure 2.9: Regular sampling

The intersection of the look angle with an Earth model is done with a projection plane that passes through a point on a grid and is perpendicular to the vector OP (Figure 2.10). By minimising the distance between the vectors OM and OM', the terrestrial coordinates of each pixel can be found (Equation 2.4). The projection plane contains the point M(x,y,z) and is perpendicular to the vector $\vec{OM}$. The point M' (x',y',z') (seen from the look direction) also therefore lies on this plane. All the points M' found during the minimisation satisfy the condition $\vec{OM} \times \vec{MM'} = 0$. The projection plane is then defined as in Figure 2.10 and Equation 2.3. Two transformation matrices are created with the solutions of the minimisation (X and Y) and are used to resample the raw image and create the final orthophoto.

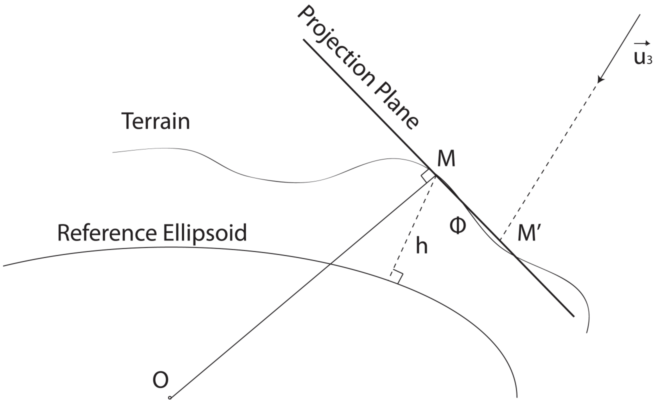

Figure 2.10: Principle of indirect orthorectification. After Leprince et al. (2007).

$$xx' + yy' + zz' - x^2 - y^2 - z^2 = 0 \tag{2.3}$$

The COSI-Corr software (Leprince et al., 2007) has implemented the indirect rigorous model. The coordinates of the pixels in the raw image solution are found by minimising the distance between the chosen point on the projection plane and the intersection of the look angles with the projection plane (Leprince et al., 2007) (Figure 2.10 and Equation 2.4).

$$\Phi(x, y) = |\vec{OM} - \vec{OM'}|^2 \tag{2.4}$$

In ortho-rectifying the post-event image, a correction of the look vectors is carried out in a similar fashion to that above (for the pre-event image), but in this case using a set of tie-points. These are identical points in the post- and pre-event images for which the ground coordinates are now known.

2.1.3 Image reconstruction

The image's grey pixel values (intensities) at these locations are determined by interpolation from the regularly-spaced image values. Both orthorectification resampling schemes, with the direct and inverse transformation matrices, generate X and Y transformation matrices that are irregular. These irregular matrices are reconstructed so that they create regular digital ortho images with a continuous surface. The reconstruction in the spatial domain involves convolving the discrete samples with a filter, where the filter is some continuous function. A sinc function is used as a foundation for filtering buildings because its Fourier transform is a 'box' function (akin to the shape of a building). The argument of the sinc function can be changed in order to increase (oversample) or reduce (downsample) the sampling rate and to create a new sampling interval. The complete theoretical reconstruction of the bandlimited signal is obtained by convolving the sampled function with the continuous sinc function (Equation 2.5)

$$(x, y) = \begin{cases} \frac{\sin(\frac{\pi x}{d_x})}{\frac{\pi x}{d_x}} \frac{\sin(\frac{\pi y}{d_y})}{\frac{\pi y}{d_y}} & \text{for } x, y \neq 0 \\ 1 & \text{for } x, y = 0 \end{cases} \tag{2.5}$$

where d_x and d_y are reconstruction periods or resampling distances, representing the maximum distance between adjacent samples in the x and y directions (Leprince et al., 2007).

However, the sinc function is infinitely long, and convolution with the theoretical ideal resampling kernel in the spatial domain is not practical, so it is approximated. There are many approaches for approximating the sinc function (Figure 2.11(a)). The simplest is to convolve the signal with a 'box' function (Figure 2.11(a)), which results in nearest-neighbour resampling. The 'box' function has the Fourier transform (Figure 2.11(d) of the sinc function, and therefore strong aliasing is associated with the nearest neighbour (Figure 2.11(d)). Quadratic and cubic polynomials, which are continuous and are of fixed length, are also used because of their ability to fit the sinc function. The cubic convolution kernel is generated by fitting cubic polynomials to sinc curves for a two-point sinc function (Figure 2.11(a)), a four or more point sinc function (Figure 2.11(f)), for each of the subsequent lobes of the sinc function.

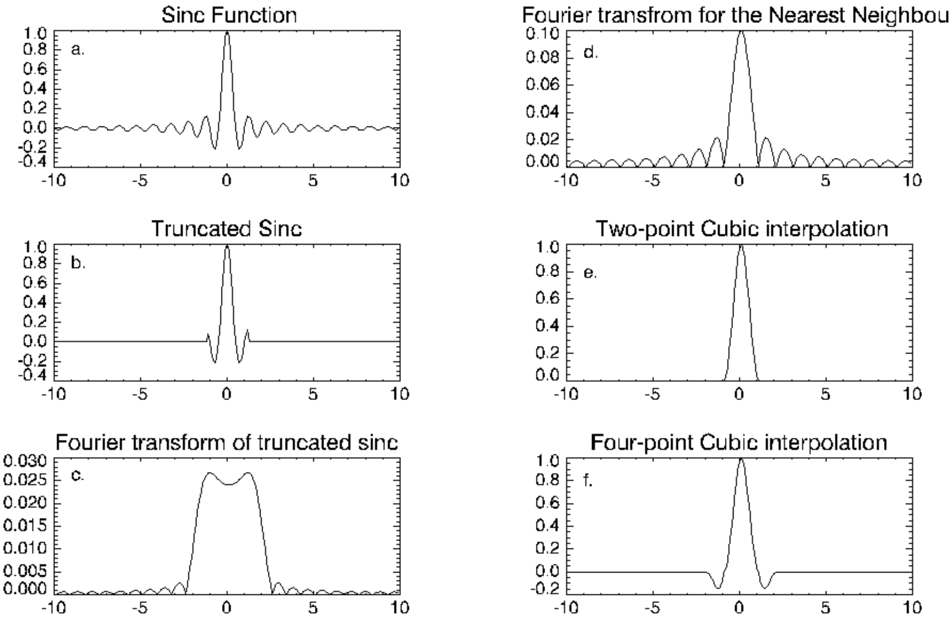

Figure 2.11: (a) shows the infinity long sinc function. (b) is the truncated sinc function and its Fourier transform in (c). (d) shows the Fourier transform of the 'box' function used as the approximation of the sinc function in the nearest neighbour interpolation. (e) and (f) are cubic kernels used in the two-point and four-point interpolation of the sinc function.

The resampling (reconstruction) in COSI-Corr is done with a truncated sinc function filter. Truncation is achieved by multiplying the sinc function with a windowing function in order to create the convolution kernel. The choice of windowing functions is large, but because of its anti-aliasing properties, COSI-Corr implements a 2D separable Kaiser window (Equation 2.6).

$$W_{K\,d_x,d_y}(x_n,y_n) = \begin{cases} \frac{I_0\beta_x \sqrt[2]{1-(\frac{x_n}{Nd_x})^2}}{I_0\beta_x}\,\frac{I_0\beta_y \sqrt[2]{1-(\frac{x_d}{Nd_y})^2}}{I_0\beta_y}, \text{for} \begin{cases} -Nd_x \leq x_n \leq Nd_x \\ -Nd_y \leq y_n \leq Nd_y \end{cases} \\ \\ 0 \qquad \text{otherwise} \end{cases} \tag{2.6}$$

I_0 represents the zero order modified Bessel function and β_x and β_y are the parameters that define the shape of the surface used (Figure 2.12). The 2D Keiser window has a width of $2N+1$, where N is the number of samples (Figure 2.12) or lobes of the sinc function.

Resampling transformation matrices obtained by direct orthorectification are used to resample four corner points of the grid and indirect resampling matrices are used to resample the rest of the points on the ground onto a regular grid. Local d_x and d_y resampling

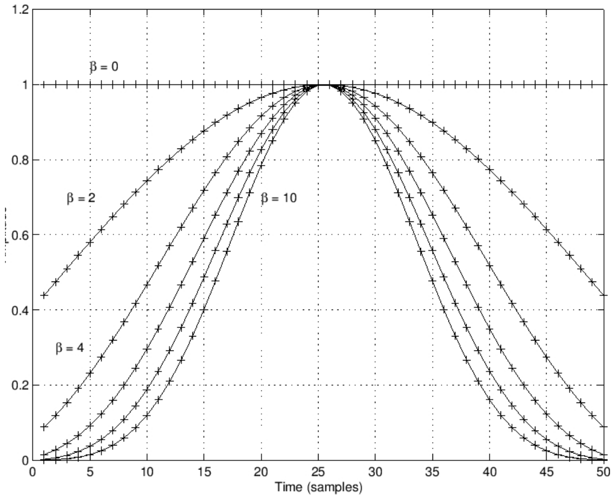

Figure 2.12: The Kaiser window used in the truncation of the sinc function. The width of the Kaiser function is determined by the time or number of samples, which correspond to the number of lobes of the sinc function

distances are determined for each point from the maximum distance with respect to eight neighbouring points. The global resampling distances for the entire transformation matrix are given by the largest local resampling distance. However, discrete convolution of the irregular transformation matrix with the filter becomes an issue as each sample point needs to be addressed separately (Leprince et al., 2007). The advantage of indirect orthorectification, used by the COSI-Corr software, is that it uses regular resampling transformation matrices making it much more straightforward to convolve with the filter.

2.2 Image correlation with sub-pixel resolution

Image matching compares the images and measures differences between them. Image matching is required in many image processing operations such as DEM-generation (stereo generation), image-registration, inner, relative and absolute orientation of aerial and satellite images, and displacement measurements between images. Image matching with sub-pixel accuracy has proved to be very valuable in the study of coseismic events, as the majority of optical satellite images (especially prior to 2000) have a spatial resolution which is greater than the surface displacements caused by earthquakes (e.g. Michel et al., 1999; van Puymbroeck et al., 2000; Dominguez et al., 2003). The sub-pixel correlation techniques in general take advantage of the fact that small displacements will result in slight changes in the image's grey pixel values that represent features on the ground. Figure 2.13 is illustrating transformation of grey values of an image caused by deformation by more than one full pixel and also by deformation casued only by a subpixel. Figure 2.13 (c) and (d) show the changes in grey pixel values for large displacements of ground features (more than one full pixel) from the original state (a) and (b), which result in shifting grey values into an entirely new location. The case depicted by Figure 2.13 (e) and (f) occurs when displacement is less than the size of a pixel (if you compare with (a) and (b)), and the intensity of grey values representing features on the ground only change slightly. This subtle grey value change is studied by variaty of sub-pixel techniques in order to obtain horizontal displacements with sub-pixel resolution.

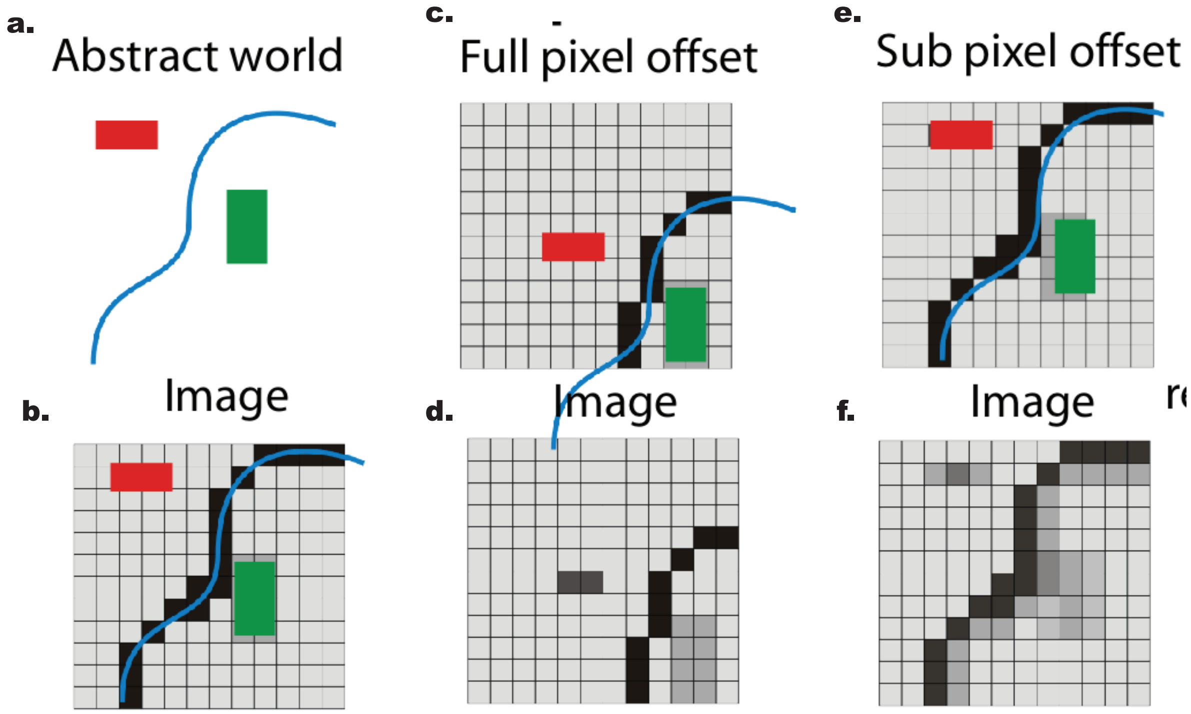

Figure 2.13: *first column* illustrates the world and its representation in the digital image. *second column* illustrates the shift of several pixels and its image represenations. *third column* represents the sub-pixel shift and its image representation - the grey values have slightly changed.

Differences between various image matching tasks, and different types of images and their properties (maps, shaded reliefs, SPOT, Landsat...), led to the development of a variety of matching algorithms with sub-pixel resolution. These can be categorised into area-based (e.g. Stumpf et al., 2014; Debella-Gilo & Kääb, 2011), feature-based (e.g. Gruen, 2012; Kieu et al., 2014), and Fourier-transform based (e.g. van Puymbroeck et al., 2000; Stone et al., 2001) algorithms. The phase-matching implemented in COSI-Corr is based on the Fourier-transfrom. It has high accuracy and is very robust even in cases where images are acquired in different light conditions. COSI-Corr software estimates horizontal displacements between the orthorectified pre- and post-event images through cross-correlation of small windows of data. The cross-correlation is carried out in the frequency domain and sub-pixel resolution of the displacement values are obtained from variations in phase differences as a function of frequency. Variations of phase in the x direction yields east-west displacements; those in the y direction yield north-south displacements.

The next section describes the method of transforming an image or a portion of an image into the frequency domain.

2.2.1 Fourier transformation of a 2D image

Fourier transforms are function operations where periodic and non-periodic signals are broken down into the sum of a series of sine and cosine functions. Grey values of the image in the spatial domain are transformed into a series of frequencies of the sine and cosine functions representing the 2D image. The properties of the Fourier transform are useful for a broad range of image-processing applications, such as filtering, smoothing, sharpening, enhancement, and restoration. The Fourier transform in its two dimensional form is given by Equation 2.7:

$$F(u,v) = \int_{-\infty}^{\infty}\int_{-\infty}^{\infty} f(x,y)e^{-i2\pi(ux+vy)}dxdy \tag{2.7}$$

where u and v are spatial frequencies in the x and y directions respectively, and F(u,v) is the 2D spectrum of f(x,y).

To analyse the digital images, which are considered to be 2D non-periodic, finite, discrete signals, the Discrete Fourier transform (DFT) is used (Equation 2.8) instead of the continuous Fourier transform. Digital images are sampled by factors of M (number of pixels along x axis) and N (number of pixels along y axis). The relations for the 2D image Fourier transform and its inverse are given by: Equation 2.8 and Equation 2.9.

$$\mathcal{F}(\omega_x, \omega_y) = \frac{1}{\sqrt{MN}} \sum_{x=0}^{M-1} \sum_{y=0}^{N-1} f(x,y) e^{-i2\pi(\frac{\omega_x x}{M} + \frac{\omega_y y}{N})} \tag{2.8}$$

$$f(x,y) = \frac{1}{\sqrt{MN}} \sum_{\omega_x=0}^{M-1} \sum_{\omega_y=0}^{N-1} f(\omega_x, \omega_y) e^{i2\pi(\frac{x\omega_x}{M} + \frac{y\omega_y}{N})} \tag{2.9}$$

where the spectral coordinates ($\omega_x = 0...M-1, \omega_y = 0...N-1$) and image coordinates ($x = 0...M-1, y = 0...N-1$) are the same for the $M \times N$ size image.

The output of the Fourier transform is a complex number that is often expressed as a magnitude (Equation 2.10) and a phase (Equation 2.19).

$$\text{Mag} = \sqrt{Rel(\mathcal{F}(\omega_x, \omega_y))^2 + Im(\mathcal{F}(\omega_x, \omega_y)^2} \tag{2.10}$$

$$\tan(\phi) = \frac{Im(\mathcal{F}(\omega_x, \omega_y))}{Rel(\mathcal{F}(\omega_x, \omega_y))} \tag{2.11}$$

where Rel is the real part of a complex number and Im the imaginary part.

Because of the separability of the 2D Fourier transform (the function can be expresed as a product of two functions, each of them depending on one variable), DFTs of digital images are achieved by taking the 1D Fast Fourier transform (FFT) of each row followed by the 1D Fourier transform of each column of the image. The FFT output is then stored in real and imaginary arrays. The range of the frequencies of the power spectrum (absolute value of DFT) tends to be very wide and is therefore displayed using a logarithmic scale. The cross seen in Figure 2.15(b), produced by the power spectrum of most natural images, does not exist in the real world, but is a result of the non-periodic nature of the 2D images. The image boundaries represent a steep discontinuity in the image grey values, which result in low frequency and high amplitude elements of the power spectrum. For viewing purposes the quadrants are swapped around so that low frequencies are in the centre of the power spectrum (Figure 2.14).

The image boundaries produce a large range of frequencies. Filtering them directly, as shown by van Puymbroeck et al. (2000), will also remove desirable frequencies, degrading

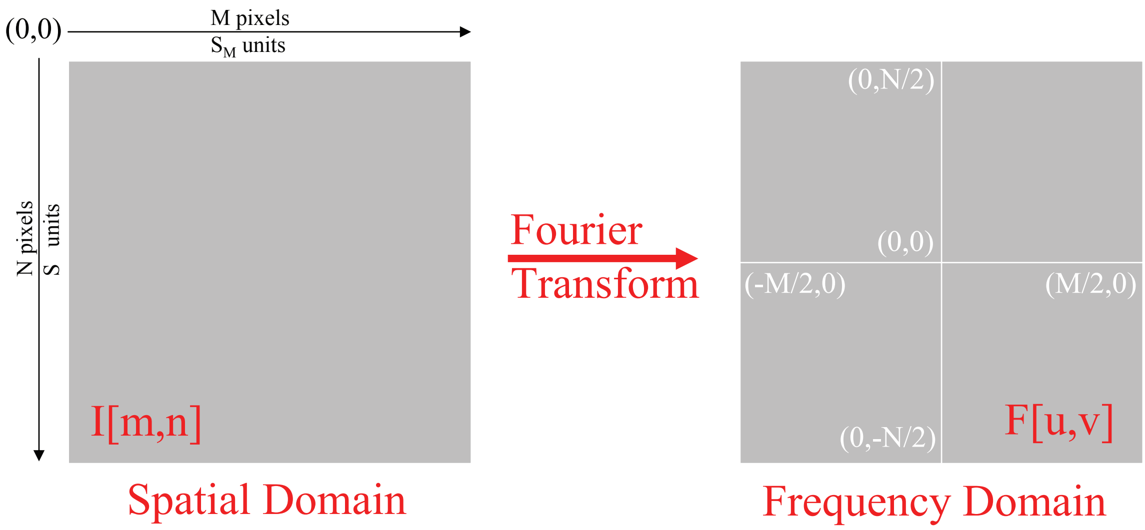

Figure 2.14: The origin of the image in spatial domain is placed in the top left corner. The origin of the image in the frequency domain is placed at the centre of the image, where the quadrants are swapped around.

the image. Aghdasi & Ward (1996) suggested extending copies of images at the image boundaries to make the image periodic to avoid discontinuities (or edge effects) and then padding with zeros. However, most authors who use the Fourier image analysis technique, weight images using windowing techniques to reduce the amplitude of discontinuities at the boundaries. The frequency spectrum of the signal is convolved with the frequency spectrum of the window function. Harris (1978) gives a summary of windowing functions, which are then convolved with the original image. The windows applied directly on the image, which are a function of the distance from the centre of the image, attenuate the image grey values towards the edges to zero (Figure 2.15(c)), making the discontinuity disappear from the image (Figure 2.15(d)). The window function is zero valued outside some chosen interval. The best window will depend on the nature of the signal and some experimenting is required to find the most suitable window for a particular data set. COSI-Corr is implementing the raised-cosine window (Equation 2.12) as the authors Leprince et al. (2007) have proven this to give a good ratio between smoothing the discontinuities and losing valuable signal (signal energy).

$$\text{raised cosine window} = \begin{cases} cos^2(\frac{\pi}{2N\beta}(|x| - N(\frac{1}{2}-\beta))), & for\ N(\frac{1}{2}-\beta) \leq |x| \leq \frac{N}{2}, \\ 1, & for\ |x| < N(\frac{1}{2}-\beta), \\ 0, & otherwise \end{cases} \tag{2.12}$$

where β is a roll-off factor which determines the shape of the window, and N is the window length.

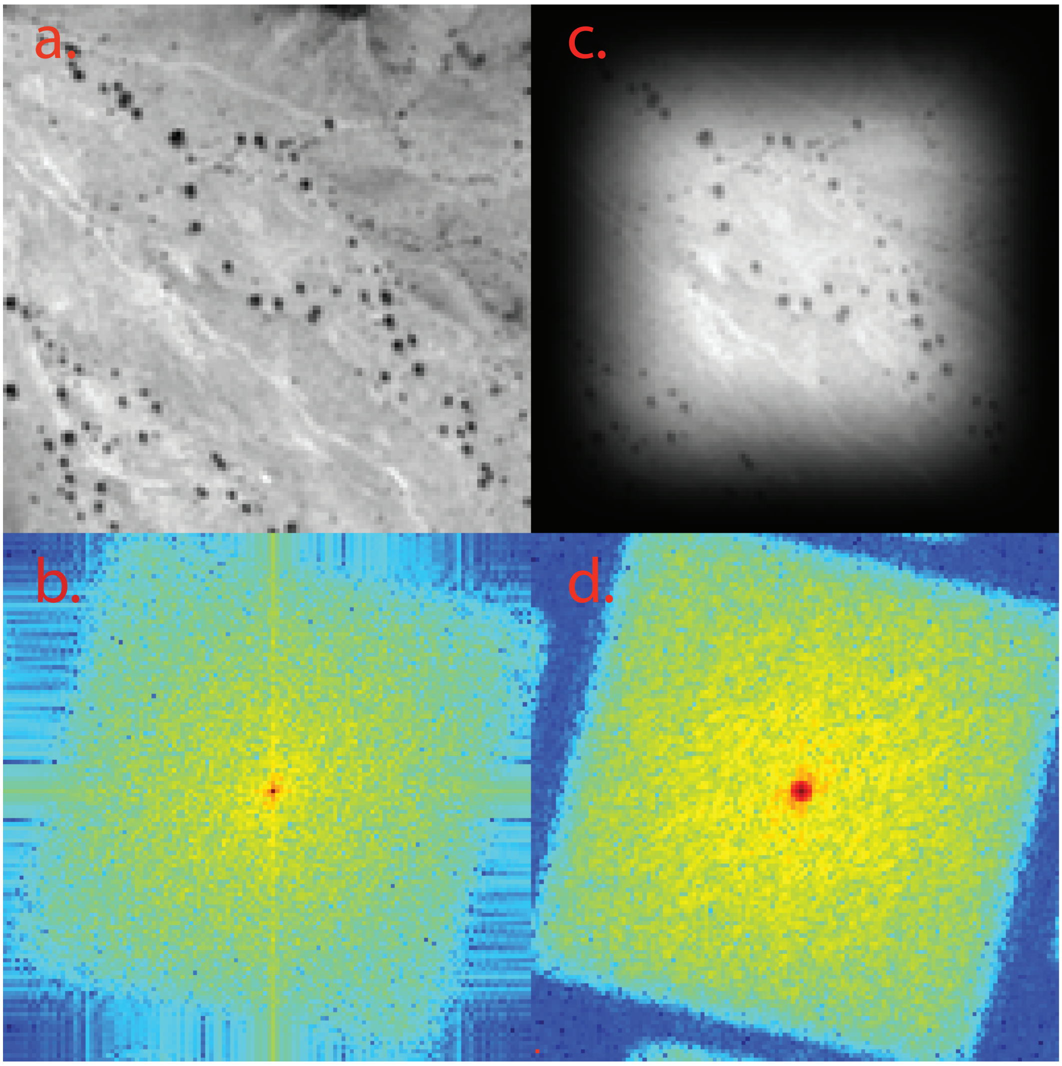

Figure 2.15: (a) shows a patch of the SPOT5 (2.5m) image (128 × 128 pixels). (b) DFT of the image (a) shows the frequencies in the shape of a cross due to the boundary effects. (c) attenuated original image multiplied with the raised cosine window. (d) FFT results for (c) with very little noise due to the boundary effects.

2.2.2 Phase correlation

The correlation between two images I_1 and I_2 in the spatial domain (Equation 2.13) produces a maximum signal at the point where the two functions are most similar:

$$C = I_1(x, y) \circ I_2(x, y) \tag{2.13}$$

where $\circ$ means correlation. The location of this signal then determines the shift between the two functions (Figure 2.16 (left)). Two images, which have been displaced with respect to each other by an offset of x_0 in the east-west (E-W) direction and y_0 in the north-south (N-S) direction can be expressed as (Equation 2.14),

$$I_2(x, y) = I_1(x + x_0, y + y_0) \tag{2.14}$$

Phase correlation is an area based correlation which analyses the pixel intensities in the frequency domain rather than spatial domain Equation 2.7. The Fourier transform of the two displaced images is given as $\mathcal{F}(I_1(x, y)) = F_1(\omega_x, \omega_y)$ and $\mathcal{F}(I_2(x, y)) = F_2(\omega_x, \omega_y)$, where ω_x and ω_y are frequencies in radians. This has the advantage of being more robust to correlated (Brown, 1992) and frequency-dependent noise. It also performs well with varying illumination, and is less computationally expensive. The convolution theorem states that the convolution of two functions in the spatial domain corresponds to the product of their Fourier transforms in the frequency domain; similarly, the correlation of two functions in the spatial domain corresponds to the product of the Fourier transform of one function and the Fourier transform of the complex conjugate of the second function in the frequency domain. The correlation in the frequency domain is normalised to improve the performance and remove the dependence of the image content (Equation 2.15)

$$r = \frac{F_1(\omega_x, \omega_y)F_2(\omega_x, \omega_y)^\star}{|F_1(\omega_x, \omega_y)F_2(\omega_x, \omega_y)^\star = e^{j(\omega_x\Delta_x + \omega_y\Delta_y)}} \tag{2.15}$$

where $F_2(x, y)^\star$ is a Fourier transform of the complex conjugate of $f(x, y)$. The determination of the horizontal displacement is based on the Fourier shift property. This states that the linear translation in the spatial domain is equivalent to a phase shift in the frequency domain (Foroosh et al., 2002). Kuglin & Hines (1975) are the first authors to take advantage of the shift property of the Fourier transform to infer integer horizontal displacements (x_0 and y_0) between two overlapping digital images (Equation 2.16).

$$\mathcal{F}_1(\omega_x, \omega_y) = \mathcal{F}_2(\omega_x, \omega_y)e^{i2\pi(\omega_x x_0 + \omega_y y_0)} \tag{2.16}$$

By substituting Equation 2.16 into Equation 2.15 the phase correlation of the hori-

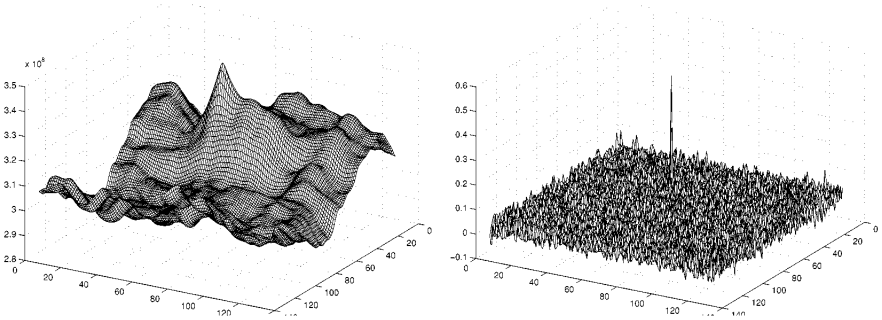

Figure 2.16: *left* is a correlation function obtained by cross-correlation method and on the *right* is a correlation function obtained using the phase matching, where the peak of the phase matching is located with more precision. After Foroosh et al. (2002).

zontal offsets is given by Equation 2.17

$$C = \frac{F_1 F_2^\star}{|F_1 F_2^\star|} = e^{i2\pi(\omega_x x_0 + \omega_y y_0)} \tag{2.17}$$

The phase correlation technique locates the peak of the correlation function with high precision (Foroosh et al., 2002), (Figure 2.16) making it superior to the sub-pixel cross-correlation method.

The solution for x_0 and y_0 can be found either in the frequency domain or in the spatial domain. If the solution is sought in the frequency domain, then x_0 and y_0 are the coefficients of a linear plane which best represents the angle of phase difference (Equation 2.18).

$$\phi = f_x a + f_y b \tag{2.18}$$

The phase matrix is extracted from the cross-correlation spectrum matrix (which is complex see Figure 2.17(c)), where Im is the imaginary part of the cross-correlation spectrum matrix and Re is the Real part.

$$\phi = \arctan(\frac{\mathrm{Im}}{\mathrm{Re}}) \tag{2.19}$$

If the solution is sought in the spatial domain then the inverse Fourier transform of Equation 2.17 is found first (Equation 2.20), then assuming continuous images the solution is given by the delta function (Equation 2.17) (Foroosh et al., 2002), the origin of which is translated for a and b in the E-W and N-S directions, respectively. The values

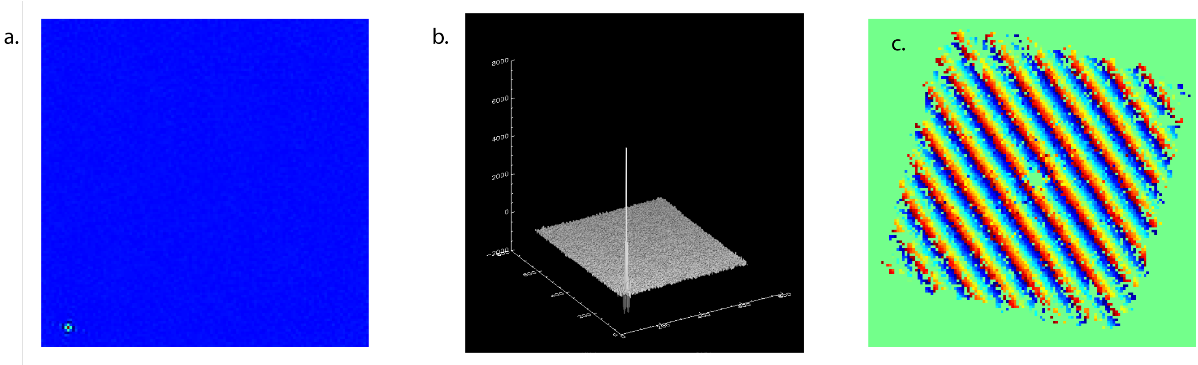

Figure 2.17: Inverse FFT of the normalised cross-power spectrum of the two image patches (128 × 128 pixels) of the same image displaced by 10 pixels in E-W direction and by 7 pixels in N-S direction from each other. (a) displays the peak at the coordinates (10,7). (b) is the same result as (a) in 3D. (c) unwrapped phase difference derived from the normalised cross-power spectrum.

of the offsets from the origin are the displacements of one image with respect to the other (Figure 2.17 (a) and (b)).

$$\mathcal{F}^{-1}(e^{(\omega_x a+\omega_y b)}) = \delta(x+a, y+b) \tag{2.20}$$

I show the principle of phase matching for an example of an image patch and its displaced copy (10 pixels in the E-W direction and seven pixels in the N-S direction). Figure 2.17 (a) and (b) show 2D and 3D inverse FFTs of the normalised cross-power spectrum. The coordinates of the peak in the bottom left corner give the displacements.

Leprince et al. (2007) and Foroosh et al. (2002) found using the convolution theorem that displacement measurements are not affected by blurring, additive white noise, or a combination of both. The method is also robust when matching across different spectral bands.

There are several caveats to the method; (i) for the discrete case the coordinates of the peak are integer values Equation 2.17, and therefore it is not possible to obtain directly the non-integer values needed for sub-pixel accuracy, (ii) phase correlation deals only with linear translation not rotation of displacements, (iii) because of the non periodic nature of digital images, edge discontinuities introduce biases in measurements, (iv) signals are subject to aliasing, (v) the performance of the method is limited in featureless areas.

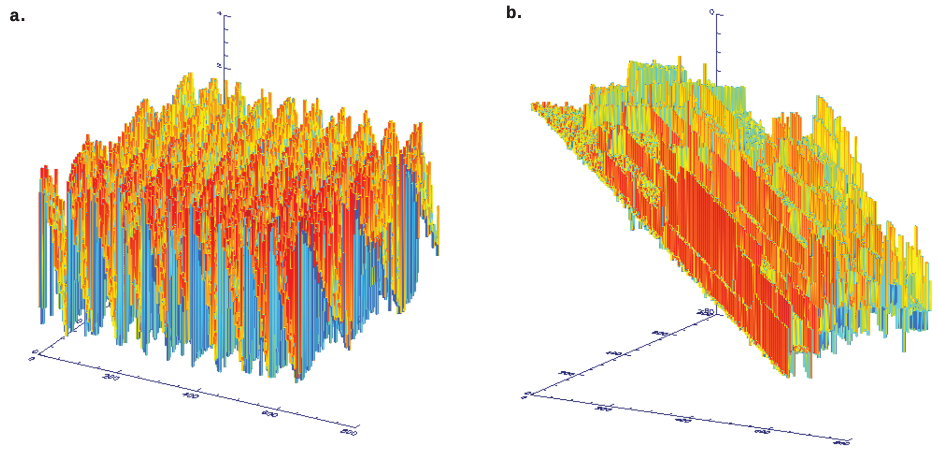

Figure 2.18: *left* wrapped 2D phase difference in 3D view. *right* attempt to unwrap 2D phase difference

2.2.3 Solving for sub-pixel horizontal displacements

Given that the original phase correlation function infers only integer values of displacements, for subpixel resolution the peak will be spread over neighbouring pixels (Hoge, 2003) so its determination is inaccurate. Several approaches have been proposed to find the displacements in sub-pixel range, both in the frequency and spatial domains. Here I present the general principles of four methods, which are widely used including the method implemented by COSI-Corr (Leprince et al., 2007).

Stone

After initial filtering (windowing and masking of the frequencies), Stone et al. (2001) uses least squares to estimate the slope of the phase difference plane in the data. Despite being very fast, this method requires unwrapping of the 2D phase, which is not necessarily always very accurate due to noise in the data. A synthetic example shows the extent of unwrapping errors seen as a result of noise in the 2D phase (Figure 2.18).

Hoge

Hoge (2003) has recognised that the normalised phase correlation matrix is a product of two vectors (Equation 2.21), and is therefore a separable matrix. The separable matrices have rank one, and Singular Value Decomposition (SVD) will yield only one non-zero singular value. However, the normalised phase correlation matrix has more non-zero

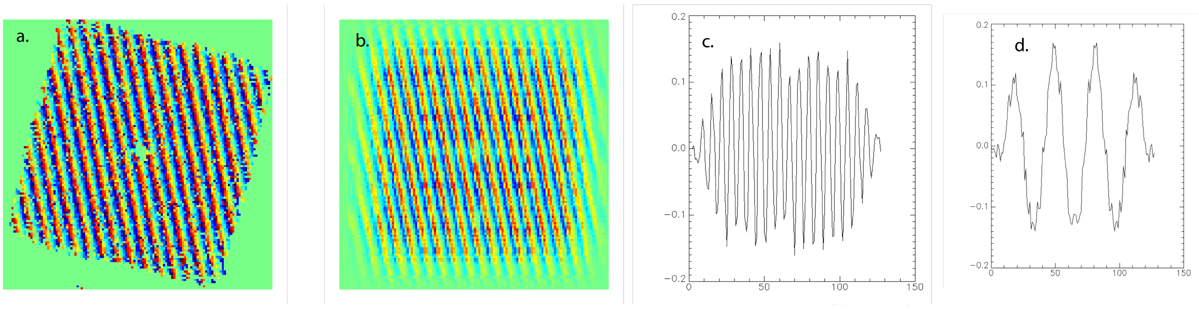

Figure 2.19: (a) unwrapped phase difference derived from normalised phase correlation matrix for two image patches displaced 20 pixels and 4 pixels in the X and Y direction respectively. $b)$ low-rank approximation - reconstruction of the phase difference with four most significant singular values. (c) unwrapped singular vector $\vec{u_1}$ has 20 peaks (d) unwrapped singular vector $\vec{v_1}$ has four peaks. The unwrapped phase of these singular vectors is a line the slope of which determines the amount of displacement

singular values due to noise in the data. The best theoretical approximation of the dominant phase signal is achieved by selecting only the first few (largest values) singular values (refered to as the low rank approximation). The less significant singular values represent noise in the data (Figure 2.18). The first non-zero singular value is the largest and contains information about the dominant signal. The singular vectors ($\vec{u}$ and $\vec{v}$) are derived by calculating the rank-one approximation.

$$C = e^{i(f_x a + f_y b)} = e^{i f_x a} e^{i f_y a} = c_1(f_x) c_2(f_y) \tag{2.21}$$

$$C = \sum_{i=1}^{k} \sigma_i \vec{u}_i \vec{v}_i^T \tag{2.22}$$

Linear coefficients of the singular vectors are the solutions for the horizontal and vertical displacements in the E-W and N-S directions (X and Y axes). The precision of the coefficients is determined by the sub-pixel level using least-squares. This makes determination of the displacements a one-dimensional unwrapping problem, which is much easier to solve than a two dimensional problem which was the case in Hoge (2003). This method is also much more robust to noise. I wrote an IDL program which calculates the normalised phase correlation matrix for an image pair, reconstructs the phase correlation matrix from the most significant singular values (Figure 2.19(b)), and plots unwrapped singular vectors (Figure 2.19(c) and (d)). A test example for an image shifted by 20 pixels in the E-W and 4 pixels in N-S directions, respectively, is shown in Figure 2.19(a).

The authors of Leprince et al. (2007) find that the unwrapping of 1D phase is not always very robust and the entire correlation matrix must be used in order to derive rank one approximation, which can be inaccurate and cause measurement bias.

Foroosh

Hassan Foroosh & Zerubia (1996) has undersampled the images in order to simulate the sub-pixel shift. This is done by reducing the integer value displacements to sub-pixel values by some amount M along the x and y axis. With the undersampled images the shift is still a pixel integer value. The main drawback in achieving the high accuracy of many sub-pixel algorithms is the quality of their interpolation (Hassan Foroosh & Zerubia, 1996).

van Puymbroeck

van Puymbroeck et al. (2000) has avoided the phase unwrapping step by finding the maximum of the norm of the projection of the computed normalised cross-spectrum, Q, on to the theoretical cross spectrum. This is obtained from the inner product of the computed and theoretical matrices (Equation 2.23). The maximum of the norm of Equation 2.23 will yield displacements Δ_x and Δ_y.

$$P_{Q,C}(\Delta_x, \Delta_y) = \sum_{\omega_x} \sum_{\omega_y} Q(\omega_x, \omega_y) e^{-i(\omega_x \Delta_x + {}_y \Delta_y)} \tag{2.23}$$

2.2.4 Leprince

Leprince et al. (2007) proposed a slightly different approach to van Puymbroeck et al. (2000), which involved finding a minimum in the weighted residual matrix between the computed normalised cross-spectrum, Q, and the theoretical normalised cross-spectrum, thereby bypassing the unwrapping step (Equation 2.24).

$$\Phi(\Delta_x, \Delta_y) = \sum_{\omega_x=-\pi}^{\pi} \sum_{\omega_y=-\pi}^{\pi} W(\omega_x, \omega_y) |Q(\omega_x, \omega_y) - e^{i(\omega_x \Delta_x + \omega_y \Delta_y)}|^2 \tag{2.24}$$

where $W(\omega_x, \omega_y)$ is the weighting function. Δ_x and Δ_y are found when the Φ is minimum. Equation 2.24 is re-formulated by Leprince et al. (2007) by recognising that the function ϕ_δ (Equation 2.25) can be expressed as Equation 2.26 because $Q(\omega_x, \omega_y) = Q_R(\omega_x, \omega_y) + iQ_I(\omega_x, \omega_y)$ and $Q_{2R}(\omega_x, \omega_y) + Q_I^2(\omega_x, \omega_y) = 1$.

$$\phi_\Delta(\omega_x, \omega_y) = W(\omega_x, \omega_y)|Q(\omega_x, \omega_y) - e^{i(\omega_x\Delta_x + \omega_y\Delta_y)}|^2 \tag{2.25}$$

$$\begin{aligned}
&\phi_\Delta(\omega_x, \omega_y) = \\
&= W(\omega_x, \omega_y)(Q(\omega_x, \omega_y) - C(\omega_x, \omega_y))(Q(\omega_x, \omega_y) - C(\omega_x, \omega_y))^* \\
&= W(\omega_x, \omega_y)(1 - Q_R(\omega_x, \omega_y)\cos(\omega_x\Delta_x + \omega_y\Delta_y) - Q_I(\omega_x, \omega_y)(\sin(\omega_x\Delta_x + \omega_y\Delta_y)
\end{aligned} \tag{2.26}$$

Each displacement Δ_x and Δ_y is then found by deriving the partial derivatives with the respect to each displacement (Equation 2.27).

$$\begin{aligned}
\tfrac{\partial\phi_\Delta(\omega_x,\omega_y)}{\partial\Delta_x} &= 2W(\omega_x, \omega_y)\omega_x(Q_R(\omega_x, \omega_y)\sin(\omega_x\Delta_x + \omega_y\Delta_y) - Q_I(\omega_x, \omega_y)\cos(\omega_x\Delta_x, \omega_y\Delta_y) \\
\tfrac{\partial\phi_\Delta(\omega_x,\omega_y)}{\partial\Delta_y} &= 2W(\omega_x, \omega_y)\omega_y(Q_R(\omega_x, \omega_y)\sin(\omega_x\Delta_x + \omega_y\Delta_y) - Q_I(\omega_x, \omega_y)\cos(\omega_x\Delta_x, \omega_y\Delta_y)
\end{aligned} \tag{2.27}$$

where the weighting matrix W is defined as

$$W_{i_1 i_2}(\omega_x, \omega_y) = \begin{array}{ll} 0, & \text{if } \mathrm{NLS}_{i_1 i_2}(\omega_x, \omega_y) \leq m(NLS_{i_1 i_2}(\omega_x, \omega_y)) \\ 1, & \text{otherwise} \end{array} \tag{2.28}$$

where m is an empirical value and Leprince et al. (2007) has found that values close to 1 give 'good' results for the majority of images. COSI-Corr has implemented the two-point step size gradient (TPSS) algorithm (Barzilai & Borwein, 1988; Leprince et al., 2007) to solve Equation 2.27. The initial values for the TPSS algorithm (Δ_{x_0} *and* Δ_{y_0}) are computed from the peak correlation method defined in Equation 2.20, which yields integers, so the initial sub-pixel values are approximated using values of both amplitude of the integer solutions and those of neighbouring pixels (Equation 2.29).

$$\begin{aligned} \Delta_{x0} &= -\frac{\sum_{i=-1}^{1}\sum_{j=-1}^{1} x_i p_{x_i,y_i}}{\sum_{i=-1}^{1}\sum_{j=-1}^{1} p_{x_i,y_i}} \\ \Delta_{y0} &= -\frac{\sum_{i=-1}^{1}\sum_{j=-1}^{1} y_i p_{x_i,y_i}}{\sum_{i=-1}^{1}\sum_{j=-1}^{1} p_{x_i,y_i}} \end{aligned} \tag{2.29}$$

The overall solution is also improved and made more robust using an iterative process that fine tunes the initial matrices for normalised cross-spectrum, Q, and weighting, W. Once the first displacements are obtained from Equation 2.27 (Δ_x^0 and Δ_y^0), the original measured normalised cross-spectrum matrix, now called Q^0, is improved by calculating the new Q^1 matrix (Equation 2.30).

$$Q^1(\omega_x, \omega_y) = Q^0(\omega_x, \omega_y)e^{-i(\omega_x\Delta_x^0 + \omega_y\Delta_y^0)} \tag{2.30}$$

Equation 2.30 is the shift theorem and the originally measured Q^0 is shifted from Q^1 by a displacement of (Δ_x^0, Δ_y^0). A new set of (Δ_x^1, Δ_y^1) is computed using Q_1. The iterative process continues until values of (Δ_x^0, Δ_y^0) converge to zero. Similarly, the weighting matrix W (or the filtering mask) is improved given the following relationships. Both Q and C matrices are normalised so that:

$$|Q(\omega_x, \omega_y - C(\omega_x, \omega_y)| \leq 2 \tag{2.31}$$

Also, as the range of values of the weighting matrix is $0 \leq W(\omega_x, \omega_y) \leq 1$, it can then be inferred that the range of values that $\Phi_\Delta(\omega_x, \omega_y)$ can take are [0,4]. Leprince et al. (2007) show that $C^0(\omega_x, \omega_y) = e^{i(\omega_x\Delta_x^0 + \omega_y\Delta_y^0)}$ and find the residual per frequency after the first minimisation (Equation 2.32).

$$\phi_\Delta^0(\omega_x, \omega_y) = W^0(\omega_x, \omega_y)|Q^0(\omega_x, \omega_y) - C^0(\omega_x, \omega_y)|^2 \tag{2.32}$$

where W^0 is the original weighting matrix. The next improved iteration for the weighting matrix W^i is computed using Equation 2.33.

$$W^i(\omega_x, \omega_y) = W^0(\omega_x, \omega_y)(1 - \frac{\Phi_\Delta^0(\omega_x, \omega_y)}{4})^n \tag{2.33}$$

Leprince et al. (2007) has chosen n = 6.

The final shift is calculated by $\Delta_x = \sum_i \Delta_x^i$ and $\Delta_y = \sum_i \Delta_y^i$.

Leprince et al. (2007) define the signal to noise ratio (SNR) which represents the quality of the correlation as (Equation 2.34).

$$\mathrm{SNR}^i = 1 - \frac{\sum\limits_{\omega_x} \sum\limits_{\omega_y} \Phi_\Delta^i(\omega_x, \omega_y)}{4 \sum\limits_{\omega_x} \sum\limits_{\omega_y} W^i(\omega_x, \omega_y)} \tag{2.34}$$

COSI-Corr Image Matching Flow Chart

Each of the steps involved in the COSI-Corr workflow for phase matching are shown in Figure 2.20. I illustrate this using an example of two image patches extracted from two orthoimages. The image patches are first prepared (*top row* and *bottom row*) before the normalised cross-spectrum matrix and its Fourier inverse are calculated. The initial displacement is estimated from the correlation peak. If the displacement is larger than one pixel, the ‘slave’ patch is re-selected, because the SNR value depends on the percentage overlap. Once the ’slave’ patch has less than one pixel displacement, the phase minimization algorithm (TPSS) is applied to find the sub-pixel value of deformation. All incremental shifts are then added together to give the total displacement.

I wrote this code based on Leprince et al. (2007) to calculate image correlation with sub-pixel accuracy. I then applied it in Chapter 5 for image correlation of pre-event and post-event lidar DEMs (Figure 5.8).

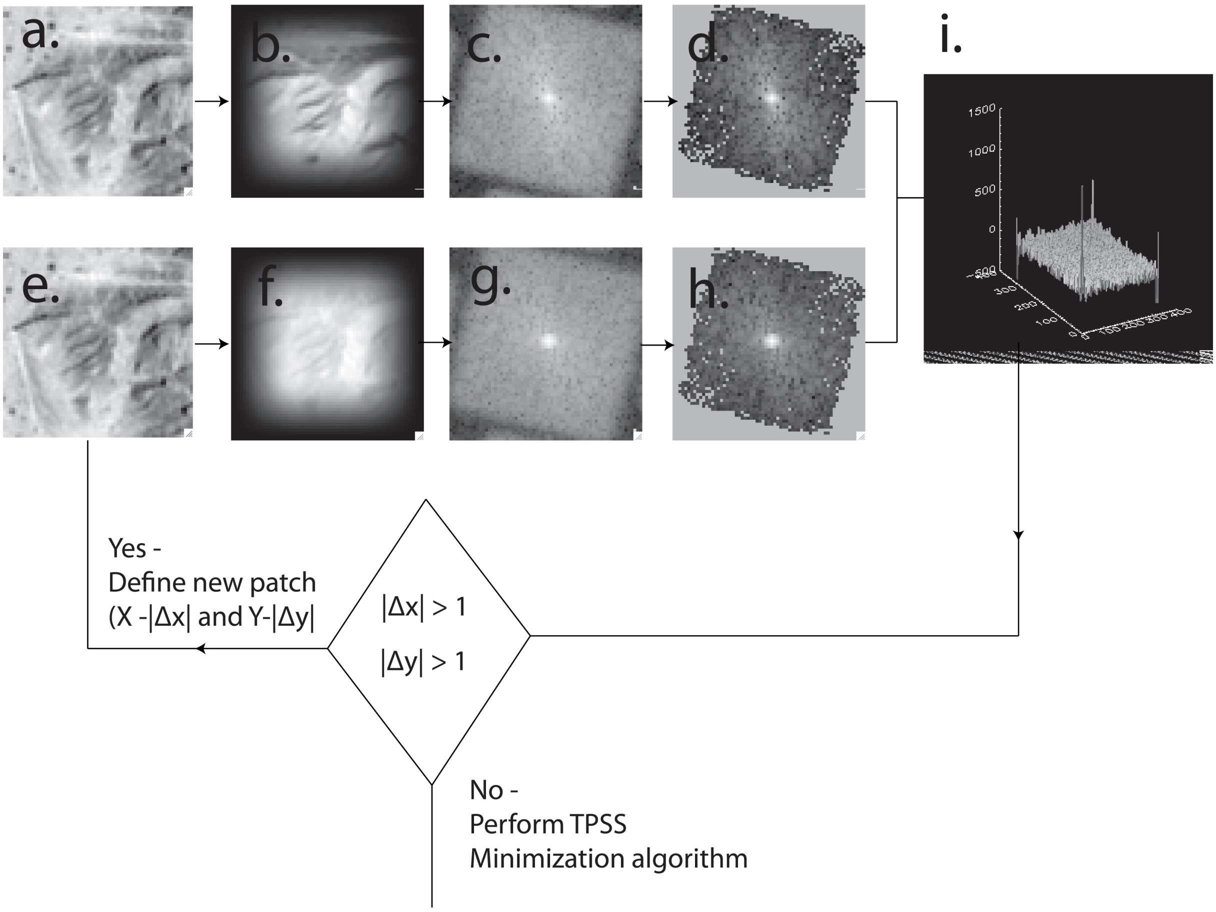

Figure 2.20: (*a*) and (*e*) are small patches of the pre-event and the post-event images respectively. (*b*) and (*f*) are the same windows as in (*a*) and (*e*) with raised cosine window applied. (*c*) and (*g*) are the results of the Fourier transformation without the boundary effect noise. (*d*) and (*h*) show the patches after some frequencies, which are most likely to corrupt the image, are filtered out. (*i*) is the 3D cross-power spectrum obtained from (*d*) and (*h*).

2.3 Practical processing steps of COSI-Corr

The steps required for processing satellite images using COSI-Corr in order to obtain the sub-pixel displacements are as follows:

- Import raw images and their metadata. COSI-Corr calculates the sensor model based on Section 2.1.1.
- Import available DEM for orthorectification.
- Import or create a reference map for acquisition of Ground Control Points (GCPs). A GCP is a point in a reference map, where the ground coordinates are known, that can also be identified in the raw SPOT image, which is to be orthorectified. Throughout this thesis I use shaded relief created from DEMs as the reference map.

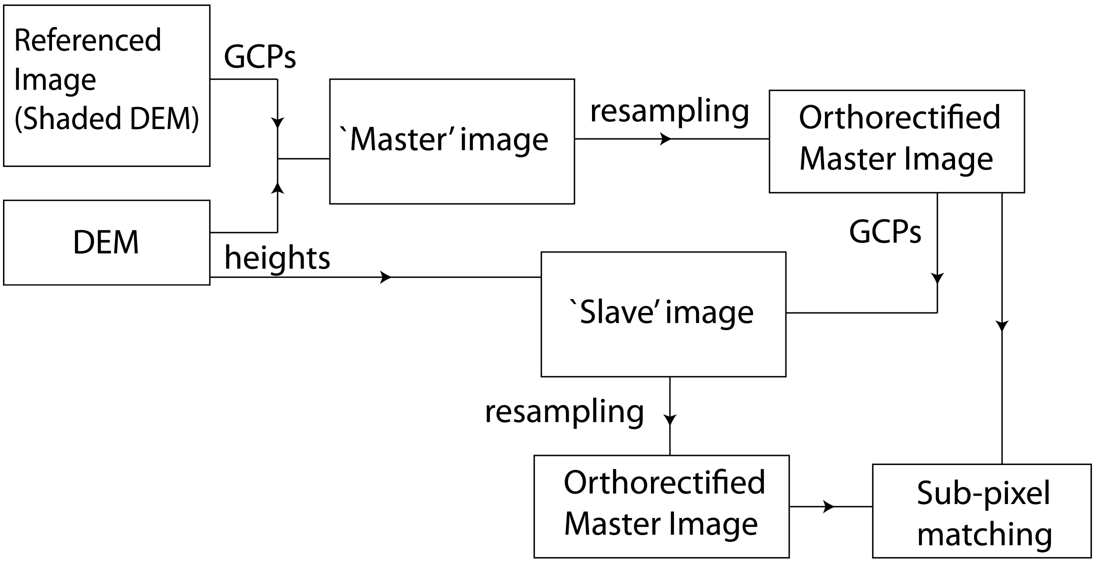

Figure 2.21: This is the COSI-Corr main workflow. The 'master' image is orthorectified (inverse orthorectification) with DEM heights and GCPs from the reference image (e.g. shaded relief from the same DEM). The 'Slave' is then orthorectified with heights from a DEM and selection of GCPs from the 'master' orthorectified image. Two orthorectified images ('master' and 'slave') are then correlated as in Figure 2.20.

- Collect GCPs for the 'master' image from the reference map. The 'master' image tends to be an image before the event, although there are cases when that is not the case.
- Orthroectification of the 'master' image.
- Collect tie-points for the 'slave' image, where the orthorectified 'master' image is the reference map. Tie-points are identical points in the post-event image and pre-event image for which the ground coordinates are now known.
- The last step is to cross correlate the orthorectified 'master' and 'slave' images as described in Section 2.2.4.

Chapter 3

Surface displacements in the 2005 Afar rifting event from satellite satellite image matching

This chapter is based on published paper from Barišin I., S. Leprince, T. Wright, and B Parsons (2009), *Surface displacements in the September 2005 Afar rifting event from satellite image matching: Asymmetric uplift and faulting*, Geophysical Research Letters, V.36(9), doi: 10.1029/2008GL036431

In this chapter I create horizontal offsets for the Dabbahu Magmatic Segment occured during the 2005 dike event in Afar, Ethiopia to reveal a detailed picture of the surface deformation caused by a rifting event not only in the far field of the rifting event, but also a very detailed deformation above the rift itself. Next, I derive the vertical offsets by combining the InSAR and its range offsets with horizontal displacements obtained by sub-pixel matching of the images. Using the horizontal displacements I fit a dislocation model of the event with complex geometry of interplay between a dike and normal faulting. Horizontal and vertical displacements laid over topography reveal that the Dabbahu segment occured away from existing the geomorphic axis.

3.1 Introduction and Setting

The Afar triple junction is the junction of two seafloor spreading centres (the Red Sea and the Sheba Rift, Gulf of Aden) with the Main Ethiopian Rift, which is transitional from continental rifting to oceanic spreading and is located in the Afar depression. Divergence between the Arabian, Nubian and Somalian plates take place on these rifts (Figure 3.1). The horizontal extension on the southern Red Sea Rift within the Afar depression has been localised on magmatic segments (Hayward & Ebinger, 1996).

These magmatic segments are formed by the injection of dikes into the upper crust from underlying magma chambers (Ebinger et al., 2008). Continental rifts are segmented by large offsets of normal faults, and many lack magmatism. The Dabbahu segment is one of only few examples of such deformation on land, the others being Krafla in north Iceland (1975-1984) (e.g. Buck, 2006), and the 1978 Asal rift in Djibouti (e.g. Cattin et al., 2005; Vigny et al., 2007). All three events are characterized by seismic swarms (that may last days, months, or years), intrusion of magma at depth, localised slip on bounding normal faults, basaltic eruptions, and fissure opening. The crustal growth of the Afar region is developed due to dike intrusions (Rowland et al., 2007b), but dike intrusions also play an important role in the continental stretching as magma intrusions facilitate extentition.

The large rifting episode in northern Afar (Dabbahu Magmatic Segment) occurred in September 2005 when 165 earthquakes were recorded, of which 15 were greater than M5, and a large vent opened up possibly due to a small eruption (Wright et al., 2006; Rowland et al., 2007a). Figure 3.2 shows the area of the large vent or fissure before and after the event on SPOT4 images.

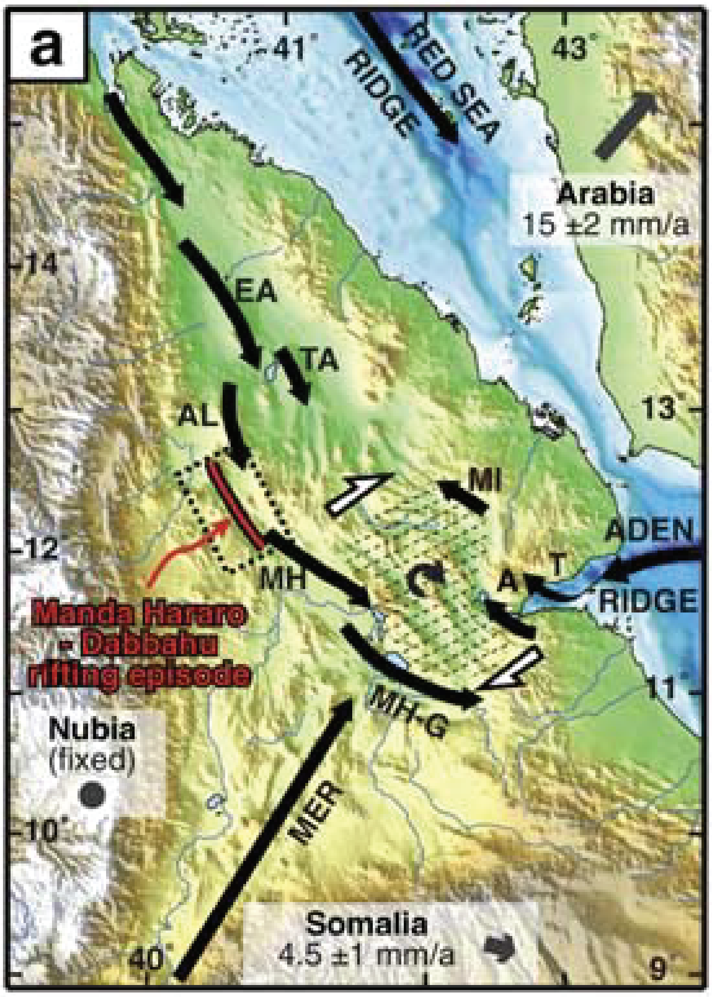

Figure 3.1: Map of the Afar triple junction. Black arrows show rift segments with Quaternary magmatic activities (Manighetti et al., 1998). Adapted from Grandin et al. (2009)

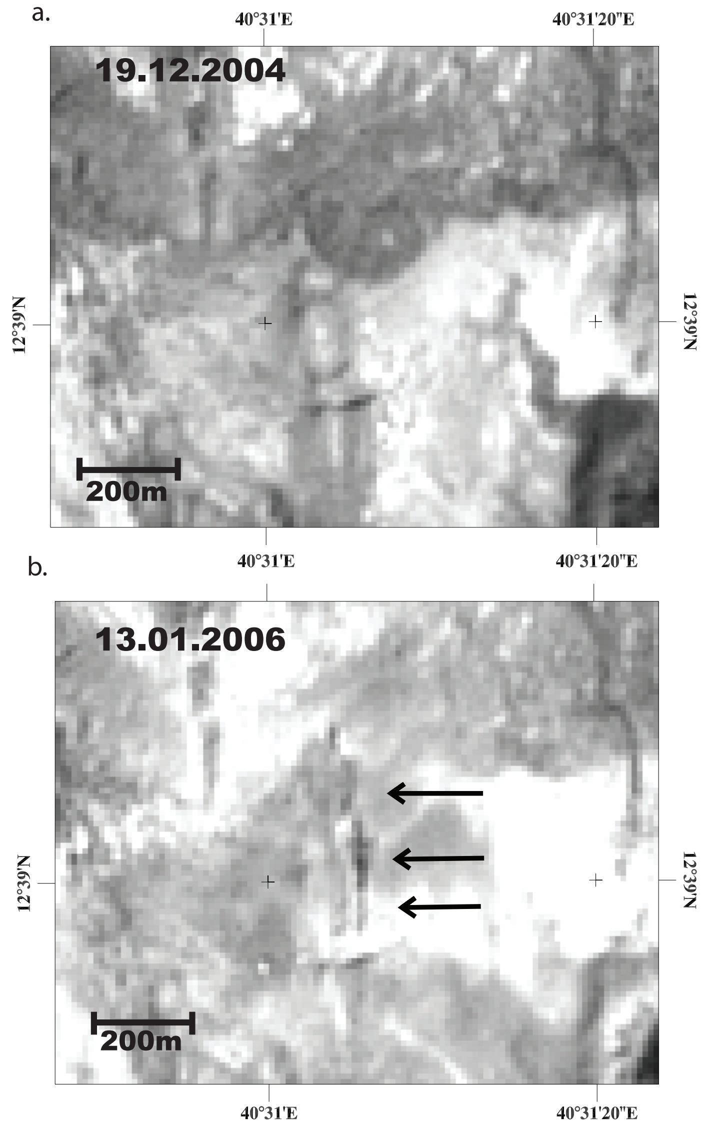

Figure 3.2: (*a*) Portion of the SPOT4 image before the September 2005 event (19.12.2004) around the area where the large rift opened. (*b*) The same area of the SPOT4 image after the September 2005 (13.01.2006) event around the area where the large rift opened. The black arrows point at the large vent that opened during the September 2005 event.

Table 3.1: Optical Satellite Images used

	Image Date	Inc.Angle °	Sun Azimuth °	Sun Elevation °
DEM generation	15.01.2001			
ASTER(15m)	07.04.2005			
	20.05.2003			
	05.02.2006			
Image matching	19.12.2004	0.48	152	49.4
SPOT4(10m)	13.01.2006	-0.22	146	49.3

3.2 Horizontal displacements

I use the COSI-Corr software (Ayoub & Leprince, 2005; Leprince et al., 2007) to find sub-pixel horizontal displacements of SPOT4-HRV1 images acquired before and after the rifting event (Table 3.1 and Figure 3.3). The arid climate of the regions provide ideal conditons for image matching as there are no seasonal changes in vegetation between both images.

I first constructed a digital elevation model (DEM) (Figure 3.10b) from several 15 m Aster stereo-pair images (Table 3.1) using the ENVI AsterDTM module, which claims absolutr accuracy of 20 m RMS in height (SULFSOFT, 2004). The individual DEMs were adjusted to the 90 m SRTM DEM and then mosaiced. Vertical differences between the ASTER and SRTM heights are in the range of 5-20 m. In addition to using this DEM as a ground reference for georeferencing the pre-event image, the DEM is used in the orthorectification of both images prior to the optical matching.

After georeferencing and orthorectification, SPOT4 images acquired before and after dike intrusion (Table 3.1) should be identical, not withstanding the effect of surface displacements and a few remaining artifacts (Leprince et al., 2007). I then correlate images with sub-pixel resolution.

Assuming that the only displacements between the two images are due to the rifting (i.e. tectonic) event, I obtained the E-W (Figure 3.4) and N-S horizontal displacements (Figure 3.5). I find that using a sliding window of size 32x32 pixels sliding with a 4-pixel step gives visually the best correlation results. The final spatial resolution of the horizontal displacement measurement maps is 40 m. I do not empirically correct the striped artifacts, which are most likely due to unmodelled spacecraft movements or CCD artefacts. The E-W component of horizontal displacement shows a maximum extension of

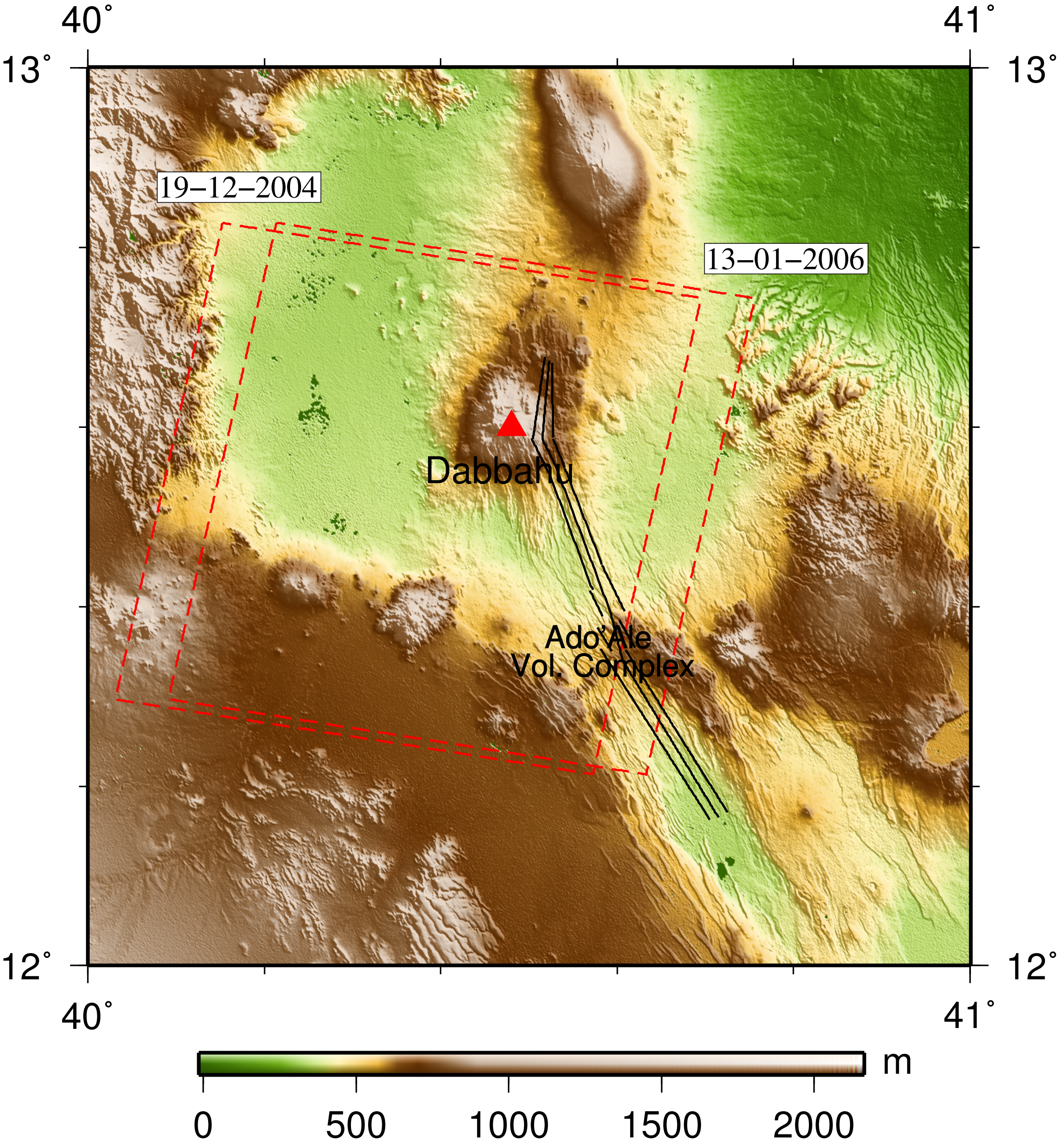

Figure 3.3: Spatial coverage of the SPOT scenes used in this study. Black lines show the rift geometry used in the Wright et al. (2006) study. My data partially cover the extent of the September, 2005 rifting event.

6 m (Figure 3.4) which agrees well with the InSAR results (Wright et al., 2006). Results of the horizontal displacement perpendicular to the rift using E-W and N-S components are shown in Figure 3.11(a). and as a velocity field in Figure 3.5. The location of the boundary between eastward and westward displacements switches from the eastern edge of the subsidence zone in the north to its western edge in the south (Figure 3.4 and Figure 3.10(b)).

The RMS of the far-field deformation measurements observed in several boxes shown in

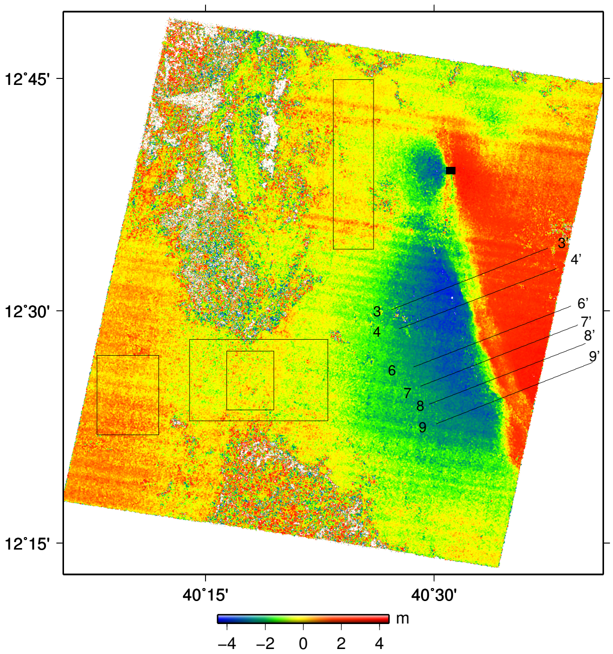

Figure 3.4: East-West displacements. From the matching of SPOT4 images. The profiles are shown in Figure 3.13. The boxes show the areas for where the RMS values are calculated.

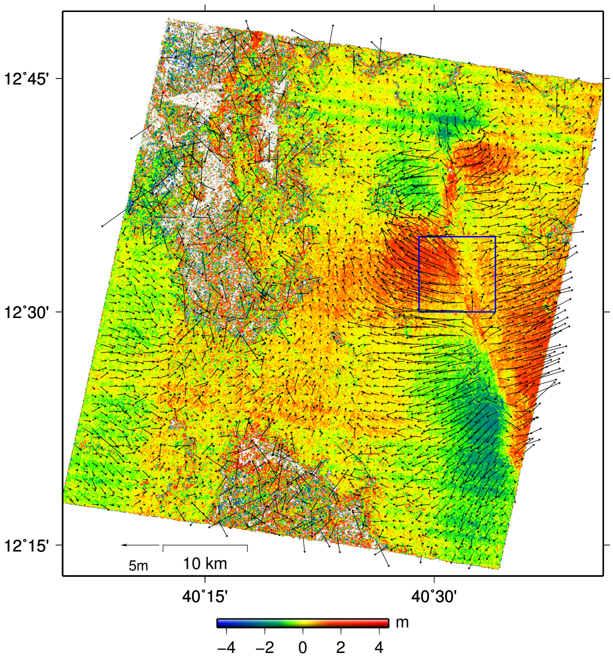

Figure 3.5: N-S displacements. From the matching of SPOT4 images. The vectors show the horizontal displacement perpendicular to the dike.

Figure 3.4 is ~40 cm, and I infer that this represents the accuracy. The correlation quality map or signal-to-noise ratio map (SNR) (Figure 3.6) shows a distribution of decorrelation across the resulting image. Areas of decorrelation are shown by darkerer colours and are located in the south of the image and one area has spread from the north-west corner towards the middle of the image.

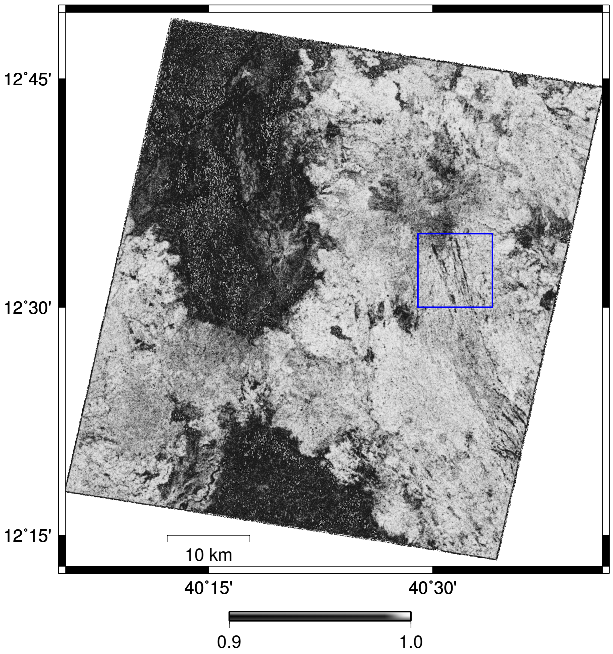

Figure 3.6: Map of the SNR of the image correlation quality.

All SPOT satellites suffer from interior orientation misaligment caused by the malfunction of the charged coupled device (CCD). Leprince et al. (2008) address this problem by deriving a calibration model to correct the CCD misalignments, which is implemented in COSI-Corr. The CCD misalignments of the SPOT4-HRV1 sensors were corrected as described in Leprince et al. (2008). There are still some artifacts left from this misalignment to the far west of the images, however, they do not affect the measurements of the rift displacements.

Close up view in the E-W displacement map highlights some sharp linear discontinuities that run parallel to some normal fault features in the topography or large surface disturbances that appear visible in the imagery (Figure 3.7). Initially, I interpreted these as locations of the active faulting and opening of the new fissures. SNR is somewhat smaller (r=0.98) in these areas which align well with these features, presumably due to surface disturbances, which may support my view of the locations of the active faults. This could not be an artifact of the topography as the incidence angles of both images are very close. It is unlikely that the shadows are a cause of the decorrelation as the sun azimuth and the sun angle are almost identical in both SPOT images (Figure 3.10), and these features align with some of the east-facing faults. However, after thorough investigation of the biases in the data derived by optical matching, it may be possible that these

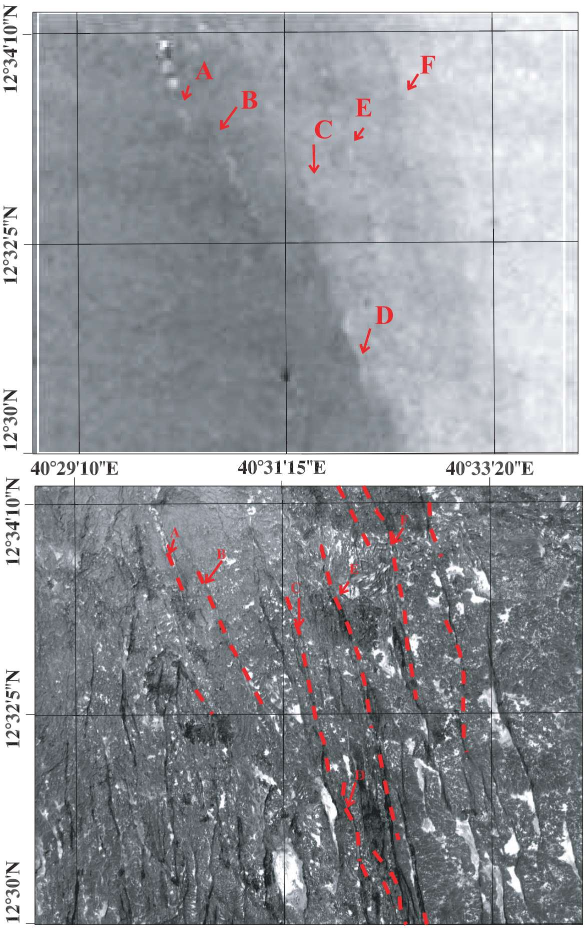

Figure 3.7: (a) Enlargement of the E-W displacement map with some linear discontinuties labelled A to F. The enlargment area is shown by the blue polygon in Figure 3.6 and Figure 3.5. (b) Portion of the orthophoto of the same geographical area as in (a). The linear discontinuties (the red lines) align well with the topographic features of the normal faults

linear features are caused by the shadowing effects of the high cliffs (see Chapter 4).

3.3 Vertical Displacements

A limitation of the optical matching method is that it yields only the horizontal components of the displacement. I extracted the vertical displacements (Figure 3.10(e) and Figure 3.9) by combining the direct horizontal displacements with InSAR line-of-sight measurements (Wright et al., 2004a). The relationship between the line-of-sight vector and the three displacements in X, Y, and Z direction is shown in Equation 3.1

$$los = \mathbf{ul} = u_x Lx + u_y ly + u_z l_z \tag{3.1}$$

where $\mathbf{u}$ is three dimensional vector of displacement and $\mathbf{l}$ is three dimensional unit

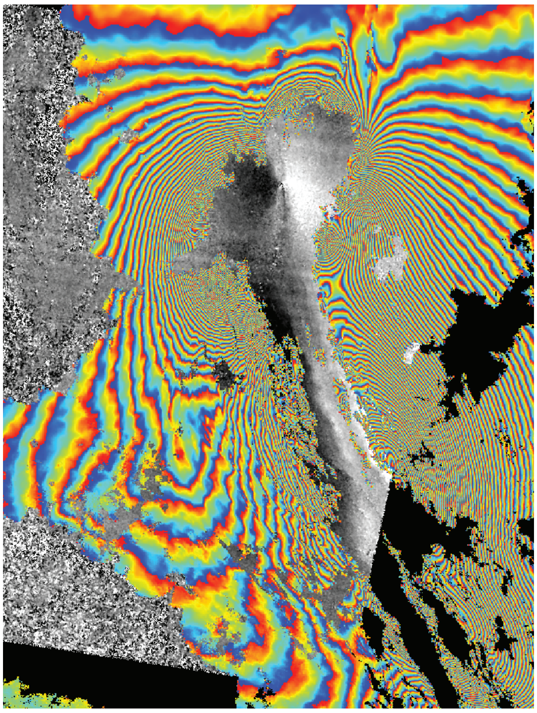

Figure 3.8: Descending Interferogram at 2.8cm interval (Wright et al., 2006) supperimposed over the E-W displacements.The gaps are decorrelation caused by the high gradient deformation.

vector. From Equation 3.1 I derive the vertical displacement

$$u_z = \frac{los - u_x l_x - u_y l_y}{l_z} \tag{3.2}$$

where I use the descending intereferogram for the los (Figure 3.8), due to its greater spatial coverage. The gaps in the interferogram are filled with lower resolution (80 m) and lower accuracy range-offset measurements (Wright et al., 2006), and u_x and u_y are dispalcements obtained from sub-pixel matching of SPOT.

The vertical displacements in Figure 3.9 and Figure 3.10(d) (also in Figure 3.12 and Figure 3.13), show asymetrical uplift of the rift flanks; the west flank uplifted by ∼1.5 m, while the east flank was uplifted by ∼1 m. Asymmetric uplift above dikes has been reported by other authors (e.g. Sigmundsson et al., 1999; Hollingsworth et al., 2012). Although the shift of the new rift axis in relation to the geomorphic rift axis in this area has been reported by Rowland et al. (2007a), my data illustrates well how the rift defined by the instantaneous vertical motion lies to the east of the topographic rift, along slightly raised topography (Figure 3.10(e), Figure 3.13, Figure 3.12). I note that the location of the boundary of the vertical subsidence on the west side of the dike lies along

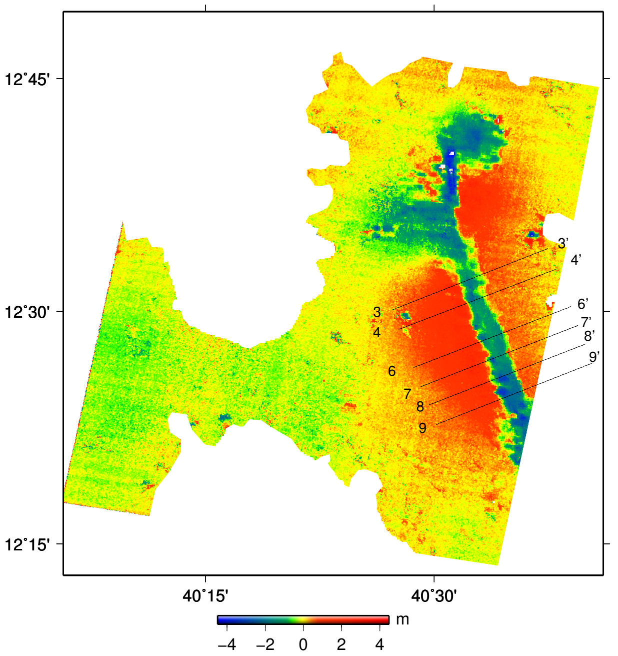

Figure 3.9: Vertical displacements derived by combining the horizontal displacements determined by matching the SPOT4 images with InSAR line-of-sight measurements.

the west-dipping normal fault seen in the topography (Figure 3.10(d), Figure 3.12 and Figure 3.13). I measure the maximum subsidence of >4 m near the large vent reported by Wright et al. (2006) and an average of 1.5 m above the dike, and few areas above dike that have subsided >2 m (Figure 3.10(d)).

Figure 3.10 shows full 3D displacement field of the 2005 Dabbahu segment.

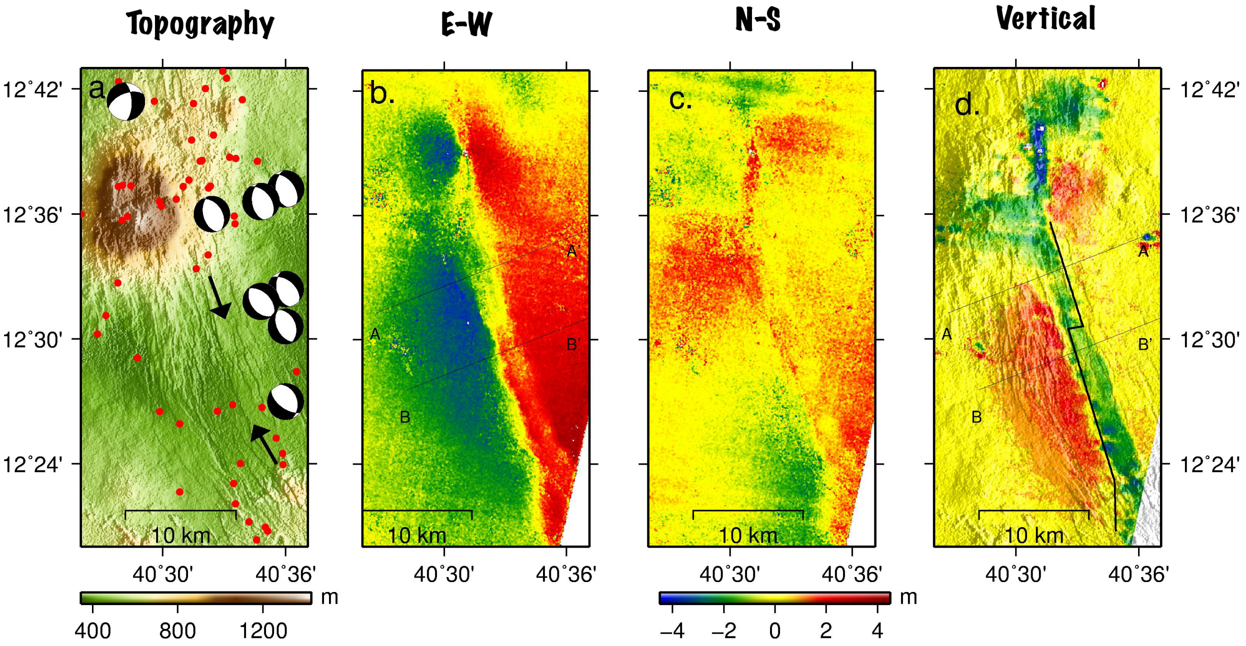

Figure 3.10: (*a*) Shaded DEM generated from Aster images showing the area affected by the dike intrusion. Two black arrows pointing at the direction of the new active dike. Focal mechanisms for earthquakes of M >5 are the CMT solutions, and red circles are relocated earthquake epicenters from Wright et al. (2006). The black dashed line shows the geomorphic rift axis. (*b*) East-west displacements from matching of SPOT4 images. Three black lines follow the location of the boundary between eastward and westward displacements. (*c*) North-south displacements from matching of SPOT4 images. (*d*) Vertical motion observed from the E-W and N-S displacements and InSAR phase measurements. AA' and BB' profiles are shown in Figure 3.13

.

3.4 Modelling of the rifting

Deformation of the shallow elastic crust can be modeled using elastic rebound theory. Studies by Wright et al. (2006) and Ayele et al. (2007) produced models of fault slip and dike opening distribution using InSAR only, which could not be resolved in the near-field because of the decorrelation caused by the high gradient defromation Figure 3.8. Based on the detailed 3D displacement field, which includes the near-field deformation, I fixed the dike geometry for a rifting system comprising a dike and normal faults. Just to test a simple scenario I model the displacements using the Okada (1985) formulation due to a tensile dislocation in a homogeneous elastic half-space. By constraining the amount of opening and location from the surface deformation I determined the bottom and top depths and the dip of the dike plane assuming uniform opening on a singular rectangular plane.

The vertical subsidence along the dike is $\sim$ 2 km wide in the northern part and widens

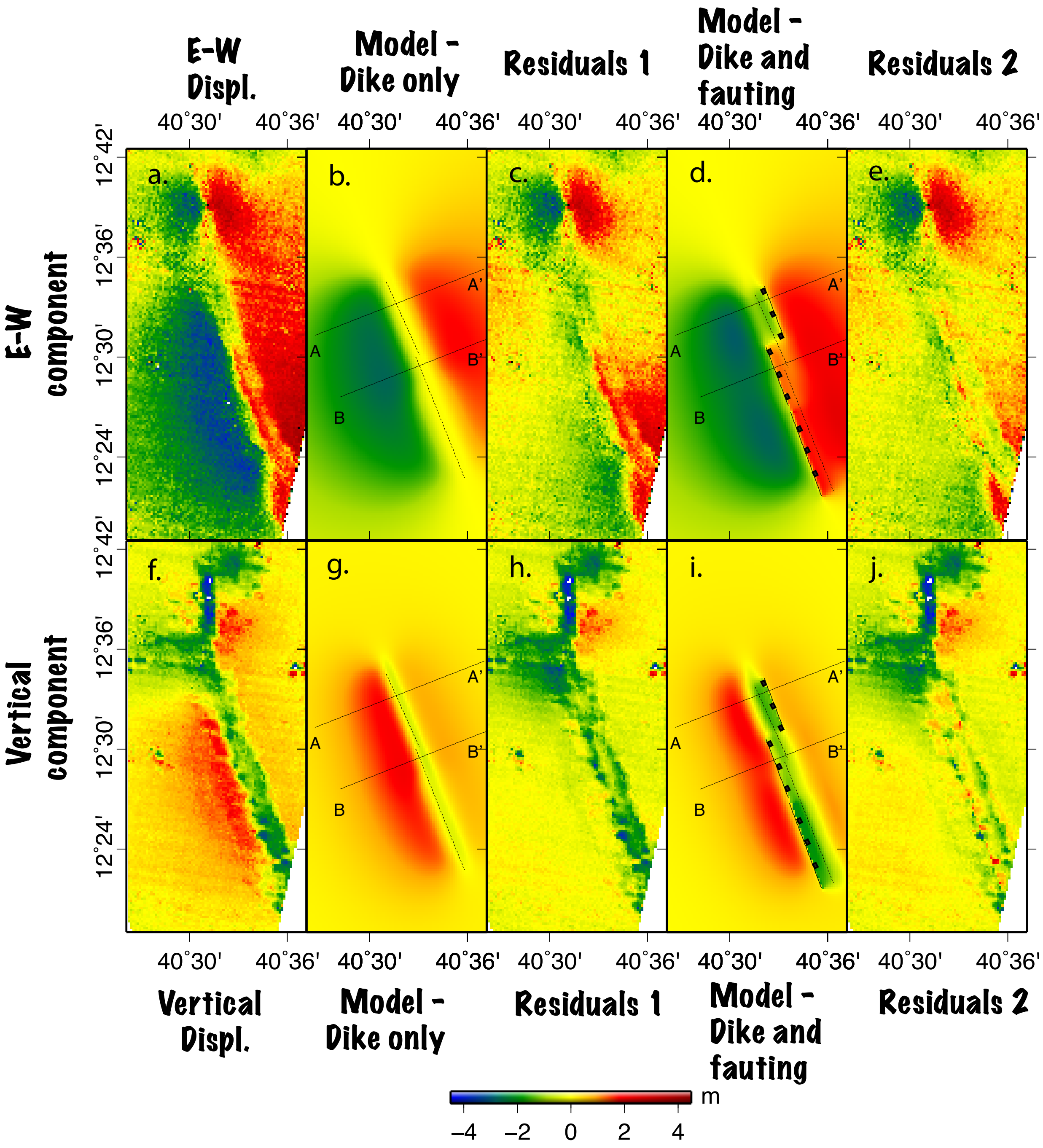

Figure 3.11: (*a*) E-W displacement. (*b*) Model for extensional opening perpendicular to the rift computed for the presence of a dike (dashed lines) only. (*c*) Residuals of (*a*) and (*b*).(*d*) Model or the presence of a dike and normal faults, which are placed on the opposite edges of the dike all dipping towards the dike. (*e*) Residuals of (*a*) and (*d*). (*f*) Vertical offset map. (*g*) Vertical projection of the model computed for the presence of a dike only. (*h*) Residuals of (*f*) and (*g*). (*i*) Vertical projection of the model for the presence of a dike and normal faults (*j*) Residuals of (*f*) and (*i*).

to ∼2.5 km in the southern part. I divided the dike into two parts (Figure 3.11b,g) and modelled them separately. From the opening displacements perpendicular to the rift I measure a 6 m extension at the surface. Referring to the results of the distributed inversion (Wright et al., 2006), I fixed the opening on the dike to 8.5 m in the northern part and 9 m in the southern part. The top depth of the dike, which controls the width of the rift at the surface, was found to be 1.4 km in the north and 1.5 km in the south. The bottom depth of the dike, which determines the width of the uplift field, was found to be 5 km in the north and in the south. From the asymmetry in vertical uplift on the flanks of the dike, I find by comparing the data with forward modelling that the best-fitting solution is to fix the dip of the dike plane at 80° west at a strike of 158° on both of the segments (Figure 3.13 and Figure 3.12). Figure 3.11(b),(g) show the modeled extensional displacment perpendicular to the rift and vertical displacements. The residuals between observed displacements and the model (Figure 3.11(c),(h)) show that the model describes well the main characteristics of the extension and uplift outside the dike. The residuals of the vertical displacements also reveal more subsidence around the northern volcanoes, making it a more circular shape (Figure 3.11(h)). I still observe areas of large residuals (larger than 1 m) above the dike that are not sufficiently explained by the only dike model.

Rubin (1992) showed that subsidence observed over dikes in Hawaii cannot be explained by the dikes alone. Rubin (1992) showed that normal faulting is required to enhance the vertical displacement. I measure $\sim$ 1.5 m of additional subsidence (Figure 3.11(h) and Figure 3.13). Furthermore, the dike model alone produces no extensional horizontal displacements within the rift (Figure 3.11(b), where I observe a strong signal and where the location of the boundary between eastward and westward displacements switches down the rift. In contrast to the geometry adopted by Wright et al. (2006), which had two normal faults on each side of the dike, I fix the geometry in the northern section with one normal fault lying along the eastern subsidence boundary that dips west, and one normal fault in the southern part that lies along the western subsidence boundary (split into two faults), dipping east (Figure 3.11(d),(i)). These normal faults form a large component of the subsidence above the dike and also explain a small amount of the extension. The profiles in Figure 3.12 and more profiles in Figure 3.13 show the improvements of this model in comparison to the simple dike model. The residuals are shown in Figure 3.11(e),(j) and the summary of the parameters that I use to fix the dike model geometry in Table 3.2.

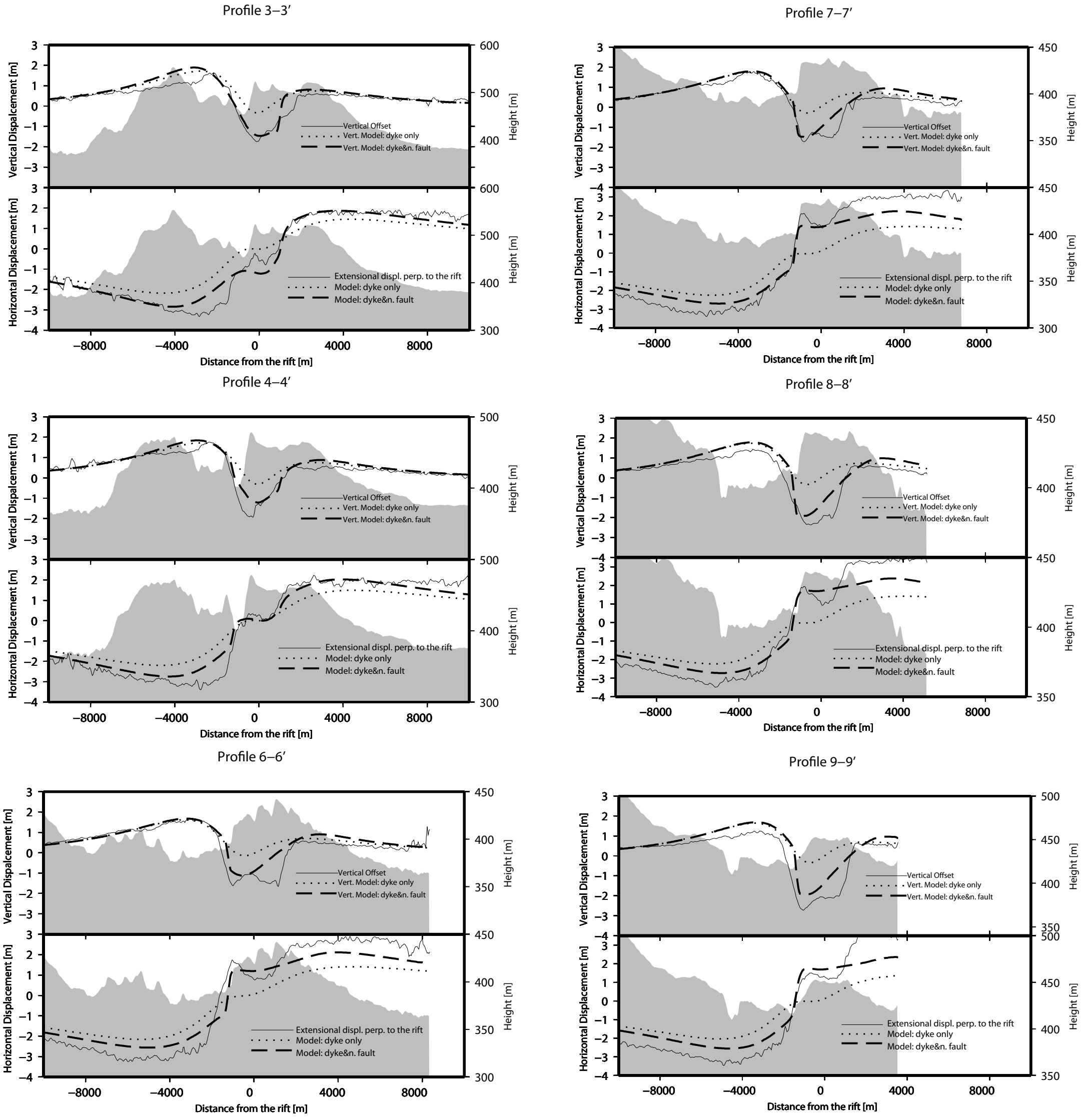

Figure 3.12: Top profiles showing the E-W displacement, simple model with dike only, and model with the dike and a normal fault. Profiles below showing vertical offsets, simple model with dike only, and model with the dike and a normal fault.

Table 3.2: Parameters used to fix the model geometry

	Opening (m)	Slip (m)	Dip (°)	Strike (°)	Top Depth (km)	Bottom Depth (km)	Length (km)
North Dike	8.5	0	80	158	1.4	5	12
South Dike	9	0	80	158	1.5	5	11
North Fault	0	3	40	160	0.1	2	6
Middle Fault	0	2.5	30	338	0.01	2	8
South Fault	0	3.8	30	340	0.05	2	10

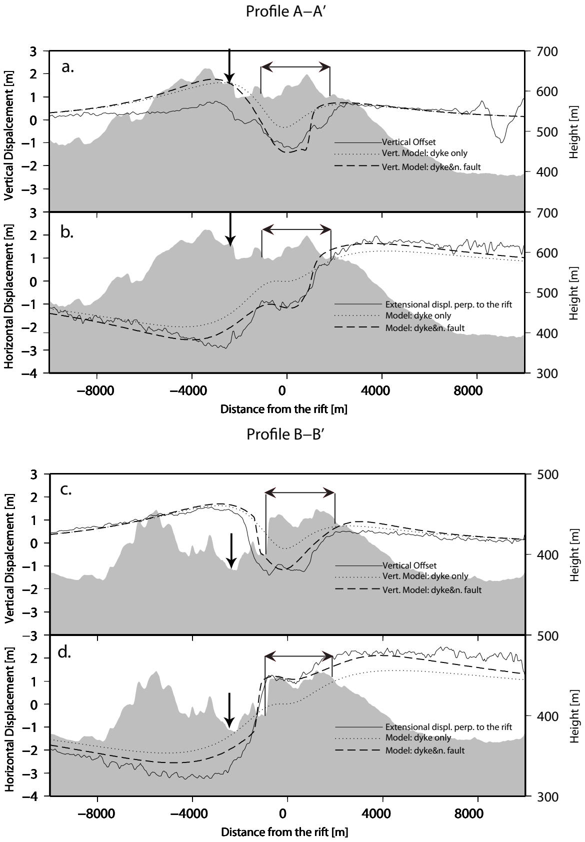

Figure 3.13: (*a*) and (*c*) Profiles of the derived vertical displacements, and the predictions of the model with a dike element only and the model with a dike and onenormal fault**ing**. (*c*) and (*d*) Profiles of the extensional displacements perpendicular to the rift, and the predictions of a model using the dike only and a model using the dike and one normal fault. Gray color shows topographic profile. Vertical arrows show the center of the geomorphic rift axis. Horizontal arrows show the extent of the new diking event.

3.5 Discussion

The ideal conditions (arid terrain, little vegetation, images from the same season) for the optical matching allowed us to produce accurate and detailed horizontal displacement maps. The combination of the image matching and InSAR has improved the 3D deformation field previously constructed by Wright et al. (2006), highlighting the asymmetric deformation, a switch in the location of the border between eastward and westward displacements, and locations of active faulting that were previously unknown. The dip of the dike to the west explains the asymmetry better than the vertical dike used in the faulting model produced by (Wright et al., 2006), although this could also be an artifact of the a ramp in the InSAR and optical datasets. Instead of having two symmetrical conjugante normal faults, by placing only one normal fault on one or other side of the dike, the observations are better explained. The RMS misfits in the far field outside the dike are ~0.4 m or smaller. Further enhancement could be made by calculating the model with distributed instead of uniform slip, although the impact of the poorly constrained bottom depth of the dike in the Okada model, which determines the extent and magnitude of the deformation in the far field, affects the results of my model. The remaining residuals within the subsiding zone, which includes some areas where RMS of vertical misfit is ~0.8 m are due to the complexities of the normal faulting geometry above the dike. The poor fit in the extreme south eastern corner of the dike (Figure 3.11(e)) is probably due to the large active structure that I observe in the data but has not been included in the model. The inferred east-dipping normal faulting, located along where the images show the west dipping fault, needs to be confirmed in the field. In fact, Hofmann (2013) using Lidar measurements clearly demonstrate existance of both east-dipping and west-dipping network of short faults (< 3400 m) on both sides of the rift as well as within the rift itself.

Chapter 4

Study of the 04.04.2010 El Mayor - Cucapah Earthquake: Data and Artefacts

This chapter and the following two are dedicated to understanding the El Mayor -Cucapah earthquake. The aim of this chapter is to analyse the artefacts present in the maps of horizontal displacements obtained by image matching with sub-pixel resolution, so that the horizontal displacement maps can be used without ambiguities. I study three groups of artefacts: long-wavelength artefacts, short-wavelength artefacts and artefacts caused by topography. In Chapter 5 I propose a new method for calculating vertical displacements directly using post-event high resolution DEM data and two of pre-event optical images, and I generate a vertical displacement map from the El Mayor-Cucapah earthquake. Chapter 6 presents the theory of Bayesian inversion, which is then used to model the geometry of the fault planes and slip distribution occuring in the El Mayor-Cucapah earthquake. I run the inversion using InSAR and optical sub-pixel matching measurements of surface displacements.

4.1 Tectonic setting of El Mayor-Cucapah earthquake

The $M_w7.2$ El Mayor-Cucapah earthquake occurred on 4th April 2010 in Baja California, Mexico. This tectonically active area links the southern San Andreas Fault zone with spreading of the East Pacific Rise in the Gulf of California (Elders et al., 1972). Relative motion between the Pacific and North American plates in the southern San Andreas fault zone is distributed over several major faults (San Jacinto, Elsinore and San Andreas), the motion being dextral strike-slip with a total relative motion of 35-40 mm/year (Johnson et al., 1994; Bennett et al., 2004). The epicentral area is also characterised by distributed faulting, containing several parallel northwest-southeast dextral strike slip faults with a normal component accommodating extension (Savage et al., 1994). It is covered by thick sediments obscuring many of the faults (Pacheco et al., 2006). The El Mayor-Cucapah earthquake did not rupture the main plate boundary fault in the area, the Cerro Prieto fault (Figure 4.1), but a number of faults to the west of it. The motion on the faults during the 2010 El Mayor-Cucapah earthquake was oblique right lateral (Fielding et al., 2010; Sandwell et al., 2010; Fletcher et al., 2010).

The Sierra Cucapah is bounded to the southwest by the Laguna Salada fault (Figure 4.1), the southern extension of the Elsinore fault (Figure 4.1) (Mueller & Rockwell, 1995). It last ruptured in 1892 with an earthquake estimated to have a moment magnitude of M_w7.2, one of the largest in recorded history in southern California (Hough & Elliot, 2004). Although the Laguna Salada fault is located in close proximity to the faults that ruptured, only minor slip near the USA-Mexico border was observed. Instead, in the area where we have mapped the vertical displacements, the main rupture seems to have been taken up on the Borrego and Pescadores faults (Axen et al., 1999; Fletcher & Spelz, 2009). These faults have been mapped as active by Jennings & Saucedo (1994). Wei et al. (2011) found that the faults involved in the northwest of the earthquake sequence dipped towards the north-east.

4.2 Data

4.2.1 Optical images

Eleven SPOT images and five DEMs were available for the analysis of the El Mayor-Cuapah earthquake. Table 4.1 lists all the available SPOT images and their properties, their spatial coverage is delineated in Figure 4.1.

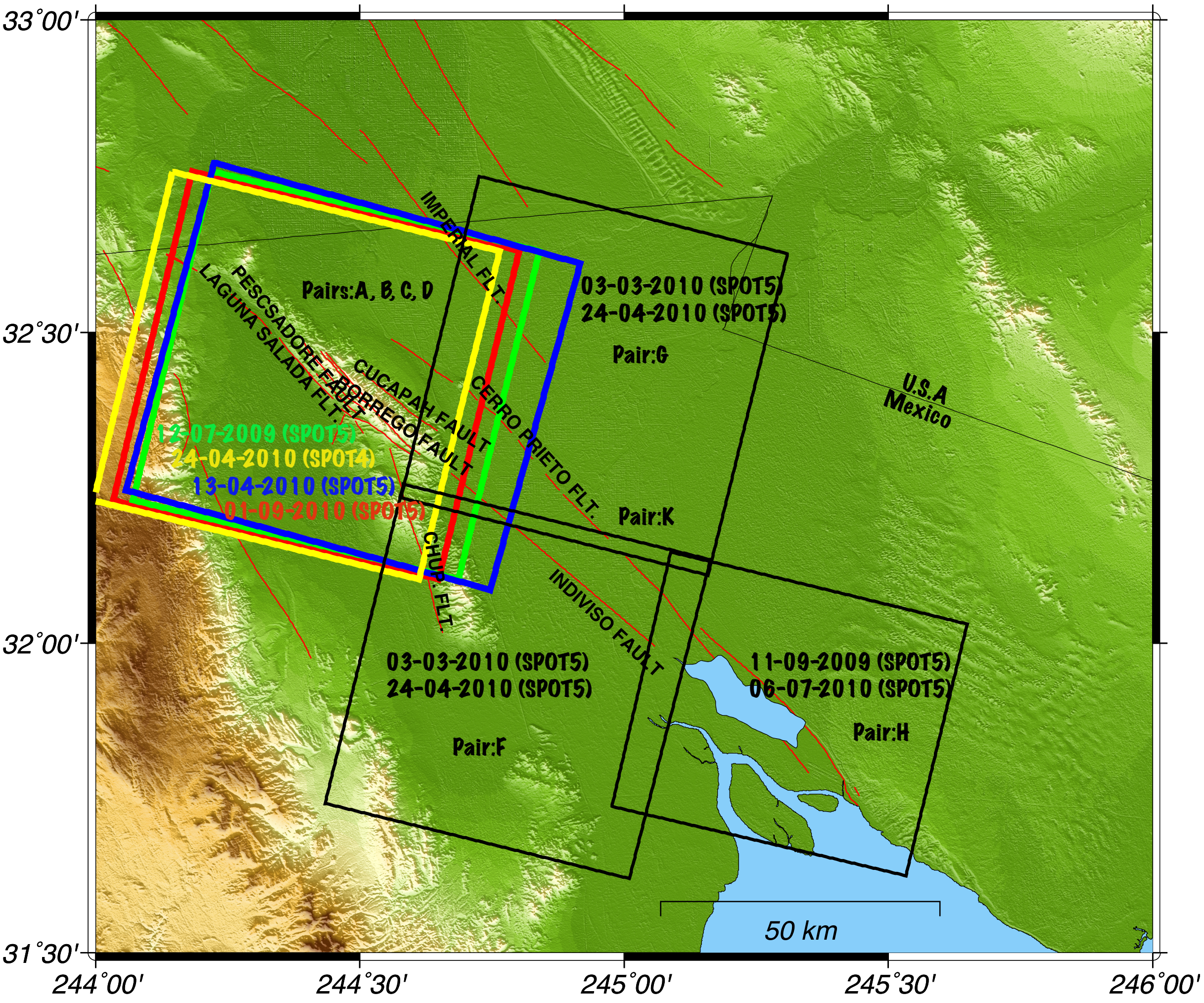

Figure 4.1: SPOT coverage of the area of the El Mayor-Cucapah earthquake

Date dd-mm-yy	Satellite	Spatial Resolution m	Incidence °	Sun Azimuth °	Sun Elevation °
09-07-2009	SPOT5	2.5	23.30	120.27	73.03
12-07-2009	SPOT5	2.5	-0.78	114	69
09-11-2009	SPOT5	2.5	-6.5	161	39
03-03-2010a	SPOT5	2.5	3.51	150	45
03-03-2010b	SPOT5	2.5	3.51	150	45
13-04-2010	SPOT5	2.5	20.35	146	62
24-04-2010a	SPOT5	5	3.81	138	64
24-04-2010b	SPOT5	5	3.81	138	64
24-04-2010c	SPOT4	10	-0.65	137	64
06-07-2010	SPOT5	2.5	-0.77	113	71
01-09-2010	SPOT5	2.5	-0.77	141	61

Table 4.1: SPOT scenes used in the study of the $M_w = 7.2$ 2010 El Mayor-Cucapah earthquake

4.2.2 DEM

Five Dems were available for the analysis of the El Mayor-Cucapah earthquake. The DEMs that are available and some of their properties are given in Table 4.2. Three different techniques were used for the DEM generation : radar interferometry, matching of stereo images and lidar.

DEM name	Resolution [m]	Technique	Planimetric error [m]	Elevation accuracy [m]
Shuttle Radar Topography Mission (SRTM)	90 m	InSAR	20	16
ASTER Global Digital Elevation Map (GDEM)	30 m	Stereo Image Matching	30	20
SPOT	20 m	Stereo Image Matching	15-30	10-20
Lidar	5 m	Direct Light Measurements		
Lidar	1 m	Direct Light Measurements	0.1	

Table 4.2: DEMs used in the study

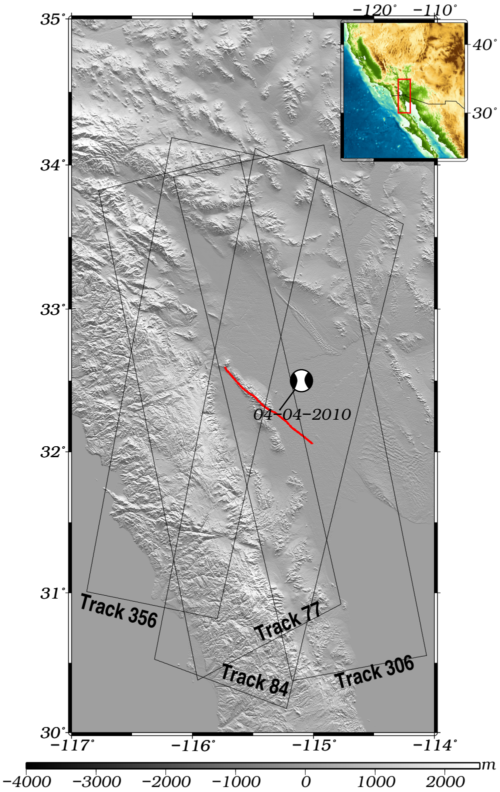

Figure 4.2: SRTM Shaded relief map of the study area. Red line shows surface rupture of the El Mayor-Cucapah earthquake. Solid rectangles indicate SARcoverage interferograms given in Table 4.3. Outlined red box in the small map at the top right indicates the area.

4.2.3 InSAR

Two SAR interferograms were acquired over ascending orbits and two SAR interferograms were acquired over descending orbits by Envisat sensor.

	ifm1	ifm2	ifm3	ifm4
Satellite	Envisat	Envisat	Envisat	Envisat
Date1	28.03.2010	28.03.2010	12.03.2010	15.09.2009
Date2	02.05.2010	02.05.2010	16.04.2010	13.04.2010
Track	77	84	356	306
Motion	Asc.	Desc.	Desc.	Asc.
Time span (days)	10	2.5	-0.77	141

Table 4.3: SAR data produced for the study of the 04.04.2010 El Mayor-Cucapah earthquake

Matching Pair Name	Image 'before' dd-mm-yy	Image 'after' dd-mm-yy	Output res. m	Inc. angle diff. °	DEM	Function
A	12-07-2009	01-09-2010	10	-1.55	SPOT 20 m	Horizontal displacements for Chapter 5
A1	12-07-2009	01-09-2010	40	-1.55	SPOT 20 m	Horizontal displacements for Chapter 6 and Chapter 2
B	12-07-2009	09-07-2009	2.5	22.52		Vertical displacements for Chapter 5
B1	12-07-2009	09-07-2009	40	22.52	Lidar 1 m	Horizontal displacements for Chapter
B2	12-07-2009	09-07-2009	40	22.52	Lidar 5 m	Horizontal displacememtns for Chapter 4
B3	12-07-2009	09-07-2009	40	22.52	SPOT	Horizontal displacements for Chapter 4
B4	12-07-2009	09-07-2009	40	22.52	SRTM	Horizontal displacement for Chapter 4
B5	12-07-2009	09-07-2009	40	22.52	GDEM	Horizontal displacement for chapter 4
C	01-09-2010	13-04-2010			None	DEM generation for Chapter 5
D1	13-04-2010	01-09-2010	40	19.58	Lidar 5 m	
D2	13-04-2010	01-09-2010	40	19.58	Lidar 1 m +Lidar 5 m	
K	03-03-2010	24-04-2010	80	7.32	SPOT 20 m	Horizontal displacements for Chapter 6
F	03-03-2010a	24-04-2010a	80	7.32	SPOT	Horizontal displacements - not used Appendix
G	03-03-2010b	24-04-2010b	80	7.32	SPOT	Horizontal displacementes - not used Appendix
H	09-11-2009	06-07-2010	40	-7.27	GDEM	Horizontal displacements not used Appendix

Table 4.4: Optical matching pairs created for the study of $M_w = 7.2$ 2010 El Mayor-Cucapah earthquake. Some matching pairs were created in reverse order from their chronological acquisition times as it made more sense to create the first orthorectified image with a smaller incidence angle.

4.3 Results

4.3.1 Optical sub-pixel matching results

I created 16 different optical matching pairs (Table 4.4), and each matching pair has been given a label (A-H). In the following text the pairs will be referred by their label rather than their 'pre' and 'post' dates.

Orthorectification and image cross-correlation were carried out using COSI-Corr software ((Leprince et al., 2007) and Chapter 2).

Correlations A, B, C, and D cover the north part of the earthquake, while correlation K, F and G cover the south part of the earthquakes. Correlation H covers the southern most part, but no tectonic signal due to the earthquake was discovered. Correlations A span the duration of the earthquake, and their incidence angle difference is very small - ideal conditons for generating horizontal maps of the deformation because topographic artefacts arising form steroscopic effect will be minimal. Correlations B predate the earthquake and they have a large incidence angle between them - suitable for studing the topographic effects as they do not contain tectonic signal. Correlation C spans the duration of the earthquake but the incidence angle difference is very large and therefore it is not suitable for horizontal displacement maps, as the steroeffect will create large topographic residuals that can not be corrected using available DEMs. Correlation D postdate the earthquake and both images have large incidence angle difference between them - creating good stereoscopic conditions for studying the topographic artefacts. Correlations F, G, and

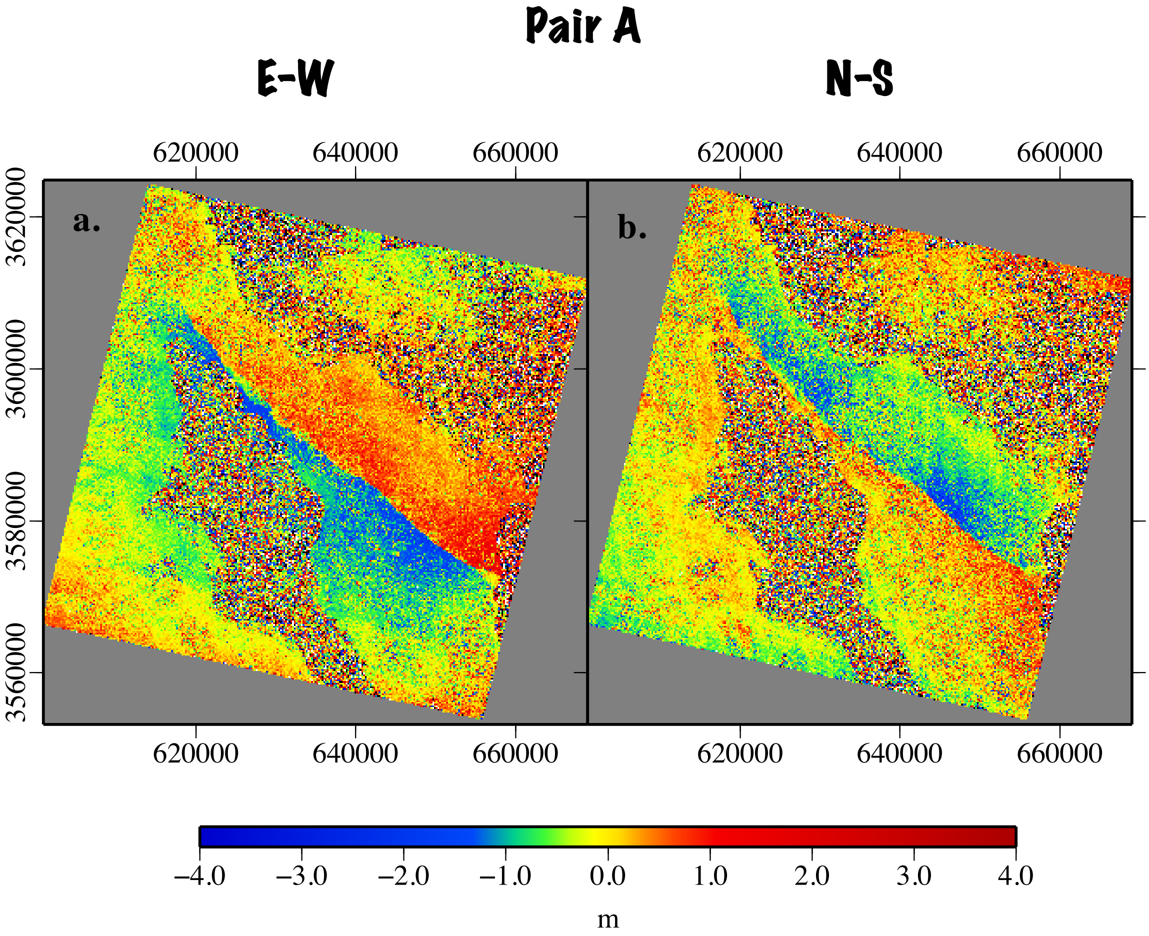

Figure 4.3: Horizontal displacement maps for the north part of the El Mayor-Cucapah earthquake obtained from matching pair A. (*a*) E-W component and (*b*) N-S component.

K span the duration of the earthquake and have small incidence angle between them. Correlation K is a composite mosaic of correlations F and G. It was possible to mosaic correlations F and G as the pre-event images come from the same SPOT track, which was also the case for the post-event images.

Here I explain the procedure for creating horizontal displacement maps for ccorrelation A. The results of image matching of pair A and pair A1 are almost identical apart from the outcome of their spatial resolution. It should be noted that the pre-event and post-event SPOT scenes used here have very small incidence angles (-0.78°,-0.77°), so that any short wavelength artefacts due to high relief should be small -i.e. there should not by any topographic artefacts (residuals) caused by a DEM that is not good enough for the orthorectification. The reference image used was a shaded relief map derived from a 20 m resolution SPOT DEM obtained though the ISIS programme (http://www.isis-cnes.fr/). In order to facilitate the identification of GCPs, the shaded relief map was constructed for sun angles equal to those at the time of the pre-event SPOT image acquisition. I identified a minimum of 15 ground control points uniformly distributed over the area of the pre-event SPOT image and the shaded relief map (Leprince et al., 2007). To minimise the effects of movement of the tie points due to the earthquake, I identified tie-points in the two images distributed uniformly over peripheral areas where the deformation was likely to be smallest. The size of the window used in the cross-correlation determines the area from which a single measurement of east-west and north-south displacement is derived, and hence the measured displacements represent an average value over the window area. Small windows provide higher resolution, but noisier measurements. Empirically, I find a window size of 32x32 pixels (the pixel size is 2.5 m) provides a reasonable signal-to-noise ratio. The matching window is stepped at constant increments over the image to obtain displacement estimates on a regular grid. An increment of half the window size is used for matching pair A1. However, because of the need to compare the vertical displacements derived here with the results of differencing the two lidar data sets in Chapter 2, I also used a smaller increment of 4 pixels, i.e. a grid spacing of 10 m. The smaller increment size means that errors between neighbouring grid points will be more highly correlated. The E-W and N-S components of the horizontal displacements, obtained for matching pair A, are shown in Figures 4.3*(a)* and 4.3*(b)* and also again in Figure 4.4, and the results for the matching pair A1 are shown in Figure 4.12.

The results show a clear discontinuity which represent the co-seismic rupture of the El Mayor-Cucapah earthquake in its northern segment. The average fault slip at the surface is 2 m with a maximum slip of 3 m, in agreement with the results of Wei et al. (2011). There are large areas of decorrelation in the southwest and northeast parts of the maps. The former are due to modifications of the desert in the Laguna Salada during the 14 months interval between images, and the latter due to agricultural activity in the Mexicali Valley.

Matching pair K was formed from merging two successive SPOT 5 scenes, acquired on the same track and on the same dates (03-03-10 and 24-04-10) for the pre-event and post-event datasets. I identified a few overlapping lines in common between the successive scenes, mosaicked the raw images in ENVI to create a long continous images. I have then created a new metadata files one for each newly formed image to reflect changes in the number of rowa. By merging consecutive scenes it is possible to study the rupture uninterrupted (Figure 4.4), which would otherwise cross separate displacement maps for pairs F (Figure 4.5) and G (Figure 4.6). The horizontal displacements show a discontinuity which represents the rupture of the El Mayor-Cucpah earthquake in its southern segment. The location of this fault was first revealed during the El Mayor-Cucapah earthquake and it has been named Indivisio Fault (Wei et al., 2011). Mosaicking the images prior to matching creates a much needed larger far-field, so that the long wavelength errors can be constrained better (Section 4.4). Initial matching of pair F has exceptionally large-long wavelength error. Figure 4.4 shows the matching results for E-W horizontal displacement for the pairs A1 and K when overlaid together, where the entire earthquake's rupture is visible.

Matching pair H covers the most southern part of the El Mayor-Cucapah earthquake. The resulting horizontal displacements are shown in Figure 4.7. No tectonic signal has been observed.

4.3.2 InSAR results

I used ESA's ENVISAT satellite data used to generate four interferograms (two ascending and two descending) that span the co-seismic 04.04.2010 $Mw7.2$ El Mayor-Cucapah event (Table 4.3). I processed the data using the JPL/Caltech ROI-PAC software (Rosen et al., 2004), and topographic effects were removed using the 3-arcsecond SRTM DEM. The InSAR displacement maps are shown in Figure 4.8 (also in Chapter 6 - Figure 6.2, Figure 6.3, Figure 6.4, Figure 6.5).

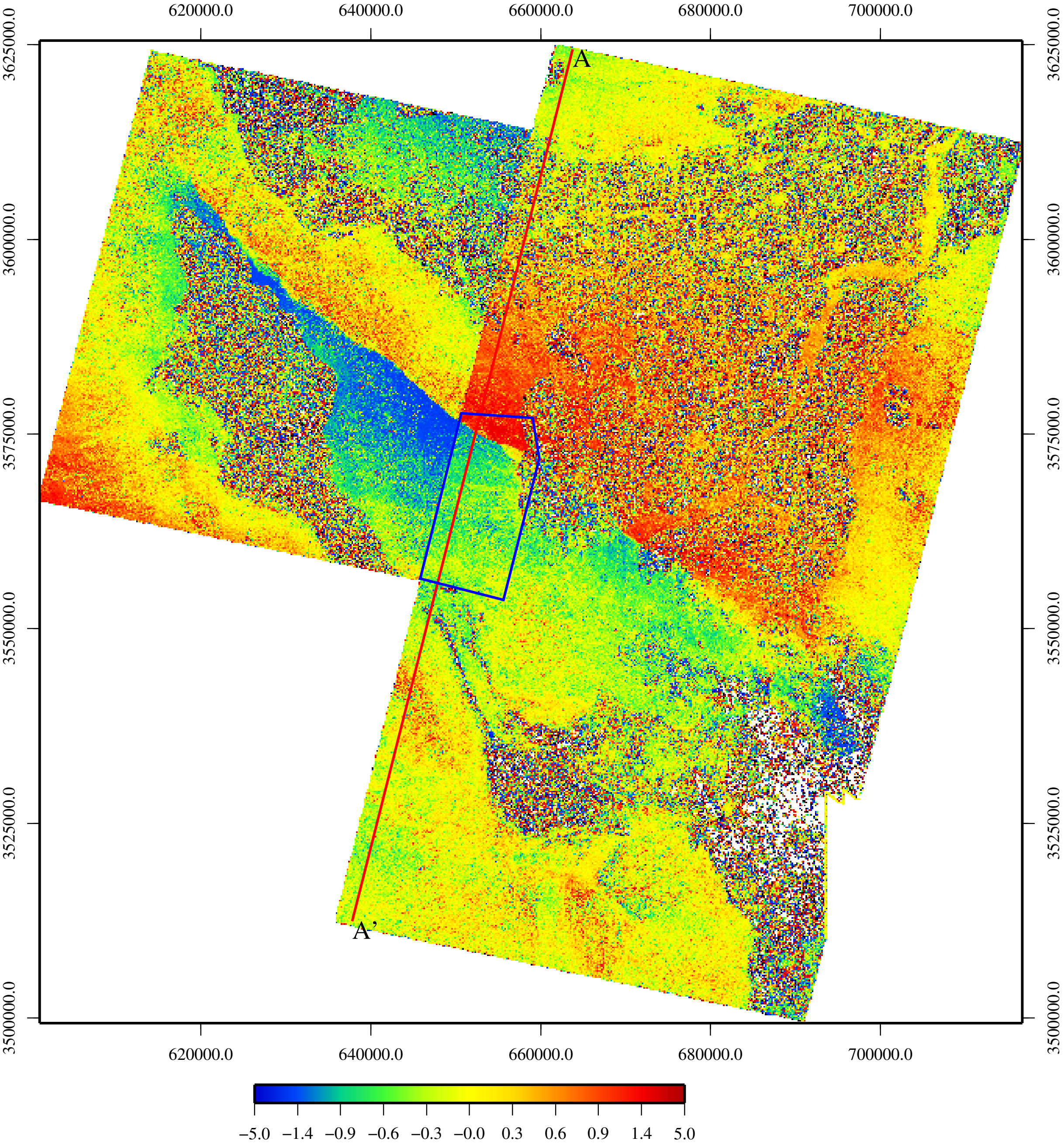

Figure 4.4: Horizontal displacements for the El Mayor-Cucapah earthquake obtained by subpixel matching of the pairs A1 and K. The blue polygon shows an area that is enlarged in Figure 4.19

.

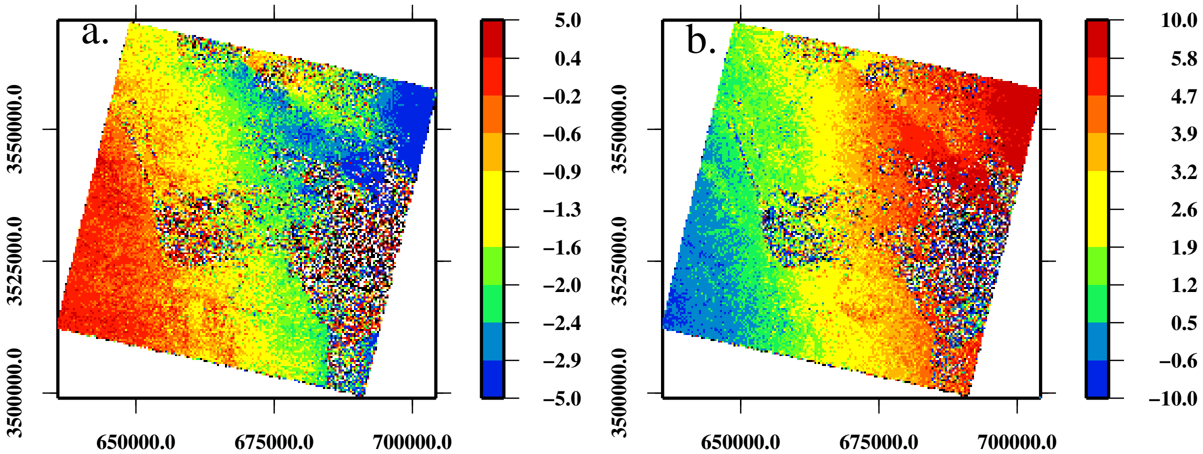

Figure 4.5: (*a*) E-W displacement map of matching pair F. (*b*) N-S displacement map of matching pair F. Linear tilts in both displacement maps are large (see Section 4.4)

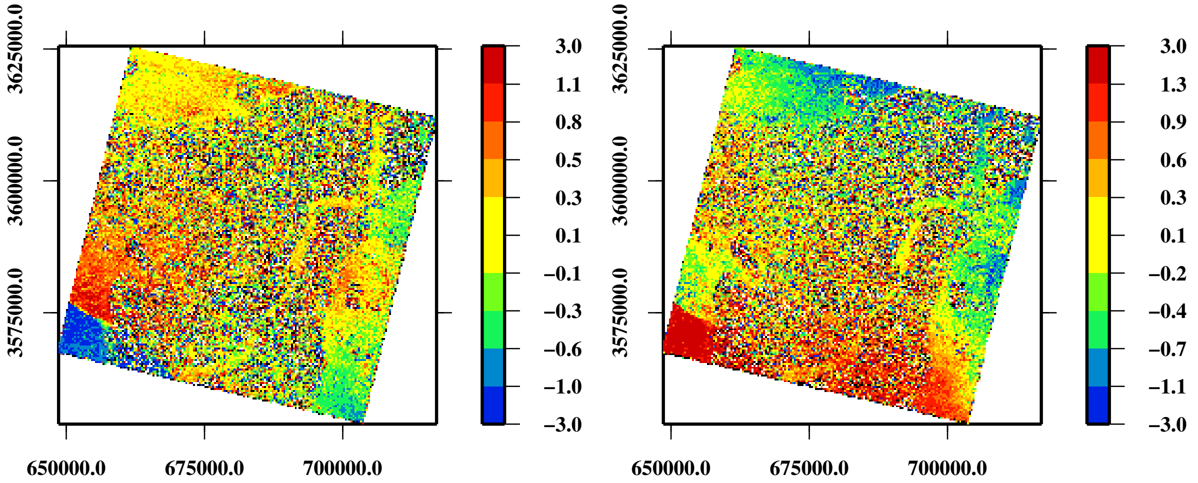

Figure 4.6: (*a*) E-W displacement map of matching pair G. (*b*) N-S displacement map of matching pair G. Values of linear tilts are very different from the ones in pair F.

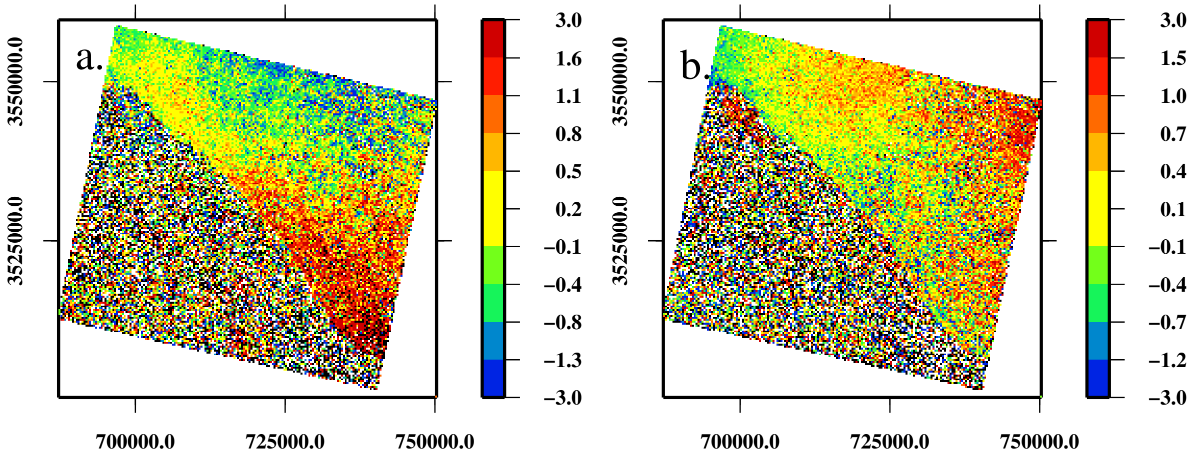

Figure 4.7: (*a*) E-W displacement map of matching pair H. (*b*) N-S displacement map of matching pair H. No tectonic signal present in this most southern dataset Figure 4.1

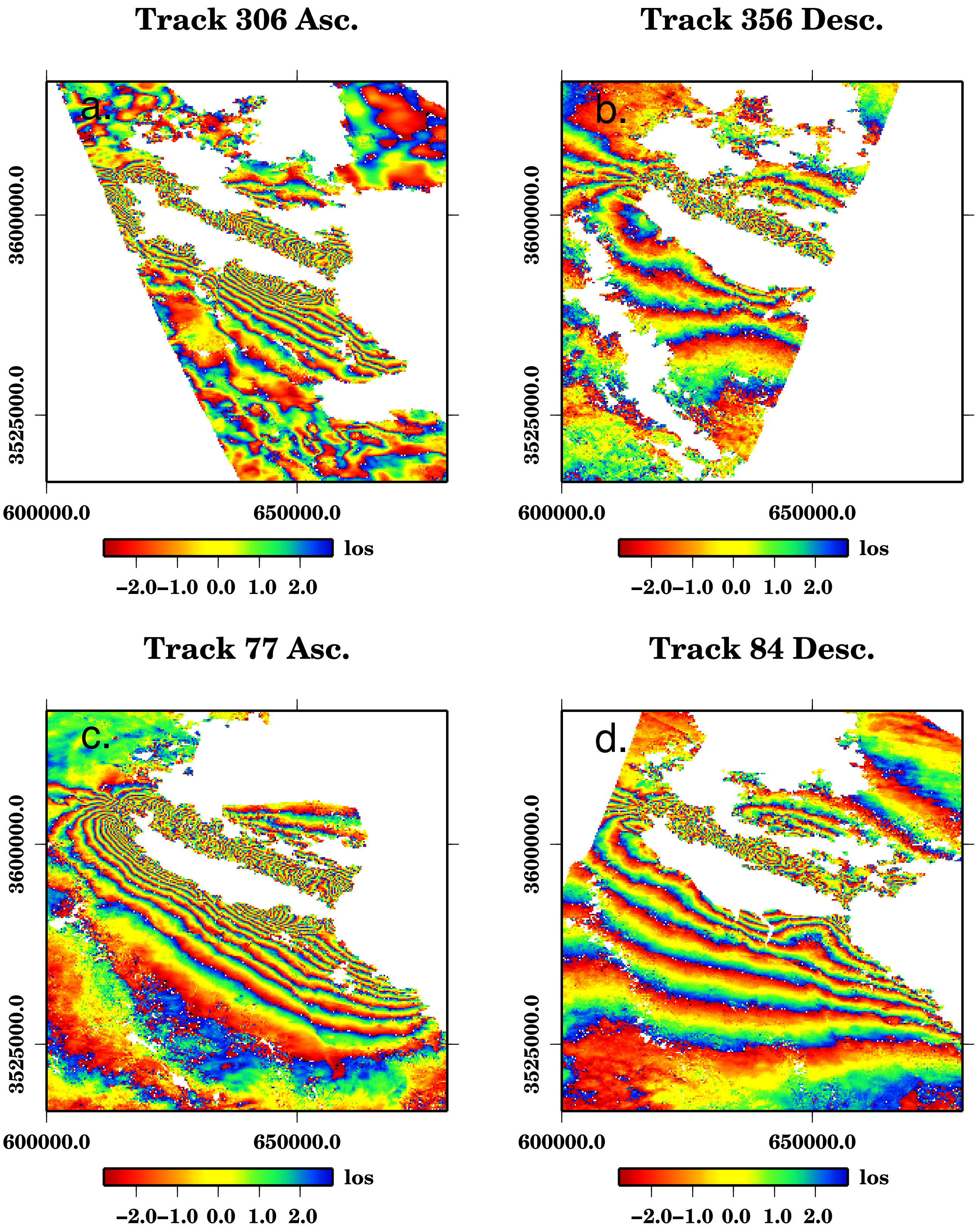

Figure 4.8: Original interferograms that span the El MAyor-Cucapah earthquake. They are shown here before unwrapping, where each fringe represents half a wavelength of deformation (2.8 cm) in the satellite line of sight. (*a*) Asending track 306. (*b*) Descending track 356. (*c*) Descending track 77. (*d*) Ascending track 84.

4.4 Orbital error (long wavelength error) in image correlation results

I find that all matching datasets have a long wavelength linear systematic error present. I also identify that this systematic error is generated during georeferencing of the raw optical images.

The essential first step for orthorectification is to find the parameters giving the exterior orientation (EO), defining the relationship between the raw image and its projection on the ground. In theory, the exterior orientation can be determined directly with a known sensor model (Toutin, 2004) and SPOT ephemeris information. However, the ephemeris information is not sufficiently accurate to directly determine attitude, the exterior orientation, and the sensor models predict only approximate and simplified trajectories for the SPOT images. The ephemeris information includes the knowledge of a look-direction vector associated with each given pixel. In order to correct for look-direction vectors COSI-Corr deploys a number of GCPs to calculate a uniform correction for all the look direction vectors at the same time.

The differences between the given look direction vector and the true look direction vector calculated for the known location of GCP is given by

$$\vec{du}(x_0, y_0) = \vec{u}_{\text{measured on satellite}}(x_0, y_0) - \vec{u}_{\text{GCPs}}(x_0, y_0) \tag{4.1}$$

where x_0 and y_0 are the coordinates of the GCP in the raw image. The correction is determined by three best-fitting planes , one for each component, approximated from discrepancy values (x, y)

$$d\vec{u}^{i}_{\text{corr}}(x, y) = \begin{bmatrix} a_0 & b_0 & c_0 \\ a_1 & b_1 & c_1 \\ a_2 & b_2 & c_2 \end{bmatrix} \begin{bmatrix} x \\ y \\ 1 \end{bmatrix} \tag{4.2}$$

where $d\vec{u}^{i}_{\text{corr}}$ is look angle correction, a_i, b_i, c_i are the coefficients for each plane with $i = 1, 2, 3$, and x and y are coordinates of the each pixel in the raw image.

In orthorectifying the post-event image, a correction for the look vectors is carried out in a similar fashion to that of the pre-event image, but in this case using three tie-points. Leprince et al. (2007) suggests selecting only three tie-points, as that is the minimum number of tie-points required to solve unambiguously the linear inversion in Equation 4.2 to obtain the look angle correction for the post-event image.

However, I show bellow that this approach, instead creates long wavelength error. I use matching pair A1 to run an investigation in order to find out how does the long wavelength error comes to be, how large these long wavelength biases are, and if there is a way of mitigating them.

The long wavelength error can be analysed through a series of residual maps. For the orthorectification of the first image I use a shaded relief map generated from SRTM Dem throughout as the reference image and a source for the GCPs. I identify a set of ground control points uniformly distributed over the area of the pre-event SPOT image and the shaded relief map (Leprince et al., 2007). I also assume that the orthorectification of the first image is correct with respect to ground reference system. Residual maps are formed between one set of E-W and N-S displacement maps generated with a fixed set of tie-points, and the other sets of the E-W and N-S displacement maps formed with varied combination of numbers, locations and distributions of the tie-points, using the same matching pair. When setting the fixed nine points I have tried to place the tie-points evenly distributed accross the image and away from the areas of the deformation. The figures in this section have green points showing the nine fixed tie-points and the purple points showing tie-points used for testing results of their different configurations.

Location of the tie-points

For the look correction (Equation 4.2) to be bias free the tie-points must be placed in the areas of stable ground between the pre-event and post-event image (Ayoub et al., 2009). Otherwise, if the image coordinates in the raw post-event image have changed, this deformation is added to their true coordinates and it will introduce bias. I have generated two post-event ortho images where I have intentionally placed three tie-points (purple) into zones of decorrelation or large deformation, which I have initially identified from the E-W displacement map previously processed with fixed nine tie-points points. At this point I use only three as according to Leprince et al. (2007) that should be sufficient.

Placing tie-points into areas of large deformation dramatically increases residuals. Not only the tie-points should be placed away from tectonic artefacts, but away from any source of bias signal such as shadowing effect or topographic artefatcs.

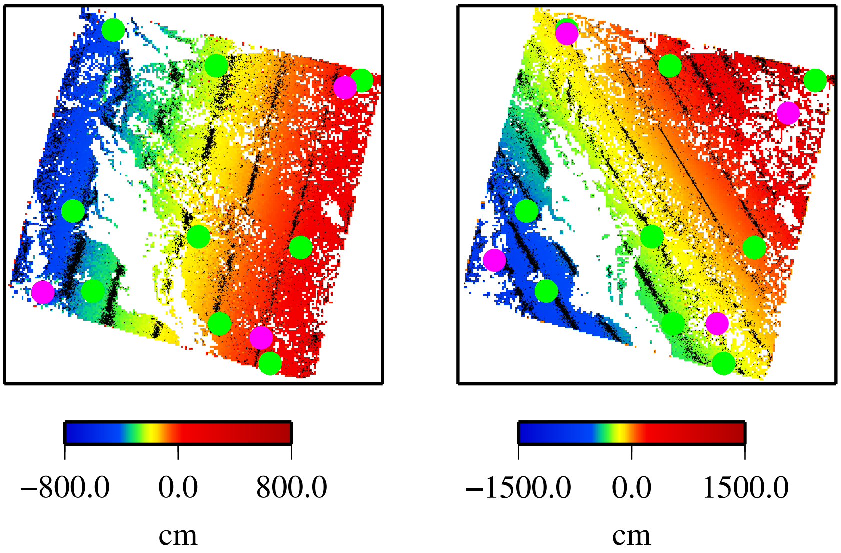

Figure 4.9: Images show results of differencing of E-W displacement maps of the same matching pair A1. Green points are nine fixed points used in orthorectification of the post-event image of pair A1, and purple points are also tie-points used for the orthrectification of the post-event image of pair A1, but are intentionally placed in the zones of high deformation. Large linear tilts can arise from placing the tie-points in the zones of deformation such as tectonic signal as well as decorrelation, topographic artefacts, or signal due to changing shadows.

Choosing where to place the tie-points should be an iterative process. After initial deformation map is formed, a check on the locations of the tie points should be performed and if some points are placed in the areas of deformation, this step of the tie-point selection should be repeated to minimise this effect.

Number of tie-points

Here I show that collecting three tie-pints alone is not enough to determine the correction of the look-directions as suggested in COSI-Corr manual. In fact choosing larger number of tie-points rather than smaller number is advisable. I have generated the post-event ortho image with three, four, five and 15 tie-points (green points in Figure 4.10) and calculated the differences between these results and the fixed result of the nine tie-points (purple points in Figure 4.10). All calculated residuals have a linear trend. The magnitude for the linear trend is the highest for the three tie-points where it reaches 1 m. For four or more tie-points the magnitude of the residual trend is less than 50 cm. In contrast to Leprince et al. (2007), who suggest that only three tie-points are sufficient, more than

3 tie-pts. without def.		3 tie-pts. with def.		4 tie-pts. without def.		4 tie-pts. with def.	
σ_x[m]	σ_y[m]	σ_x[m]	σ_y[m]	σ_x[m]	σ_y[m]	σ_x[m]	σ_y[m]
0.007	0.001	0.001	0.0008	0.044	0.028	2.69	0.61

Table 4.5: The table shows the mis-fit values for Easting (X) and Northing (Y) for the results of Equation 4.2. The first column show the mis-fit values for only three tie-points carefully placed in the areas of no deformation and in the second column the results of the mis-fit are shown when one of those three tie-points is placed in the zone of high deformation. It is impossible to tell which case has a tie-point placed in the zone of deformation. Third and fourth column show the results of the mis-fit when four tie-points are selected. If all four tie-points are selected in the zone of no-deformation the mis-fit will be very small, but if one of those points is placed in the zone of high deformation the mis-fit values signals it.

three tie-points will form an over-determined solution in Equation 4.2 and reduce the magnitude of the long wavelength errors possibly caused by any outlier tie-point.

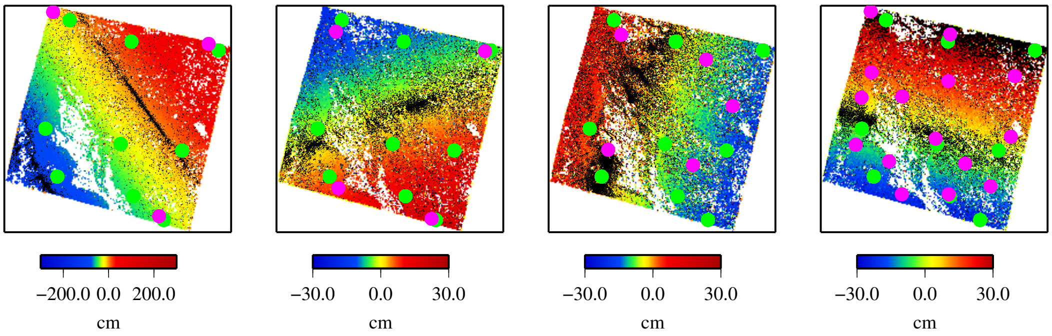

Figure 4.10: Calculated residuals obtained by differencing different outcomes of the E-W displacement maps of the pair A for different number of tie-points. The number of magenta tie-points changes from (*a*) three, (*b*) four, (*c*) five and (*d*) fifteen, whilst the E-W displacement processed with nine fixed green points remain the same. The black lines are contours produced using GMT.

Table 4.5 shows the misfit values for the case when there are only three tie-points and the case when there are four tie-points. From mis-fit results for three points it is impossible to tell if the tie-points are placed in zones of deformation or not, whilst the mis-fit of four tie-points clearly shows that some of the points introduce large mis-fit. I find that the report that COSI-Corr produces to state the accuracy of the post-event orthorectification is misleading as it is based on only three tie-points.

Spatial distribution of the tie-points

I have tested if certain spatial distributions of tie-points control the shape and/or the magnitude of the long wavelength error. Although it may be tempting to place the tie-points in only one side of the image that may not be affected by the deformation, that will create collinearity and linear trend will shoot to several meters (Figure 4.11). This could potentially create a non-linear (quadratic shape surface) long wavelength error that may be very hard to remove from the datasets. However, the discussion of the quadratic surface long wavelength error is beyond the scope of the work in this thesis.

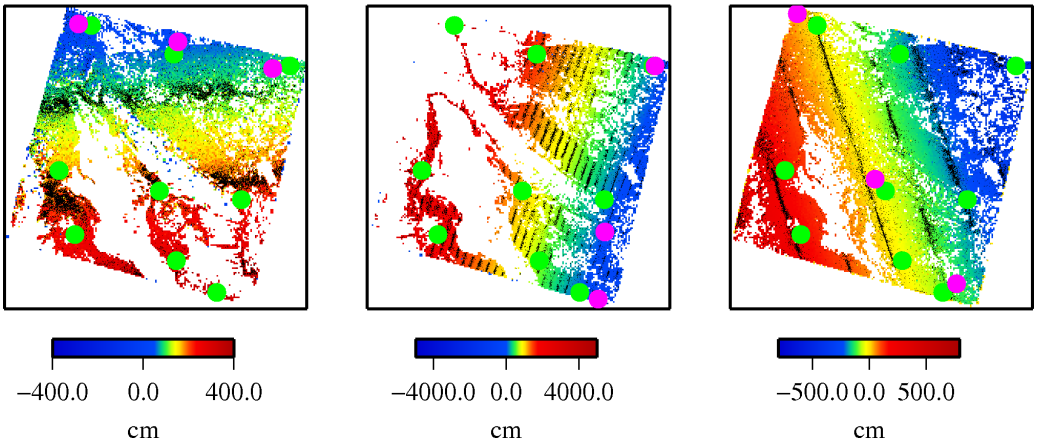

Figure 4.11: The results of calculated residuals obtained by differencing E-W displacement maps processed using three collinear tie points (magenta points) with the E-W displacement map processed with nine fixed evenly distributed tie-points (green points). The black lines are contours produces using GMT.

Removing and minimising long-wavelength errors from horizontal displacements maps

The pattern and the magnitude of the residual outputs show how placing the tie points in the areas of large defromation, can result in extremely large long-wavelengh error (tens of meters) (Figure 4.9, Figure 4.10, Figure 4.11). However, this long-wavelenght error can be small, but it can change the nature of the tectonic signal. I therefore suggest some steps during the selection of the tie-points:

1. Avoid placing tie-points in any areas of deformation if possible. Iterate through this step before the tie-points are placed in the areas of the least deformation.

2. Use more then three tie-points and use the mis-fit values as an indicator of goodness of the points.

3. Avoid placing the tie-points in one side of the image and distribute them as evenly as possible.

Given the small size of the image, it is not possible to completely avoid the effects of displacement on the tie-points, and errors in the tie-point coordinates will result in errors in the linear coefficients in Equation 4.2. The long-wavelength error is removed by estimating a linear relationship $u = Ax + By + C$, where u is the displacement, x and y are horizontal coordinates, and A, B and C are constants, that best fits each component of displacement in the far field, i.e. at distances from the fault where displacements due to the earthquake are as small as possible. Displacements from this linear relationship are then subtracted from the initial estimates. I find that the gradient of the linear plane can vary from a few centimeters to few meters per hundred kilometres. The linear tilts can also be identified by solving for the parameters of the linear plane for each dataset in the modelling (Chapter 5). Figure 4.12 and Figure 4.13 show the results after all above is applied for mathcing pair A1 and matching pair K, respectively.

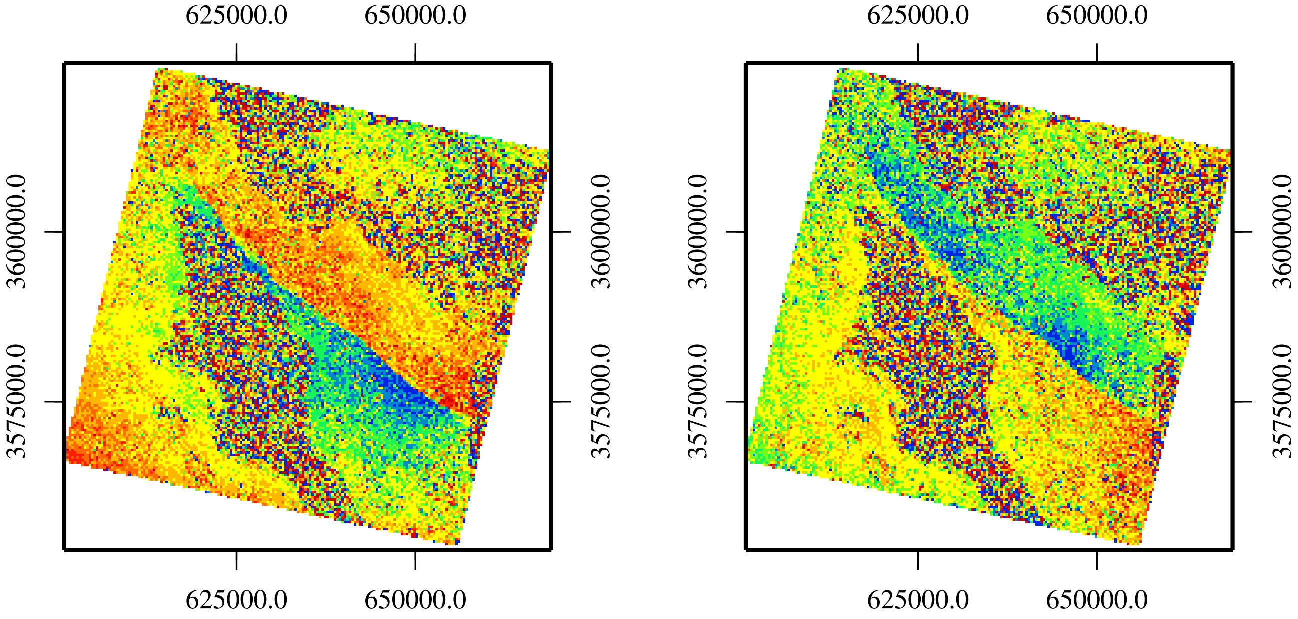

Figure 4.12: E-W and N-S displacement maps of matching pair A1. No apparent large linear tilt is observable as the tie-points have been placed according to the findings in the text.

4.4.1 Absolute accuracy of orthorectification

During the orthorectification of images I followed the above findings in order to secure accurate matching. However, by inspecting the overlapping areas of the pre-event ortho images of matching pairs A1 and K I find a large mismatch of the image features between the two ortho images Figure 4.14. Both ortho images were orthorectified with the same 20 m DEM, which was also used as a source for GCPs in the form of a shaded relief. This is an area of very flat terrain where topographic relief can not be the source of distortions,

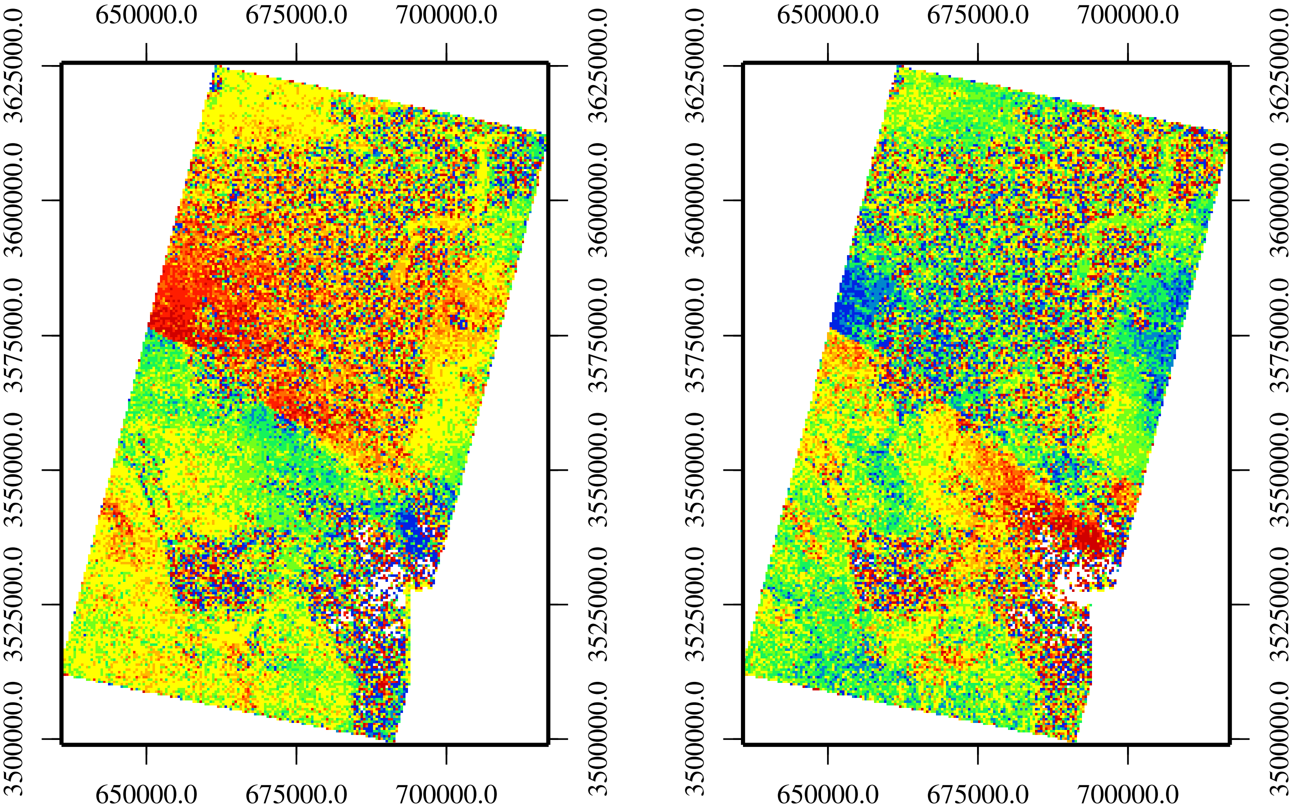

Figure 4.13: E-W and N-S displacement maps of matching pair K. No apparent large linear tilt is observable as the tie points have been placed according to the findings in the text. Long datasets improved the chances of finding the right locations of the tie-points.

and the error probbaly comes from the errors of the GCPs used to co-register the imaegs.

Figure 4.14: Image shows an area where two ortho images overlap. To the left is a portion of 12-07-09 ortho image and to the right is a portion of 03-03-10 ortho image.

4.5 Short wavelength artefacts

In this section I discuss decorrelation, and bias signals caused either by bright and/or dark parts of images and changing shadows.

4.5.1 Decorrelation

Decorrelation is an artefact characterised by a high frequency noise. It looks like an outlier in an area that otherwise has a consistent displacement field (Figure 4.12 and Figure 4.13). This is typically caused by man-made changes and when differences between pre-event and post-event image are too large, or the parallax distances are bigger than the matching windows due to inaccurate orthorectification.

I have written a code based on the Equation 4.3 which investigates the standard deviation of individual image windows, and then decides on a given criterion if the window area of the displament map is affected by decorrelation and has to be removed. The SNR values are given for each pixel but becasue there is a large scatter between the neighbouring values and it is not possible to use these values as a good spatial tool to identify cohesively areas of decorrelation.

$$r = \frac{1}{A}\sqrt{\frac{\sum_{i=0}^{m}\sum_{j=0}^{n}(x_{ij} - \bar{x})^2}{(mn-1)}} \tag{4.3}$$

where m and n are the dimensions of the chosen window, x_{ij} values of the each element in the window, $\bar{x}$ is a mean value of the window. The expression under the square root represents a standard deviation of the estimated window. A is the maximum value of the windows' standard deviation across the entire image. The higher values of the normalised spatial standard deviation indicate larger variability of displacement values for a given window and can be classified as decorrelation. The cut-off values of the spatial standard deviation that will form the filter is determined heuristically.

My IDL code, which masks decorrelation values/areas from the displacement maps, is based on normalised spatial standard deviation for variable window size (Equation 4.3). I found that the most robust solutions are obtained for window size either 3x3 or 5x5 pixels.

Figure 4.15(a) and Figure 4.16(a) show the results of the normalised spatial standard deviation for the pairs A and K while Figure 4.15(b) and Figure 4.16(b) show the masks derived from the normalised spatial standard deviation used for filtering of the displacements results. The filtered E-W and N-S displacement maps for the pairs A1 and D are shown in Figure 4.15(c) and (d) and Figure 4.16 (c) and (d) respectively. The largest decorrelation comes from temporal differences in the agricultural land and changes that occurred over the time in the areas of Laguna Salada desert.

4.5.2 Bright and dark areas

Although very bright and very dark areas in general cause decorrelation, I have identified areas where very bright and very dark areas in the image can create coherent but erroneous signal. The reason for this behaviour is not understood. My IDL algorithm removes displacement values that are result of image matching of very bright and very dark areas. The algorithm creates a mask based on equalization of pre-event and post-event ortho

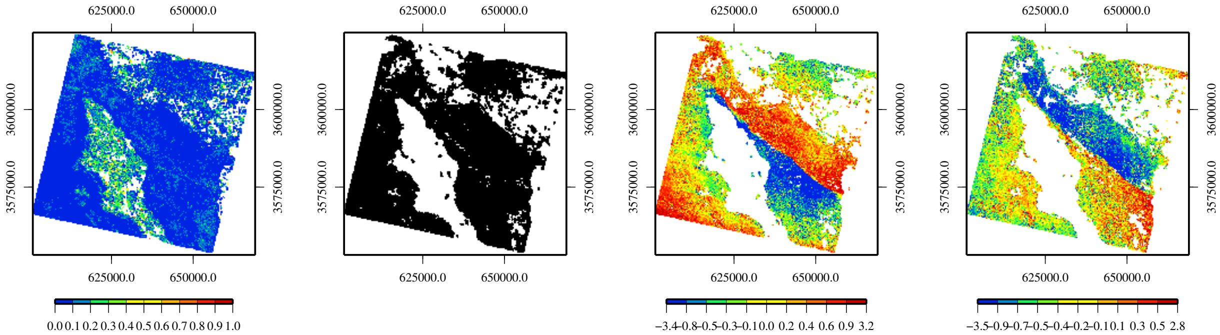

Figure 4.15: (*a*) The normalised spatial standard deviation of pair A1. (*b*) A mask used for filtering of the displacement maps, where white areas mask out the areas of high spatial criterium. (*c*) E-W displacement maps after automatic filtering. (*d*)The N-S displacement maps after automatic filtering.

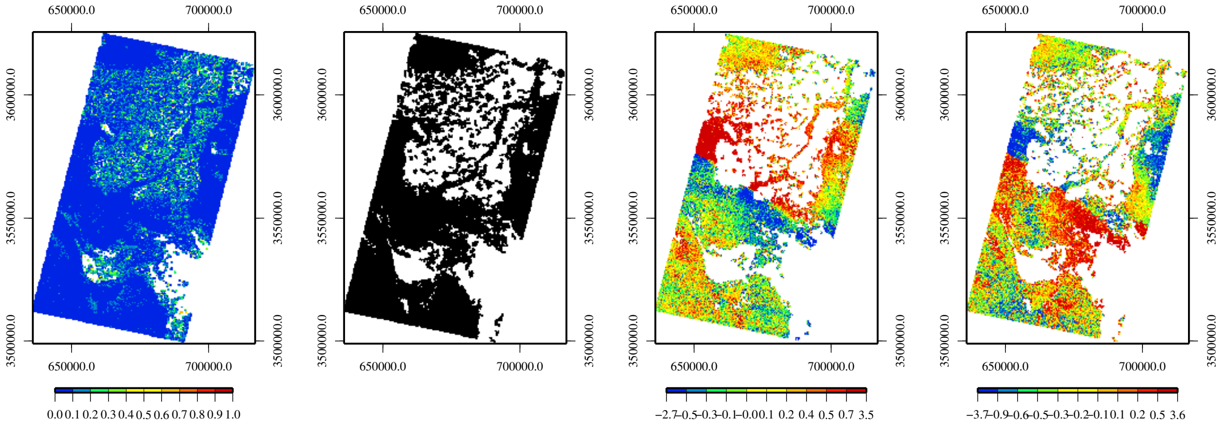

Figure 4.16: (*a*) The normalised spatial standard deviation of pair K. (*b*) The mask used for filtering of the displacement maps, where white areas mask out the areas of high spatial criterium. (*c*) E-W displacement maps after automatic filtering. (*d*) The N-S displacement maps after automatic filtering.

image. Once the ortho images are normalised, areas of very high and very low image values are identified and converted into a mask, which is then used to filter the displacement maps. Figure 4.17 and Figure 4.18 show masks, and results of the filtered E-W and N-S displacements for the pair A and K respectively.

4.5.3 Shadows

Figure 4.19 shows an inset of the N-S displacement map for the matching pairs A1 and K. The extent of the inset is shown by the blue polygon in Figure 4.4. Amidst the tectonic signal, a channel-shaped signal is also observable. An initial thought was that this signal is caused by alluvial erosion as it appears to be correlated with topography. However, the sign of the signal in the N-S displacement fields within these channels is opposite for the overlapping area for the matching pairs A1 and K.

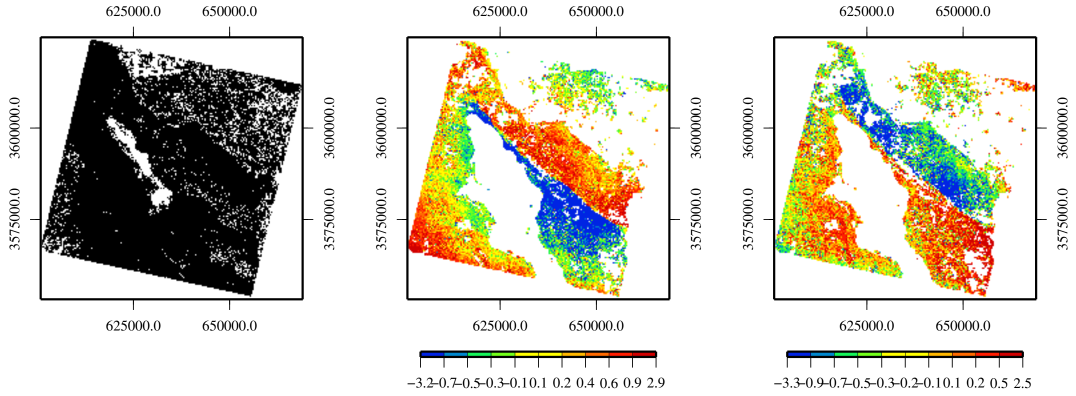

Figure 4.17: (*a*) A1 mask created in order to remove the signal from very bright and very dark areas for the pair A. The white areas show the coverage of areas of saturated with high and low pixel values in the ortho images. (*b*) The E-W displacement results after this erroneous signal has been removed. (*c*)The N-S displacement results after this erroneous signal has been removed.

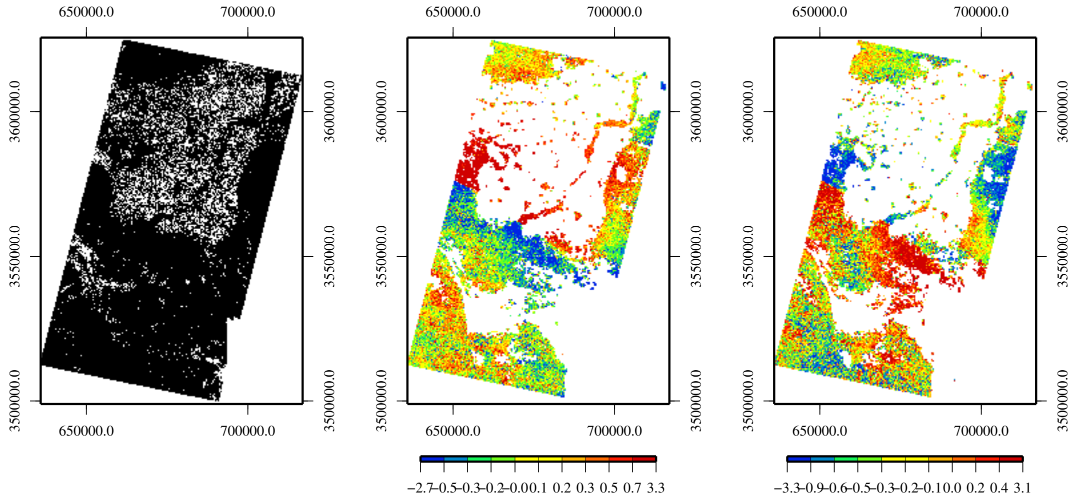

Figure 4.18: (*a*) The normalised spatial standard deviation of pair K. (*b*) A mask used for filtering of the displacement maps, where white areas mask out the areas of high spatial variability. (*c*) E-W displacement maps after automatic filtering. (*d*) The N-S displacement maps after automatic filtering.

On closer inspection of the raw SPOT image I found that these areas are covered with scattered trees/bushes no more than 2-3 m high and a few meters apart and they constitute vegetation coverage in dry valleys. This type of vegetation is wide, spread especially across matching pair K. This observation suggest an interesting hypothesis that the observed horizontal displacement signal is caused by changes in the trees' shadows between the pre-event and post-event image. Figure 4.20 shows sun positions for the pre-event and post-event images, the location and the extent of the shadows for matching pair A1 and Figure 4.21 shows the same as in Figure 4.20 but for specific sub settings of the matching pair K. The reconstructed apparent horizontal displacements in the E-W

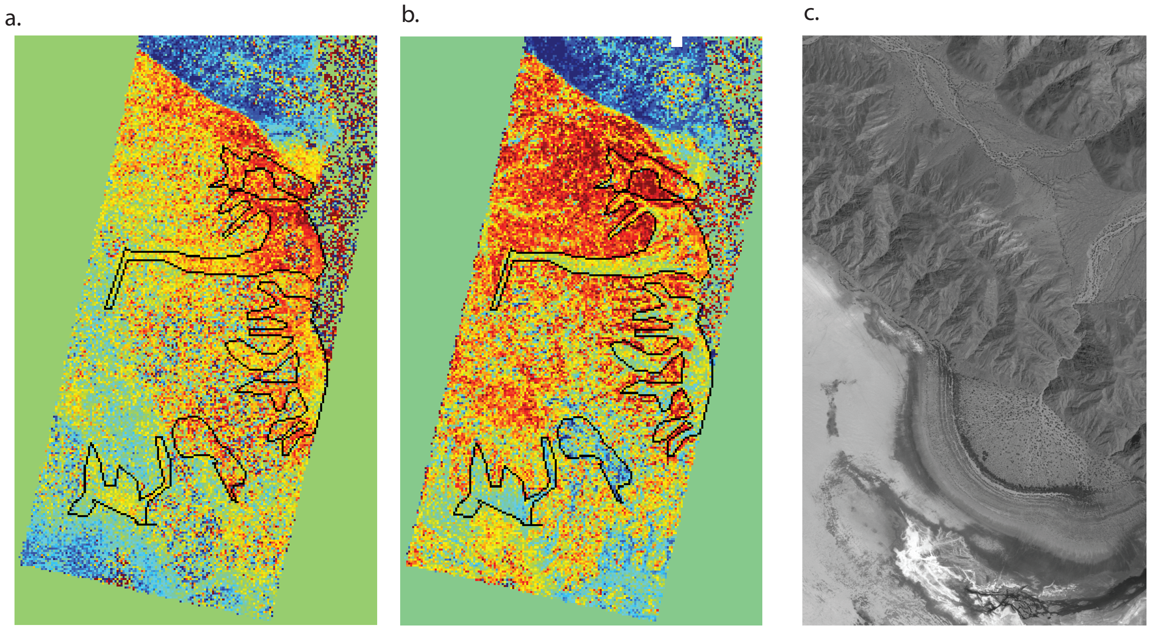

Figure 4.19: This figure shows the area that was marked as a blue polygon in Figure 4.4. (*a*) shows the N-S displacements for the pair A1 and (*b*) shows the N-S displacements for the K matching pair. The black polygons are the same for the left and the right images and they have been digitised from the orthoimage to show the extent of the scattered vegetation. Note the reversal of the sign of the signal within black polygons. (*c*) show a typical surface coverage, the black spots scatterd accross the image are the individual trees.

and N-S direction are calculated for a 2 m long pole.

The results for pair A1 show that the configuration of its shadows would create a very small negligible positive signal in the E-W direction and a negative signal in the N-S direction (Figure 4.20). For matching pair K the E-W and N-S displacement maps will have a negative bias signal (Figure 4.21), the N-S component being also large.

To test this hypothesis I have used a small sample area from the lidar 1 m dataset. The sample area was selected so that some areas are covered with trees, marked by red polygons (Figure 4.22 and Figure 4.23). I have generated two shaded relief images, each one simulating the sun position as in pre-event images and post-event images of the matching pair A1, and another two for the matching pair K. Figure 4.22(*b*) shows the lidar 1 m sample area shaded with sun position information for the pre-event image of the matching pair A1. Image matching with sub-pixel resolution was applied to the lidar samples shaded as described above to mimic illumination settings as that of pairs A1 and K Figure 4.23. A coherent horizontal displacement signal appears despite the fact that there was no displacement between the two matched images.

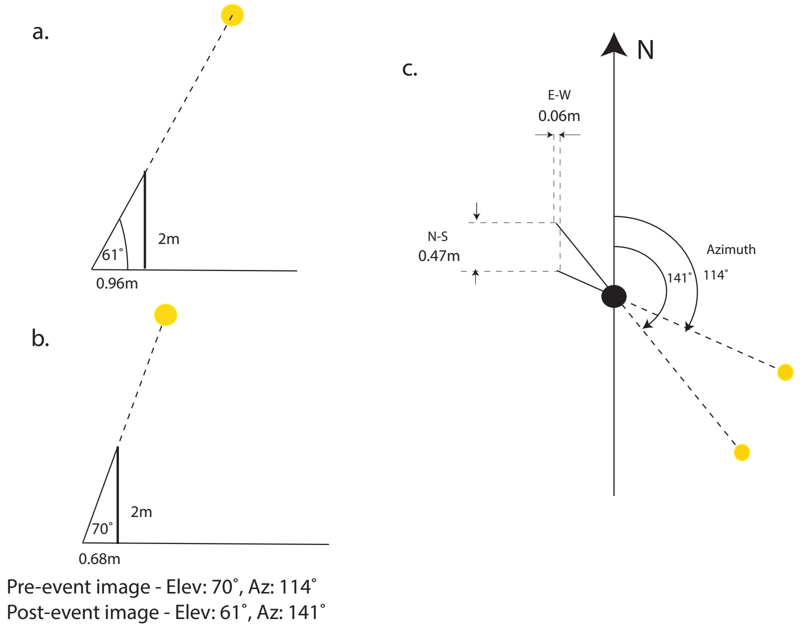

Figure 4.20: The sun's azimuth and elevation settings for the matching pair A1 and corresponding E-W and N-S projections of the displacements due to the shadow changes. (*a*) shows the length of the shadow for the sun position (Elevation: 70 °and Azimuth: 114 °) in the pre-event image (*b*) shows the length of the shadow for the post-event image for the sun position (Elevation: 61 °and Azimuth 141 °. (*c*) The plan view of both shadows and their differences expressed in meters for the E-W and the N-S component.

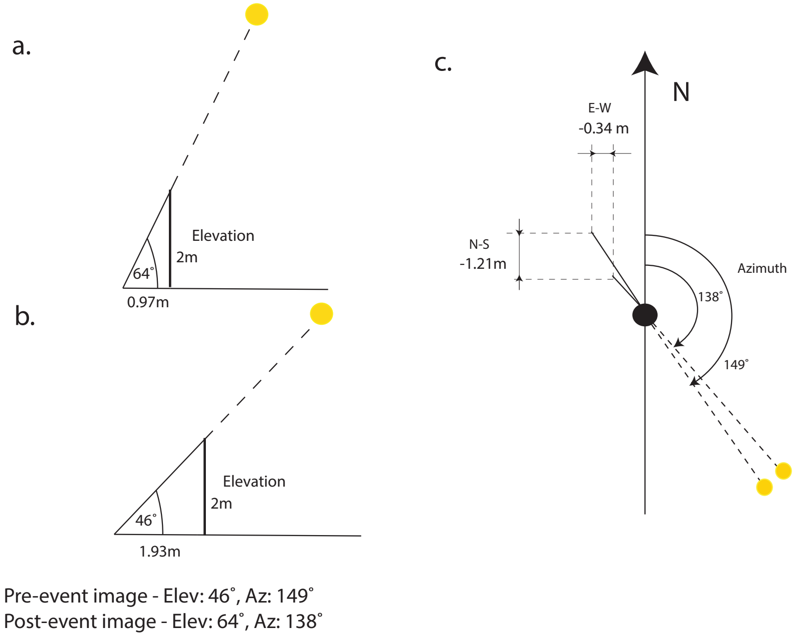

Figure 4.21: The sun's azimuth and elevation settings for the matching pair K and corresponding E-W and N-S projections of the displacements due to the shadow changes. (*a*) shows the length of the shadow for the sun position (Elevation: 46 °and Azimuth: 149 °) in the pre-event image (*b*) shows the length of the shadow for the post-event image for the sun position (Elevation: 64 °and Azimuth 138 °. (*c*) The plan view of both shadows and their differences expressed in meters for the E-W and the N-S component.

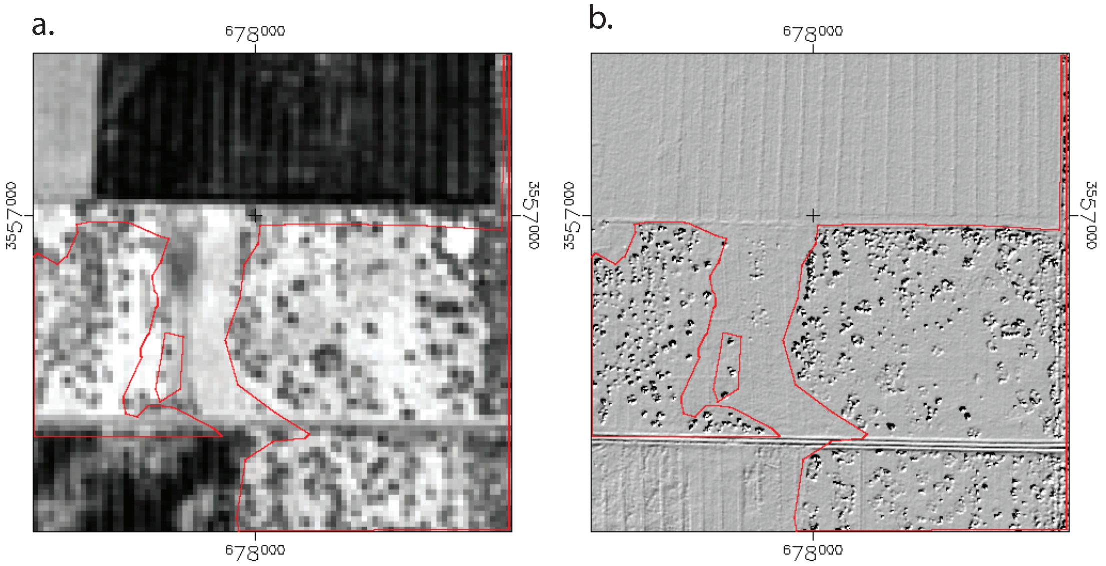

Figure 4.22: (*a*)A section of the 12-07-2009 orthoimage contains some flat area and some areas covered with the sparse vegetation (black dots). (*b*) The same area as in a shaded DEM from 1 m Lidar DEM.

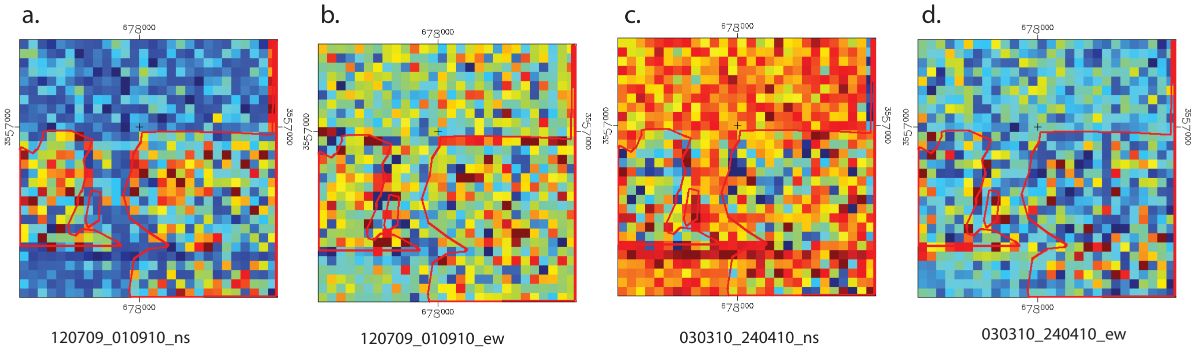

Figure 4.23: The results of the sub-pixel matching of the shaded images, which were formed to reflect the sun settings of matching pair A1 and K. (*a*) N-S displacement of matching pair A1. (*b*) E-W displacement of matching pair A1. (*c*) N-S displacement of matching pair K. (*d*) E-W displacement of matching pair K.

N-S displacement for the pair A1 in the area that is covered with trees has a positive signal as it is expected from the calculations in Figure 4.20. The E-W component of the pair A1 in the same area has more noise than the surrounding areas but the magnitude of the signal is the same as that of the surrounding area, again this is in agreement with the calculations in Figure 4.20. The E-W and N-S displacement of the pair K corresponds to the calculations of Figure 4.21, where in both displacement maps the signal is more negative than the surrounding areas.

I have written an algorithm in Interactive Data Language (IDL) programming language which removes (mask out) this bias signal from the displacement maps. The algorithm identifies trees in one of the ortho images of the matching pair based on the spectral reflectance values of the trees (dark patch on a bright background), their geometric shapes (mainly round), their size (up to 60 pixels), and their topographic locations (slope is less than 15°). Once the trees are identified the mask is formed to remove the bias caused by changing shadows from the displacement maps.

1. The image is initially split into small regular size patches or windows. The size of the patch is adjustable but I find that the 128x128 pixel size patch produce the most reliable results (Figure 4.24(a)).
2. Histogram equalisation is applied to normalise the patch and then mask out all the pixel values which have spectral reflectance value larger than 70 (Figure 4.24(b)).
3. Each individual entity of pixels is assigned a unique number - an ID (Figure 4.24(d)).
4. The entities smaller than three pixels and larger than 60 pixels are removed as they are likely to be either noise or they are far too large to be a tree. Some small trees will be removed but they are not likely to create a large signal (Figure 4.24(e)).
5. A mask for each tree is padded with pixels on each side to reflect the matching window size used (Figure 4.24(e)).
6. Tree masks that are located on the slope larger than 15° are removed (Figure 4.24(g)).
7. The window patches are merged to form a mask for the entire displacement map.

For the future work other inputs can be added such as Normalized Difference Vegetation Index (NDVI) and lidar data to improve the identification of the trees and calculation and correction of the bias - rather than removal of the signal all together. Also, adding the knowledge of the measurements' gradients, especially away from the fault, will secure far-field consistency.

Berthier et al. (2005) also reported that the shifting shadows can cause a bias if the images, that are being matched on the sub-pixel level, have their sun position in different locations. They suspected that large shadows that boulders cast next to a glacier, the motion of which they were studying, cause bias in otherwise stable ground.

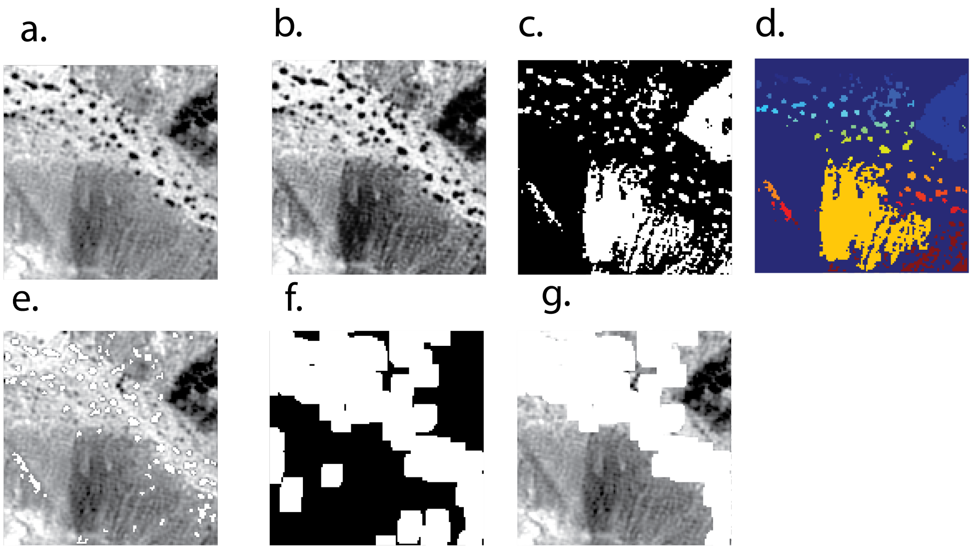

Figure 4.24: Steps of the algorithm for creating a mask for scattered vegetation. (*a*) The orthorectified images are split into regular image patches or windows (e.g. dimensions of 128x128 pixels). A window containing dark sparse vegetation (*b*) For each window the histogram is equalized. (*c*) Only the pixel values less than some heuristically chosen (dark) value are chosen. (*d*)Each of these areas become an entity and receives its own ID. Each entity is checked for the size and only entities smaller than 60 pixels and larger than 3 pixels are not filtered out. (*e*) Remaining entities are overlaid over the original image patch. It shows that the trees have been correctly identified. (*f*) Each individual entity is then expanded as each shadow from an individual tree will affect entire matching window. Once these entities are expanded they merge and create bigger entities. Very small individual entities are removed. (*g*) Final mask overlaid over the original image patch.

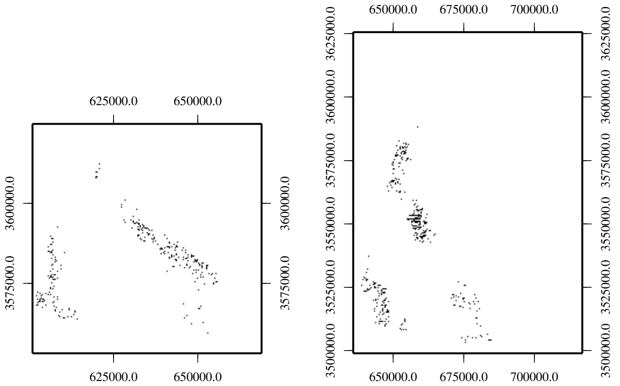

Figure 4.25: On the left is a mask for bias signal caused of changing shadows due to topography for matching pair A1, and on the right is a mask that removes the bias signal of changing shadows due to the topography for matching pair K.

I have also masked out the bias signal in the areas where slopes of hills and mountains cast a shadow based on slope gradient and shadow intensity for pairs A1 and K. The mask is shown in Figure 4.25.

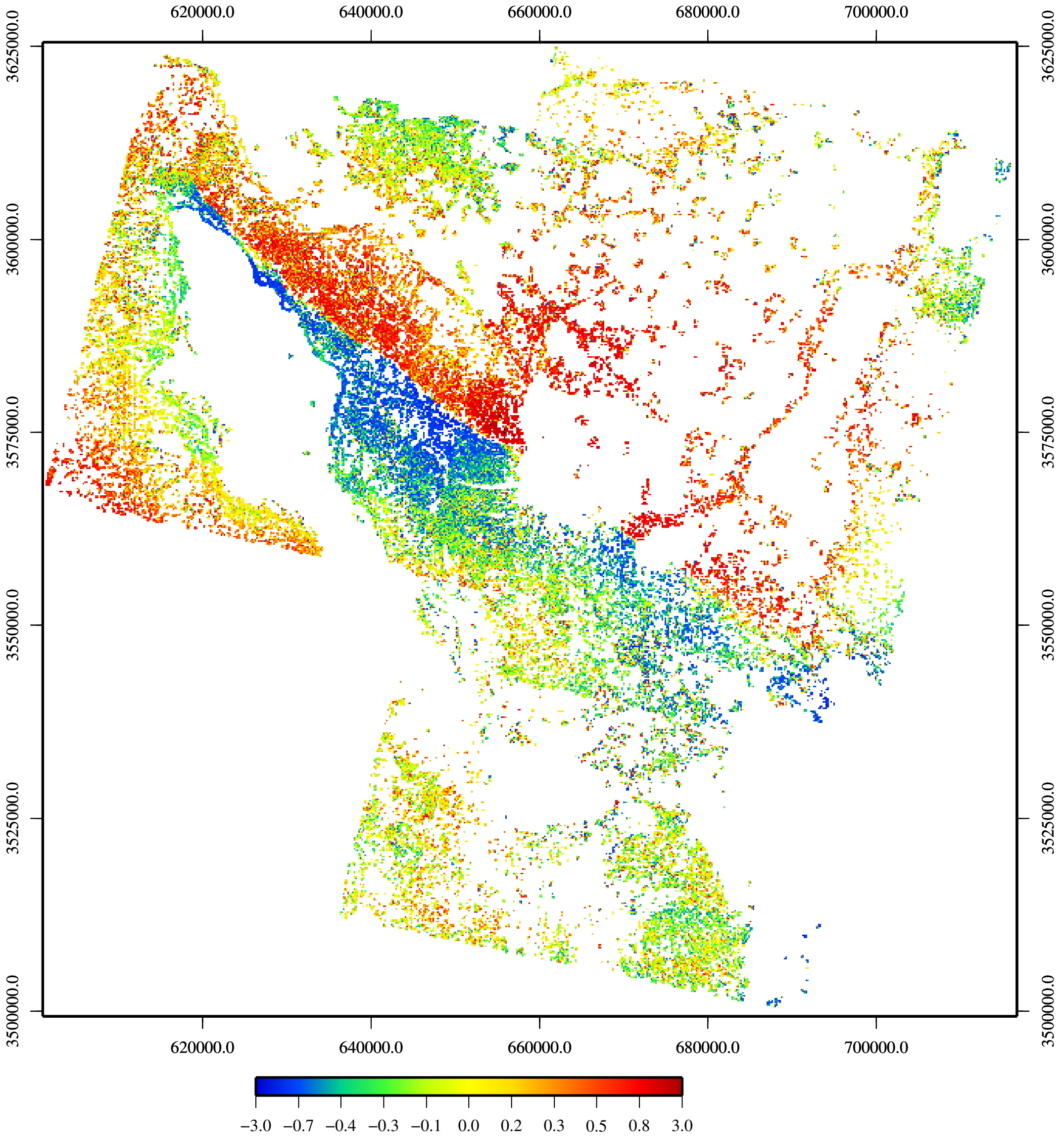

Figure 4.26: Mosaic of the E-W displacements of the pair C1 and K after all the corrections have been applied.

4.5.4 The final image

The Figure 4.26 is the same as Figure 4.4 but with all the corrections applied to the mathcing pairs A1 and K. Although the data appears much less noisy there are still areas that have unexplained deformation such as the bottom left corner of the pair A1 and the deformation signal in the south is not very coherent. In the south the rupture did not come all the way to the surface and it is not so strong as in the north. This clean dataset can now be used in determinig the slip distribution on the fault using inversion.

4.6 Topographic artefacts

The artefacts in horizontal displacement fields due to topography arise from an insufficiently accurate DEM used in orthorectification. Topographic artefacts manifest only when matching pairs have large differences between the images' incidence angles (stereo-pair), but for nadir images acquired by pushbroom satellites these artefacts are minimal (Leprince et al., 2007).

4.6.1 Literature review on DEM accuracies

There has been many reports on the accuracy of the available DEMs such as SRTM DEM, GDEM DEM and SPOT DEM. Rabus et al. (2003) reports absolute horizontal accuracy of 20 m and absolute vertical accuracy of 16 m for the 90 m SRTM DEM. However, Gorokhovich & Voustianiouk (2006) challenged this report and produced the evidence that the absolute vertical accuracy is two to four times worse then that, especially on the slopes higher than 10°. The absolute vertical accuracy of the 30 m GDEM has been analysed by many authors validating the data against either some more precise and higher-order accuracy DEM or against discrete GPS points. The analyses have been done for several areas scattered across the world. Hirt et al. (2010) in Australia find that the RMS of the absolute vertical accuracy is 15 m, Miliaresis & Paraschou (2011) find for the island of Nisiros in Greece an absolute vertical accuracy with an RMS of 14 m, and Chrysoulakis et al. (2011) report an RMS of 11 m for the whole of Greece. However, a global analysis by Guth (2010) found evidence that the GDEM has fewer topographic details than SRTM, and in flat areas has worse vertical accuracy (many artefacts of processing) than SRTM. He concludes that the GDEM tiles should be resampled down to the 90 m in order to use less memory space, and to better depict the actual resolution of the data. Carroll (2010) states that the planimetric accuracy of SPOT 20 m DEM data is in the range of 15 m and 30 m and the absolute elevation accuracy 10 m to 20 m. For both available lidar DEMs used in this study, an accuracy report has not been published. From the method and the equipment used for generating the lidar 1 m DEM, it is expected that the absolute elevation accuracy to be within 10 cm, and I show in Chapter 5 that the pre-earthquake Lidar is quite poor.

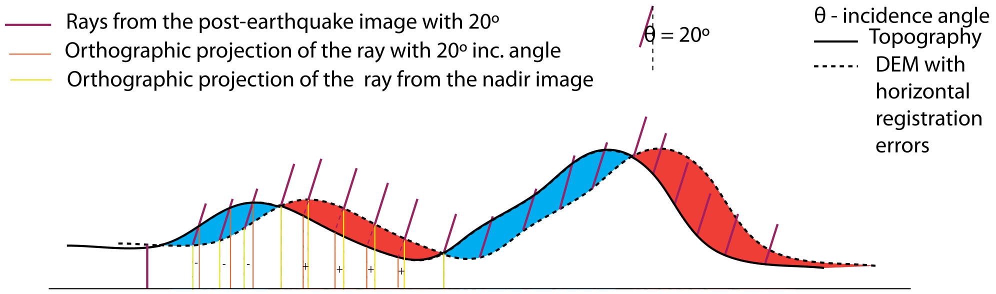

Figure 4.27: Effect of the horizontal mis-registration on horizontal displacements. One side of the high slope will cause the pixels to be projected into location on the projection plane with more positive values and the other side of high slope will cause projection of pixels with more negative values. During the image matching these erroneous locations will be measured as horizontal bias and it will have shaded relief like effect.

4.6.2 Estimation of DEM accuracy via image matching

Photogrammetrical background

Both horizontal and vertical DEM inaccuracies project into displacement maps as a bias in horizontal displacements. Pure horizontal inaccuracies are referred to as mis-registration of the DEM with respect to the image that is to be orthorectified, and they lead to systematic bias in the displacement of the orthorectified pixels (Figure 4.27). The displacement bias are measured during the image matching and it will appear as shaded relief effect in the horizontal displacement maps.

A lower resolution DEM, i.e. a DEM that doesn't match the spatial resolution of the images and therefore lacks vertical accuracy, can cause apparent horizontal displacements as well. Figure 4.28 illustrates a case like that where thin black line represents a course DEM, and the dashed black line represents real topography. An orthorectified pixel that is not supported by the correct height will be projected erroneously into the projection plane (Kraus, 2004).

$$\Delta R_2 = \Delta h \tan \delta \tag{4.4}$$

where ΔR_2 is horizontal displacement Δh is the DEM vertical error and δ is the image incidence angle.

The erroneous horizontal projection (the size of which on a flat terrain is proportional to incidence angle and DEM height error) will be measured by the image matching, as an apparent horizontal displacement (Equation 4.4). Table 4.6 lists the smallest DEM

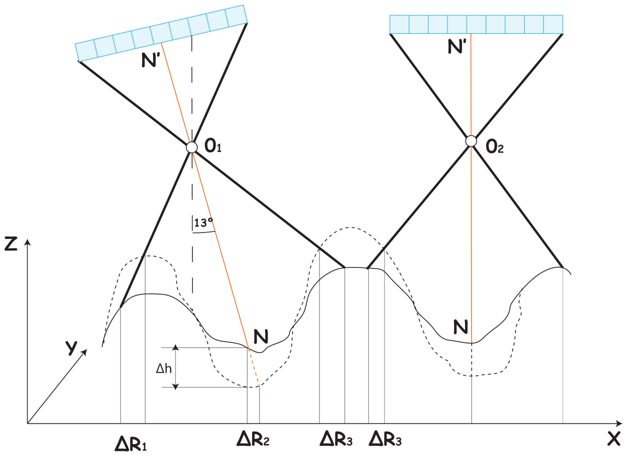

Figure 4.28: Illustrations of several examples how DEM vertical errors cause the planimetric errors in the orthophoto. The solid line represents an inaccurate DEM while the dashed line is a representation of the accurate terrain height. The errors increase radialy from the nadir of the image. Left scene shows an example where the image has incidence angle of 13°. On the right is a scene with 0° incidence angle. O_1 and O_2 are focal points of the optical system.

$i°$	1	5	10	15	20	25	27
dh(m)	140	28	14	9	7	5.5	5

Table 4.6: Vertical DEM errors for SPOT5 resulting in a positional error is greater than the pixel size. i is incidence angle and dh is the vertical error.

vertical error that would result in a positional error of one pixel. Although positional errors larger then one pixel are most obvious to the naked eye, smaller vertical errors will create sub-pixel positional errors which will also have an impact on sub-pixel-matching and inferred tectonic offsets.

Because of the SPOT pushbroom sensor and the near-polar SPOT orbit the orbital plane has an azimuth of 8.8° with respect to north at the equator and 13 ° inclination at 32°N – the north component of the apparent horizontal displacements (topographic artefacts) is much smaller than the east component. If the magnitude of the apparent horizontal displacement is l and the east and north components are e and n respectively, the total horizontal displacement is given by $l = \sqrt{(e^2 + n^2)}$. However, because the north component is small and relatively noisy, the estimation of the topographic artefacts at a latitude of 32° is $l = e/\cos 13° = 1.026e$. Therefore, any effect due to departures of the look direction from perpendicular to the satellite track will be negligible.

DEMs and image matching

The horizontal and vertical accuracy of five available DEMs can be studied through the E-W displacement results of the image matching for two pre-event or two post-event images (that do not span an earthquake) with stereo properties. The matching pairs which fullfil those conditions are B2, B3, B4, B5, D1, D2 and D3 (Table 4.4).

Matching pairs labeled by B were acquiref before the earthquake, and hence contain no tectonic signal. However, the difference between their incidence angles is large and the disparity comes from topographic artefacts due to differences in how they were orthorectified, this is further discussed in Section 5.3.4. Matching pairs B1-B5 have the same pre-event and post-event images as pair B, but I have orthorectified them with different DEMs in order to directly study DEM errors (Section 4.6). Similary, matching pairs D1 (Figure 4.33) and D2 (Figure 4.32) were acquired after the earthquake and are therefore only suitable for studying DEM errors (Section 4.6).

Figure 4.29 shows a section of an E-W displacement map for matching pair B2. The raw images were orthorectified with the 5 m lidar DEM, which does not fully cover the whole image. Image correlation in essence measures a horizontal distance between the two same points on the ground. This represents the horizontal component that can be used for calculation of absolute height at that point (Equation 4.4). The top half of the Figure 4.29 is an example of horizontal misregistration of the DEM, and the measured distances are smaller or larger than expected due to misregistration of the height to each image pixel. The topographic artefacts give a shaded relief-like effect. The bottom half of Figure 4.29 is an example when a DEM was absent from the orthorectification. The image pixels are projected onto the projection plane without any height support, and their horizontal locations in two images are far from the correlact location and far from each other. The matching windows are not wide enough to find the common terrain detail and the decorrelatio fails. Terrain features on the ground are much close when the terrain is flat and matching windows are large enough to make the correlation work, which is the case around the large area of decorrleation in the bottom part of Figure 4.29.

Figure 4.30 shows the results of E-W displacement maps obtained by image matching for the matching pairs B2, B3, B4, B5. The images and DEMs used for their orthorec-

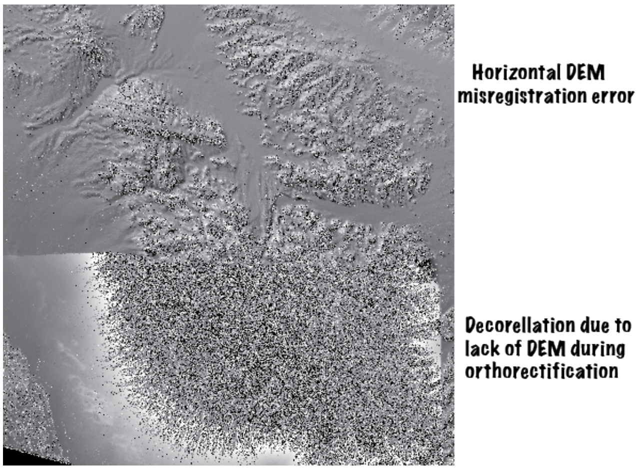

Figure 4.29: An area of E-W displacement of matching pair B2. It contains three types of topographic artefatcs. Top part is caused by horizontal mis-registration, and the bottom part is caused by lack of any DEM, which can either create decorrelation or apparent horizontal displacement that can be used in generation of DEM.

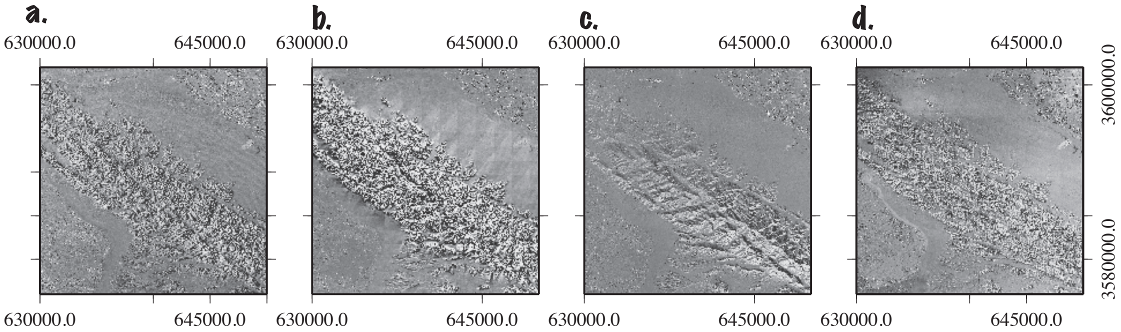

Figure 4.30: The same area of the E-W displacement obtained from the same pre-event and pot-event images matching pair, however processed with different DEMs. (*a*) matching pair B3 is processed with SPOT 20 m. (*b*) matching pair B2 is processed with SRTM. (*c*) matching pair B4 is processed with lidar 5 m. (*d*) matching pair B5 is processed with GDEM.

tification were acquired pre-earthquake for an area of the Cucapah mountain range. Topographic artefacts which manifest as decorrelation are present for the results in the matching pairs B1, B2 and B3, indicating that the vertical accuracy of SPOT 20 m DEM, SRTM and GDEM is not sufficient for orthorectification of oblique SPOT 2.5 m images.

The results for matching pair B2 and especially B3 exhibit shaded DEM-like effect indicating the horizontal mis-registration between image and the DEM used for the orthorectification. I tried to quantify a horizontal-misregistration (Table 4.6) by showing the results of the mis-registration of the first image of the matching pair with shaded DEM using 15-20 GCPs. The SPOT 20 m DEM has large mis-registration, which would explain the topographic artefacts caused by horizontal DEM accuracy. Although, the 5 m lidar data has a small amount of mis-registration, the topographic artefacts that gradually

DEM name	Envi RMS [m]	COSI-Corr Reported Misregistration Easting Mean [m]	 Standard Dev. [m]	 Northing Mean [m]	 Standard Dev.[m]	 Normalised Mean [m]	 Standard. Dev [m]
SRTM 90m	30	8	50	1.8	111	8	122
GDEM 30m	17	0.59	4.2	-0.12	7.4	0.6	8.2
SPOT 20m	17	2.67	30.44	1.50	11.89	3.06	32.68
Lidar 5m	5	0.09	1.6	0.04	1.25	0.1	2.03
Lidar 1m	7.48	0.04	0.93	0.02	0.77	0.04	1.21

Table 4.7: Mis-registration as a result of registering the '12-07-2009' image to the shaded DEM using 15-20 GCPs for five available DEMs. Both COSI-Corr software and Envi's ortho module are used for comparison.

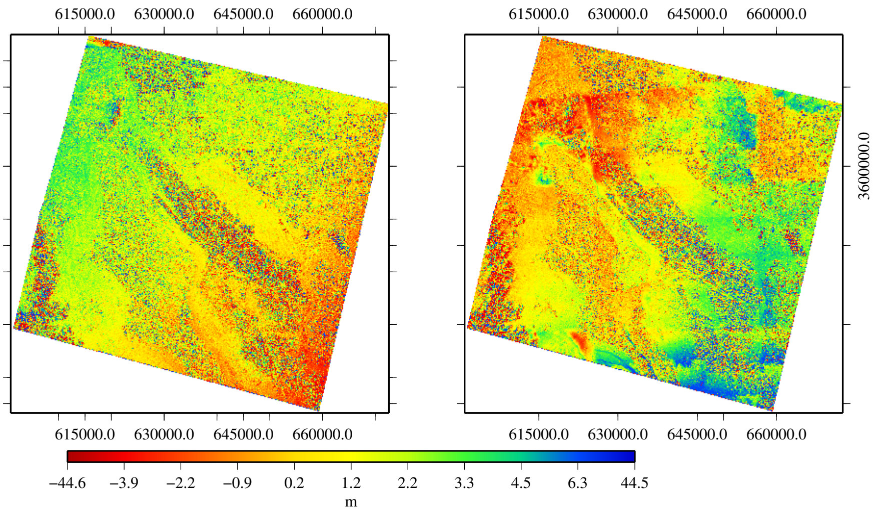

Figure 4.31: On the left is complete E-W displacement for B3 matching pair. On the right is complete E-W displacement for B5 matching pair. Note large discontinuities in E-W displacement map of B5 matching pair. These are probably casued by inaccuratly mosaiced GDEM dataset.

increase towards the right end of Figure 4.30(c), are caused by purely horizontal inaccuracy, i.e. the image is not registered accurately to the 5 m lidar DEM. The horizontal mis-registration for SRTM DEM is obscured by much bigger vertical limitation.

Although the decorrelation due to the vertical accuracy of GDEM for the matching pair B5 appears to be smallest among the four results in Figure 4.30 and there is no evidence of the topographic artefact due to the horizontal DEM error, the topographic artefacts here are the result of GDEM being a mosaic of non-consistent datasets. Comparison between the entire E-W displacement maps of pairs B3 and B5 highlights random discontinuities across B5 matching pair's E-W displacement map Figure 4.31. The discontinuities represent the locations where various parts of GDEM were joined. The random discontinuities are clear evidence that the GDEM DEM has some accuracy concerns in the low terrain as reported in Guth (2010), and in the absence of any other data it should be treated with caution in active tectonic studies.

An area of the E-W and N-S displacement maps of the matching pair D2 is shown in

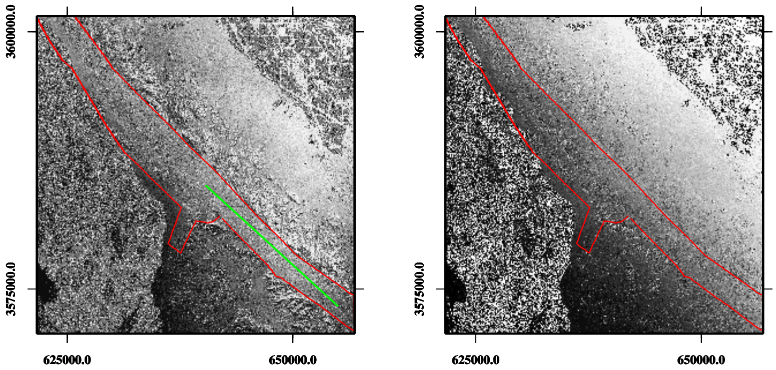

Figure 4.32: A close up view of an area of E-W and N-S displacement maps of matching pair D2. The red line delineates the spatial extend of lidar 1 m. (*a*) E-W component has no topographic artefacts within a narrow band where post-lidar DEM was used for the orthorectification. Outside the red box large topographic artefacts are caused by horizontal mis registration of lidar 5 m. (*b*) N-S component does not show any topographic artefacts.

Figure 4.32, where red polygon shows the boundary of the lidar 1 m DEM used for the orthorectification of images. There are no topographic artefacts within the red polygon, which demonstrates that lidar 1 m DEM is accurate enough to orthorectify SPOT 2.5 m oblique images. Due to a very narrow spatial coverage of the lidar 1 m DEM (Figure 5.4), I have combined it with the 5 m lidar DEM, which has produced horizontal topographic artefacts outside the red polygon.

Introduction into Chapter 5

My final example is the matching pair D1, which has both images that form a stereo-pair acquired after the earthquake, but both are orthorectified with lidar 5 m DEM which was collected before the earthquake. Figure 4.33 shows a close up of two areas of the E-W displacement map, where a red polygon delineates the lidar 1 m DEM coverage. As previously shown, this DEM has horizontal inaccuracies, which show up as a shaded relief effect. Apart from this signal another signal can be observed that is similar to the earthquake discontinuities and it has the same location as the El Mayor-Cucapah rupture. This faint discontinuity represents the topographic artefact caused by changes in the image content of the post-event images casued by the earthquake, which do not reflect the pre-event lidar DEM structures.

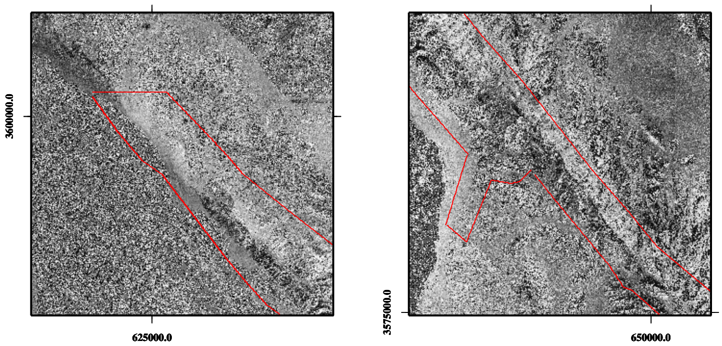

Figure 4.33: Close up view of an area of E-W displacement map of matching pair D1. Apart from the expected topographic artefacts, an earthquake signal is observable.

4.7 Discussion

The idea for the next chapter comes from the last example where if the reverse is true, i.e if image correlation is applied to two images acquired before the event which are orthorectified with a DEM collected after the event, the resulting E-W displacement map will contain both "real" horizontal and apparent horizontal displacement due to the earthquake's vertical motion. With the exception that the lidar 1 m DEM is accurate enough to orthorectify oblique SPOT 2.5 m images and it does not contain any horizontal inaccuracies that could interfere with the result.

Chapter 5

Co-seismic vertical displacements from a single post-seismic lidar DEM: Example from the 2010 El Mayor-Cucapah earthquake

This chapter is based on published paper from Barišin I.,Hinojosa-Corona A., Parsons B., (2015), *Co-seismic vertical displacements from a single post-seismic lidar DEM: example from the 2010 El Mayor-Cucapah earthquake*, Geophysical Journal International, V.202(1).

5.1 Introduction

Measurements of surface displacements produced by earthquakes and volcanic intrusions provide invaluable information about processes occurring at depth. Ideally, one would use a full three-dimensional displacement field to better constrain earthquake sources. InSAR can measure millimetric-accuracy displacements in the line of sight of the radar, e.g. Massonnet et al. (1993). Wright et al. (2004b) show that a 3D displacement field can be derived in principle by combining several InSAR data sets with different look angles.

In practice, the near-polar orbits of the current SAR satellites mean that measurements are effectively only made in two distinct directions. The displacements in both horizontal dimensions may also be measured directly by image cross-correlation with sub-pixel resolution of two satellite or aerial images, one pre-event and one post-event (Leprince et al., 2007).

Lidar measurements of topography have recently emerged as an effective tool for studying earthquakes, Cunningham et al. (e.g. 2006); Zielke et al. (e.g. 2010). At present, apart from the 2010 Mw 7.2 El Mayor-Cucapah earthquake, few other earthquakes have lidar coverage both before and after the event (Duffy et al., 2013; Nissen et al., 2014). Nissen et al. (2012, 2014) obtained 3D surface displacement fields by point-matching pre-event and post-event lidar digital elevation data on a simulated earthquake and a real earthquake respectively, whilst Oskin et al. (2012) have differenced the lidar datasets of the El Mayor-Cucapah earthquake, and obtained the vertical displacements occurring in the earthquake directly. However, the study by Nissen et al. (2014) failed to generate a signal in the vicinity of the surface rupture. The Oskin et al. (2012) study did not account for the effects on the vertical motion of the horizontal displacement produced by the earthquake, and was therefore only able to investigate displacements located on slopes of less than 3°.

In practice, because lidar measurements are costly and restricted to relatively small areas, earthquakes where there is pre-event coverage are likely to remain limited in number. However, once the earthquake has occurred, the area of deformation may be targeted with lidar. Here I present a method whereby it is possible to generate measurements of vertical displacements in the absence of pre-event lidar data. This is achieved by using pre-event optical images and a post-event high-resolution digital elevation model (DEM). The method takes advantage of the fact that there are many archived pre-event satellite images, and that post-event lidar is likely to be flown after an earthquake.

I test this methodology in the case of the M_w 7.2 El Mayor-Cucapah earthquake and compare the results with the results of the differencing technique (Oskin et al., 2012). Using optical satellite imagery, InSAR and seismology, Wei et al. (2011) have calculated a kinematic model of the earthquake. They found a 120 km long rupture that propagated both to the north-west of the epicentre through the Sierra Cucapah and to the south-east on the newly-identified Indiviso fault. Due to data availability (lack of suitable SPOT scenes in the southern part of that region), I restrict this study to that of the vertical displacements due to rupture on the faults in the Sierra Cucapah region north of the epicentre.

5.2 Vertical displacements from apparent horizontal displacements

To estimate vertical displacements I make use of two pre-event, stereoscopic satellite images and a high-accuracy post-event lidar DEM. The geometrical principle behind the method is illustrated in Figure 5.1 for the simple case in which a flat land surface is imaged by two satellites before an earthquake and then undergoes uniform vertical uplift on one side of a fault. Orthorectification, the process by which geometrical distortions caused by terrain relief are removed, projects points from the raw satellite images onto a reference plane. In this process, a DEM is used in order to project the points into the correct location, creating a planimetric image (Kraus, 1992; Novak, 1992). However, the images were acquired before the vertical uplift had occurred; if they are then orthorectified with a DEM generated after the earthquake, the orthorectified images will contain an error (hollingsworth2012). A given point will not project onto its location before the earthquake (B′ in Figure 5.1), but will be displaced (B1 and B2 in Figure 5.1). The apparent horizontal displacements between the two images at each point can be estimated using image cross-correlation (by measuring distance d in Figure 5.1), and will reflect the topographic change contained in the post-earthquake DEM (Figure 5.1). Making use of the sine rule, the apparent horizontal displacement d is related to the change in height h in this simple example by

$$h = d\frac{\cos i_1 \cos i_2}{\sin(i_1 + i_2)} \tag{5.1}$$

where i_1 and i_2 are the incidence angles in the two images. SPOT's pushbroom sensor give rise to a linear central projection (i.e. each scan line has independent central

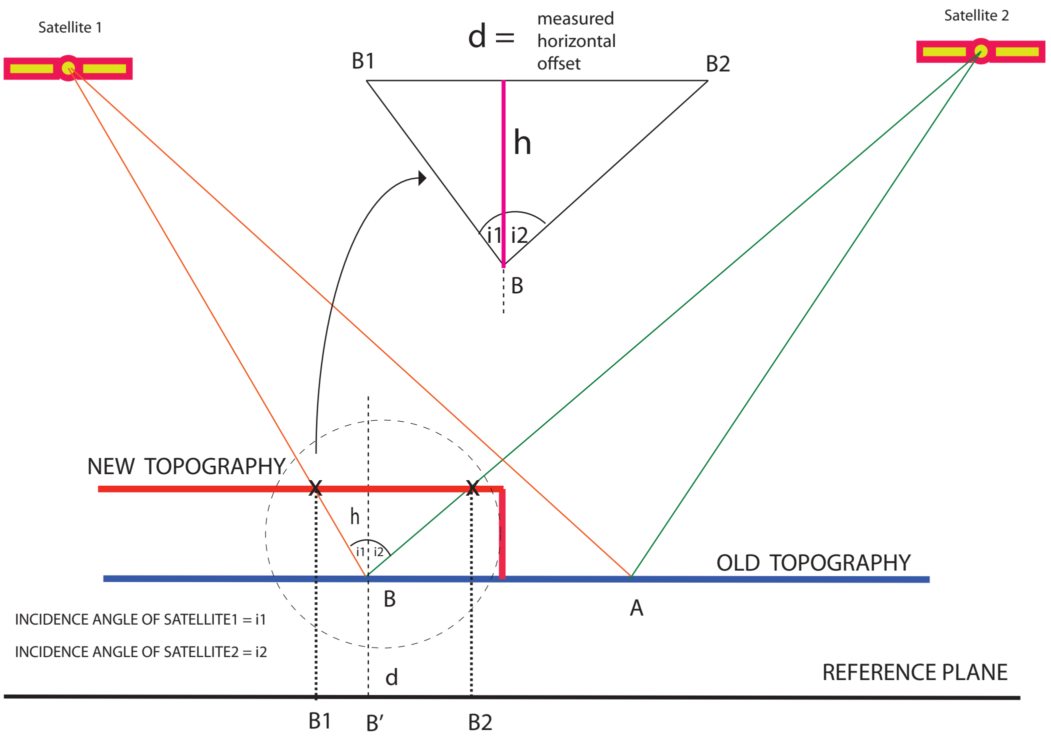

Figure 5.1: Sketch showing the geometry for orthorectification in a simple example where both images obtained before the event have large incidence angles. The red line represents the new topography in this example, and the blue line represents the original heights when the images were acquired. Point B has undergone a vertical displacement, whereas point A is unchanged.

projection), rather than a central projection for the entire image. The parallax due to height changes should be estimated in the scan line direction. Given the near north-south satellite tracks, the stereoscopic effect will produce much larger apparent east-west displacements than those in the north-south direction. This is discussed in more detail in section 5.3.4. In the real case examined in section 5.3, one of the two images has a near-nadir incidence angle ($i_1 \approx 0$). In this case equation (5.1) reduces to $h = d \cot i_2$. This geometry is less favorable due to a smaller base-to-height ratio (which defines height accuracy against planimetric accuracy); however, the estimation of apparent horizontal displacements is still possible with image cross-correlation with sub-pixel resolution (Morgan et al., 2008).

In general, heights will vary from point-to-point and I require expressions for vertical displacements when they occur on sloping terrain (Figure 5.2); the gradient of heights λ is positive when heights increase from left to right. As before I assume that image 1 is viewed from the left with incidence angle i_1 and image 2 from the right with incidence

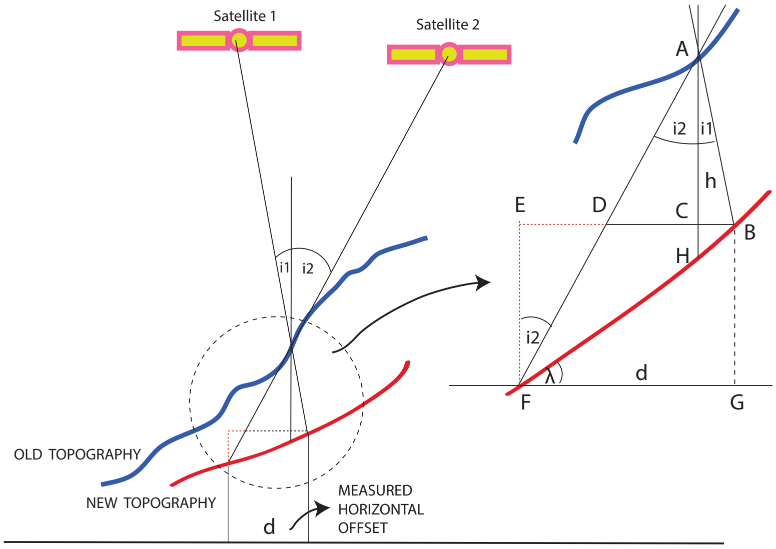

Figure 5.2: Sketch showing the geometry of orthorectification for the case of vertical displacement on a slope.

angle i_2.

I derive a step-by-step expression relating the change in height h to the apparent horizontal displacement d in the presence of a topographic slope λ. The notation follows that given in Figure 5.2.

I note that $h = \overline{AH}$ and $d = \overline{FG}$. Applying the sine rule to triangle $\overline{ABH}$

$$\frac{\overline{AH}}{\sin(\lambda + (90 - i_1))} = \frac{\overline{AB}}{\sin(90 - \lambda)} \tag{5.2}$$

and hence

$$\overline{AH} = \frac{\overline{AB}\cos(\lambda - i_1)}{\cos\lambda} \tag{5.3}$$

I also have the following expression for $\overline{FG}$:

$$\begin{aligned}\overline{FG} &= \overline{EB} = \overline{ED} + \overline{DB} \\ &= \overline{EF}\tan i_2 + \overline{DB} \\ &= \overline{FG}\tan\lambda\tan i_2 + \overline{DB} \\ &= \frac{\overline{DB}}{(1 - \tan\lambda\tan i_2)} \end{aligned} \tag{5.4}$$

To connect equations (5.3) and (5.4) we apply the sine rule to triangle $\overline{ABD}$:

$$\begin{aligned} \frac{\overline{DB}}{\sin(i_1+i_2)} &= \frac{\overline{AB}}{\sin(90-i_2)} \\ \overline{AB} &= \frac{\overline{DB}\cos i_2}{\sin(i_1+i_2)} \end{aligned} \tag{5.5}$$

and hence combining equations (5.3), (5.4) and (5.5), we find that

$$\begin{aligned} \overline{AH} &= \frac{\overline{DB}\cos i_2 \cos(\lambda - i_1)}{\cos\lambda \sin(i_1+i_2)} \\ &= \frac{\overline{FG}(1-\tan\lambda\tan i_2)\cos i_2\cos(\lambda-i_1)}{\cos\lambda\sin(i_1+i_2)} \\ &= \frac{\overline{FG}\cos(\lambda-i_1)\cos(\lambda+i_2)}{\cos^2\lambda\sin(i_1+i_2)} \end{aligned} \tag{5.6}$$

$$h = \frac{d\cos(\lambda-i_1)\cos(\lambda+i_2)}{\cos^2\lambda\sin(i_1+i_2)} \tag{5.7}$$

where $h = \overline{AH}$ and $d = \overline{GF}$ in Figure 5.2. The apparent asymmetry between the terms in the numerator of equation 5.7 results from measuring the incidence angles in opposite senses in Figure 5.2. The lack of perfect symmetry with respect to an exchange of i_1 and i_2 results from the fact that, as defined in Figure 5.2, angle i_2 is measured clockwise from the vertical whereas angles i_1 and λ are measured anticlockwise. When $\lambda = 0$, the expression in equation (5.6) reduces to that in equation (5.1) as expected.

In an earthquake, the earth's surface undergoes both horizontal and vertical displacements. In the presence of pre-existing topographic relief, the horizontal displacements will produce changes in height through the advection of topography. The total change in height Dh at a point is made of two components:

$$Dh = \delta h + \mathbf{u}\cdot\nabla h \tag{5.8}$$

where $\mathbf{u}$ is the horizontal displacement vector. The first component is the actual vertical displacement at that point and the second component the height change resulting from the advection of topography. Assuming the horizontal displacements have been estimated, the true vertical displacement can be obtained from the total height change by

$$\delta h = Dh - \mathbf{u} \cdot \nabla h \tag{5.9}$$

Equation 5.9 may be used to correct a post-event lidar DEM to produce a DEM that differs from the pre-event topography only by the vertical displacements. When the images are orthorectified using this corrected DEM, the apparent horizontal displacements will provide estimates of the vertical displacements alone.

5.2.1 Algorithm overview

Here I outline the steps employed to derive vertical displacements. In order to keep the description of each step concise, we defer more detailed technical explanations to later in the text. A full work flow diagram summarizing the processing is given in Figure 5.3.

Step 1 The pre-event image is orthorectified with the aid of Ground Control Points (GCPs) located on a reference map (e.g. a pre- or post-earthquake shaded DEM) with properly registered horizontal coordinates. The post-event image is orthorectified using tie-points identified on the first (pre-event) orthorectified image. For the near-nadir images, topographic artefacts will be small and non-lidar DEMs with coverage across the whole of the image (e.g. a SPOT DEM) can be used.

Step 2 Horizontal displacements are estimated by applying image ccorrelation to pre-event and post-event nadir images using COSI-Corr. All displacement maps obtained by COSI-Corr have a certain degree of long wavelength error present that needs to be removed before proceeding to the next step. The source and nature of the long wavelength error is discussed in section 4.4.

Step 3 The horizontal displacements are used to remove the advective component of height change from the post-event lidar DEM. Instead of implementing Equation 5.9 we use a Lagrangian approach. For each grid point in the post-event lidar DEM, we calculate the horizontal coordinates it had before the displacement $\mathbf{u}$ and then resample the DEM onto a regular grid.

Step 4 The corrected post-event lidar DEM is used to orthorectify two stereoscopic pre-event images acquired at different times with a large incidence angle difference. In order to obtain a DEM over the whole area of the images, as required by the COSI-Corr orthorectification scheme, the post-seismic lidar DEM was mosaicked with a DEM generated using SPOT5 stereo-pairs (see section 5.3.3).

Step 5 Apparent horizontal displacements due to vertical displacements are calculated by image correlation of the two pre-event images using COSI-Corr. The GCPs and tie-points used in orthorectifying these images were placed only within the region of the post-event lidar to keep the registration of the images tied precisely to the post-event lidar. Placing the tie points within the deformation zone results in a long-wavelength error that must be removed.

Step 6 Apparent horizontal displacements are converted to vertical displacements using Equation 5.7.

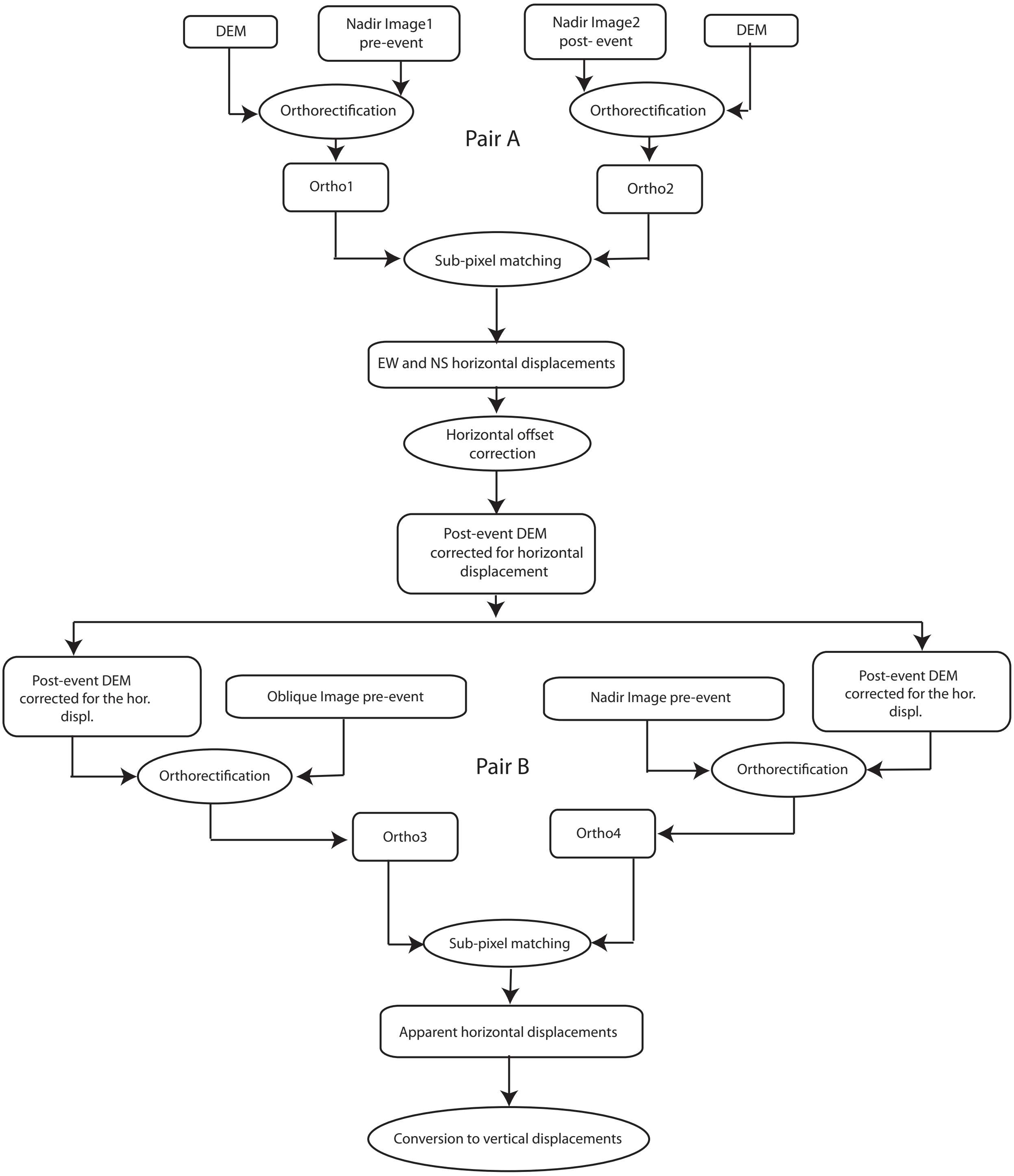

Figure 5.3: Processing steps and work flow of the method discussed in the text.

5.3 Case study of the M_w 7.2 2010 El Mayor - Cucapah earthquake

This section describes the processing steps in detail for the case of the M_w 7.2, 2010 El Mayor-Cucapah earthquake.

5.3.1 Data sets

There are two lidar DEM datasets of this area (Table 4.2). The pre-earthquake lidar DEM has 5 m spatial resolution and broad coverage (Figure 5.4). The post-event lidar DEM, with 1 m spatial resolution, was acquired in August 2010, four months after the earthquake. It covers a narrow strip along the earthquake rupture as outlined in Figure 5.4. The post-event lidar DEM is used in the estimation of vertical displacements around the fault as described above. In addition, I use differences between the two lidar DEMs, as described in Oskin et al. (2012), to validate the vertical displacements estimated from image matching, except that here we first correct for the effects of the horizontal advection of topography.

I make use of four panchromatic SPOT5 2.5 m images at different steps in the analysis outlined above (Table 4.1, Figure 5.4). From these images, I selected three image pairs with different viewing geometries (Table 4.4). Pair A1 is formed from two near-nadir images, one acquired before the earthquake (12-07-2009) and the other after the earthquake (01-09-2010) (Table 4.4). Pair A1 is used to determine the horizontal displacements occurring in the earthquake. Pair B consists of two pre-event images (09-07-09/12-07-09), one of which is obliquely viewed, and the other is near-nadir. Image matching of this pair provides apparent horizontal displacements and hence estimates of vertical displacements. The third pair, Pair C (01-09-2010/13-04-2010) is used to construct a 2.5 m resolution post-earthquake DEM in order to orthorectify the images of pair B over their entire area. This DEM is constructed using Envi DEM generation tool.

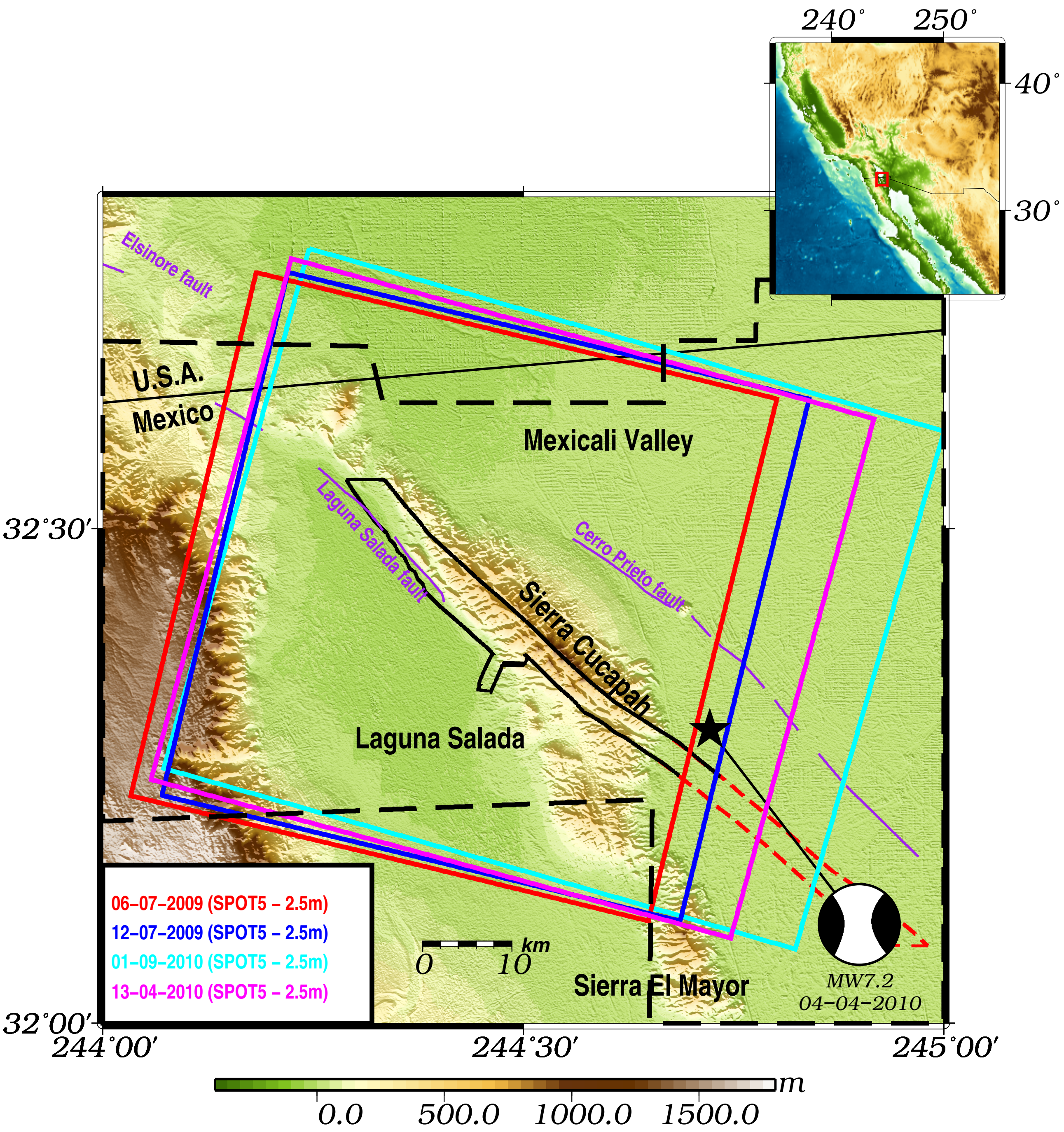

Figure 5.4: Topographic map of the epicentral area of the 2010 Mw7.2 El Mayor-Cucapah earthquake. The dark blue, light blue, magenta and red rectangular boxes show the areas covered by the SPOT panchromatic images used in this study (Table 4.1). The narrow black polygon marks the area covered by the post-earthquake lidar 1 m resolution DEM used in this study. The dashed red polygon, which is a continuation of the black one, shows the extent of the post-earthquake lidar dataset not used in this study. The black dashed polygon marks the area covered by the pre-earthquake lidar 5 m resolution DEM. The focal mechanism of the earthquake is from the USGS. The inset shows the location of this figure within south-western North America. The purple lines show the locations of faults in the region.

5.3.2 Removal of topographic advection from the post-event lidar DEM

I use the horizontal displacements produced by the earthquake from correlation of image pair A (Figure 4.4, and Section 4.3) which have nominal spatial resoultion of 10 m. I also resampled the lidar differences to 10 m. The post-event lidar DEM contains height changes relative to pre-event topography due to the horizontal advection of topographic relief as well as vertical displacement (Equation 5.8). To remove the advection component from the post-event DEM, I first resample the DEM and E-W/N-S displacement fields on the same uniform 2.5 m grid, then calculate the pre-earthquake horizontal coordinates for each node of the DEM by subtracting corresponding E-W and N-S displacements. This corrected post-event DEM on an irregular grid is then resampled onto a uniform 2.5 m grid. In order to

5.3.3 A composite DEM

Although I had a post earthquake 2.5 m SPOT DEM availaible I show here a working example how it is possible to create a full coverage DEM even in situations when such DEM is not available. In order to obtain the apparent horizontal displacements for the pre-event image pair B resulting from the vertical displacements, I must first orthorectify the images. I am only interested in these displacements for the area of the high-resolution post-earthquake lidar DEM. However, COSI-Corr requires full DEM coverage of each image as the orthorectification algorithm initializes the process at the four corners of the image (Leprince et al., 2007). For the area outside that of the post-event lidar, I derived DEMs with a 2.5 m sampling by applying ENVI's DEM generation module (www.exelisvis.com/envi) to both image pairs B and C (Table 4.4), then combining them in order to minimise areas of decorrelation. This DEM was supplemented by a small strip in the south with the pre-event lidar DEM to achieve full coverage for both images. I then mosaicked this DEM with the post-earthquake lidar DEM, using the latter for the area around the fault. I note that each constituent DEM in the composite DEM has been geo-registered differently, and therefore may not be perfectly aligned.

5.3.4 Vertical displacements

The apparent horizontal displacements between the two pre-earthquake images in pair B were obtained by using the COSI-Corr software (Leprince et al., 2007) to orthorectify the images and correlate them to sub-pixel accuracy in the manner described in section 4.3. In orthorectifying the first SPOT image in this pair, I used GCPs identified in a shaded relief map constructed from the same composite DEM for sun angles as were used at the time of the image acquisition. In this case, their locations were restricted to the area of the post-event lidar DEM in order to avoid introducing different geo-registration regimes. A long wavelength error correction was made in the same way as for the true horizontal displacements.

Because of the near-polar SPOT orbit – its orbital plane has an azimuth of 8.8° with respect to north at the equator and 13 ° inclination at 32°N – the north component of the apparent horizontal displacements is much smaller than the east component. If the magnitude of the apparent horizontal displacement is l and the east and north components are e and n respectively, the total horizontal displacement is given by $l = \sqrt{(e^2 + n^2)}$. However, because the north component is small and relatively noisy, we estimate the magnitude of the apparent horizontal displacement at a latitude of 32° to be $l = e/\cos 13^\circ = 1.026e$. Any effect due to departures of the look direction from perpendicular to the satellite track will be negligible. The east component of the apparent horizontal displacement is shown in Figure 5.5. I used a very small window step for the correlation (4 pixels x 2.5 m windo size). The results of correlation for the regions of high decorrelation resulted in erroneous signal.

Inside the area of the post-earthquake lidar DEM, the accurate DEM ensures accurate geo-correction and orthorectification, whereas outside it we observe large artefacts caused by the mis-registration between the images and DEM. The areas of decorrelation due to vegetation change are similar to those seen in the matching of pair A (Figure 4.3), even though there are only three days between the images in pair B. Figure 5.6(a) shows the vertical displacements derived in the manner described above, and Figure 5.6(b) the apparent horizontal displacements, just for the area of the the post-earthquake lidar DEM. These figures look similar, (a) being derived from (b) using Equation 5.7 in Step 6.

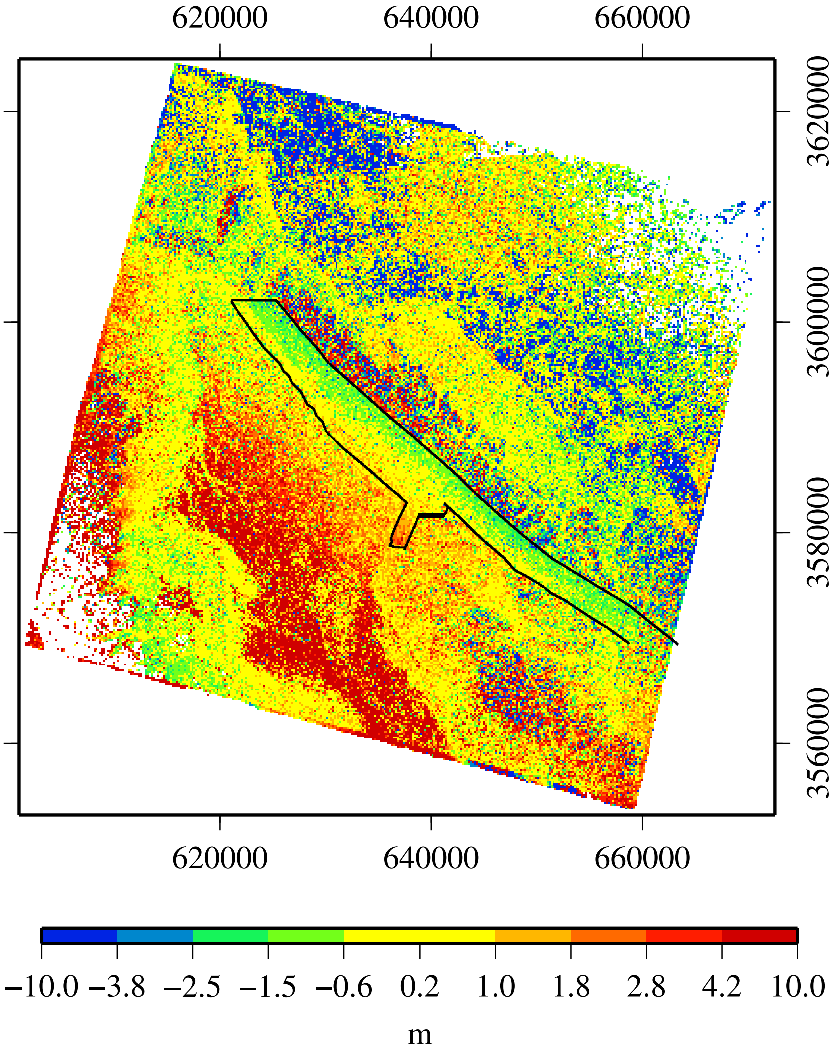

Figure 5.5: East component of apparent horizontal displacements obtained by image cross-correlation of the 'B' stereopair. The black polygon delineates the coverage of the post-earthquake lidar.

The pattern of the vertical displacements in the predominantly flat area to the north-west (see also Figure 5.9) appears to be very similar to the results obtained in the Oskin et al. (2012) study (Figure 5.7). Further south there is a single line of discontinuity that matches the location of the earthquake rupture derived from the horizontal displacements (Figure 5.13(a)).

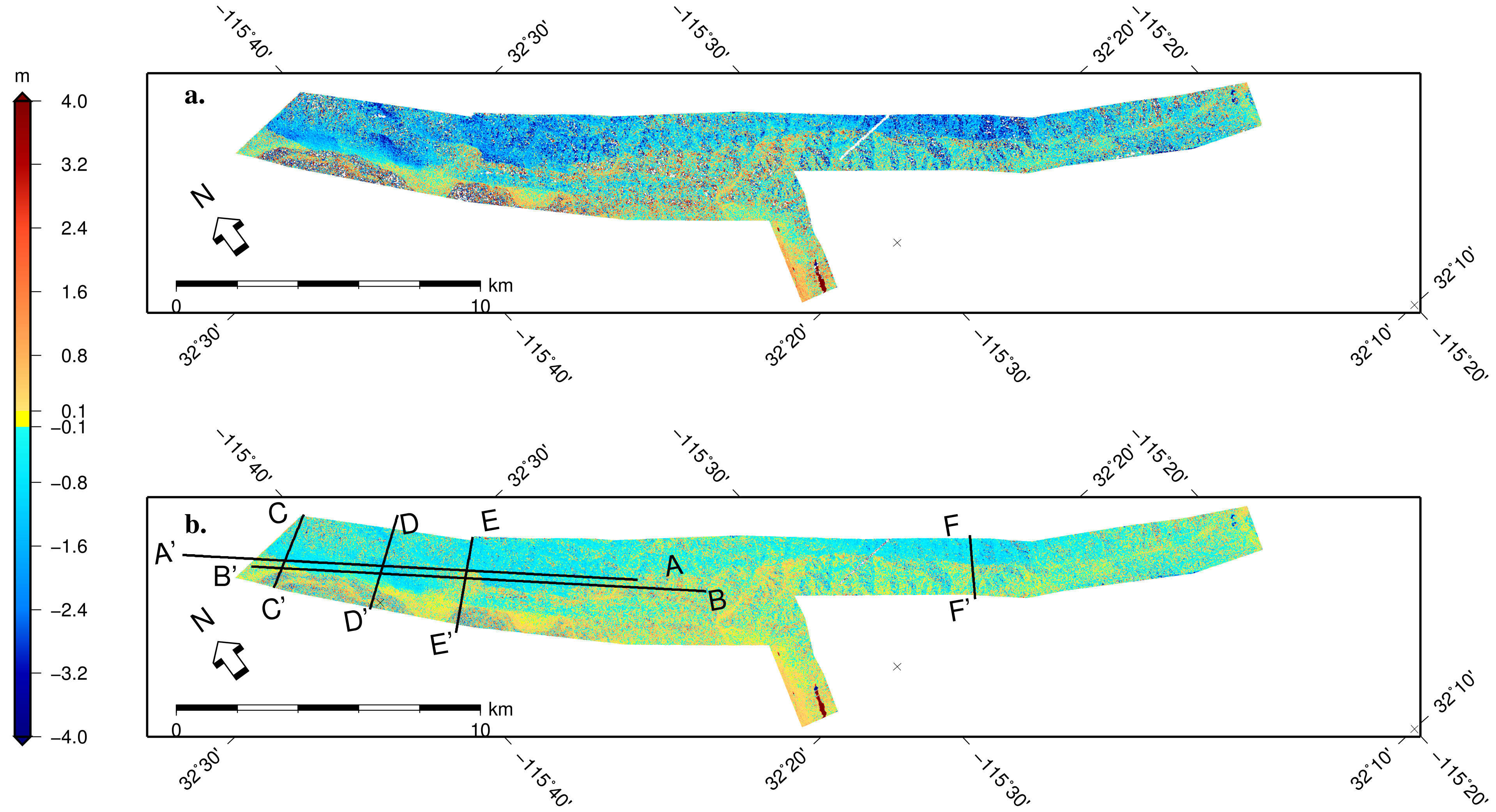

Figure 5.6: (*a*) Final calculated vertical displacements; (*b*) The apparent horizontal displacements for the area of the post-event lidar DEM shown by the black polygon in Figure 5.5. Topographic artifacts are small and the main displacement signal is caused by the vertical displacement due to the earthquake. The black lines are locations of the profiles given in Figure 5.11.

5.4 The vertical displacement field

5.4.1 Differencing the pre-event and post-event lidar DEMs

I validate the vertical displacements estimated above by comparing our results to the results of differencing the pre-earthquake and post-earthquake lidar datasets. Initially, I calculate the difference between these two datasets directly, as done in Oskin et al. (2012) but apart from the areas where the slopes are less than 3°, the differences are dominated by effects caused by the advection of topography and where the vertical displacement signal is obscured (Figure 5.7(a)). We correct the post-event lidar DEM for the horizontal advection of topography as previously described, and then recalculate the difference. The output shows a much clearer signal across the entire field along the fault (Figure 5.7(b)). I observe the distinct signal of a fault that has subsided along its north-eastern side and uplifted to the south-western, and a branching pattern with many smaller faults in the north-eastern segment.

Although the recalculated differences are significantly improved, there is still substantial topographic noise. This is partially due to differences in the spatial resolution and mis-registration of the two lidar datasets. The mis-registration can be quantified by matching shaded relief derived from the two lidar DEMs directly. This image correlation was undertaken using software that I wrote and customized following methods used in Leprince et al. (2007); the east and north displacements that result from this matching are shown in Figure 5.8. The east-west displacements (Figure 5.8(b)) clearly show the rupture and near-field displacement fields, but are also obscured by a few stripes in the N-S direction. However, the north-south component shows a regular striped pattern in the N-S direction (Figure 5.8(a)). This is an artefact resulting from the merging of lidar data on individually flown swaths, the lines directly corresponding to the edges of the flight-lines during the point cloud acquisition. Glennie et al. (2014) found warping of the scan-lines and large systematic errors at the scan-line edges due to the large off-nadir scan angle in the pre-event lidar dataset.

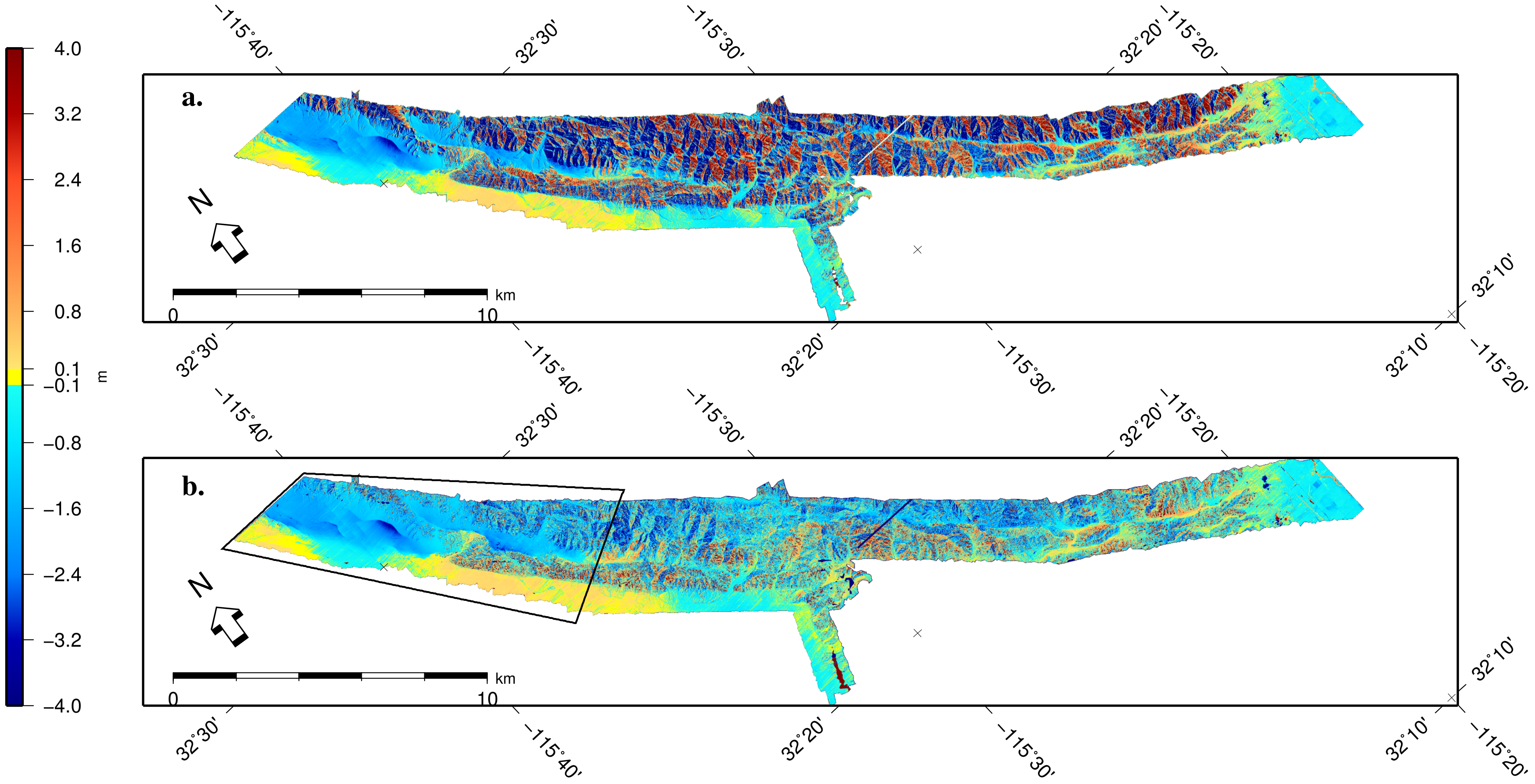

Figure 5.7: Two difference datasets using the pre-event and post-event lidar DEMs, where the 1 m post-event DEM was resampled to 5 m. (*a*) Simple difference between the two datasets without allowing for the advection of topography caused by the earthquake (Oskin et al., 2012); (*b*) The same result but the calculated E-W and N-S displacements were used to correct the post-event lidar DEM for advection of topography. The noise is considerably smaller in this case, the topographic artefacts due to the horizontal advection being reduced. The black polygon shows the area covered in Figure 5.9.

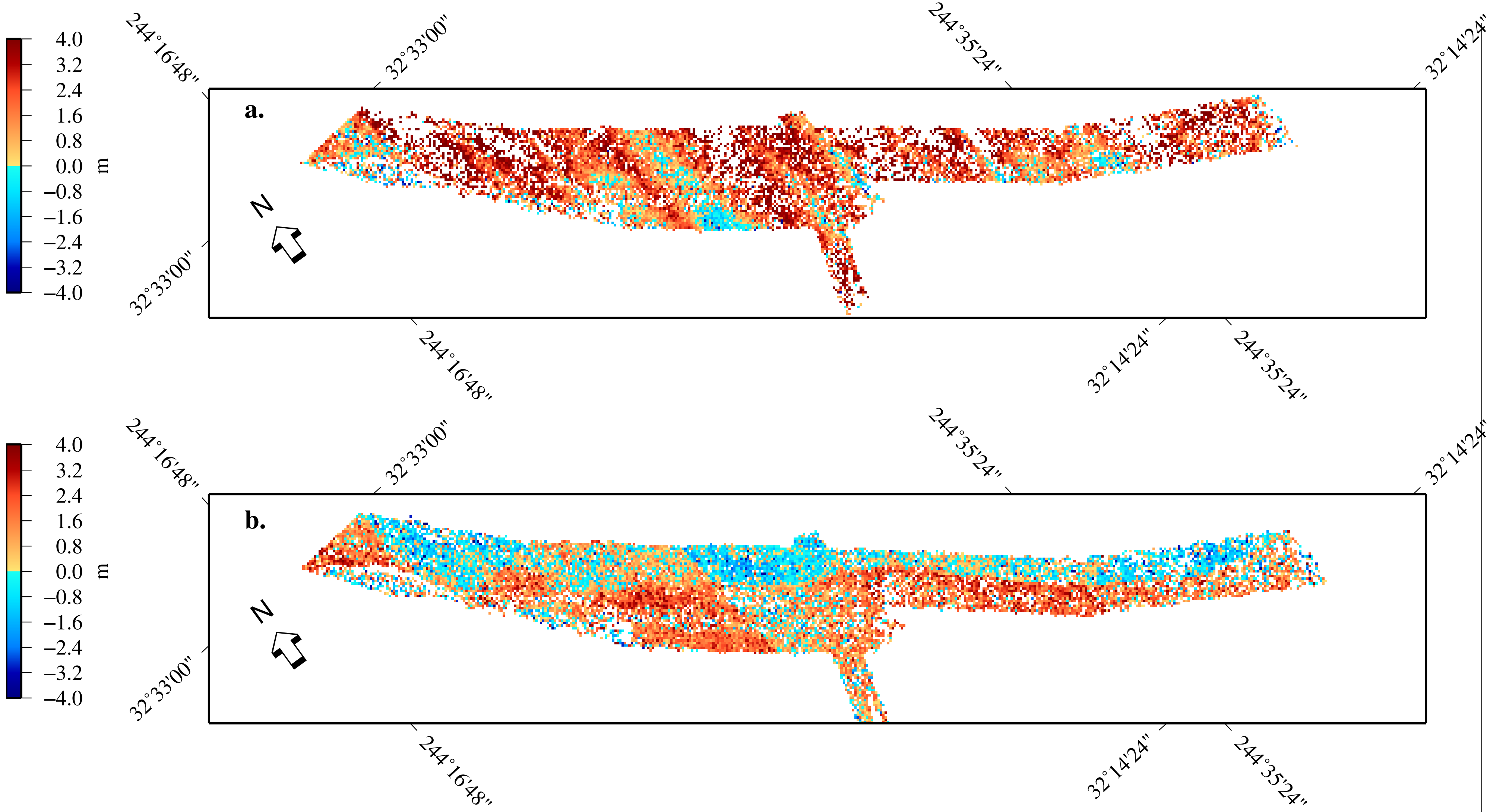

Figure 5.8: The horizontal displacements as a result of image cross-correlation with sub-pixel resolution of the pre-earthquake and post-earthquake shaded lidar DEM: (*a*) The N-S component of the horizontal displacement. The striping is caused by the misalignment of the point clouds from the individual flight lines in the pre-event lidar DEM. The N-S displacements alternate between positive and negative displacement reaching a magnitude of 5 m and more in places; (*b*) The E-W horizontal displacement. The horizontal displacement due to the earthquake is the main signal.

5.4.2 Validation of the vertical displacements

I chose to make a detailed comparison of the differences between the pre- and post-event lidar DEMs and the vertical displacements derived here for the top north-western region of the earthquake rupture. The topography of this area is a mixture of a very flat desert plain and some high relief that is an ideal setting to assess my method. Figure 5.9(a) shows a close-up view of the differences between the two DEMs, Figure 5.9(b) shows the vertical displacements obtained by the method described in this chapter, and Figure 5.9(c) is the difference between the two estimates of vertical displacement. They both show the same discontinuities and the same patterns of uplift and subsidence, which agrees with mapped rupture in the field by Fletcher et al. (2014) and shown in Figure 5.13. Although the differences between these two estimates of vertical displacement are very noisy, there is little remaining signal associated with faulting. Figure 5.10*(*a) compares histograms for the subsidence area north-east of the rupture (hanging-wall area) only. The histogram mean for both data sets is -1.34 m, the standard deviation for the differences between the lidar DEMs is 1.1 m, and the standard deviation for our method is 1.2 m. Figure 5.10(b) compares histograms only for the south-western part from the rupture (footwall area). The mean and standard deviation from differencing the lidar DEMs are -11 cm and 0.83 m respectively, and the mean and standard deviation for our method is -7 cm and 1.31 m respectively.

A different comparison between the two datasets is made in Figure 5.11 along profiles, the locations of which are shown in Figure 5.6(b). Red lines show the differences between the two lidar DEMs including the correction for horizontal advection of topography, and blue lines the vertical displacements obtained by image matching. For the reasons discussed in 5.4.1 and by Glennie et al. (2014), differencing lidar DEMs creates greater short wavelength noise in areas of high topographic relief (Figure 5.11), despite the fact that I have removed the height change due to horizontal advection. Also, the study by Nissen et al. (2014) shows another example where differencing pre-event and post-event lidars suffers from mis-registration. Our method registers the images used in correlation directly to the lidar DEM which ensures that the topographic artefacts in the vertical displacement field will be minimal. However, the lidar DEM used in our method must not contain

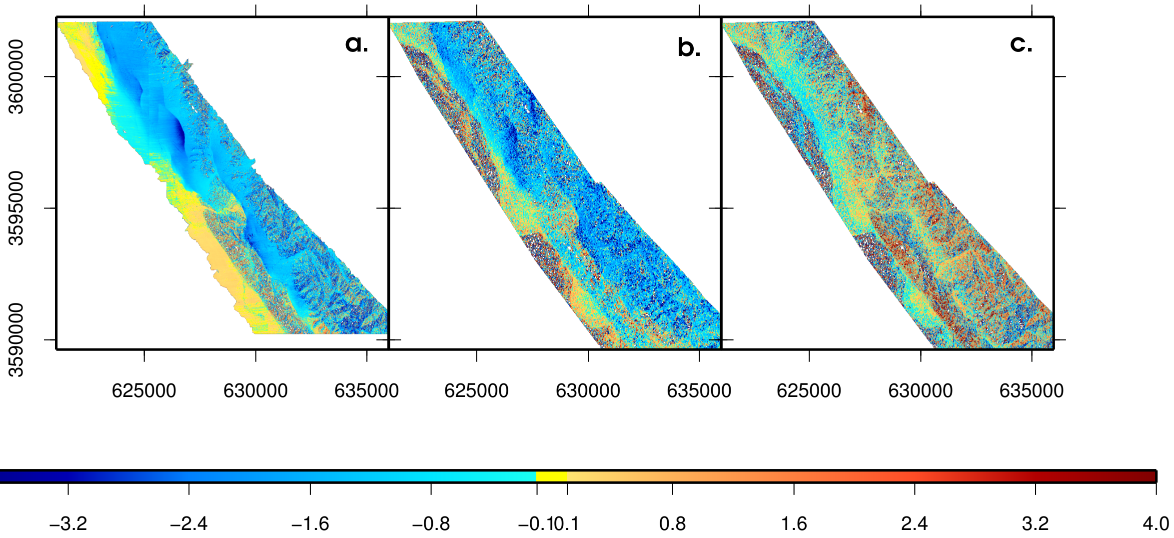

Figure 5.9: The NW area (black polygon in Figure 5.7(*b*)) of the post-earthquake lidar used to validate the results of my method versus differencing of the DEMs. *(a).* Vertical displacements obtained by differencing of pre- and post-earthquake lidar DEMs, when the post-earthquake lidar DEM was corrected for horizontal advection. *(b).* Vertical displacements obtained using the method described here. *(c).* Calculated differences between changes in height from (*a*) and (*b*). There is a good agreement between the two estimates of vertical displacement, but both techniques suffer from short wavelength noise although in different locations due to different origins of the short wavelength error.

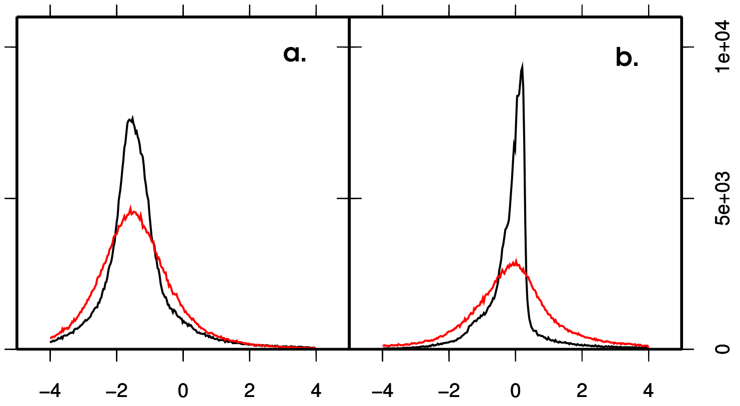

Figure 5.10: The black lines show histograms of vertical displacements obtained by differencing two DEMs, and red lines show histograms for vertical displacements obtained by my method for the area in Figure 5.9. (*a*) shows histograms for the hanging-wall area only; both datasets have the same mean: -1.34 m. The standard deviation for differencing lidar method is 1.05 m and for my method is 1.2 m. (*b*) shows histograms for the footwall area; both histograms have near-zero mean. The standard deviation for differencing lidar DEMs is 0.8 m because it is mainly flat relief; our method is 1.3 m, consistent with the hanging-wall area.

systematic errors between scan-lines.

Correlation of images is very sensitive to changes in image textures, which results in areas of decorrelation. Agricultural, urban and forested land surfaces, or in this case shifting sand, are the major causes of decorrelation which could obscure the signal. The window size (80 m) in this study, is a limiting factor in achieving higher resolution mea-

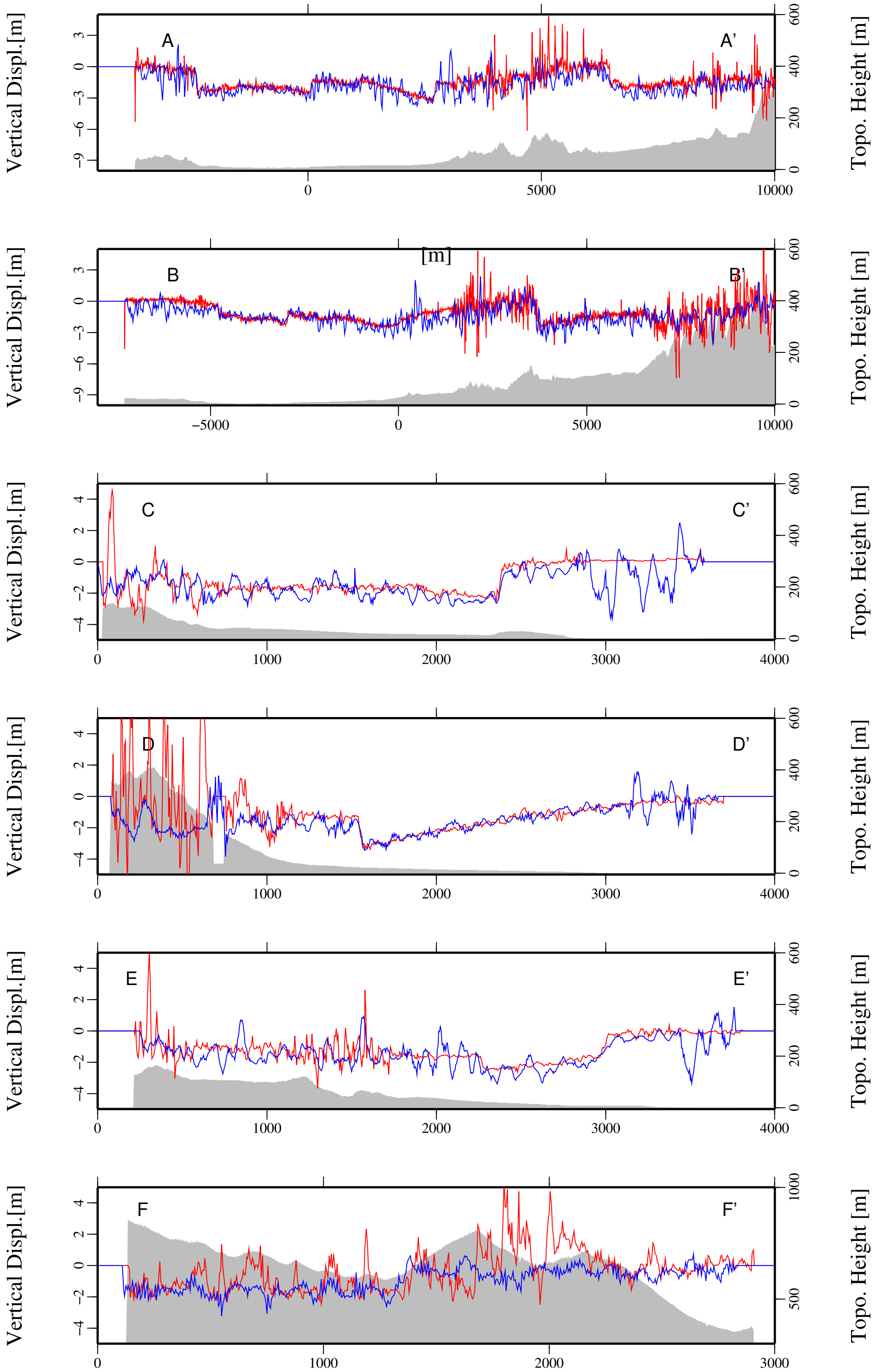

Figure 5.11: Profiles across the vertical displacement obtained by differencing the two lidar DEMs (red profiles) and the vertical displacements obtained with the method described here (blue profiles). A-A′ and B-B′ profiles are longer profiles running along the long side of the data set, C-C′, D-D′, E-E′, F-F′ profiles are fault-normal (Figure 5.6(*b*)). The grey areas show the underlying topography.

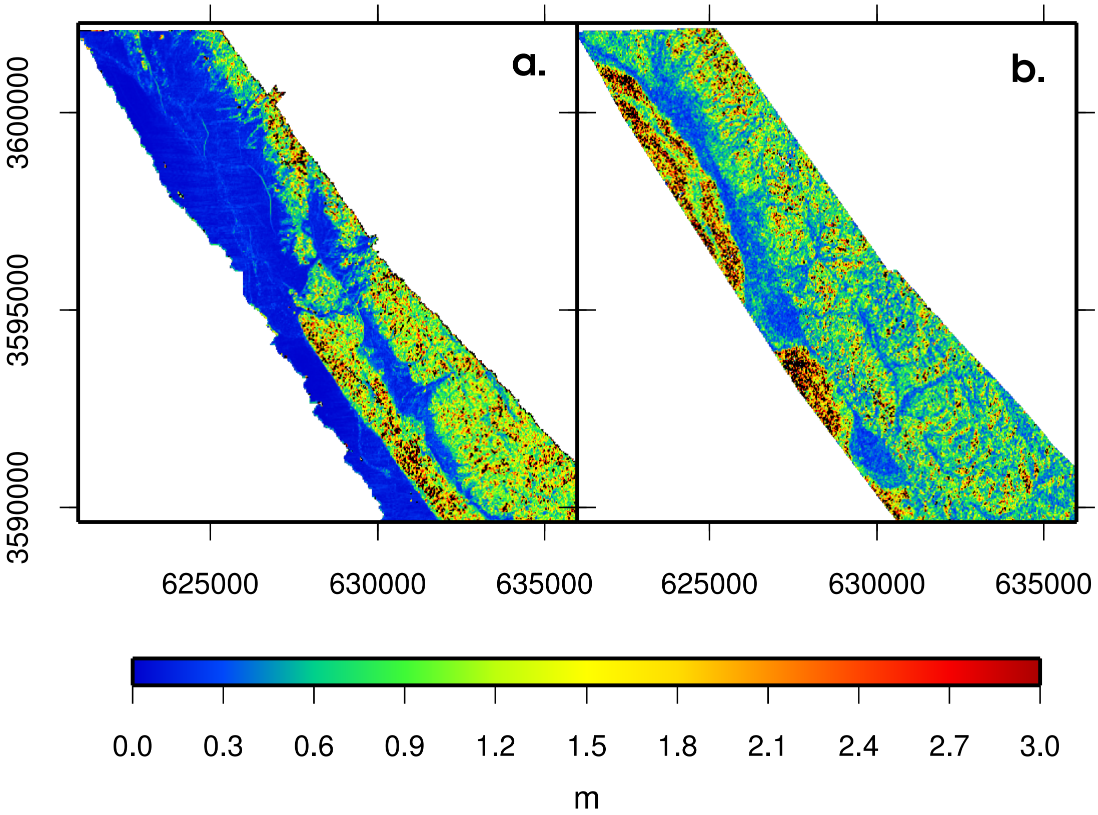

Figure 5.12: *(a)* RMS variability for 3x3 windows of vertical displacements obtained by differencing lidar DEM for that area of Figure 5.9. *(b)* RMS variability for 3x3 windows of vertical displacements obtained by approach introduced in this paper.

surements. Figure 5.12(*a*) shows the root mean square error (RMS) for 3x3 windows for the lidar differences with advection correction and Figure 5.12*(b)* shows the RMS for each 3x3 window using my method. The overall RMS of my approach is higher than the lidar diffrence for the areas with flat relief, however, it is more uniform across the whole scene.

5.5 How these finidngs fit in with the local tectonics

I have overlaid the traces of the active faults mapped by Fletcher & Spelz (2009) in the Sierra Cucapah range over the horizontal displacement map (Figure 5.13(*a*)) and new traces mapped by Fletcher et al. (2014) over the vertical displacement maps for the area of the post-seismic lidar DEM (Figure 5.13(*b*)). The horizontal displacements show clearly that, as the rupture propagated to the northwest from the epicentre (Wei et al., 2011; Uchide et al., 2013)), it jumped from the Pescadores fault to the Borrego fault through the Puerta Accommodation Zone (Figures 5.13(*a*) and 5.13(*b*)). Likewise, the discontinuity in the vertical displacement follows the Pescadores fault closely in the southeast (Figure 5.13) with a throw down to the northeast, and it can be followed as it crosses the Sierra Cucapah to join the Borrego fault around 32°27'N and 115°36'W. Although the signal is noisy, topographic profiles (Figure 5.14) show a small vertical offset to the order of 20-30 cm in many places at, or close to, the location of the rupture seen in the horizontal displacement fiels, as it crosses between the mapped faults. Thus I am able to detect relatively small vertical displacements in an area of rough topography, enabling the rupture to be characterised fully as it crosses the mountains. The sense of motion in the southeast of this area is down to the northeast. In the northwest of the area, where the topographic relief is low, the faulting is distributed across several branches and the vertical displacements on some of these branches switches to down to the southwest. However, the overall subsidence across the area is down to the north-east, in agreement with the sense of throw on the mapped faults across the Sierra Cucapah (Fletcher & Spelz, 2009).

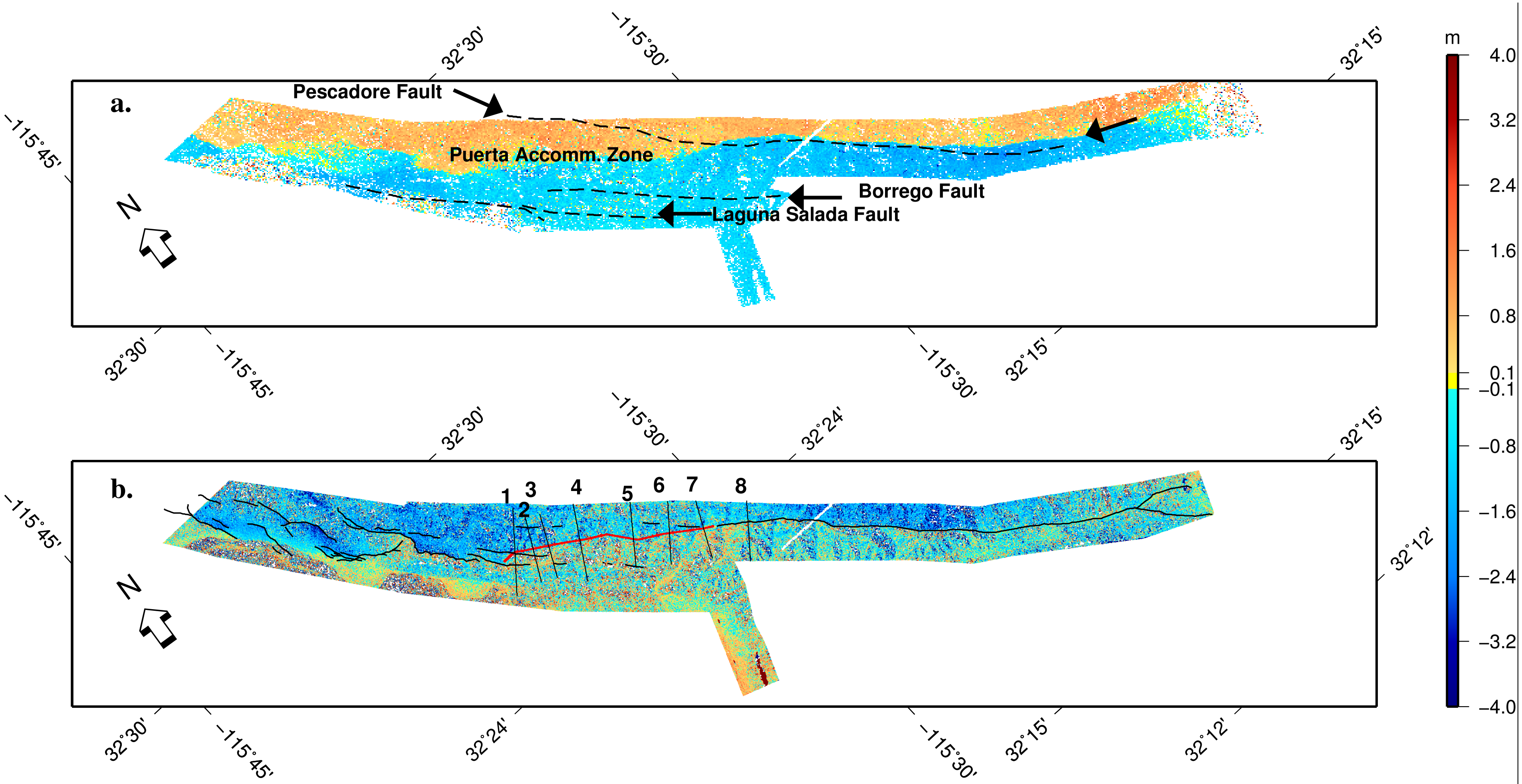

Figure 5.13: (*a*) E-W horizontal displacements. Black dashed lines show the faults mapped before the El Mayor-Cucapah earthquake by Fletcher & Spelz (2009) (downloaded from `http://response.scec.org/node/273` site in 2010). (*b*) Vertical displacements for the area of the post-seismic lidar DEM. Black thin solid lines show new fault traces mapped by Fletcher et al. (2014) after the earthquake. Red line shows fault trace obtained from the horizontal displacement map that crosses the Puerto Accommodation Zone. Numbered lines denote the location of the topographic profiles shown in Figure 5.14.

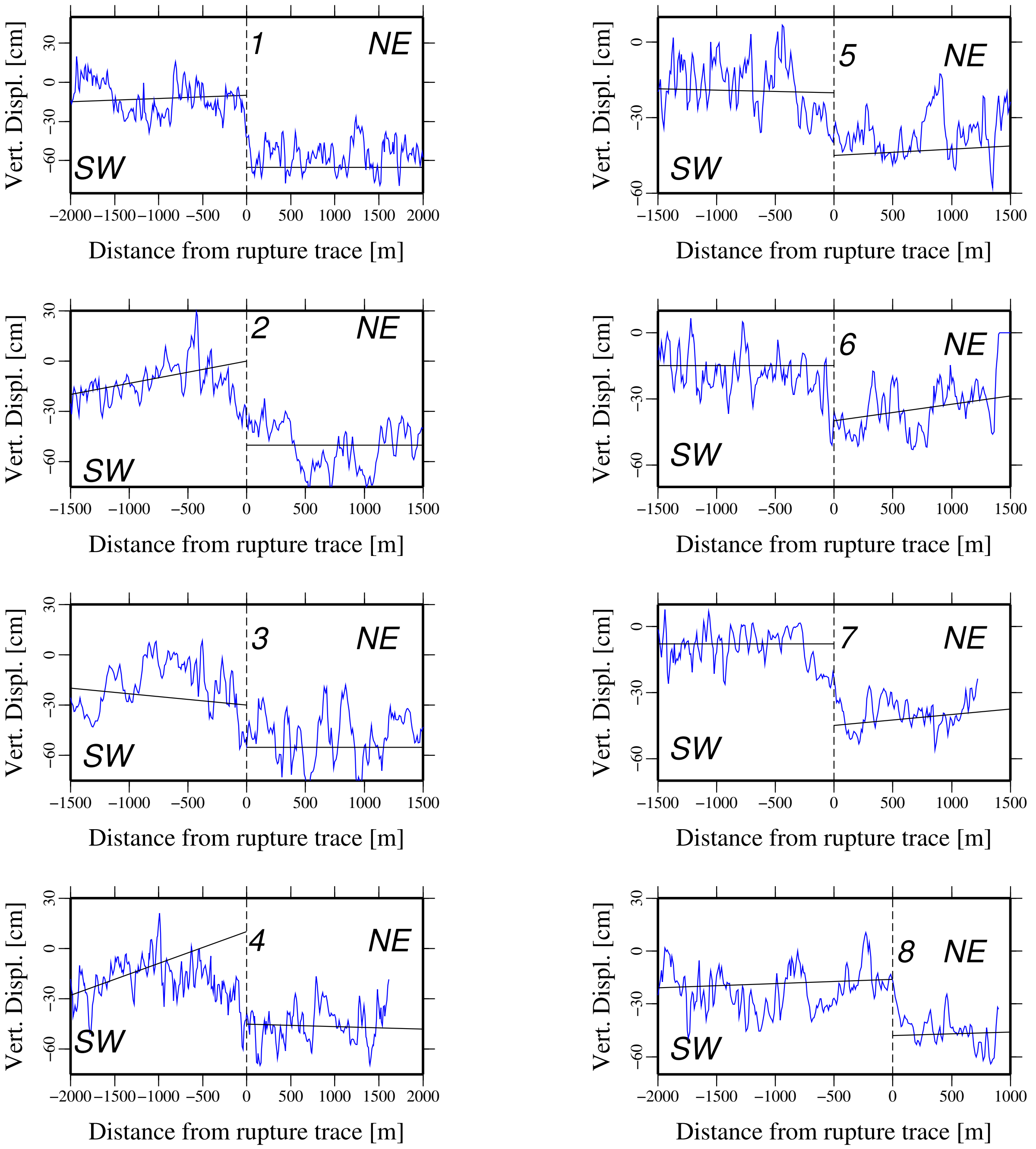

Figure 5.14: Topography along the profiles indicated in Figure 5.13. They have been aligned along the trace of rupture determined from the horizontal displacement map showing the location of the rupture as it goes through the mountains. The straight lines are the best-fitting lines of the topographic profiles on each side of the rupture trace. We used COSI-Corr Stacking Profile tool.

5.6 Conclusion

I have presented a geometrical principle showing how it is possible to determine post-event vertical displacements from one stereo-pair of images acquired before an earthquake and a precise DEM generated afterwards. I have then demonstrated this principle in the case of the 2010, M_w 7.2 El Mayor-Cucapah earthquake. The vertical displacements derived are in agreement with the vertical displacements obtained by differencing the pre- and the post-event DEMs. The same principle could be applied in the reverse order, for example if a very accurate and precise pre-event DEM exists, it can be coupled with a post-event stereo-pair in order to obtain the vertical displacements. I have also demonstrated that with only four satellite archived images and a Lidar DEM, I was able to estimate both horizontal and vertical displacements, and derive a DEM of the area. This technique provides a model of directly studying vertical displacements using satellite technology, caused by an earthquake or any other tectonic event in regions where a precise and accurate DEM may be available only post-event. Although I have used SPOT5 stereo imagery in this study, other higher-resolution images could equally well be used, such as Worldview or Pleiades.

Chapter 6

Slip distribution and fault geometry of the 04.04.2010 Mw7.2 El Mayor-Cucapah earthquake

Section 6.2 of this chapter is based on published paper from Barlow, J., Barisin I., Rosser N., Petley D., Densmore A., and Wright T. (2015), *Seismically-induced mass movements and volumetric fluxes resulting from the 2010 M w= 7.2 earthquake in the Sierra Cucapah, Mexico*, Geomorphology, Vol.230.

Section 6.2 of this chapter is also submitted by Zhou Y., Elliott J.,Prsons B., Barisin I., and Walker R., to Journal of Geophysical Research, 2015, *Assessing the ability of Pleiades stereo imagery to determine height changes in earthquakes: a case study for the El Mayor-Cucapah epicentral area.*

6.1 Theory background of earthquake source model

Physicaly earthquakes can be described as a shear dislocation propagating along a surface (i.e. plane) in an elastic medium (Steketee, 1958). After an initial shock that initiates the earthquake, the slip spreads across a fault plane. The pattern of the slip on the plane reveals the area that has ruptured, but more importantly, it reveals the areas that did not rupture, and that will pose an earthquake hazard in the future (Avouac et al., 2015). Earthquakes release elastic waves, which are studied from observations on the global network of the seismometers, or as a surface deformation with geodetic observations, which is the subject of this chapter.

Earthquakes are modelled as elastic dislocation on a fault plane split into a number of patches (Steketee, 1958). The model provides a relationship between 3D deformation on the surface and the slip on the patch. The displacement on the surface is the sum of a series of discrete sources on the fault plane. For the static case, i.e. when the evolution of the rupture in time is neglected, the displacement on the surface can be expressed as the sum of slips of each patch at depth (Equation 6.1, (Minson et al., 2013))

$$d(X) = \sum_{j=1}^{2} \sum_{k_1}^{n} U_j^k g_j^k(X) \tag{6.1}$$

where n_s are source locations, U is final slip in jth direction (for fault planes only two dimensions are used), at the kth source. g is a Green function dependant on displacements X.

Okada (1985) obtained analytical expressions for displacements, strains and tilts due to shear and tensile faults in an elastic half-space. He found that the magnitude of slip has a linear relationship with the surface deformation, but the relationship of the surface deformation with the geometry of the fault plate (strike, slip, rake, location, length, top and bottom depth) is not linear.

The relationship between the displacements and slips on the patch are linear and the expression Equation 6.1 can be rewritten in a matrix form:

$$\mathbf{d} = G(\mathbf{m})\mathbf{s} + \epsilon \tag{6.2}$$

where G($\mathbf{m}$) is a Green's function matrix (forward model), $\mathbf{m}$ is a vector of unknown parameters, $\mathbf{s}$ is a vector of slip distribution for all patches, $\mathbf{d}$ is a vector with the observations/measurements, and ϵ represents measurement uncertainty. Finite fault earthquake source inversion is an inherently undetermined problem, as there are more unknowns than there are surface observations, and there is no unique solution to the inverse problem.

Linear inversion of Equation 6.2 is all that is required to obtain the slip distribution from the geodetic observations. However, the relationship between the parameters **m** of the fault geometry and the displacements is not a linear one and the solution is obtained by minimising a function

$$\Phi(s) = ||\sqrt{\sum_{d}}(\mathbf{d} - G_d\mathbf{s})||^2 + \alpha^2||Ls||^2 \tag{6.3}$$

where $\sum_d$ is the data covariance, L is smoothing operator and α is the smoothing factor.

I invert the InSAR to infer fault geometry for the 2010 El Mayor-Cucapah earthquake. I use two inversion methods; the traditional well-conditioned optimised inversion that produces a single source model, and Bayesian sampling which returns a collection of solutions. Both methods have advantages and disadvantages but despite the fact that the Bayesian has much slower convergence, the results include the probability distribution for each parameter i.e. their error estimation is calculated together with results. Using the Bayesian approach I will attempt to show that it is possible to run joint inversion of InSAR and optical data on several fault planes in Chapter 6.

6.2 Source model obtained by numerical optimization method followed by linear least-squares approach

I modelled the 2010 El Mayor-Cucapah earthquake as a slip on a series of rectangular dislocations embedded in an elastic half-space (Okada, 1985). The position of the fault rupture can be located to within a few tens of metres from the optical sub-pixel matching data (e.g. Barišin et al., 2009). We found several changes in strike direction along the rupture for the portion of the fault within the study area. In the model I divided the rupture into four separate planar faults. The interferometric data were down-sampled using a quadtree algorithm (Jónsson et al., 2002) and a hybrid Monte Carlo downhill simplex algorithm (Wright et al., 1999). I inverted the data for the geometry and uniform slip on each of these four fault planes whilst keeping their surface intersections constant.

Table 6.1: Geometric fault parameters for four fault segments fixed from the sub-pixel matching and slip inversion

Parameter	Segment 1	Segment 2	Segment 3	Segment 4
Strike (°)	325	309	314	297
Dip (°)	66	66	66	70
Length (km)	14	17	12	10
Centroid lon (km)	622.68	633.70	644.90	653.89
Centroid lat (km)	3602.46	3591.06	3581.46	3575.03

Table 6.2: Model Parameters inferred for fault geometry of El Mayor-Cucapah earthquake using Wright et al. (2003)

Once the best-fit geometry had been found, I divided the fault planes into 2x2 km patches and solved for the best-fitting slip distribution (Wright et al., 2003). The fixed geometric parameters of the four segments can be viewed in Table 6.2. The distributed slip model shows a maximum fault slip of 6 m at shallow depth of 5 km at the south-east end of segment 4. The fault is right-lateral and predominantly strike-slip, with the maximum surface offset of 3 m in the central part of the rupture. The dip-slip component is dipping to the east at a dip angle of 66° and the maximum vertical offset of the surface inferred from the model is 2 m in the central zone of the rupture (Figure 6.1). The root mean square (RMS) misfit between the model predictions and InSAR data vary slightly for each dataset, but is in the range of 1.7 - 2.5 cm (Figure 6.2).

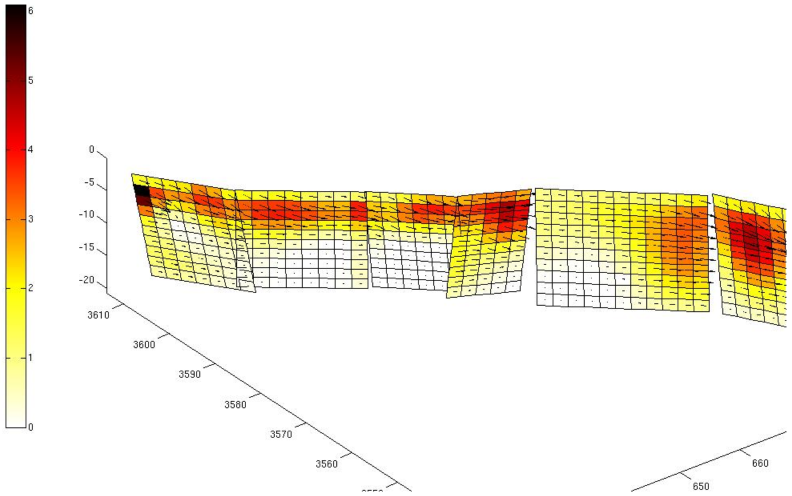

Figure 6.1: Distributed slip model obtained from the inversion of four interferograms - two decending and two ascending, using four fault planes, and ignoring the two at the south. View from south-west.

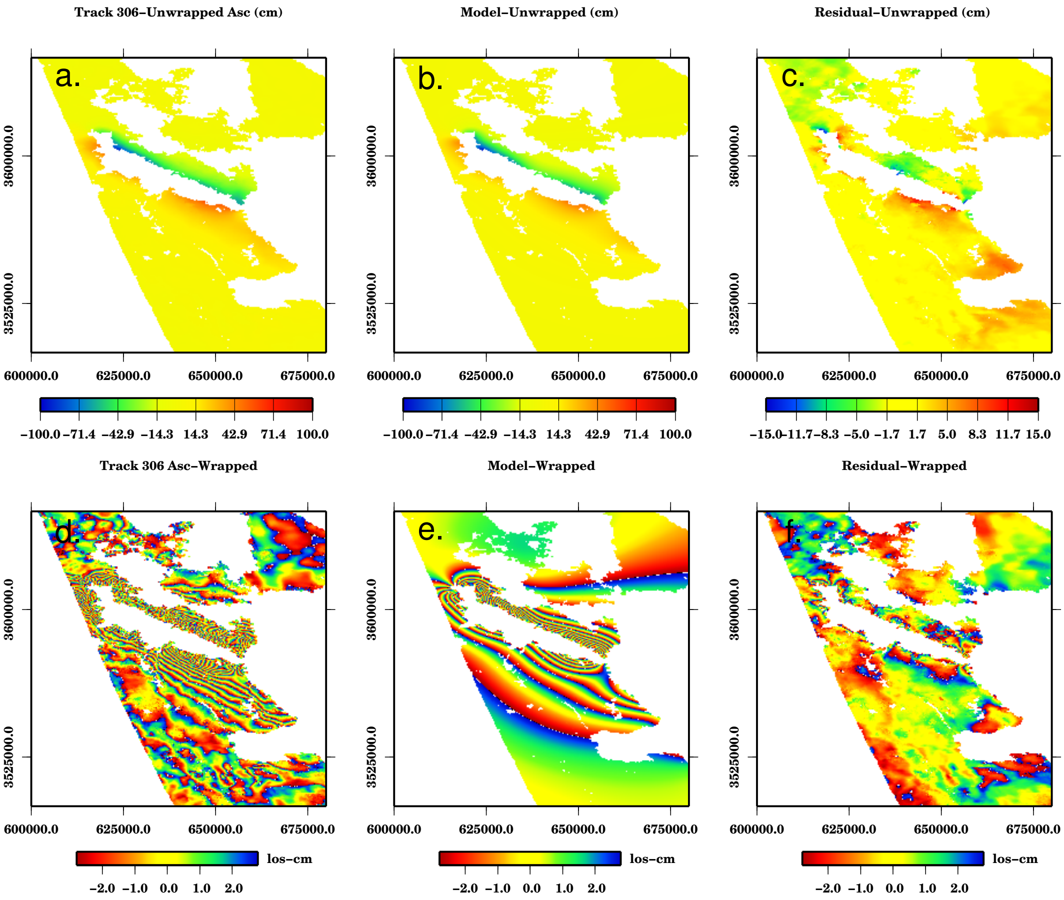

Figure 6.2: (a) Unwrapped co-seismic interferogram from ascending satellite Track 306. (b) Slip distributed model from all four interfereograms projected in unwrapped LOS of the Track 306. (c) Unwrapped residuals from Track 306 interferogram and the model in (b). (d) wrapped original interfereogram for Track 306. Each fringe represents half wave-length of deformation (2.8 cm) in the satellite LOS. (e) Distributed slip model projected in unwrapped LOS of the Track 306. (f) Wrapped residuals of InSAR dataset from the model for all four interfereograms.

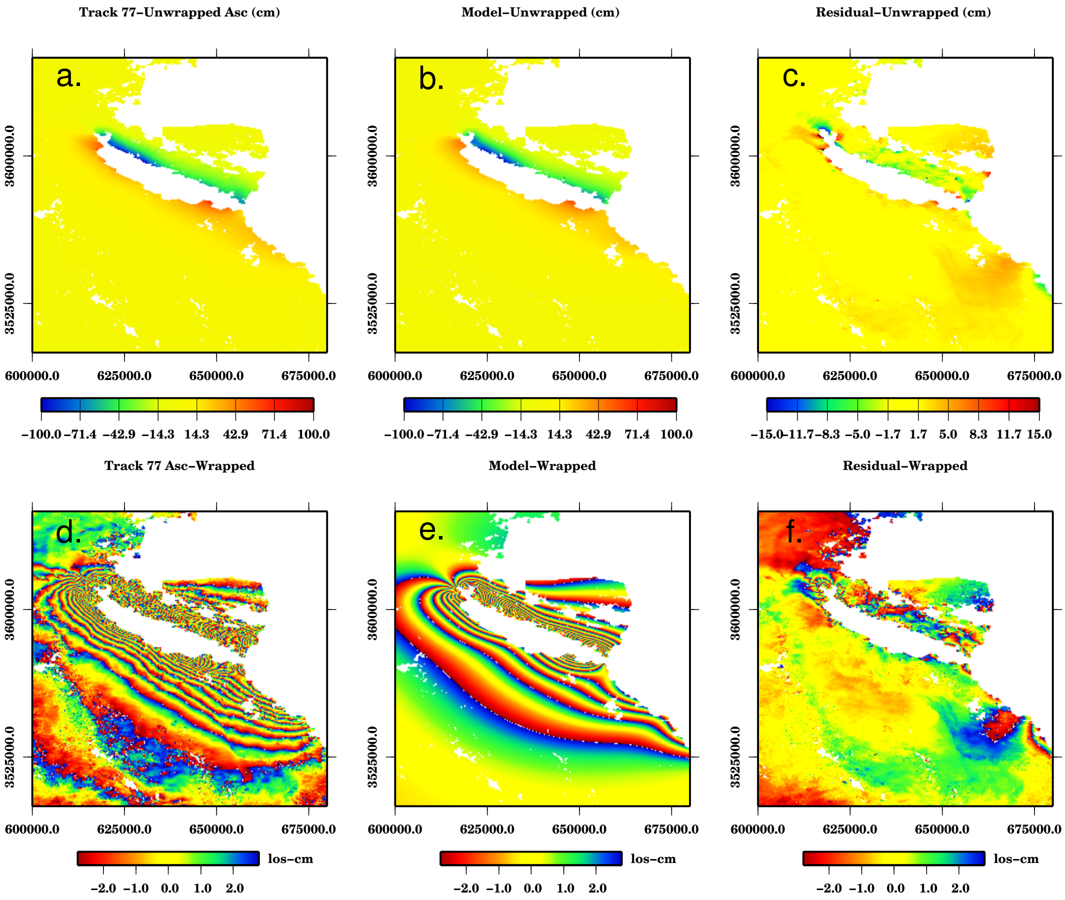

Figure 6.3: (*a*) Unwrapped co-seismic interferogram from ascending satellite Track 77. (*b*) Slip distributed model from all four interfereograms projected in unwrapped LOS of the Track 77. (*c*) Unwrapped residuals from Track 77 interferogram and the model in (*b*). (*d*) wrapped original interfereogram for Track 77. Each fringe represents half wave-length of deformation (2.8 cm) in the satellite LOS. (*e*) Distributed slip model projected in unwrapped LOS of the Track 77. (*f*) Wrapped residuals of InSAR dataset from the model for all four interfereograms.

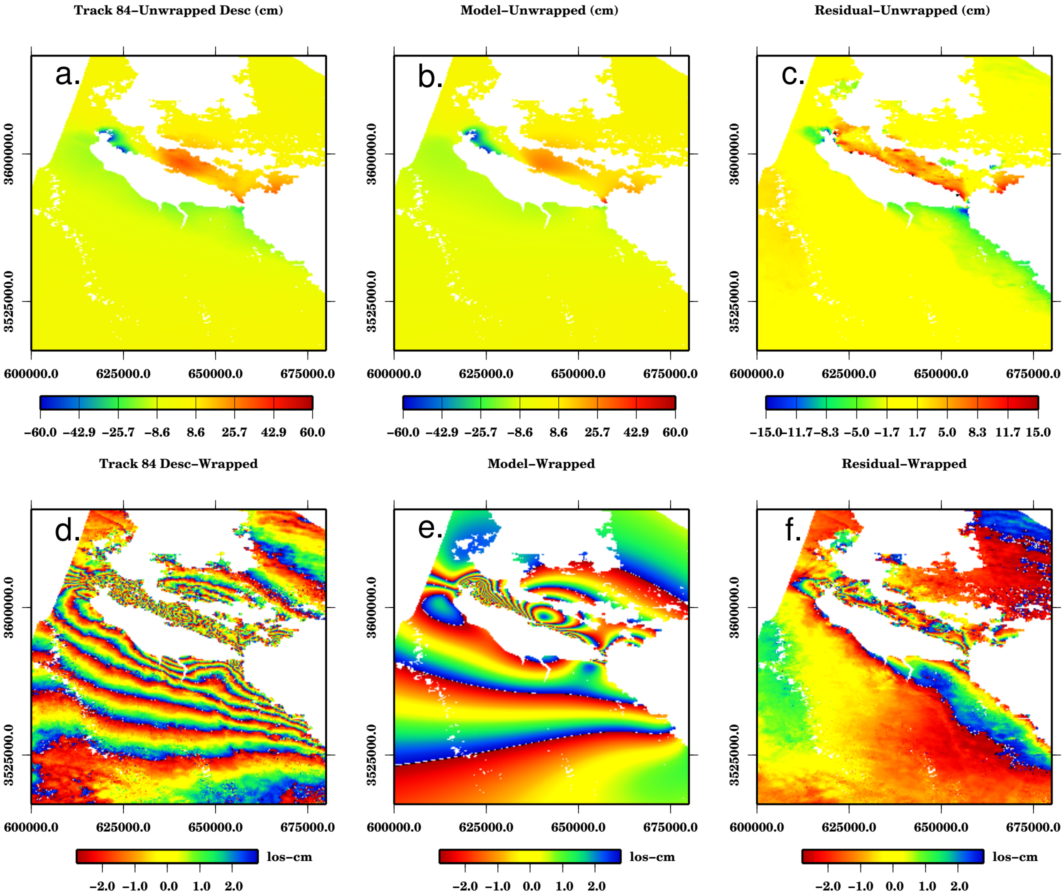

Figure 6.4: (*a*) Unwrapped co-seismic interferogram from ascending satellite Track 84. (*b*) Slip distributed model from all four interfereograms projected in unwrapped LOS of the Track 84. (*c*) Unwrapped residuals from Track 84 interferogram and the model in (*b*). (*d*) wrapped original interfereogram for Track 84. Each fringe represents half wave-length of deformation (2.8 cm) in the satellite LOS. (*e*) Distributed slip model projected in unwrapped LOS of the Track 84. (*f*) Wrapped residuals of InSAR dataset from the model for all four interfereograms.

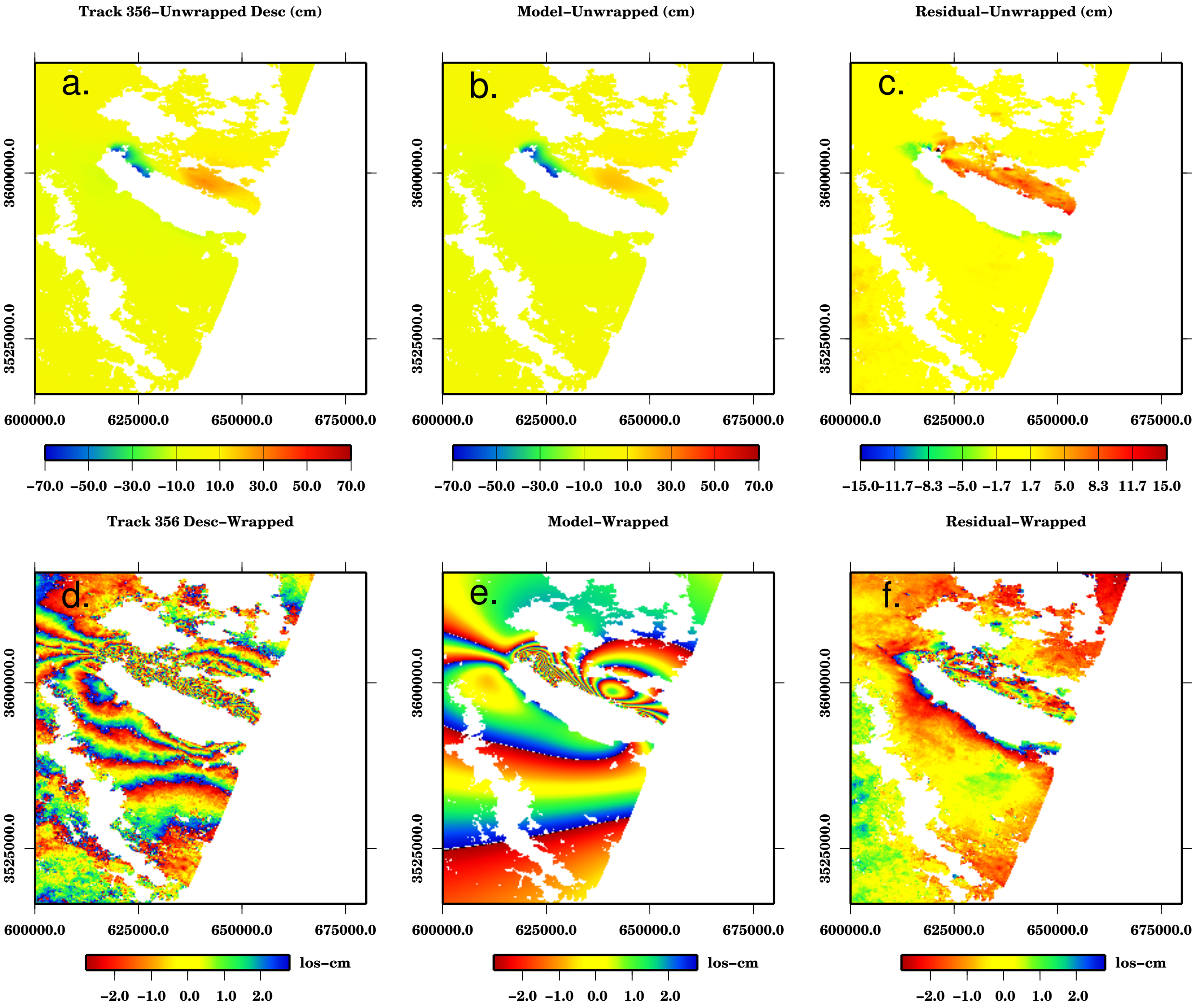

Figure 6.5: (*a*) Unwrapped co-seismic interferogram from ascending satellite Track 356. (*b*) Slip distributed model from all four interfereograms projected in unwrapped LOS of the Track 356. (*c*) Unwrapped residuals from Track 356 interferogram and the model in (*b*). (*d*) wrapped original interfereogram for Track 356. Each fringe represents half wave-length of deformation (2.8 cm) in the satellite LOS. (*e*) Distributed slip model projected in unwrapped LOS of the Track 356. (*f*) Wrapped residuals of InSAR dataset from the model for all four interfereograms.

6.3 Theory background on Bayesian formulation for solving earthquake source models

6.3.1 Why use Bayesian inversion for source models of earthquakes?

The most complete description of a finite fault aims to resolve the spatio-temporal slip on the fault, and a model that defines the relationship between the measurements and the spatio-temporal slip on the fault is called the earthquake source model. Optimisation methods (Press et al., 1990) used for solving the non-linear solution such as downhill simplex method (Clarke et al., 1997), (Wright et al., 1999), quasi-Newton method (Williams et al., 1993) or Powell's conjugate gradient descent method (Wright et al., 2003) are used to obtain the geometrical parameters of the fault planes for uniform slip which is then followed by standardised linear inversion for the spatial distribution of slip on fault planes. However, Sun et al. (2008) find that uniform-slip assumption can bias the fault geometry solution.

Many earthquakes that have been modelled in the past often have more than one solutions of the source model and the results of the source models vary widely; see for example the 1992 Landers earthquake (Figure 6.6). The modelling differs in the type of techniques and datasets available, but it is important to note that all the models fit the observation data equally well and it is unclear which solution is the relaistic one (Cohee & Beroza, 1994; Wald & Heaton, 1994; Cotton & Campillo, 1995; Hernandez et al., 1999).

The Bayesian inversion produces a fully probabilistic solution of each unknown model parameter and creates an ensemble of solutions rather than just one. There is no need for complex inversion algorithms, which can introduce non-physical assumptions to the solution. Because the forward models are used only, there is no need for matrix inversions apart from the inversion of covariance matrices at the beginning. The approach is very intuitive and physical properties of the datasets can be used to constrain the results of the solution. However, the main application is when inverting for many different datasets in joint inversions where some intuitive decisions can be made in order to influence the final

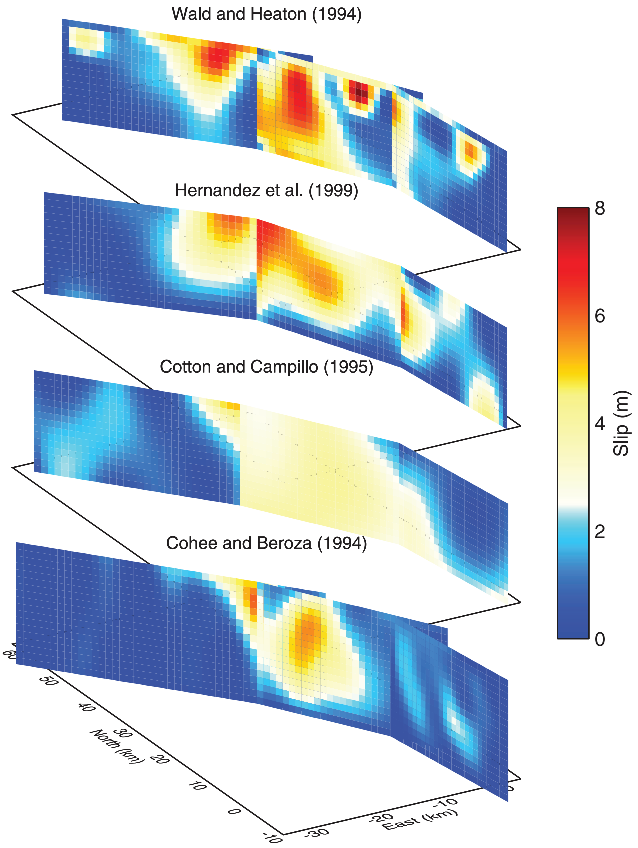

Figure 6.6: Four solutions for the 1992 M_w 7.3 Landers earthquake. Reproduced from Minson et al. (2013)

result. And finally, the Bayesian approach solves for model uncertainties, whereas the model uncertainties for optimization models are obtained by running inconvenient tests of resolutions (Minson et al., 2013).

6.3.2 Bayesian approach

The Bayesian solution is based on Bayes' theorem (Bayes & Price, 1763) (Equation 6.4),

$$p(\mathbf{m}|\mathbf{d}) = \frac{p(\mathbf{d}|\mathbf{m})p(\mathbf{m})}{p(\mathbf{d})} \tag{6.4}$$

which states that the posterior probability density function (PDF) p($\mathbf{m}|\mathbf{d}$) is proportional to the prior PDF p($\mathbf{m}$) on model parameters and to the data likelihood p($\mathbf{d}|\mathbf{m}$) (Equation 6.4). Term p($\mathbf{m}$) means the probability of model parameters and this is referred to as a prior. Terms p($\mathbf{d}|\mathbf{m}$) and p($\mathbf{m}|\mathbf{d}$) are used to express conditional probability, so the likelihood function represents conditional probability (i.e. how likely) that data ($\mathbf{d}$)

will occur given unknown model parameters ($\mathbf{m}$), and the posterior PDF represents conditional probability of a set of model parameters $\mathbf{m}$ occurring, given a set of observations $\mathbf{d}$, which is the joint probability of data $\mathbf{d}$ and unknown model parameters $\mathbf{m}$.

A Bayesian analysis synthesises two sources of information about the unknown parameters of interest: sample data expressed formally by the likelihood function, and additional information in the form of the prior distribution. Prior distribution helps to strengthen the values of the parameters, it will reduce computational time if some physical boundaries are known and can be introduced a priori, and priors can be introduced based on the physics of the problem, which may not be part of the forward model.

Jackson (1979) started using prior information about model parameters in linear inversions, and it was later adapted for non-linear cases using probability theory (Tarantola & Valette, 1982; Matsu'ura & Hasegawa, 1987). Initially, Bayesian interference in earthquakes' source studies have been used for the seismic studies, but recently there has been some studies that have recognised the convenience of the method for joint inversions of seismic and crustal observations (e.g. Yokota et al., 2011).

6.3.3 Bayesian formulation

Likelihood function

Likelihood function p($\mathbf{d}|\mathbf{s}$, $\mathbf{m}$) measures a fit between the model predictions ($\mathbf{m}$) and slip on the fault $\mathbf{s}$ with observed data ($\mathbf{s}$) and can also be viewed as a function that connects model and observed data. Assuming that the errors are described with Gaussian probability distribution with zero-mean, the likelihood function for one dataset can be written as Equation 6.5.

$$p(\mathbf{d}|\mathbf{s},\mathbf{m}) = \mathcal{N}(\mathbf{d}|G(\mathbf{m}),\Sigma_d) = \frac{1}{\sqrt{(2\pi)|\Sigma_d|}} e^{-\frac{1}{2}([\mathbf{d}-G(\mathbf{m})\mathbf{s}]^T\Sigma_d^{-1}[\mathbf{d}-G(\mathbf{m})\mathbf{s}])} \tag{6.5}$$

where Σ_d is variance-covariance matrix of a particular data set and G($\mathbf{m}$) is a forward model from (Equation 6.2), $\mathbf{d}$ is observation vector and $\mathcal{N}$ is a symbol for normal distribution. The exponential part of the Equation 6.5 is a least-square misfit function, which is minimised in the optimization solutions (Duputel et al., 2014).

For the study with a joint distribution (optical and InSAR datasets in this case) the expression for the likelihood function is a product of the likelihood functions for each independent data set (Equation 6.6).

$$p(\mathbf{d}_1, \mathbf{d}_2, ...\mathbf{d}_n|\mathbf{m}) = p(\mathbf{d}_1|m)p(d_2|m)...p(\mathbf{d}_n|\mathbf{m}) = \prod_{i=1}^{n} p(\mathbf{d}_i|\mathbf{m}) \tag{6.6}$$

where n is the number of the datasets.

It is assumed that the errors stem only from the observations, and the uncertainties in the forward model itself are ignored, although the likelihood would depend on errors that come from imperfect modelling (crustal properties). Recently investigators (Beck & Katafygiotis, 1998; Duputel et al., 2014; Minson et al., 2013, 2014) have tried to estimate the model errors using the Bayesian approach to find out the impact on earthquake source models. A Bayesian approach to inversion of earthquake source mechanisms yields a full non-linear inversion for the simultaneous estimation of fault geometry parameters, distribution of slip on faults, smoothing parameter, and orbital ramps, and all this without simplifying the formulation of the physical/forward model and without a priori knowledge about the fault geometry (Decriem et al., 2010).

6.3.4 Choice of a priori distribution

A priori information p(**m**) allows introducing the information of the physics of the problem that will constrain the model estimates and help reduce, already very expensive, computational time. The prior probability density function on model parameters can be of any form. For the a priori distribution any distribution function can be chosen based on the knowledge about the specific parameter.

If only lower and upper bounds of a parameter are known then the uniform prior PDF is assigned (Equation 6.7).

$$\begin{cases} \dfrac{1}{m_{max} - m_{min}} & \text{for} \quad m_{min} < m < m_{max} \\ 0 & \text{otherwise} \end{cases} \tag{6.7}$$

The prior information for earthquake source modelling is available from several different sources. From seismological observations, it is possible to obtain some prior information about the extent of a faulting region, the average magnitude and direction of slip vectors. This sort of prior information can be treated in the same way as observed data, since the degree of its uncertainty is fairly definite. Another sort of prior information comes from physical consideration for earthquake rupture such as the spatial variation of fault slip must be smooth to some degree because of the finiteness in the fracture strength of actual rocks. In the classical inversion methods, this sort of prior information has been used in an implicit way to judge whether or not the inverted result is physically reasonable.

Using Bayesian inference, the parameters such as strike, dip, slip, and location are expressed in terms of posterior density functions. Specifically, I choose uniform distributions to constrain the rake, slip and dip parameters and I set the boundaries broad enough to encompass all plausible values. I constrain the dip to vary from 40 to 120 degrees, the rake to vary from 0 - 360 and slip to reach the maximum value of 100 m. I also constrain the slip to be always positive as this knowledge is based on the physics of the problem.

Some authors (Fukuda & Johnson, 2008) use smoothing of distributed slip to reduce (unrealistic) rough slip distribution (Equation 6.8). This information acts as the prior information. Others consider the smoothing as a constraint on the model design and argue that this is a non-physical property and it makes it difficult to interpret the inversion results (Minson et al., 2013, 2014).

In calculating the posterior distribution I have included this option of being able to calculate the smoothing according to Fukuda & Johnson (2008) who derived this prior distribution based on the Laplace's expression (Equation 6.8).

$$Ls = \delta = ||Ls||^2 \tag{6.8}$$

where L is Laplacian operator and δ is an M dimensional vector that determines the smoothness of the slip distribution. The finite difference approximation of the Laplacian operator L acts as a smoothing operator and is added to the physical model (Equation 6.8). Fukuda & Johnson (2008) assumed that δ follows a Gaussian distribution of 0 mean and covariance matrix $\alpha^2\mathbb{I}$, i.e. $\delta \approx \mathcal{N}(0, (\alpha)^2\mathbb{I})$, where $\mathbb{I}$ is an identity matrix and α^2 is a scale factor that determines the magnitude of δ. So the prior PDF of $\mathbf{s}$ given α^2 is expressed as $\mathcal{N}(0, \alpha^2(L^T L))$ (Equation 6.9)

$$p(\mathbf{s}|\alpha^2) = (2\pi\alpha^2)^{-\frac{M}{2}}\sqrt{|L^T L|}e^{[-\frac{1}{2\alpha^2}(L\mathbf{s})^T(L\mathbf{s})]} \tag{6.9}$$

The scalar factor α determines the relative weight of the smoothing and it defines the trade-off between magnitude of smoothing and the model fitness to the data, which is always a challenge when done by eye. However, by using the Bayesian approach α is treated as any other unknown parameter and the optimum solution is expressed as a posterior PDF. When there are many parameters with a priori knowledge then the total a priori knowledge distribution is obtained as a multiple of all the individual a priori distributions

$$p(m) = \prod p(m_i) = \mathcal{U}(\mathrm{dip}_{min}, \mathrm{dip}_{max})\mathcal{U}(\mathrm{rake}_{min}, \mathrm{rake}_{max})\mathcal{U}(0, \mathrm{slip}_{max}))\mathcal{N}(0, \alpha^2(\mathbf{L}^T\mathbf{L}^{-1}))\mathcal{U}(0, \alpha_{max}) \tag{6.10}$$

where i is a number of a priori PDFs, $\mathcal{U}$ denotes uniform distribution and $\mathcal{N}$ denotes a Gaussian distribution.

Minson et al. (2013) used the information from the seismic moment tensor because it reveals the average rake and the total amount of slip summed over all fault patches to form a priori PDF. This a priori PDF should be added to the code in future work in order to further improve the convergence and further constrain the model solution.

6.3.5 A posteriori

A posteriori PDF is a solution to the inverse problem and is calculated as a product of the likelihood function and a priori PDF - both discussed in above two sections. The solution for each unknown parameter is expressed as a PDF. Bayes theorem (Equation 6.4) with the actual unknown paramaters can be expressed more explicitly for our specific case (Fukuda & Johnson, 2008) (Equation 6.11).

$$p(\mathbf{s}, \alpha^2) \propto p(\mathbf{d}|\mathbf{s}, \alpha^2)p(\mathbf{s}|\alpha^2) \tag{6.11}$$

Substituting the solutions for the likelihood function (Equation 6.5) and the total a priori PDF (Equation 6.10) in Equation 6.11, the expression for a posterior PDF for one dataset is:

$$p(\mathbf{s},\alpha^2|\mathbf{d}) = \begin{cases} (\alpha^2)^{-\frac{M}{2}} e^{[-\frac{1}{2}(\mathbf{d}-\mathbf{Gs})^T\Sigma_d^{-1}(\mathbf{d}-\mathbf{Gs})+\frac{1}{\alpha^2}(\mathbf{Ls})^T(\mathbf{Ls})]} \\ \quad\text{for} \quad \mathbf{s}>0, \alpha^2>0 \\ \quad 0 \quad \text{otherwise} \end{cases} \tag{6.12}$$

and inserting the Equation 6.12 into the Equation 6.6 we obtain a posterior PDF for multiple data sets with smoothing.

$$p(\mathbf{s},\alpha^2|\mathbf{d}_1,\mathbf{d}_2,...\mathbf{d}_n) = \begin{cases} \prod_{k=1}^{n}\left\{(\alpha^2)^{-\frac{M}{2}} e^{\left[-\frac{1}{2}(\mathbf{d}_k-\mathbf{G}_k\mathbf{s})^T\Sigma_k^{-1}(\mathbf{d}_k-\mathbf{G}_k\mathbf{s})+\frac{1}{\alpha^2}(\mathbf{Ls})^T(\mathbf{Ls})\right]}\right\} \\ \quad\text{for} \quad \mathbf{s}>0, \alpha^2>0 \\ \quad 0 \text{ otherwise} \end{cases} \tag{6.13}$$

In order to avoid values close to zero when calculating the exponential expression in Equation 6.12 and Equation 6.13, this expression is converted into a logarithmic form (Equation 6.14)

$$p(\mathbf{s},\alpha^2|\mathbf{d}_1,\mathbf{d}_2,...\mathbf{d}_n) = -Mlog(\alpha) - \frac{1}{2}\sum_{i=1}^{n}(\mathbf{G}_i\mathbf{s}-\mathbf{d}_i)^T\Sigma_i(\mathbf{G}_i\mathbf{s}-\mathbf{d}_i) - \frac{\mathbf{Ls}}{2\alpha} \tag{6.14}$$

However, in systems with many unknown parameters, randomly generating samples of the posterior distribution is not feasible. Instead of going through all the possible random combinations a Markov Chain Monte Carlo (MCMC) approach offers a more efficient way to generate samples from the joint posterior distribution.

6.3.6 MCMC

A Monte Carlo Markov Chain (MCMC) sampling algorithm is used to estimate discrete a posteriori PDF (the integral of the area underneath a PDF curve equals 1). Monte Carlo algorithms are based on the Law of Large Numbers which states that $E(x)->E(x')$

as $n- > \infty$ where E(x) is the expected random value and E(x') is the target value, and n is number of simulations. A Detailed description of the theory of convergence of random numbers is given in Meyn & Tweedie (1993). The Markov Chain method produces a chain of random variables, with a property which states that the current probability distribution depends only on the probability distribution of the current state, and not on any probability distribution of any previous states (e.g. MacKay, 1998; Fukuda & Johnson, 2008) (Equation 6.15):

$$p(m_5|m_1, m_2, m_3, m_4) = p(m_1|m_4) \tag{6.15}$$

where $m_1, m_2, ...m_4$ are the previous states of the parameter samples and m_5 is the current state of the parameter sample. The Metropolis algorithm is one of the MCMC's most popular algorithms (Metropolis & Ulam, 1949; Metropolis et al., 1953). The collection of samples that is used to represent each unknown parameter as the posterior probability distribution will depend on the Metropolis rule. MCMC represents a class of sampling algorithms where random mathematical process undergoes transition from one state to another and it produces a chain of random variables.

It starts with initial unknown parameter estimates and it generates a new set of random samples at the next iteration by randomly perturbing the initial parameters or proposal probability density. The Metropolis algorithm determines the next random sample in four steps (Minson et al., 2013) using a chosen proposal distribution $q(m_i|m_old)$. Given a large number of samples, the chain will converge to its stationary distribution (also called an equilibrium distribution), which represents a steady state in the chain's behaviour.

The new states are determined by transition probability $P(x(t)|x(t-1))$, where $x(t-1)$ is the previous state and x(t) is the current state, i.e. the probability of the proposal state is compared with the probability of the current state. If the current state has higher probability than the previous state, the new state is accepted. If the state has lower probability then acceptance probability is calculated and if the current state satisfies certain conditions the current state is accepted, otherwise the previous state becomes the current state. The chain will converge to the probability density p(x) independent of the initial starting value x_0 (Gamerman & Lopes, 2006; MacKay, 1998).

Algorithm for running MCMC

- Initialize the unknown parameters.
- Set the parameter counter
- Generate the candidate state by varying the parameters
- If $\sigma^2 \leq 0$ then reject the candidate state and remain on the current state. Increse the counter for one.
- Compute an acceptance probability $P_{\text{accept}} = min(1, \frac{p(x|d)}{p(x'|d)})$
- Generate a random number u from the interval $[0, 1]$ of the uniform distribution.
- If $u \leq P_{\text{accept}}$ then accept the candidate state. if $u > P_{\text{accept}}$ then reject candidate state and remain at the current state.
- Increase the parameter counter j = j+1. If j is less than the number of parameters then return to the step 3. Otherwise return to the step 2 and increase sample counter.

However, a full Bayesian solution to an inverse problem using only prior constraints based on the physics of the process being modelled can be very computationally expensive, especially for high-dimensional problems like seismic rupture models. However, as computer power is constantly increasing this method is gaining more and more interest, and new sampling algorithms have been devised in order to take advantage of parallel processing techniques (Minson et al., 2013).

6.3.7 Results of Bayesian inversion

I have adapted the Bayesian inversion code based on the formulation given in Fukuda & Johnson (2008). I have further changed it so the code can jointly solve the inversion for any number of horizontal displacement datasets and InSAR datasets - instead of only one ascending and one descending InSAR dataset, I can simultaneously find solutiona for any number of fault planes. I have also added the capability to solve for linear tilt parameters for each datasets.

I run several test inversions and I compared them with existing models to show that the code is producing reliable earthquake source models, although the best indicator of model goodness is its fit to the data. As an example I use two InSAR tracks (Track 77 and Track 84) and run it with seven fault planes.The intention is to run all four InSAR datasets independently from the sub-pixel optical datasets and compare their results.

Variance-covariance matrix

The noise structures in observations are quantified with a variance-covariance matrix. A Covariance function is a measure of how much two observations are similar i.e observations that are spatially closer are more likely to be similar. Estimation of covariance functions can be obtain through calculating the structure function (Tatarski, 1961). A structure function provides insight into the noise structure and spatial dependences present in the observations and therefore it is used in studies which describe atmospheric turbulences in InSAR observations (e.g. Zebker et al., 1997; Hanssen, 2001; Lohman & Simons, 2005). However, it is often assumed that the system is a second-order stationary process (Hanssen, 2001) and measurements are homogeneous and isotropic i.e. the spatial structures are consistent in all directions. In such a simplified case Equation 6.16 represents structure function which depends only on the scalar distance r between observations.

$$2\gamma(r) = \frac{1}{N(r)} \sum_{N(h)} [z(u) - z(u+r)]^2 \tag{6.16}$$

A semi-variogram is a plot of a semi-variance function i.e. it relates semivariance to sampling lag and it quantifies spatial correlation. The shape of theorethical semi-variogram models, is characterised by three parameters. The range is related to the size of the noise structures in the measurements and is a distance at which the measurements are no longer correlated, the nugget effect refers to the variability of the data that can not be explained by distance between the observations (distances smaller than the shortest sampling interval) and it represents the measurement error or a variance at the random field, and the sill is a variance of the data. Fitting a model semi-variogram through empirical semi-variogram is done heuristically, and a range of functions are used in practice. The most common are exponential, spherical, linear, and Gaussian. The relation between

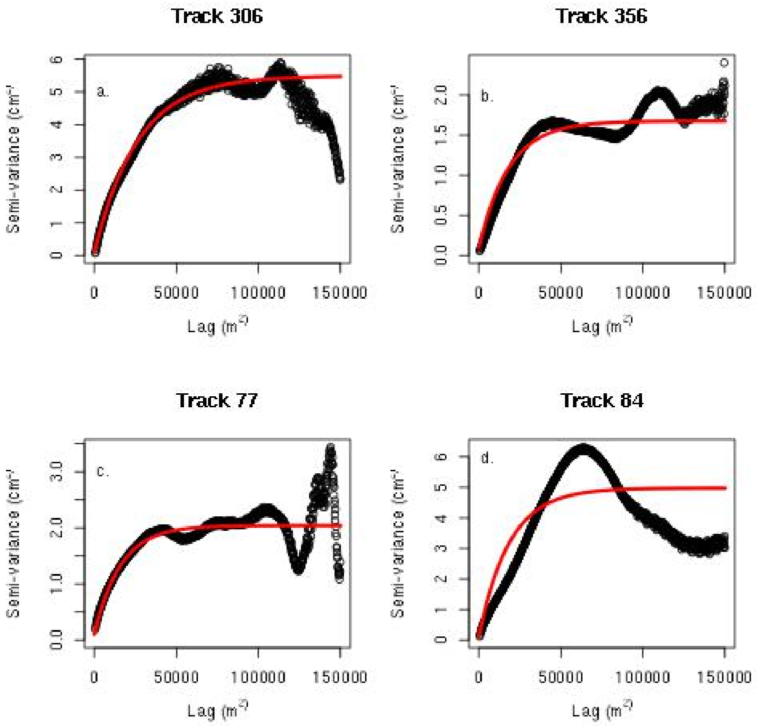

Figure 6.7: Semivariograms for four InSAR datasets.

structure function and covariance function is expressed as in Equation 6.17 (Lohman & Simons, 2005)

$$C(r) = C(0) - \gamma(r)/2 = \sigma^2 - \gamma(r)/2 \tag{6.17}$$

In practice the area used for estimation of the empirical semi-variogram does not contain tectonic signal of interest and it is detrended before the analysis is performed. I use freely available "R" package (R Core Team, 2013) to obtain empirical semi-variograms and to model the theoretical semivariance function. All my semi-variograms models use the simplest form of exponential function as that is the function commonly used as the first approximation. The far-field area is downsampled from 80 m to 200 m so as to make the computation time viable.

Semivariograms for Track 84 and Track 77 have a curve fit which does not level off suggesting that there still may be some systematic tilt left with the data. However, on the closer inspection, this was an indicator that there was a quadratic phase ramp present in both datasets.

This is a very simple semi-variogram analysis and modelling of the semi-variogram,

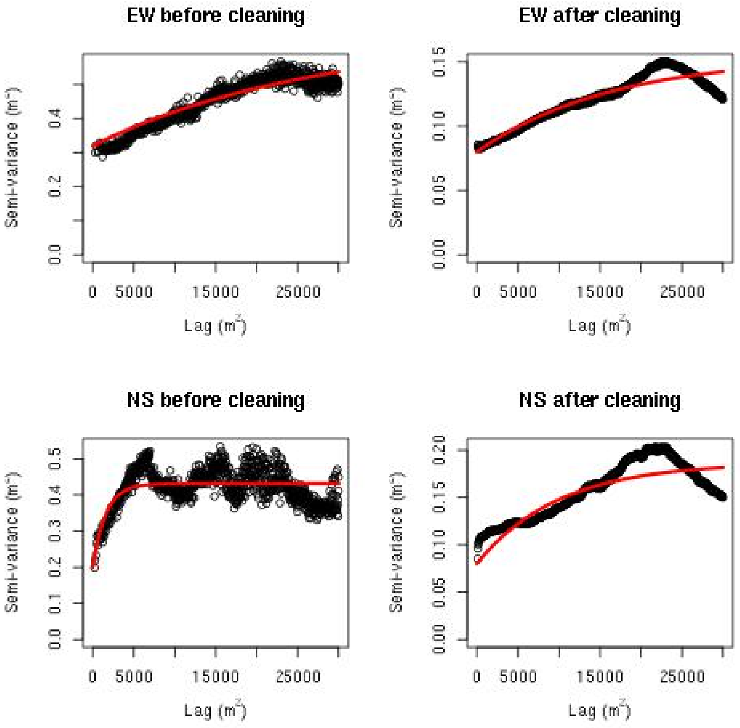

Figure 6.8: Empirical semivariogram data and modelled semivariograms (red lines) for the E-W and N-S displacement maps before and after cleaning the data (see Chapter 4) of mathcing pair K.

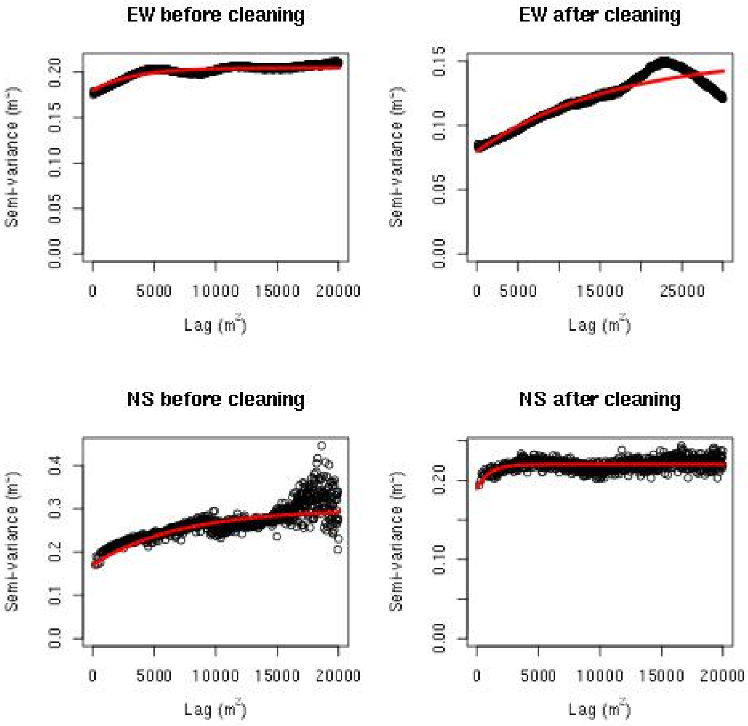

Figure 6.9: Empirical semivariogram data and modelled semivariograms (red lines) of the E-W and N-S displacement maps before and after cleaning the data (see Chapter 4) of matching pair A1.

with assumption of the stationarity, homogenity and isotropy. However, more in depth studies of the semi-variagrams can reveal spatial structures which can have properties of periodicity, anisotropy or zonal anisotropy (Knospe & Jonsson, 2010).

Bayesian inversion with two InSAR datasets and seven planes

I test my Bayesian inversion code by running one ascending (track 77) and one descending (track 356) interferogram. I define the geometry of the earthquake from the surface displacements obtained by optical matching. I split the fault into seven segments with the same depth of 12 km. Unlike the conventional optimization inversion methods where one of the unknown parameters in the inversion is the depth of the fault. Bayesian inversion simply defines the fault deep enough so that slip can be accomodated and the rest of the patches are simply left empty. Data used in Bayesian inversions are sampled points derived using a quadtree algorithm (e.g. Jónsson et al., 2002) and shown in Figure 6.10.

Model shown in Figure 6.11 is only one of the solutions from the inversion. This model shown here is constructed from the values of the mean posterior PDF.

Models obtained by the Bayesian approach and the approach in Section 6.2 are very compatible, which gives me confidence that the Bayesian code is operational. The slip distribution is fairly uniformly spread across the shallow depths of 10-12 km in agreement with Wei et al. (2011). Here in the text I refer to the first fault plane as the most northerly one and the seventh fault plane is the most southerly. The peak slip (7 m) is located on the third plane. An area between fault planes four and five - the zone of the earthquake's epicentre, does not have very high peak (max. slip of 5 m) but it is characterised with a large slip patch. It is not clear what is creating an anomalous strong signal in the most southern corner of the fault plane seven, as there are few InSAR observations in that region to constrain the inversion. What is interesting from this result is that it is possible to learn about variations of the dip on faults' planes as the earthquake propagates. I choose to use seven planes, which is a challenge to implement with the method described in Section 6.2. With Bayesian inversion their dip values have been determined simultaneously with other parameters. I observe that the first fault plane is around 70 °, but the second, third, and the fourth planes are fairly shallow and their values range between 55 °and 63 °. The fifth

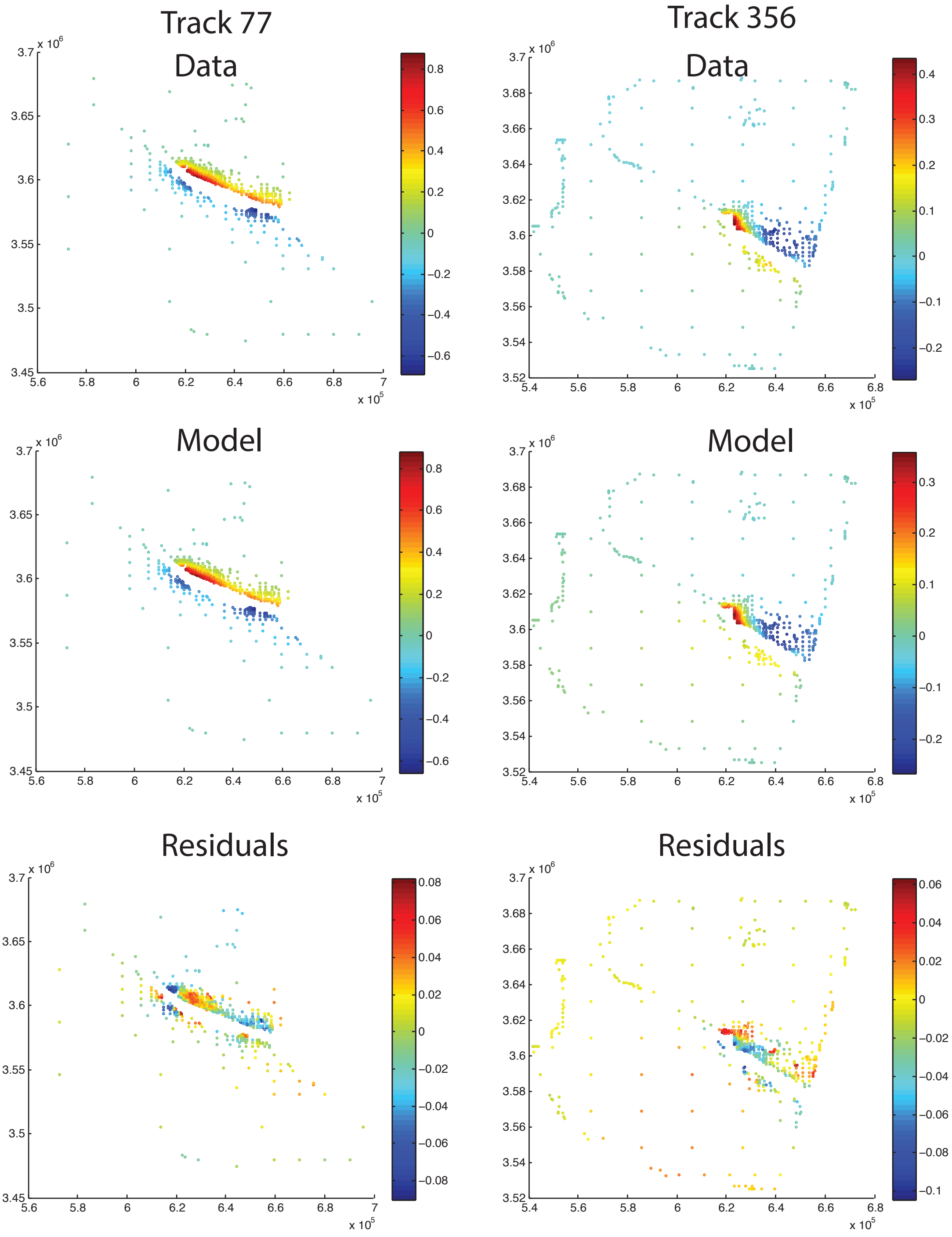

Figure 6.10: I show data format for the track 77 and track 356 used in Bayesian inversion followed by the model, and then followed by the map of their differences.

and the sixth fault plane are becoming steeper and they have similar values of around 70 °as the first fault plane. It is now possible to study the gradual variation of dip on the fault planes at depth. Geometry derived by Wei et al. (2011) had only one fault plane in the northern segment, and the dip of that plane is an average value of many faults.

Although the InSAR data that I use here can not constrain the deformation in the

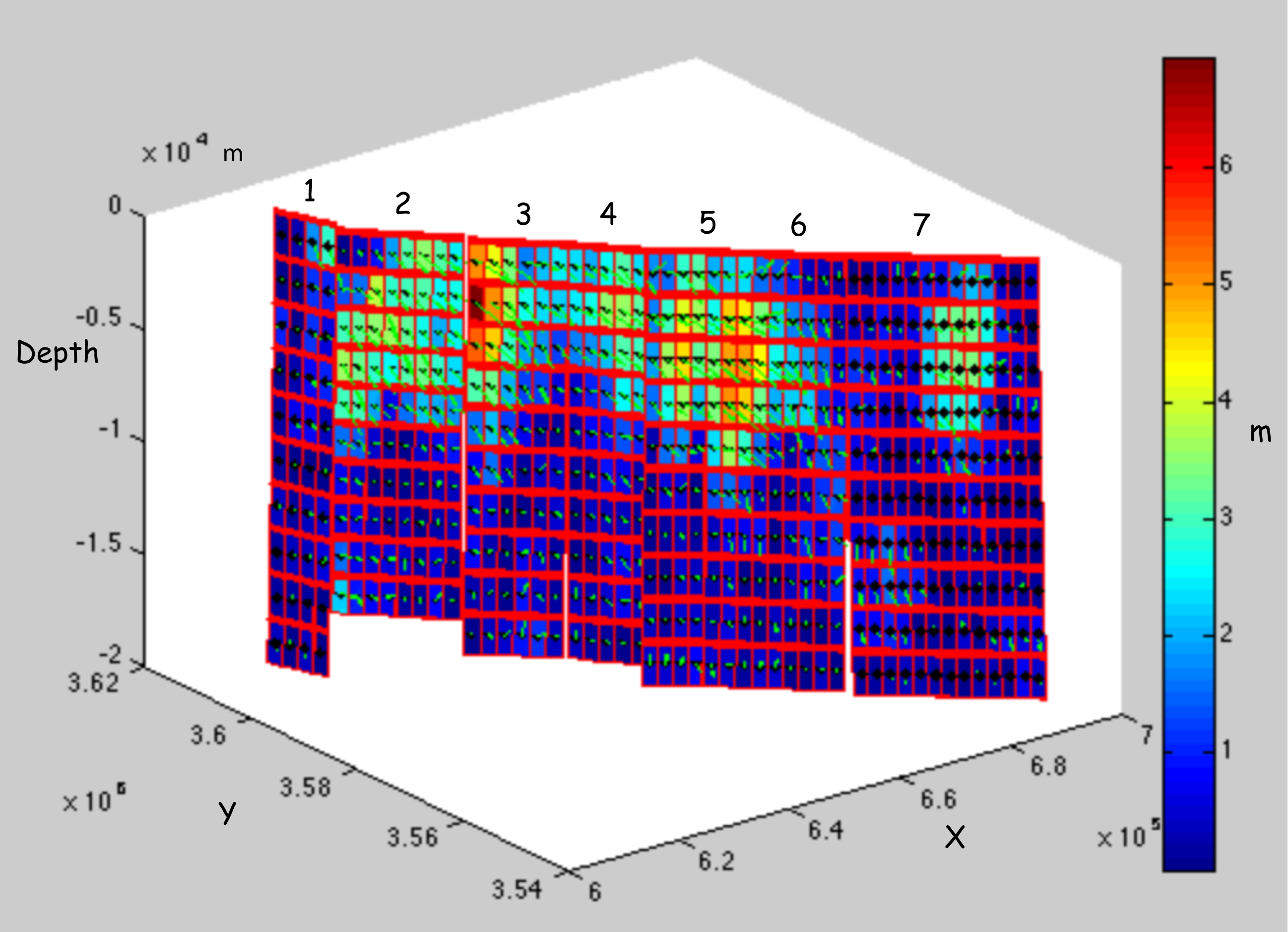

Figure 6.11: 3D distribution slip model from Bayesian inversion. One ascending and one descending interferogram were used in inversion. The model is constructed from the average values of the paramaters' posterior probability distributions.

Table 6.3: Geometric fault parameters strike, centroid, and length for seven fault segments are fixed from the sub-pixel matching and dip is obtained by Bayesian slip inversion of two interferograms.

Parameter	Segment 1	Segment 2	Segment 3	Segment 4	Segment 5	Segment 6	Segment 7
Strike (°)	334	310	307	314	302	307	305
Dip (°)	72	63	56	64	72	73	92
Length (km)	8.5	16.7	13	10	8	18	25
Centroid lon (km)	618.200	625.525	637.000	646.000	653.000	663.729	681.160
Centroid lat (km)	3608.680	3598.500	3588.180	3580.640	3574.940	3567.140	3554.240

southern segment, it appears that the switch between dipping signs of the two fault planes used to describe the El Mayor-Cucapah earthquake by Wei et al. (2011) is probably not that sudden, and instead it follows a more gradual change. Fault plane dip values are listed in Table 6.3 and can be directly compared with the inferred values of dip in Section 6.2.

The actual results of inversion are shown in Figure 6.12. This figure shows the posterior probability distribution for dip, maximum slip and maximum rake for each fault plane. Dip on the fault is well constrained apart from the last fault plane which has hardy any data in the vicinity to constrain the inversion. Again, the maximum slip is well constrained

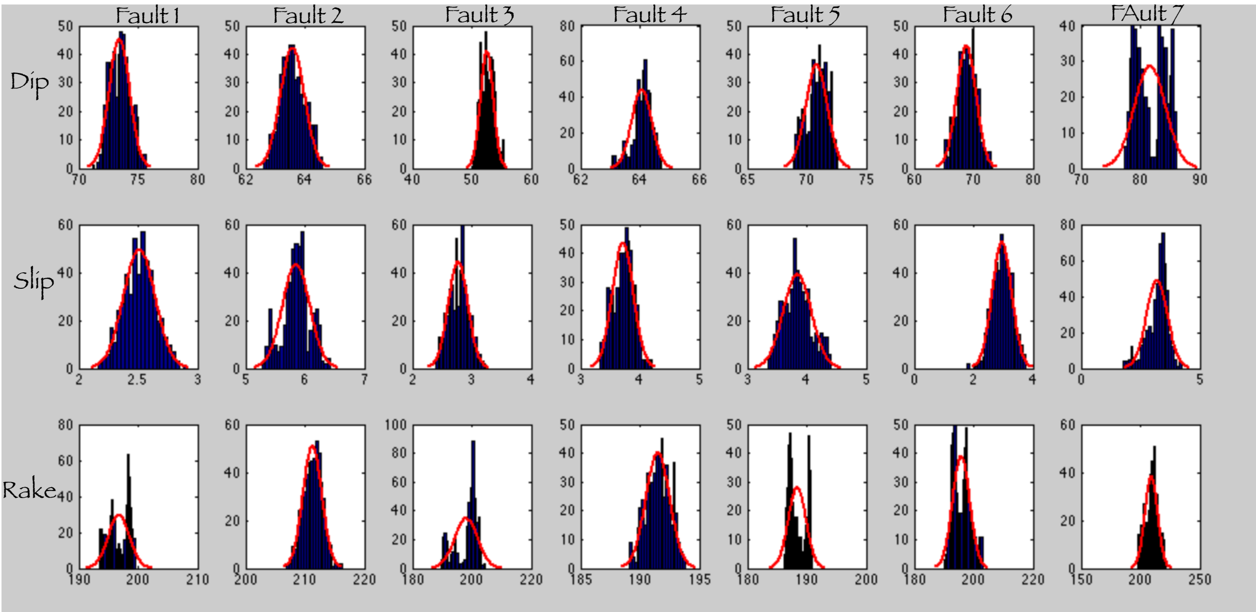

Figure 6.12: Posterior probability distribution for dip, maximums slip and maximum rake parameters

on all fault planes apart from the last one when the distribution is skewed to one side. The least constrained parameter in this case is rake, and there are large uncertanties on the first, third, fifth and sixth fault planes. The rake depends on the fixed smoothing values choosen.

Bayesian inversion of four InSAR datasets and seven planes

I used all four interferograms (track 77, track, 84, track 356, and track 306) in the Bayesian inversion and the new model Figure 6.13 has very similar charteristics to the model calculated with only two interferograms. Again, large slip patch in the southern corner remains unexplained. Values of dips are slightly different from the ones derived for the case of two interferograms, which is expected with the addition of more data. However, prompted by the results of Wei et al. (2011) I have used a priori of 65°as a lower dip boundary for all fault planes in order to constrain the dip not to go any shallower, but the second and the fourth fault plane hit the boundary and probably this constraint has affected the results overall. The model shows that the dip on some parts of the northern segment is relatively shallow. In terms of the overall fit, the model derived from four interferograms has slightly larger errors, but localised on a few spurious points. This is expected when there is a larger number of datasets. In both cases of inversion, I have

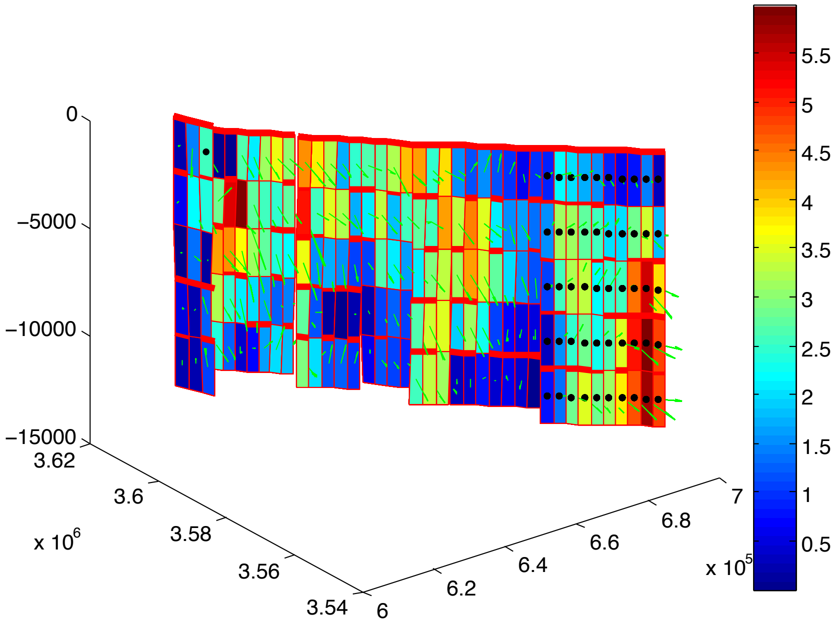

Figure 6.13: 3D distribution slip model from Bayesian inversion, where four interfereograms were used. The model is constructed from the average values of the parameters' posterior PDF.

Table 6.4: Geometric fault parameters strike, centroid, and length for seven fault segments are fixed from the sub-pixel matching and dip is obtained by Bayesian slip inversion of the four interfograms.

Parameter	Segment 1	Segment 2	Segment 3	Segment 4	Segment 5	Segment 6	Segment 7
Strike (°)	334	310	307	314	302	307	305
Dip (°)	82	65	70	67	75	75	90
Length (km)	8.5	16.7	13	10	8	18	25
Centroid lon (km)	618.200	625.525	637.000	646.000	653.000	663.729	681.160
Centroid lat (km)	3608.680	3598.500	3588.180	3580.640	3574.940	3567.140	3554.240

not let the inversion solve for the smoothing which remains fixed. Ideally, no smoothing should be applied to keep the solution physical, but for the case of the inversion of two interferograms I fixed the smoothing to a very low value and in the case of inversion of four interferograms I fixed it to a slightly higher value. The current smoothing algorithm applies the algorithm to each fault plane separately, but if smoothing is to be applied, the new algorithm should be put in place so that it applies to all fault planes simultaneously. Table 6.4 lists the inferred fault dips on the seven fault planes derived from Bayesian inversion of crustal measurements from the four interferograms.

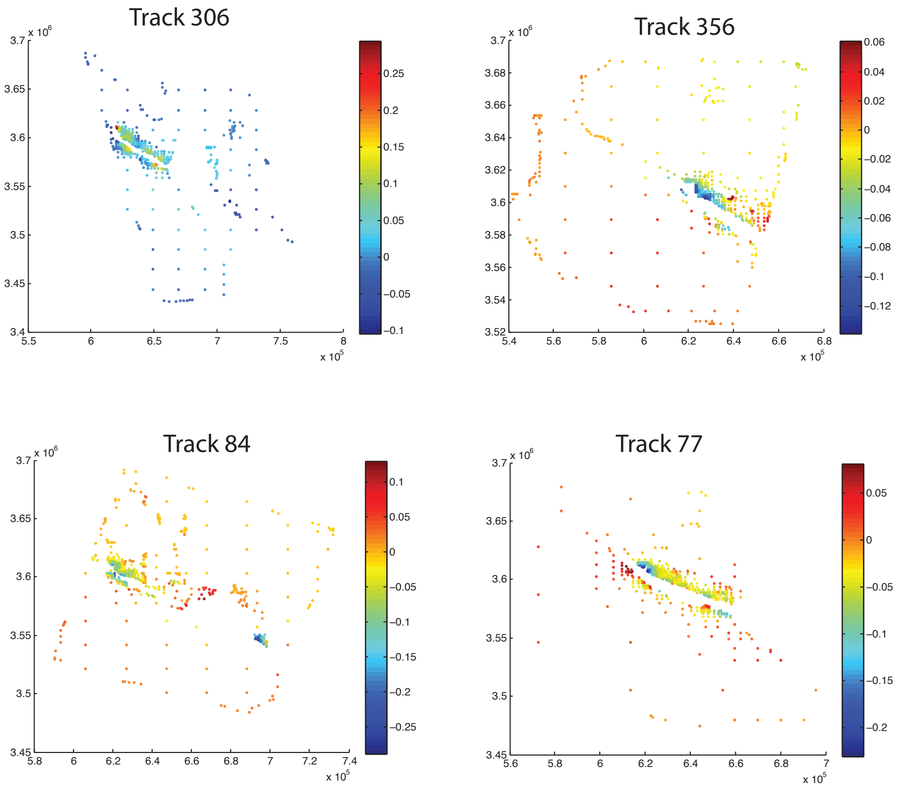

Figure 6.14: Differences between data and the model for all four interferograms (track 77, track 84, track 306, track 356).

6.4 Future work

Putting in place Bayesian algorithm that can perform inversion on multiple sets of InSAR data and multiple fault planes simultanously is only the first step. The next step is to incorporate the crustal deformations obtained by sub-pixel optical matching as they add constraints to the model in the near field of the earthquke and can reveal detailed information about slip near the surface. Seismic waves are another source of constraints that brings valuable information how the rupture develops over the time.

Chapter 7

Conclusions and Discussion

Optical sub-pixel matching technique are undisputedly the only satellite geodetic technique which can precisely map newly ruptured fault traces in detail, measure displacement directly on the fault, as well as horizontal deformation across the fault zone and the deformation in the near field.

The geometry of the fault from the surface and the distribution of slip on the fault are important in understanding the dynamics of earthquakes. This information is valuable for defining the geometry (location, strike and length) of faults; and to constrain the slip on upper fault patches for source models of co-seismic events computed by InSAR datasets and seismic waveform modelling.

7.1 Summary of results

7.1.1 Chapter 3

In Chapter 3 I construct horizontal displacement maps from SPOT4 images for the Dabbahu segment in Afar. The maps have revealed detailed surface linear discontinuities showing the geometry of the dyke, and previously unknown locations of active faulting. Horizontal displacements revealed 3 m of opening and deflation of two nearby volcanoes. I constructed a vertical displacement field by combining InSAR line-of-sight data with horizontal displacements. I found that the area bounded between two normal faults subsided 2 m, and regions to the west and to the east of the dyke experienced asymmetric uplift, i.e. more uplift occurred on the east side. I have constructed a forward dislocation model with uniform slip to explain the deformation at depth. The dip of the dike to the west explains the asymmetric pattern better than the vertical dike used in the faulting model produced by (Wright et al., 2006). Instead of having two symmetrical conjugate normal faults, by placing only one normal fault on one or other side of the dike, the observations are better explained.

I attempted to make further enhancements by calculating a model with distributed instead of uniform slip by inverting the data using a hybrid Monte Carlo downhill simplex algorithm (Wright et al., 1999). I found that despite the ideal conditions (arid terrain, little vegetation, images from the same season), biases in the horizontal displacement datasets were too large and the inversions were unsuccessful.

7.1.2 Chapter 4

In Chapter 4 I constructed 15 horizontal displacements maps (E-W and N-S) of the El Mayor-Cucapah region using 10 SPOT5 images. I identified that all horizontal displacement maps obtained by sub-pixel matching have some degree of long wavelength bias associated with them. I also find that the direction and amount of the long wavelength bias is different for E-W and N-S components of the horizontal displacement. I found that the source of this bias comes from the fact that the algorithm employed in *Cosi-corr* for look angle correction of the post-seismic orthoimage is based on three ground control points acquired from the pre-event orthoimage, which are not necessarily always located in a region of no displacement. I also found that the E-W and N-S displacement maps are riddled by many short wavelength effects that optical sub-pixel matching captures . I identify three groups of short wavelength biases: shadows (either caused by topographic structures or vegetation), very bright and very dark regions, and biases caused by topography. I developed four separate algorithms for masking out the shadowing effects caused by topography, vegetation, very bright and dark areas in the image, and decorrelation effects, and this helps highlight the areas not favourable for the location of the ground control points and also cleans the displacement maps for the inversions. I derived a new way of assessing the quality of DEMs by using optical sub-pixel correlation with images without tectonic signal and with large difference in their incidence angles. I found that the globally available Aster DEM has some inconsistency in flat regions.

Chapter 5

In Chapter 5 I showed that optical sub-pixel matching can be used to determine the post-event vertical displacement field using only one post-event lidar dataset with some archived optical images. I have also shown that vertical displacements obtained by simply differencing pre-event and post-event DEMs, no matter how accurate they are, is not accurate, and it is necessary to correct the post-event DEM for horizontal displacements first.

I have demonstrated this principle in the case of the 2010, M_w 7.2 El Mayor-Cucapah earthquake and shown the distribution of vertical displacement on the fault and in the close vicinity of the fault.

Chapter 6

In Chapter 6 I constructed source models of the 2010, El Mayor-Cucapah earthquake in two ways: inversion using a traditional optimization method, and a inversion by Bayesian approach. I find that the Bayesian approach can simultaneously solve slip distribution on many fault planes and generate the geometric parameters.

I have constructed the source model using InSAR data, but despite the cleaning of the optical sub-pixel datasets in Chapter 4 I was once more unable to perform the inversion using the traditional approach, as the function minimum could not be reached. In this case I suspect that the long wavelength biases are too large, or there are still short wavelength biases present in the data that are preventing the function‘s minimum from being found. A Bayesian approach to inversion offers a complete evaluation of the trade offs and includes covariances of each dataset that weigh them separately during the joint inversion. With a Bayesian approach any complex forward model can be tackled without the need for finding the function‘s minimum.

I adapted Bayesian code written originally by Andy Hooper following the methodology from Fukuda & Johnson (2008) for finding the earthquake source model with slip distribution on the fault. I have adapted the code so that it runs a pure Bayesian inversion rather than using Akaike‘s Bayesian Inversion Criterion (Akaike, 1980). The smoothing of the slip distribution is imbedded in the code so that Bayesian inversion simultaneously solves for the best smoothing parameter along with all the other parameters.

I have added to the code the ability to run any number of InSAR and optical sub-pixel matching datasets on any number of fault planes. The number of planes did not seem to increase the computational time, but it made it much easier to constrain the fault plane‘s geometrical parameters than was the case with constraining many fault planes in a traditional way of adding each plane manually.

I have modelled separately covariance matrices for each InSAR and optical sub-pixel dataset. Each covariance matrix describes the error structures in the observations and I find that the inversion is highly sensitive to the design of the covariance matrices. Covariance matrices weigh datasets differently during the inversions, and techniques that have inherently lower accuracy will contribute less to the final solution. This is the area that probably requires more investigation. I have successfully used Bayesian code for inversion of two interferograms and four interferograms for solving the source mechanism of the El Mayor-Cucapah earthquake.

7.2 Limitations of techniques and future work

A number of techniques and algorithms are discussed throughout this thesis with the purpose of creating 3D displacement maps of the deformation due to earthquakes. They are then used to infer processes at depth. I believe that sub-pixel optical matching is the best approach when it comes to measuring the 3D displacements on the Earth, because the geometry of the system allows measurements directly in three dimensions, rather than in line-of-sight direction only in the case of InSAR. In addition, although optical matching can not penetrate through cloud coverage, it does not have issues with the atmospheric delays and the need to implement complicated and very unstable weather models to reduce atmospheric signals caused by water vapour.

In order for sub-pixel optical matching to become a technique of choice for more accurate and continuous measurements of the earth‘s surface, a number of limitations need to be overcome.

7.2.1 Sub-pixel optical Image Matching

7.2.2 Images

One of the biggest limitations for optical sub-pixel matching is the quality of images. To achieve an image suitable for sub-pixel matching several things are required: the repeat coverage interval should be as small as possible, spatial coverage on the ground should be as large as possible, ground sampling distances should be as small as possible, and the knowledge of satellites orbits should be as accurate as possible. Despite the array of different satellite families that are collecting optical images of the earth, none of them have all these qualities. SPOT and Landsat satellites have large land coverage, but the whole strips rather than individual scenes are more desirable for matching, as shown in Chapter 4. This is something that only SPOT6 and SPOT7 have recently made available. The ground sampling distances have been increasing steadily over time and currently they stand at 0.31 m acquired by the WorldView-3 satellite. However, high spatial resolution almost inevitably means very small land coverage, which makes the processing cumbersome, and creates lack of stable ground. However, the processing could be very simple if the satellites orbits are precisely known. SPOT and Landsat provide information for very stable orbits, but unfortunately they are not stable enough for the image sub-pixel matching, hence the long wavelength error. Ideally the satellites should record their positions much more frequently, similar to Lidar acquisitions. Unfortunately some of the new family of satellites do not provide any information about their orbits at all and without accurate positioning of pre-event and post-event image the correlation is simply not possible, unless new algorithms can be devised to yield accurate position of the images without the knowledge of the precise orbits.

Another advantage of accurate trajectories is the ability to merge scenes across the strips and create wide areas of stable ground. Precise orbits are not the only limitations that images suffer from. Variability between the seasons has a huge effect on sub-pixel matching, creating decorelations and biased signals in the images as discussed in Chapter

4. Stable satellites such as SPOT and Landsat have a very long repeat coverage interval which creates these effects. Recently Planet Lab's have launched more than a hundred small satellites which are acquiring images of the earth in real time. The orbits of these satellites are unknown and they have a spatial resolution of 3 m. If we are to use these images for observing 3D displacements of the earth, a new set of algorithms would be required, perhaps combined with GPS on the ground.

The incidence angles of these images are large and rather than having the nadir images that was required to create 2D horizontal displacements without topographic effects, most of the matching pairs would have a stereo-effect between them, and hence large topographic errors.

DEMs

Very high resolution DEMs can help to overcome two limitations of optical sub-pixel matching: creating 2D displacements maps from very high spatial resolution images which is not yet possible, and creating 2D displacement maps from the images with stereo-effects. Ideally these DEMs should be made from the stereo images simultaneously acquired with images used for orthorectification and matching. They should have the resolution required so that topographic effects/residuals do not appear.

7.2.3 Cosesimic inversions and joint inversions in general

We should put more effort in combining different sources of information about earthquake activities and in general about active tectonics to obtain detailed knowledge of the system. Although performing finite fault earthquake inversion can be computationally expensive using Bayesian approach, clever choices of the prior information reduces the time of the inversions drastically. For example, moment magnitude already used by some authors (Minson et al., 2013) would constrain the rakes on the fault more precisely.

Given that all of the geometric parameters of the fault planes are known apart from the dips of the fault planes, simply using Bayesian inversion to solve for the dip followed by simple linear inversion of the slip on the fault would drastically reduce the computational speed.

The Bayesian approach creates an ideal environment for calculating joint inversions of all possible datasets, where each dataset can contribute within the constraints specific to each technique. Seismic data contributes to a very precise timing of slip development, while the high spatial density observation of InSAR and optical sub-pixel matching datasets contribute to deriving a fine slip distribution pattern on a fault.

Covariance matrices describe the error budget of each dataset but also error structures that are present in the data. There should be more investigation to understand these matrices, as the model design is very sensitive to their content.

Bibliography

Aghdasi, F. & Ward, R., 1996. Reduction of boundary artifacts in image restoration, *Image Processing, IEEE Transactions on*, **5**(4), 611 –618.

Akaike, H., 1980. Likelihood and the bayes procedure, *Trabajos de estadística y de investigación operativa*, **31**(1), 143–166.

Árnadóttir, T., Jónsson, S., Pollitz, F. F., Jiang, W., & Feigl, K. L., 2005. Postseismic deformation following the june 2000 earthquake sequence in the south iceland seismic zone, *Journal of Geophysical Research: Solid Earth (1978–2012)*, **110**(B12).

Artemjev, M. & Kaban, M., 1991. Isostatic processes and intracontinental orogenesis, *Journal of Geodynamics*, **13**(1), 77–86.

Artyushkov, E., 1973. Stresses in the lithosphere caused by crustal thickness inhomogeneities, *Journal of Geophysical Research*, **78**(32), 7675–7708.

Avouac, J.-P., Meng, L., Wei, S., Wang, T., & Ampuero, J.-P., 2015. Lower edge of locked main himalayan thrust unzipped by the 2015 gorkha earthquake, *Nature Geoscience*.

Axen, G. J., Fletcher, J. M., Cowgill, E., Murphy, M., Kapp, P., MacMillan, I., Ramos-Velázquez, E., & Aranda-Gómez, J., 1999. Range-front fault scarps of the sierra el mayor, baja california: Formed above an active low-angle normal fault?, *Geology*, **27**(3), 247–250.

Ayele, A., Jacques, R., Kassim, M., Kidane, T., Omar, A., Tait, S., Nercessian, A., de Chabalier, J.-B., & King, G., 2007. The volcano-seismic crisis in Afar, Ethiopia, starting September 2005, *Earth and Planetary Science Letters*.

Ayoub, F. & Leprince, S., 2005. User-Guide to COSI-CORR v1.0 co-registration of optically sensed images and correlation.

Ayoub, F., Leprince, S., & Avouac, J.-P., 2009. Co-registration and correlation of aerial photographs for ground deformation measurements, *ISPRS Journal of Photogrammetry and Remote Sensing*, **64**(6), 551–560.

Bagley, B. & Nyblade, A. A., 2013. Seismic anisotropy in eastern africa, mantle flow, and the african superplume, *Geophysical Research Letters*, **40**(8), 1500–1505.

Barišin, I., Leprince, S., Parsons, B., & Wright, T., 2009. Surface displacements in the september 2005 afar rifting event from satellite image matching: Asymmetric uplift and faulting, *Geophysical Research Letters*, **36**(7).

Barišin, I., Hinojosa-Corona, A., & Parsons, B., 2015. Co-seismic vertical displacements from a single post-seismic lidar dem: Example from 2010 el mayor-cucapah earthquake, *GJI*, p. in review.

Barzilai, j. & Borwein, J., 1988. Two-point step size grasient methods, *IMA Journal of Numerical Analysis*, **8**, 141–148.

Bayes, M. & Price, M., 1763. An essay towards solving a problem in the doctrine of chances. by the late rev. mr. bayes, frs communicated by mr. price, in a letter to john canton, amfrs, *Philosophical Transactions (1683-1775)*, pp. 370–418.

Beck, J. L. & Katafygiotis, L. S., 1998. Updating models and their uncertainties. i: Bayesian statistical framework, *Journal of Engineering Mechanics*, **124**(4), 455–461.

Bennett, R. A., Friedrich, A. M., & Furlong, K. P., 2004. Codependent histories of the san andreas and san jacinto fault zones from inversion of fault displacement rates, *Geology*, **32**(11), 961–964.

Berthier, E., Vadon, H., Baratoux, D., Arnaud, Y., Vincent, C., Feigl, K., Remy, F., & Legresy, B., 2005. Surface motion of mountain glaciers derived from satellite optical imagery, *Remote Sensing of Environment*, **95**(1), 14–28.

Bird, P. & Piper, K., 1980. Plane-stress finite-element models of tectonic flow in southern california, *Physics of the earth and planetary interiors*, **21**(2), 158–175.

Bonner, J. L., Blackwell, D. D., & Herrin, E. T., 2003. Thermal constraints on earthquake depths in california, *Bulletin of the Seismological Society of America*, **93**(6), 2333–2354.

Brace, W. & Kohlstedt, D., 1980. Limits on lithospheric stress imposed by laboratory experiments, *J. geophys. Res*, **85**(B11), 6248–6252.

Bridges, N., Ayoub, F., Avouac, J., Leprince, S., Lucas, A., & Mattson, S., 2012. Earth-like sand fluxes on mars, *Nature*, **485**(7398), 339–342.

Brown, L. G., 1992. A survey of image registration techniques, *ACM Comput. Surv.*, **24**, 325–376.

Buck, W., 2006. The role of magma in the development of the afro-arabian rift system, *Geological Society, London, Special Publications*, **259**(1), 43–54.

Bürgmann, R. & Dresen, G., 2008. Rheology of the lower crust and upper mantle: Evidence from rock mechanics, geodesy, and field observations, *Annual Review of Earth and Planetary Sciences*, **36**(1), 531.

Bürgmann, R., Ergintav, S., Segall, P., Hearn, E. H., McClusky, S., Reilinger, R. E., Woith, H., & Zschau, J., 2002. Time-dependent distributed afterslip on and deep below the izmit earthquake rupture, *Bulletin of the Seismological Society of America*, **92**(1), 126–137.

Burov, E. & Gerya, T., 2014. Asymmetric three-dimensional topography over mantle plumes, *Nature*, **513**(7516), 85–89.

Burov, E. B., 2011. Rheology and strength of the lithosphere, *Marine and Petroleum Geology*, **28**(8), 1402–1443.

Byerlee, J., 1978. Friction of rocks, *Pure and applied geophysics*, **116**(4-5), 615–626.

Çakir, Z., de Chabalier, J.-B., Armijo, R., Meyer, B., Barka, A., & Peltzer, G., 2003. Coseismic and early post-seismic slip associated with the 1999 izmit earthquake (turkey), from sar interferometry and tectonic field observations, *Geophysical Journal International*, **155**(1), 93–110.

Carroll, D., 2010. The accuracy of spot maps on a continental scale @ONLINE.

Cattin, R., Doubre, C., De Chabalier, J.-B., King, G., Vigny, C., Avouac, J.-P., & Ruegg, J.-C., 2005. Numerical modelling of quaternary deformation and post-rifting displacement in the asal–ghoubbet rift (djibouti, africa), *Earth and Planetary Science Letters*, **239**(3), 352–367.

Chen, L. & Lee, L., 1993. Rigorous generation of digital orthophotos from spot images, *pers*, **59**, 655–661.

Chen, W.-P. & Molnar, P., 1983. Focal depths of intracontinental and intraplate earthquakes and their implications for the thermal and mechanical properties of the lithosphere, *J. geophys. Res*, **88**(B5), 4183–4214.

Chlieh, M., Avouac, J.-P., Hjorleifsdottir, V., Song, T.-R. A., Ji, C., Sieh, K., Sladen, A., Hebert, H., Prawirodirdjo, L., Bock, Y., et al., 2007. Coseismic slip and afterslip of the great mw 9.15 sumatra–andaman earthquake of 2004, *Bulletin of the Seismological Society of America*, **97**(1A), S152–S173.

Chrysoulakis, N., Abrams, M., Kamarianakis, Y., et al., 2011. Validation of the aster gdem for the area of greece., *Photogrammetric Engineering & Remote Sensing*.

Clarke, P., Paradissis, D., Briole, P., England, P., Parsons, B., Billiris, H., Veis, G., & Ruegg, J.-C., 1997. Geodetic investigation of the 13 may 1995 kozani-grevena (greece) earthquake, *Geophysical Research Letters*, **24**(6), 707–710.

Cohee, B. P. & Beroza, G. C., 1994. Slip distribution of the 1992 landers earthquake and its implications for earthquake source mechanics, *Bulletin of the Seismological Society of America*, **84**(3), 692–712.

Contreras-Reyes, E. & Osses, A., 2010. Lithospheric flexure modelling seaward of the chile trench: implications for oceanic plate weakening in the trench outer rise region, *Geophysical Journal International*, **182**(1), 97–112.

Cotton, F. & Campillo, M., 1995. Stability of the rake during the 1992, landers earthquake. an indication for a small stress release?, *Geophysical research letters*, **22**(14), 1921–1924.

Crosby, A., 2007. An assessment of the accuracy of admittance and coherence estimates using synthetic data, *Geophysical Journal International*, **171**(1), 25–54.

Cunningham, D., Grebby, S., Tansey, K., Gosar, A., & Kastelic, V., 2006. Application of airborne LiDAR to mapping seismogenic faults in forested mountainous terrain, southeastern Alps, Slovenia, *Geophysical Research Letters*, **33**, –.

Debella-Gilo, M. & Kääb, A., 2011. Sub-pixel precision image matching for measuring surface displacements on mass movements using normalized cross-correlation, *Remote Sensing of Environment*, **115**(1), 130–142.

Decriem, J., Árnadóttir, T., Hooper, A., Geirsson, H., Sigmundsson, F., Keiding, M., Ófeigsson, B., Hreinsdóttir, S., Einarsson, P., LaFemina, P., et al., 2010. The 2008 may 29 earthquake doublet in sw iceland, *Geophysical Journal International*, **181**(2), 1128–1146.

Dominguez, S., Avouac, J.-P., & Michel, R., 2003. Horizontal coseismic deformation of the 1999 chi-chi earthquake measured from spot satellite images: Implications for the seismic cycle along the western foothills of central taiwan, *Journal of Geophysical Research: Solid Earth (1978–2012)*, **108**(B2).

Duffy, B., Quigley, M., Barrell, D. J., Van Dissen, R., Stahl, T., Leprince, S., McInnes, C., & Bilderback, E., 2013. Fault kinematics and surface deformation across a releasing bend during the 2010 M_w 7.1 Darfield, New Zealand, earthquake revealed by differential lidar and cadastral surveying, *Geological Society of America Bulletin*, **125**, 420–431.

Duputel, Z., Agram, P. S., Simons, M., Minson, S. E., & Beck, J. L., 2014. Accounting for prediction uncertainty when inferring subsurface fault slip, *Geophysical Journal International*, p. ggt517.

Ebinger, C., Keir, D., Ayele, A., Calais, E., Wright, T., Belachew, M., Hammond, J., Campbell, M., & Buck, R., 2008. Capturing magma intrusion and faulting processes during continental rupture: Seismicity of the Dabbahu (Afar) rift, *Journal of Geophyiscal Research*.

Elders, W. A., Rex, R. W., Robinson, P. T., Biehler, S., & Meidav, T., 1972. Crustal spreading in southern california: The imperial valley and the gulf of california formed by the rifting apart of a continental plate, *Science*, **178**(4056), 15–24.

Elliott, J., Biggs, J., Parsons, B., & Wright, T., 2008. Insar slip rate determination on the altyn tagh fault, northern tibet, in the presence of topographically correlated atmospheric delays, *Geophysical Research Letters*, **35**(12).

Ellis, S., Beavan, J., Eberhart-Phillips, D., & Stöckhert, B., 2006. Simplified models of the alpine fault seismic cycle: stress transfer in the mid-crust, *Geophysical Journal International*, **166**(1), 386–402.

England, P. & McKenzie, D., 1982. A thin viscous sheet model for continental deformation, *Geophysical Journal International*, **70**(2), 295–321.

England, P. & Molnar, P., 2015. Rheology of the lithosphere beneath the central and western tien shan, *Journal of Geophysical Research: Solid Earth*.

Fialko, Y., 2004. Evidence of fluid-filled upper crust from observations of postseismic deformation due to the 1992 mw7. 3 landers earthquake, *Journal of Geophysical Research: Solid Earth (1978–2012)*, **109**(B8).

Fielding, E., Wei, S., Leprince, S., Sladen, A., Simons, M., Avouac, J., Briggs, R., Hudnut, K., Helmberger, D., Hensley, S., et al., 2010. Kinematic fault slip model from joint inversion of teleseismic, gps, insar and subpixel-correlation measurements of the 2010 el mayor-cucapah earthquake and postseismic deformation, in *AGU Fall Meeting Abstracts*, vol. 1, p. 08.

Fletcher, J., Rockwell, T., Teran, O., Masana, E., Faneros, G., Hudnut, K., Gonzalez, J., Gonzalez, A., Spelz, R., & Mueller, K., 2010. The surface ruptures associated with the el mayor-borrego earthquake sequence, *Geological Society of America, Cordilleran section, Abstract LB1-5, Anaheim, California*.

Fletcher, J. M. & Spelz, R. M., 2009. Patterns of quaternary deformation and rupture propagation associated with an active low-angle normal fault, laguna salada, mexico: Evidence of a rolling hinge?, *Geosphere*, **5**(4), 385–407.

Fletcher, J. M., Teran, O. J., Rockwell, T. K., Oskin, M. E., Hudnut, K. W., Mueller, K. J., Spelz, R. M., Akciz, S. O., Masana, E., Faneros, G., et al., 2014. Assembly of a large earthquake from a complex fault system: Surface rupture kinematics of the 4 April 2010 El Mayor–Cucapah (Mexico) Mw $_7$.2 earthquake, *Geosphere*, **10**, 797–827.

Foroosh, H., Zerubia, J., & Berthod, M., 2002. Extension of phase correlation to subpixel registration, *IEEE Transaction on Image Processing*, **11**(3).

Fukuda, J. & Johnson, K. M., 2008. A fully bayesian inversion for spatial distribution of fault slip with objective smoothing, *Bulletin of the Seismological Society of America*, **98**(3), 1128–1146.

Gamerman, D. & Lopes, H. F., 2006. *Markov chain Monte Carlo: stochastic simulation for Bayesian inference*, CRC Press.

Gan, W., Zhang, P., Shen, Z.-K., Niu, Z., Wang, M., Wan, Y., Zhou, D., & Cheng, J., 2007. Present-day crustal motion within the tibetan plateau inferred from gps measurements, *Journal of Geophysical Research: Solid Earth (1978–2012)*, **112**(B8).

Garthwaite, M. C., Wang, H., & Wright, T. J., 2013. Broadscale interseismic deformation and fault slip rates in the central tibetan plateau observed using insar, *Journal of Geophysical Research: Solid Earth*, **118**(9), 5071–5083.

Glennie, C. L., Hinojosa-Corona, A., Nissen, E., Kusari, A., Oskin, M. E., Arrowsmith, J. R., & Borsa, A., 2014. Optimization of legacy lidar data sets for measuring near-field earthquake displacements, *Geophysical Research Letters*, **41**, 3494–3501.

Gorokhovich, Y. & Voustianiouk, A., 2006. Accuracy assessment of the processed srtm-based elevation data by cgiar using field data from usa and thailand and its relation to the terrain characteristics, *Remote Sensing of Environment*, **104**(4), 409–415.

Grandin, R., Socquet, A., Binet, R., Klinger, Y., Jacques, E., de Chabalier, J.-B., King, G., Lasserre, C., Tait, S., Tapponnier, P., et al., 2009. September 2005 manda hararo-dabbahu rifting event, afar (ethiopia): constraints provided by geodetic data, *Journal of Geophysical Research: Solid Earth*, **114**(B8).

Grandin, R., Socquet, A., Doin, M.-P., Jacques, E., de Chabalier, J.-B., & King, G., 2010. Transient rift opening in response to multiple dike injections in the manda hararo rift (afar, ethiopia) imaged by time-dependent elastic inversion of interferometric synthetic aperture radar data, *Journal of Geophysical Research: Solid Earth (1978–2012)*, **115**(B9).

Gruen, A., 2012. Development and status of image matching in photogrammetry, *The Photogrammetric Record*, **27**(137), 36–57.

Gugan, D. & Dowman, I., 1988. Topographic mapping from spot imagery, *Photogrammetric engineering and Remote Sensing*, **54**(10), 1409–1414.

Guth, P., 2010. Geomorphometric comparison of aster gdem and srtm, in *ASPRS/CaGIS 2010 Fall Specialty Conference, Orlando, FL*, pp. 15–19.

Hamling, I. J., Wright, T. J., Calais, E., Lewi, E., & Fukahata, Y., 2014. Insar observations of post-rifting deformation around the dabbahu rift segment, afar, ethiopia, *Geophysical Journal International*, **197**(1), 33–49.

Hammond, J., Kendall, J.-M., Stuart, G., Ebinger, C., Bastow, I., Keir, D., Ayele, A., Belachew, M., Goitom, B., Ogubazghi, G., et al., 2013. Mantle upwelling and initiation of rift segmentation beneath the afar depression, *Geology*, **41**(6), 635–638.

Hammond, J., Kendall, J.-M., Wookey, J., Stuart, G., Keir, D., & Ayele, A., 2014. Differentiating flow, melt, or fossil seismic anisotropy beneath ethiopia, *Geochemistry, Geophysics, Geosystems*, **15**(5), 1878–1894.

Hansen, S. E., Nyblade, A. A., & Benoit, M. H., 2012. Mantle structure beneath africa and arabia from adaptively parameterized p-wave tomography: Implications for the origin of cenozoic afro-arabian tectonism, *Earth and Planetary Science Letters*, **319**, 23–34.

Hanssen, R. F., 2001. *Radar Interferometry*, Kluwer Academic Publishers.

Harris, F., 1978. On the use of windows for harmonic analysis with the discrete fourier transform, *Proceedings of the IEEE*, **66**(1), 51 – 83.

Hassan Foroosh, M. B. & Zerubia, J., 1996. Subpixel image registration by estimating the polyphase decomposition of cross poer spectrum, *Proceedings CVPR '96, 1996 IEEE Computer Society Conference on Computer Vision and Pattern Recognition*, pp. 532–537.

Hayward, N. & Ebinger, C., 1996. Variations in the along-axis segmentations of the Afar rift system, *Tectonics*, **15**(2), 244–257.

Hearn, E., Johnson, K., & Thatcher, W., 2010. Space geodetic data improve seismic hazard assessment in california: Workshop on incorporating geodetic surface deformation data into ucerf3; pomona, california, 1–2 april 2010, *Eos, Transactions American Geophysical Union*, **91**(38), 336–336.

Hearn, E. H., Bürgmann, R., & Reilinger, R. E., 2002. Dynamics of izmit earthquake postseismic deformation and loading of the düzce earthquake hypocenter, *Bulletin of the Seismological Society of America*, **92**(1), 172–193.

Herman, F., Anderson, B., & Leprince, S., 2011. Mountain glacier velocity variation during a retreat/advance cycle quantified using sub-pixel analysis of aster images, *Journal of Glaciology*, **57**(202), 197–207.

Hernandez, B., Cotton, F., & Campillo, M., 1999. Contribution of radar interferometry to a two-step inversion of the kinematic process of the 1992 landers earthquake, *Journal of Geophysical Research*, **104**(B6), 13083–13099.

Hirt, C., Filmer, M., & Featherstone, W., 2010. Comparison and validation of the recent freely available aster-gdem ver1, srtm ver4. 1 and geodata dem-9s ver3 digital elevation models over australia, *Australian Journal of Earth Sciences*, **57**(3), 337–347.

Hofmann, B., 2013. *How do faults grow in magmatic rifts? LiDAR and InSAR observations of the Dabbahu rift segment, Afar, Ethiopia*, Ph.D. thesis, Faculty of Environment, School of Earth and Environmet, The University of Leeds.

Hofton, M. & Foulger, G., 1996. Postrifting anelastic deformation around the spreading plate boundary, north iceland, 1. modeling of the 1987-1992 deformation field using a viscoelastic earth structure, *JOURNAL OF GEOPHYSICAL RESEARCH-ALL SERIES-*, **101**, 25–403.

Hoge, W., 2003. A subspace identification extension to the phase correlation method [mri application], *Medical Imaging, IEEE Transactions on*, **22**(2), 277 –280.

Hollingsworth, J., Leprince, S., Ayoub, F., & Avouac, J.-P., 2012. Deformation during the 1975–1984 krafla rifting crisis, ne iceland, measured from historical optical imagery, *Journal of Geophysical Research: Solid Earth (1978–2012)*, **117**(B11).

Hough, S. E. & Elliot, A., 2004. Revisiting the 23 february 1892 laguna salada earthquake, *Bulletin of the Seismological Society of America*, **94**(4), 1571–1578.

Huang, M.-H., Bürgmann, R., & Freed, A. M., 2014. Probing the lithospheric rheology across the eastern margin of the tibetan plateau, *Earth and Planetary Science Letters*, **396**, 88–96.

Jackson, D. D., 1979. The use of a priori data to resolve non-uniqueness in linear inversion, *Geophysical Journal International*, **57**(1), 137–157.

Jackson, J., 2002. Strength of the continental lithosphere: time to abandon the jelly sandwich?, *GSA today*, **12**(9), 4–9.

Jackson, J., McKENZIE, D., Priestley, K., & Emmerson, B., 2008. New views on the structure and rheology of the lithosphere, *Journal of the Geological Society*, **165**(2), 453–465.

Jennings, C. W. & Saucedo, G. J., 1994. *Fault activity map of California and adjacent areas, with locations and ages of recent volcanic eruptions*, California Department of Conservation, Division of Mines and Geology.

Johnson, H. O., Agnew, D. C., & Wyatt, F. K., 1994. Present-day crustal deformation in southern california, *Journal of Geophysical Research: Solid Earth (1978–2012)*, **99**(B12), 23951–23974.

Johnson, K. M., Bürgmann, R., & Larson, K., 2006. Frictional properties on the san andreas fault near parkfield, california, inferred from models of afterslip following the 2004 earthquake, *Bulletin of the Seismological Society of America*, **96**(4B), S321–S338.

Jolivet, R., Grandin, R., Lasserre, C., Doin, M.-P., & Peltzer, G., 2011. Systematic insar tropospheric phase delay corrections from global meteorological reanalysis data, *Geophysical Research Letters*, **38**(17).

Jónsson, S., Zebker, H., Segall, P., & Amelung, F., 2002. Fault slip distribution of the 1999 mw 7.1 hector mine, california, earthquake, estimated from satellite radar and gps measurements, *Bulletin of the Seismological Society of America*, **92**(4), 1377–1389.

Jonsson, S., Segall, P., Pedersen, R., & Björnsson, G., 2003. Post-earthquake ground movements correlated to pore-pressure transients, *Nature*, **424**(6945), 179–183.

Keir, D., Hamling, I. J., Ayele, A., Calais, E., Ebinger, C., Wright, T. J., Jacques, E., Mohamed, K., Hammond, J. O., Belachew, M., et al., 2009. Evidence for focused magmatic accretion at segment centers from lateral dike injections captured beneath the red sea rift in afar, *Geology*, **37**(1), 59–62.

Kieu, H., Pan, T., Wang, Z., Le, M., Nguyen, H., & Vo, M., 2014. Accurate 3d shape measurement of multiple separate objects with stereo vision, *Measurement Science and Technology*, **25**(3), 035401.

Knospe, S. H. & Jonsson, S., 2010. Covariance estimation for dinsar surface deformation measurements in the presence of anisotropic atmospheric noise, *Geoscience and Remote Sensing, IEEE Transactions on*, **48**(4), 2057–2065.

Kraus, K., 1992. *Photogrammetry Fundamentals and Processes*, Dummler Verlag, Bonn, 1st edn.

Kraus, K., 2004. *Photogrammetry: Geometry from Images and Laser Scans*, Walter de Gruyter GmbH, 2nd edn.

Kuglin, C. & Hines, D., 1975. The phase correlation image alignment method, *Proceedings of the IEEE 1975 International conference on the Cybernetics and Society*, pp. 293–300.

Lachenbruch, A. H., Sass, J., & Galanis, S., 1985. Heat flow in southernmost california and the origin of the salton trough, *Journal of Geophysical Research: Solid Earth (1978–2012)*, **90**(B8), 6709–6736.

Lambeck, K., 1988. *Geophysical geodesy*, Clarendon Oxford.

Lekić, V. & Romanowicz, B., 2011. Inferring upper-mantle structure by full waveform tomography with the spectral element method, *Geophysical Journal International*, **185**(2), 799–831.

Leprince, S., Barbot, S., Ayoub, F., & Avouac, J.-P., 2007. Automatic and precise orthorectification, co-registration and sub-pixel correlation of satellite images, application to ground deformation measurements, *IEEE Transaction on Geoscience and Remote Sensing*, **45**(6), 1529–1557.

Leprince, S., Muse, S., & Avouac, J.-P., 2008. In-flight ccd distortion calibration for pushbroom satellites based on subpixel correlation, *IEEE Transactions on Geoscience and Remote Sensing*, **46**(9), 2675–2683.

Levitt, D. A. & Sandwell, D. T., 1995. Lithospheric bending at subduction zones based on depth soundings and satellite gravity, *Journal of Geophysical Research: Solid Earth (1978–2012)*, **100**(B1), 379–400.

Li, Z., Muller, J.-P., Cross, P., & Fielding, E. J., 2005. Interferometric synthetic aperture radar (insar) atmospheric correction: Gps, moderate resolution imaging spectroradiometer (modis), and insar integration, *Journal of Geophysical Research: Solid Earth*, **110**(B3).

Lohman, R. B. & Simons, M., 2005. Some thoughts on the use of insar data to constrain models of surface deformation: Noise structure and data downsampling, *Geochemistry, Geophysics, Geosystems*, **6**(1).

MacKay, D. J., 1998. Introduction to monte carlo methods, in *Learning in graphical models*, pp. 175–204, Springer.

Maggi, A., Jackson, J., Mckenzie, D., & Priestley, K., 2000. Earthquake focal depths, effective elastic thickness, and the strength of the continental lithosphere, *Geology*, **28**(6), 495–498.

Manighetti, I., Tapponnier, P., Gillot, P., Jacques, E., Courtillot, V., Armijo, R., Ruegg, J., & King, G., 1998. Propagation of rifting along the arabia-somalia plate boundary: Into afar, *Journal of Geophysical Research: Solid Earth*, **103**(B3), 4947–4974.

Massonnet, D. & Feigl, K. L., 1998. Radar interferometry and its application to changes in the earth's surface, *REVIEWS OF GEOPHYSICS-RICHMOND VIRGINIA THEN WASHINGTON-*, **36**, 441–500.

Massonnet, D., Rossi, M., Carmona, C., Ardagna, F., Peltzer, G., Feigl, K., & rabaute, T., 1993. The displacement field of the landers earthquake mapped by the radar interferometry, *Nature*, **364**(6433), 138.

Matsu'ura, M. & Hasegawa, Y., 1987. A maximum likelihood approach to nonlinear inversion under constraints, *Physics of the earth and planetary interiors*, **47**, 179–187.

McCaffrey, R., 2002. Crustal block rotations and plate coupling, *Plate boundary zones*, pp. 101–122.

McKenzie, D., Jackson, J., & Priestley, K., 2005. Thermal structure of oceanic and continental lithosphere, *Earth and Planetary Science Letters*, **233**(3), 337–349.

McKenzie, D. P. & Parker, R. L., 1967. The north pacific: an example of tectonics on a sphere, *Nature*, **216**, 1276–1280.

Meade, B. J. & Hager, B. H., 2005. Block models of crustal motion in southern california constrained by gps measurements, *Journal of Geophysical Research: Solid Earth (1978–2012)*, **110**(B3).

Metropolis, N. & Ulam, S., 1949. The monte carlo method, *Journal of the American statistical association*, **44**(247), 335–341.

Metropolis, N., Rosenbluth, A. W., Rosenbluth, M. N., Teller, A. H., & Teller, E., 1953. Equation of state calculations by fast computing machines, *The journal of chemical physics*, **21**(6), 1087–1092.

Meyn, S. P. & Tweedie, R. L., 1993. Stability of markovian processes iii: Foster-lyapunov criteria for continuous-time processes, *Advances in Applied Probability*, pp. 518–548.

Michel, R., Avouac, J.-P., & Taboury, J., 1999. Measuring ground displacements from sar amplitude images: application to the landers earthquake, *Geophysical Research Letters*, **26**(7), 875–878.

Mikhail, E., Bethel, J., & McGlone, J., 2001. *Modern Photogrammetry*, John Willey and Sons, Inc.

Miliaresis, G. & Paraschou, C., 2011. An evaluation of the accuracy of the aster gdem and the role of stack number: a case study of nisiros island, greece, *Remote Sensing Letters*, **2**(2), 127–135.

Minson, S., Simons, M., & Beck, J., 2013. Bayesian inversion for finite fault earthquake source models i?theory and algorithm, *Geophysical Journal International*, p. ggt180.

Minson, S., Simons, M., Beck, J., Ortega, F., Jiang, J., Owen, S., Moore, A., Inbal, A., & Sladen, A., 2014. Bayesian inversion for finite fault earthquake source models–ii: the 2011 great tohoku-oki, japan earthquake, *Geophysical Journal International*, **198**(2), 922–940.

Molnar, P. & Lyon-Caen, H., 1988. Some simple physical aspects of the support, structure, and evolution of mountain belts, *Geological Society of America Special Papers*, **218**, 179–208.

Molnar, P., Anderson, H. J., Audoine, E., Eberhart-Phillips, D., Gledhill, K. R., Klosko, E. R., McEvilly, T. V., Okaya, D., Savage, M. K., Stern, T., et al., 1999. Continuous deformation versus faulting through the continental lithosphere of new zealand, *Science*, **286**(5439), 516–519.

Morgan, G., Liu, J., & Yan, H., 2008. Sub-pixel stereo-matching for dem generation from narrow baseline stereo imagery, in *Proceedings of the Geoscience Remote Sensing Symposium, Boston, 2008*, vol. 3, pp. 1284–1287.

Mueller, K. J. & Rockwell, T. K., 1995. Late quaternary activity of the laguna salada fault in northern baja california, mexico, *Geological Society of America Bulletin*, **107**(1), 8–18.

Nissen, E., Krishnan, A. K., Arrowsmith, J. R., & Saripalli, S., 2012. Three-dimensional surface displacements and rotations from differencing pre-and post-earthquake lidar point clouds, *Geophysical Research Letters*, **39**(16).

Nissen, E., Maruyama, T., Arrowsmith, J. R., Elliott, J. R., Krishnan, A. K., Oskin, M. E., & Saripalli, S., 2014. Coseismic fault zone deformation revealed with differential lidar: Examples from japanese M_w 7 intraplate earthquakes, *Earth and Planetary Science Letters*, **405**, 244–256.

Nooner, S. L., Bennati, L., Calais, E., Buck, W. R., Hamling, I. J., Wright, T. J., & Lewi, E., 2009. Post-rifting relaxation in the afar region, ethiopia, *Geophysical Research Letters*, **36**(21).

Novak, K., 1992. Rectification of digital imagery, *Photogrammetric Engineering and Remote Sensing*, **58**(3), 339–344.

Okada, Y., 1985. Surface deformation due to shear and tensile faults in a half-space, *Bulletin of the seismological society of America*, **75**(4), 1135–1154.

Oskin, M. E., Arrowsmith, J. R., Corona, A. H., Elliott, A. J., Fletcher, J. M., Fielding, E. J., Gold, P. O., Garcia, J. J. G., Hudnut, K. W., Liu-Zeng, J., & Teran, O. J., 2012. Near-field deformation from the el mayor?cucapah earthquake revealed by differential lidar, *Science*, **335**(6069), 702–705.

Pacheco, M., Martín-Barajas, A., Elders, W., Espinosa-Cardeña, J. M., Helenes, J., & Segura, A., 2006. Stratigraphy and structure of the altar basin of nw sonora: Implications for the history of the colorado river delta and the salton trough, *Revista Mexicana de Ciencias, Geológicas*, **23**(1), 1–22.

Parsons, B. & Sclater, J. G., 1977. An analysis of the variation of ocean floor bathymetry and heat flow with age, *J. geophys. Res*, **82**(5), 803–827.

Peltzer, G. & Tapponnier, P., 1988. Formation and evolution of strike-slip faults, rifts, and basins during the india-asia collision: An experimental approach, *Journal of Geophysical Research: Solid Earth (1978–2012)*, **93**(B12), 15085–15117.

Peyret, M., Dominguez, S., Cattin, R., Champenois, J., Leroy, M., & Zajac, A., 2011. Present-day interseismic surface deformation along the longitudinal valley, eastern taiwan, from a ps-insar analysis of the ers satellite archives, *Journal of Geophysical Research: Solid Earth*, **116**(B3).

Pollitz, F. F., Peltzer, G., & Bürgmann, R., 2000. Mobility of continental mantle: Evidence from postseismic geodetic observations following the 1992 landers earthquake, *Journal of Geophysical Research: Solid Earth (1978–2012)*, **105**(B4), 8035–8054.

Pollitz, F. F., Bürgmann, R., & Thatcher, W., 2012. Illumination of rheological mantle heterogeneity by the m7. 2 2010 el mayor-cucapah earthquake, *Geochemistry, Geophysics, Geosystems*, **13**(6).

Press, W. H., Flannery, B. P., Teukolsky, S. A., & Vetterling, W. T., 1990. Numerical recipes.

R Core Team, 2013. R: A language and environment for statistical computing, ISBN 3-900051-07-0.

Rabus, B., Eineder, M., Roth, A., & Bamler, R., 2003. The shuttle radar topography mission?a new class of digital elevation models acquired by spaceborne radar, *ISPRS Journal of Photogrammetry and Remote Sensing*, **57**(4), 241 – 262.

Reid, H. F., 1910. *The mechanics of the earthquake*, vol. 2, Carnegie institution of Washington.

Riazanoff, S., 2004. *SPOT 123-4-5 Geometry Handbook*.

Rollins, C., Barbot, S., & Avouac, J.-P., 2015. Postseismic deformation following the 2010 m= 7.2 el mayor-cucapah earthquake: Observations, kinematic inversions, and dynamic models, *Pure and Applied Geophysics*, **172**(5), 1305–1358.

Rosen, P. A., Henley, S., Peltzer, G., & Simons, M., 2004. Update Repeat Orbit Interferometry Package Released, *EOS Transactions*, **85**, 47–47.

Rowland, J., Baker, E., Ebinger, C., Keir, D., Kidane, T., Biggs, J., Hayward, N., & Wright, T., 2007a. Fault growth at a nascent slow-spreading ridge: 2005 Dabbahu rifting episode, Afar, *Geophysical Journal International*, **442**(20).

Rowland, J., Baker, E., Ebinger, C., Keir, D., Kidane, T., Biggs, J., Hayward, N., & Wright, T., 2007b. Fault growth at a nascent slow-spreading ridge: 2005 dabbahu rifting episode, afar, *Geophysical Journal International*, **171**(3), 1226–1246.

Rubin, A., 1992. Dike-induced faulting and graben subsidence in volcanic rift zones, *Journal of Geophysical Research*, **97**, 1839–1858.

Rychert, C. A., Hammond, J. O., Harmon, N., Kendall, J. M., Keir, D., Ebinger, C., Bastow, I. D., Ayele, A., Belachew, M., & Stuart, G., 2012. Volcanism in the afar rift sustained by decompression melting with minimal plume influence, *Nature Geoscience*, **5**(6), 406–409.

Ryder, I., Parsons, B., Wright, T. J., & Funning, G. J., 2007. Post-seismic motion following the 1997 manyi (tibet) earthquake: Insar observations and modelling, *Geophysical Journal International*, **169**(3), 1009–1027.

Sandwell, D. T., Wei, M., Gonzales, J., Gonzales, A., Lipovski, B., Funning, G., Fialko, Y., Mellors, R., Agnew, D., PET-ERSON, R., et al., 2010. Insar and gps measurements of crustal deformation from the el mayor earthquake: liquefaction and triggered slip, *Cordilleran section, Abstract LB1-8, Anaheim, California*.

Savage, J., Lisowski, M., King, N., & Gross, W., 1994. Strain accumulation along the laguna salada fault, baja california, mexico, *Journal of geophysical research*, **99**(B9), 18109–18.

Scheidt, S. P. & Lancaster, N., 2013. The application of cosi-corr to determine dune system dynamics in the southern namib desert using aster data, *Earth Surface Processes and Landforms*, **38**(9), 1004–1019.

Scherler, D., Leprince, S., & Strecker, M. R., 2008. Glacier-surface velocities in alpine terrain from optical satellite imagery?accuracy improvement and quality assessment, *Remote Sensing of Environment*, **112**(10), 3806 – 3819.

Scherler, D., Bookhagen, B., & Strecker, M. R., 2011. Spatially variable response of himalayan glaciers to climate change affected by debris cover, *Nature geoscience*, **4**(3), 156–159.

Sigmundsson, F., Durand, P., & Massonnet, D., 1999. Opening of an eruptive fissure and seaward displacement at Piton de la Fournaise volcano measured by radarsat satellite radar interferometry, *Geophysical Research Letters*, **26**(5), 533–536.

Simmons, N., Myers, S., & Johannesson, G., 2011. Global-scale p wave tomography optimized for prediction of teleseismic and regional travel times for middle east events: 2. tomographic inversion, *Journal of Geophysical Research: Solid Earth (1978–2012)*, **116**(B4).

Simmons, N. A., Forte, A. M., & Grand, S. P., 2007. Thermochemical structure and dynamics of the african superplume, *Geophysical Research Letters*, **34**(2).

Simons, M., Fialko, Y., & Rivera, L., 2002. Coseismic deformation from the 1999 mw 7.1 hector mine, california, earthquake as inferred from insar and gps observations, *Bulletin of the Seismological Society of America*, **92**(4), 1390–1402.

Sonder, L. J. & England, P. C., 1989. Effects of a temperature-dependent rheology on large-scale continental extension, *Journal of Geophysical Research: Solid Earth (1978–2012)*, **94**(B6), 7603–7619.

Stamps, D., Flesch, L., Calais, E., & Ghosh, A., 2014. Current kinematics and dynamics of africa and the east african rift system, *Journal of Geophysical Research: Solid Earth*, **119**(6), 5161–5186.

Steketee, J., 1958. On volterra's dislocations in a semi-infinite elastic medium, *Canadian Journal of Physics*, **36**(2), 192–205.

Stone, H., Orchard, M., Chang, E.-C., & Martucci, S., 2001. A fast direct fourier-based algorithm for subpixel registration of images, *Geoscience and Remote Sensing, IEEE Transactions on*, **39**(10), 2235 –2243.

Stumpf, A., Malet, J.-P., Allemand, P., & Ulrich, P., 2014. Surface reconstruction and landslide displacement measurements with pléiades satellite images, *ISPRS Journal of Photogrammetry and Remote Sensing*, **95**, 1–12.

SULFSOFT, 2004. Asterdtm 2.2:installation and user's guide.

Sun, J., Shen, Z., Xu, X., & Bürgmann, R., 2008. Synthetic normal faulting of the 9 january 2008 nima (tibet) earthquake from conventional and along-track sar interferometry, *Geophysical Research Letters*, **35**(22).

Suncar, O. E., Rathje, E. M., & Buckley, S. M., 2013. Deformations of a rapidly moving landslide from high-resolution optical satellite imagery, *Proc., GeoCongress 2013*, pp. 269–278.

Tapponnier, P., Peltzer, G., & Armijo, R., 1986. On the mechanics of the collision between india and asia, *Geological Society, London, Special Publications*, **19**(1), 113–157.

Tarantola, A. & Valette, B., 1982. Generalized nonlinear inverse problems solved using the least squares criterion, *Rev. Geophys. Space Phys*, **20**(2), 219–232.

Tatarski, V., 1961. Wave propagation in a turbulent medium, *Engl. transl. RA Silvermann.) New York: McGraw-Hill*.

Thatcher, W. & Pollitz, F. F., 2008. Temporal evolution of continental lithospheric strength in actively deforming regions, *GSA TODAY*, **18**(4/5), 4.

Tong, X., Sandwell, D., & Smith-Konter, B., 2013. High-resolution interseismic velocity data along the san andreas fault from gps and insar, *Journal of Geophysical Research: Solid Earth*, **118**(1), 369–389.

Toutin, T., 2004. Review article: Geometric processing of remote sensing images: models, algorithms and methods, *International Journal of Remote Sensing*, **25**(10), 1893–1924.

Uchide, T., Yao, H., & Shearer, P. M., 2013. Spatio-temporal distribution of fault slip and high-frequency radiation of the 2010 El Mayor-Cucapah, Mexico earthquake, *Journal of Geophysical Research*, **118**, 1546–1555.

van Puymbroeck, N., Michel, R., Binet, R., Avouac, J.-P., & Taboury, J., 2000. Measuring earthquakes from optical satellite images, *Optical Society of America*, **39**(20).

Vigny, C., de Chabalier, J.-B., Ruegg, J.-C., Huchon, P., Feigl, K. L., Cattin, R., Asfaw, L., & Kanbari, K., 2007. Twenty-five years of geodetic measurements along the tadjoura-asal rift system, djibouti, east africa, *Journal of Geophysical Research: Solid Earth (1978–2012)*, **112**(B6).

Wald, D. J. & Heaton, T. H., 1994. Spatial and temporal distribution of slip for the 1992 landers, california, earthquake, *Bulletin of the Seismological Society of America*, **84**(3), 668–691.

Wallace, L. M., Beavan, J., McCaffrey, R., Berryman, K., & Denys, P., 2007. Balancing the plate motion budget in the south island, new zealand using gps, geological and seismological data, *Geophysical Journal International*, **168**(1), 332–352.

Walters, R., Holley, R., Parsons, B., & Wright, T., 2011. Interseismic strain accumulation across the north anatolian fault from envisat insar measurements, *Geophysical research letters*, **38**(5).

Wang, H., Wright, T., & Biggs, J., 2009. Interseismic slip rate of the northwestern xianshuihe fault from insar data, *Geophysical Research Letters*, **36**(3).

Watts, A. & Ten Brink, U., 1989. Crustal structure, flexure, and subsidence history of the hawaiian islands, *Journal of Geophysical Research: Solid Earth (1978–2012)*, **94**(B8), 10473–10500.

Watts, A., Bodine, J., & Steckler, M., 1980. Observations of flexure and the state of stress in the oceanic lithosphere, *Journal of Geophysical Research: Solid Earth (1978–2012)*, **85**(B11), 6369–6376.

Watts, A., Karner, G., & Steckler, M., 1982. Lithospheric flexure and the evolution of sedimentary basins, *Philosophical Transactions of the Royal Society of London A: Mathematical, Physical and Engineering Sciences*, **305**(1489), 249–281.

Wei, S., Fielding, E., Leprince, S., Sladen, A., Avouac, J.-P., Helmberger, D., Hauksson, E., Chu, R., Simons, M., Hudnut, K., et al., 2011. Superficial simplicity of the 2010 el mayor-cucapah earthquake of baja california in mexico, *Nature geoscience*, **4**(9), 615–618.

Wessel, P., 1992. Thermal stresses and the bimodal distribution of elastic thickness estimates of the oceanic lithosphere, *Journal of Geophysical Research: Solid Earth (1978–2012)*, **97**(B10), 14177–14193.

White, R. & McKenzie, D., 1989. Magmatism at rift zones: the generation of volcanic continental margins and flood basalts, *Journal of Geophysical Research: Solid Earth (1978–2012)*, **94**(B6), 7685–7729.

Wiens, D. A. & Stein, S., 1984. Intraplate seismicity and stresses in young oceanic lithosphere, *Journal of Geophysical Research: Solid Earth (1978–2012)*, **89**(B13), 11442–11464.

Williams, C., DeAngelo, J., & Galanis, P., 2012. Heat flow in the salton trough revisited and implications for regional tectonics, in *AGU Fall Meeting Abstracts*, vol. 1, p. 08.

Williams, C. R., Arnadottir, T., & Segall, P., 1993. Coseismic deformation and dislocation models of the 1989 loma prieta earthquake derived from global positioning system measurements, *Journal of Geophysical Research: Solid Earth (1978–2012)*, **98**(B3), 4567–4578.

Wolf, R. P. & Dewitt, B., 2000. *Elements of Photogrammetry with Applications in GIS*, McGraw Hill, 3rd edn.

Wright, T., Parsons, B., Jackson, J., Haynes, M., Fielding, E., England, P., & Clarke, P., 1999. Source parameters of the 1 october 1995 dinar (turkey) earthquake from sar interferometry and seismic bodywave modelling, *Earth and Planetary Science Letters*, **172**(1), 23–37.

Wright, T., Fielding, E., & Parsons, B., 2001. Triggered slip: observations of the 17 august 1999 izmit (turkey) earthquake using radar interferometry, *Geophysical Research Letters*, **28**(6), 1079–1082.

Wright, T., Parsons, B., & Lu, Z., 2004a. Toward mapping surface deformation in three dimensions using insar, *Geophysical Research Letters*, **31**.

Wright, T., Parsons, B., & Lu, Z., 2004b. Toward mapping surface deformation in three dimensions using insar, *Geophysical Research Letters*, **31**(1).

Wright, T., Ebinger, C., Biggs, J., Ayele, A., Yirgu, G., Keir, D., & Stork, A., 2006. Magma-maintained rift segmentation at continental rupture in the 2005 Afar dyking episode, *Nature*, **442**(20).

Wright, T. J., 2002. Remote monitoring of the earthquake cycle using satellite radar interferometry, *Philosophical Transactions of the Royal Society of London A: Mathematical, Physical and Engineering Sciences*, **360**(1801), 2873–2888.

Wright, T. J., Lu, Z., & Wicks, C., 2003. Source model for the mw 6.7, 23 october 2002, nenana mountain earthquake (alaska) from insar, *Geophysical Research Letters*, **30**(18).

Wright, T. J., Parsons, B., England, P. C., & Fielding, E. J., 2004c. Insar observations of low slip rates on the major faults of western tibet, *Science*, **305**(5681), 236–239.

Yan, Z. & Clayton, R., 2007. Regional mapping of the crustal structure in southern california from receiver functions, *Journal of Geophysical Research: Solid Earth (1978–2012)*, **112**(B5).

Yokota, Y., Koketsu, K., Fujii, Y., Satake, K., Sakai, S., Shinohara, M., & Kanazawa, T., 2011. Joint inversion of strong motion, teleseismic, geodetic, and tsunami datasets for the rupture process of the 2011 tohoku earthquake, *Geophysical Research Letters*, **38**(7).

Zebker, H. A., Rosen, P. A., & Hensley, S., 1997. Atmospheric effects in interferometric synthetic aperture radar surface deformation and topographic maps, *Journal of Geophysical Research: Solid Earth (1978–2012)*, **102**(B4), 7547–7563.

Zhu, L. & Kanamori, H., 2000. Moho depth variation in southern california from teleseismic receiver functions, *Journal of Geophysical Research B*, **105**(B2), 2969–2980.

Zielke, O., Arrowsmith, J. R., Ludwig, L. G., & Akçiz, S. O., 2010. Slip in the 1857 and earlier large earthquakes along the Carrizo plain, San Andreas fault, *Science*, **327**, 1119–1122.